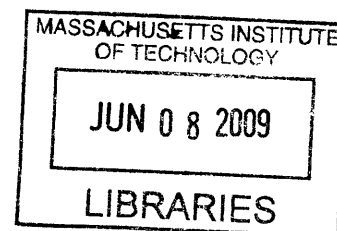


Validation of angle-resolved polarized light scattering spectroscopy as a diagnostic tool for pre-cancer detection

by

Maxim M. Kalashnikov
B.S., Moscow Institute of Physics and Technology (1999)



Submitted to the Department of Chemistry
in partial fulfillment of the requirements for the degree of

ARCHIVES

Doctor of Philosophy

at the

MASSACHUSETTS INSTITUTE OF TECHNOLOGY
June 2009


© Massachusetts Institute of Technology 2009. All rights reserved.

Author Department of Chemistry
March 24, 2009

Certified by Prof. Michael S. Feld
Professor of Physics and Director, G.R. Harrison Spectroscopy Laboratory
Thesis Supervisor

Accepted by Prof. Robert W. Field
Haslam and Dewey Professor of Chemistry
Chairman, Department Committee on Graduate Students

This doctoral thesis has been examined by the following thesis committee:

Professor Michael S. Feld 

Professor Robert W. Field _____

Professor Mounji G. Bawendi _____


Dr. Kamran Badizadegan _____


Validation of angle-resolved polarized light scattering spectroscopy as a diagnostic tool for pre-cancer detection

by

Maxim M. Kalashnikov

Submitted to the Department of Chemistry
in partial fulfillment of the requirements for the degree of
Doctor of Philosophy

Abstract

Light scattering spectroscopy has emerged as a valuable diagnostic tool for cancer diagnoses in the past ten years. The interaction of light with cellular structures brings out information about morphological changes accompanying malignancy at early stages. The virtue of this technique is to extract key morphological information such as size distribution of nucleus and submicron-sized particles with minimal data acquisition and model-based data analysis. This enables wide area screening and onsite analysis, critical to the clinical applications. The extracted information, however, strongly depends on the selection of the specific model of the cell/tissue scattering and on constraints from prior knowledge about the sample, leaving the validity of the information questionable.

The main focus of this thesis work is to validate various models of cell/tissue scattering used in light scattering spectroscopy. Conventional intensity-based light scattering spectroscopy, which records intensity distribution at the angular plane, was set up to measure angular and wavelength distribution of scattered light in cell monolayers, cell suspensions and rat esophagus tissues for both forward and backward scattering. Morphological information was extracted from cell models such as the cell model based on Mie theory and the power-law model. At the same time, field-based microscopy was used to measure 3D refractive index distributions of single live cells and to provide intensity-based light scattering spectroscopy with a more realistic optical model of a cell. From the index tomogram, the contribution of individual organelles and cellular components to the light scattering was determined without the need for modeling. Indeed, field-based microscopy was used as a validation tool for the various models and assumptions used in the intensity-based approach.

Two types of scattering behavior had been previously reported for a visible range of wavelengths and an angular range of forward-to-backscattering in cells and tissues: an oscillatory behavior of scattering intensity in angle near exact forward and exact backward scatterings associated with cell body or nuclei, and smooth power-like behavior in wavelength for all scattering angles except near forward scattering.

This study addresses two key questions related to the two types of behavior mentioned above: feasibility of extracting nuclear size distribution from oscillatory behavior, and extracting cellular parameter(s) characterizing smooth power law decay.

To answer the first question, we performed a light scattering study with a single cell using field-based microscopy. Relative contributions to forward scattering of the cell border, the nucleus and other sub-cellular structures were established for the HT29 cell. Nuclear scattering is found to be small compared to the cell border scattering and sensitive to scattering by other sub-cellular structures.

In agreement with single cell results, the cell border signal dominates forward scattering in cell suspensions of HeLa cells. This was confirmed by modeling with Mie theory and by index-matching the cell-media interface. Cell border signal was not observed in backscattering from cell suspensions, even with the use of large particle signal enhancement methods. Thus, the nuclear signal is estimated to be a few orders of magnitude below the current system sensitivity level and mixed with other scatterers' signals. The main scattering feature is a smooth power law in scattering wavelength.

The exponent characterizing smooth power law decay, can separate normal and pre-cancerous tissues within the same tissue type, such as rat esophagus tissue. The range of power law exponents observed in the rat tissue experiments overlaps with the range of power law exponents extracted from HeLa, HT29 and T84 monolayers. Therefore, the power law exponent does not have enough dynamic range to separate independent samples with quite different morphology.

In conjunction with the last statement, the power law behavior is explained by three different morphological base sets: the Mie model, describing cell as a collection of spheres, the Fourier model, in which cell is described as combination of periodic structures with a continuous range of spatial frequencies, and a fractal model, in which index fluctuations inside the cell are described by von Karman correlation function. Although all three models can explain the power law behavior, the Fourier model is the most feasible one, because, unlike the other models, no assumptions are made about structure of the sample.

Thesis supervisor: Michael S. Feld

Title: Professor of Physics and Director, G.R. Harrison Spectroscopy Laboratory

Acknowledgments

I would like to thank my advisor Professor Michael Feld for sharing with me his way of conducting scientific research. During many (more than average!) years in Spectroscopy Laboratory, I have learned to approach scientific problems with diligence, and that some of the seemingly dead-end problems do have resolution, if enough time and effort is in place. I respect Professor Feld's devotion to science and his ability to successfully manage cutting edge multi-project research.

I would also like to thank Professor Feld for providing me not only with his own advice and supervision, but also with an excellent support group. First, Dr. Martin Hunter, a post-doctorial fellow in Spectroscopy Laboratory, with whom I pulled quite a few all-nighters doing rat esophagus tissue studies. He was leading the project in all aspects during tissue studies for quite a few years. In the end, he became a fractal guy, but did not manage to turn me into one. Dr. Chung-Chieh Yu helped me a lot in designing, building and testing the best intensity-based light scattering instrument ever built in the laboratory. Finally, without Dr. Wonshik Choi and his recent work (only about 3 years old to date), my thesis would be at least 40 pages shorter and probably would have 40% less scientific weight. The results of collaborative effort on studying of single cell index tomograms provided an excellent support and backbone for my cell monolayer and cell suspension data analysis. Dr. Kamran Badizadegan helped me a lot with the cell biology aspects of the research. He taught me how to grow cells in the first place, and also was a very good person to get feedback from on general research problems.

When one runs into a wall in research, a light chat with one of his or her colleagues helps a lot. I did a lot of chatting with Condon, Zoya and my friend Jelena. My great respects also go to the "Korean body" in our lab. They show a great combination of diligence, politeness, helpfulness and friendliness, especially, the ones with whom I interacted with the most: Wonshik, Niyom, Yongjin and Seungeun.

I would also like to thank my family, especially my wife Essie and my son Andrushka, and my friends for always being there for me. The last 11 months of my PhD really took all of my time and took me away from them. I am happy about the work I have accomplished, and I am extremely glad to return back to the normal life with my family and friends.

Contents

Abstract	3
Acknowledgments	5
Contents.....	6
List of figures.....	10
List of tables.....	20
Introduction.....	21
Background and significance	23
2.1 Light scattering spectroscopy and cancer diagnosis	23
2.2 Light scattering from cells and tissues	24
2.2.1 Sub-cellular structural basis for light scattering	24
2.2.2 Modeling light scattering from cells.....	26
2.2.3 Contribution of cells to tissue scattering	27
2.3 Current work motivation and significance.....	27
References.....	28
Characterization of biological samples: rat esophagus cancer model and cell lines.....	32
3.1 Cell lines: HT29, HeLa, T84	32
3.1.1 Cell line selection.....	32
3.1.2 Cell sample growth and preparation	33
3.1.3 Cell sample characterization	35
3.2 Rat Esophageal Cancer Model	37
3.2.1 Animal Model Selection.....	37
3.2.2 Rat esophagus study protocol.....	38
3.2.3 Tissue sample preparation, registration and grading	38
References.....	43
Theoretical modeling of light scattering	45
4.1 Mie theory for spherical scatterer.....	45
4.1.1 Mie theory solution.....	45
4.1.2 Definition of scattering parameters.....	48
4.1.3 Describing properties of Mie solution: Analytical approximations.....	49
4.2 Born approximation of weak scattering	52
4.3 Rytov approximation of weak change in phase.....	53

References.....	54
Design principles and calibration of light scattering instruments	55
5.1 Principles of Fourier-plane and Image plane light scattering spectroscopy	55
5.1.1 Fourier-plane imaging	55
5.2 Numerical simulations and instrument optimization using Mie theory	56
5.2.1 Numerical implementation of Mie theory	56
5.2.2 Mie-optimized detection of large and small particles in angle	57
5.2.3 Implementation of Mie optimization in wavelength.....	59
5.2.3 Simulating experimental data.....	61
5.2.4 Analyzing experimental data.....	64
5.3 Instruments for intensity-based light scattering measurements: Forward/Backscattering at $\varphi=45^\circ$ combined instrument.....	66
5.3.1 Experimental system design.....	67
5.3.2 Experimental system alignment	71
5.3.3 Measuring instrument response and calibration.....	72
5.3.4 Forward scattering Mie analysis of bead suspensions	76
5.3.5 Backscattering Mie analysis of beads.....	79
5.3.6 Bead mixtures.....	82
5.4 Instruments for intensity-based light scattering measurements: Phi-differential backscattering parallel.....	84
5.4.1 Experimental system, alignment and calibration	84
5.4.2 Bead mixtures.....	85
5.5 Instruments for intensity-based light scattering measurements: Polarization gating for backscattering	86
5.5.1 Experimental system description	86
5.5.2 Bead calibration	87
5.5.3 R99 correction factor	87
5.5.4 Effect of incidence angle	89
5.5.5 Rotating Fourier Plane.....	90
References.....	92
Sub-cellular contributions to single cell scattering and index tomogram manipulation	93
6.1 Optical diffraction tomography using Born/Rytov approximations	93
6.2 Solving direct scattering problem using Born/Rytov/Projection approximation in angle	95

6.2.1 Obtaining angular scattering from tomogram using Born/Rytov approximations .	95
6.2.2 Validation of Rytov/Born approximations using Mie theory.....	96
6.2.3 Validity of Rytov/Born/Projection approximation in reproducing original scattering data	99
6.2.4 Effect of shape on Mie interpretation of scattering from tomogram	101
6.3 Extracting the contribution of sub-cellular components to the scattering distribution	103
6.3.1 Manipulating cell index tomogram.....	103
6.3.2 Mie analysis of Born approximation scattering from manipulated tomograms....	105
6.3.3 Cell boundary or nucleus boundary versus heterogeneous structures in the cell..	106
6.4 Study single cell scattering in wavelength.....	108
6.5 Extrapolation of single cell study to multi-cellular systems.....	111
References	113
Experiments with cell monolayers and suspensions.....	114
7.1 Forward and backscattering of cell suspensions	114
7.1.1 Expanding single cell results to multi-cellular systems.....	114
7.1.2 Measurements of HT29 and HeLa cell suspensions in forward scattering	116
7.1.3 Analyzing HeLa cell suspension data	117
7.1.4 Index-matching experiment in forward scattering.....	120
7.1.5 Index-matching experiment in backscattering	121
7.1.6 Backscattering system sensitivity and cell-media interface scattering.....	123
7.2 Backscattering from cell monolayers.....	125
7.2.1 Large particle signal through enhancement methods	125
7.2.2 Measuring power law in backscattering of cell monolayers	127
7.2.3 Modeling power law in backscattering.....	129
References	136
Experiments with rat esophagus tissue.....	137
8.1 Extracting power laws from rat esophagus.....	138
8.1.1 Polarization gating	138
8.1.2 Polarized scattering measurements from rat tissues: Normal vs. NMBA-treated	139
8.2 Analysis of power laws in rat esophagus data	141
8.2.1 Power law exponent in wavelength of Normal vs. NMBA groups	141
8.2.2 Polarized scattering measurements from rat tissues: Chemopreventive control vs. NMBA-chemopreventive group.....	142
8.2.3 Polarized scattering measurements from rat tissues: Epithelial data.....	143

8.2.4 Polarized scattering measurements from rat tissues: Correlating power law exponent and sample thickness	146
8.2.5 Testing polarization gating: Bead suspensions of varying optical density	147
8.3 Von Karman Analysis of power laws in rat esophagus	149
8.3.1 Von Karman-Born model	149
8.3.2 Applying von Karman to rat data analysis	151
References	152
Impact of the current work on modeling scattering from cells and tissues.....	154
9.1 Summary of experimental methods, single cell, cell monolayer/suspension and rat tissue results	154
9.1.1 Experimental methods	154
9.1.2 Single cell results	156
9.1.3 Cell monolayer and cell suspension results.....	157
9.1.4 Rat tissue experiments in backscattering.....	160
9.2 Modeling scattering from cells. Comparison with previously published works	161
9.2.1 Unified model of scattering based on single cell and cell monolayer studies.....	161
9.2.2 <i>Other works with HT29, HeLa and T84 cell monolayers</i>	164
9.2.3 Other cell monolayer/suspension scattering studies	167
9.2.4 Relevance of other tissue studies	172
9.3 Conclusion and future studies design.....	173
9.3.1 Conclusion and summary of this thesis and published works.....	173
9.3.2 Future designs of light scattering studies	175
References	175
Appendix	178
Feasibility of extracting nuclear morphology from tissue backscattering	178
References:.....	181
Curriculum Vitae	183

List of figures

Figure 2 1 H&E stained image of human cervix	24
Figure 2 2 Sub-cellular structure a) Schematic representation of cellular organelles b) Phase contrast image of SiHa cell sample	25
Figure 2 3 Modeling cell structure from a scattering standpoint a) Nucleus with index n_1 surrounded by cytoplasm n_0 b) Nucleus in an average refractive index of cell n_0 plus cell n_0 in the media n_2 c) Collection of small spheres	26
Figure 3 1 Cell holder geometries a) Two #1 thickness coverslips (1), cells (2) are in-between b) Plastic dish ((3), $\varnothing 50$ mm*7 mm height) with glass bottom ((4) $\varnothing 25$ mm, #0), cells (2) on top of glass bottom covered by #1 glass coverslip (1) c) Two #0 thickness coverslips (1), cells (2) on the bottom coverslip, sticky insert ((5), $\varnothing 20$ mm)	33
Figure 3 2 Phase contrast and fluorescence images for three cell monolayers at 40x	35
Figure 3 3 Phase contrast image of HT29 cell suspension, 20x	36
Figure 3 4 Camera photographs of various rat samples in a sample holder. Measurement spots are marked (black circles). Histopathological section sites are marked (green lines). a) Normal rat tissue sample b) Extracted epithelium of a normal sample c) Dysplastic rat tissue sample with papilloma.....	39
Figure 3 5 H&E histological sections of rat esophageal tissue at 20x a) Normal section: three epithelium sub-layers, K-keratin, I-intermediate, B-basal, and connective tissue C. b) Dysplastic tissue and its properties: increase in cellular density of basal cell layer (1), increase in density of intermediate layer (2), thickening of keratin (3)	40
Figure 3 6 H&E histological sections of rat esophageal tissue at 10x a) Uniformity of normal tissue section b) Variability of dysplastic tissue sample	41
Figure 3 7 H&E histological sections of rat esophageal epithelium a) Normal section b) Dysplastic section	42
Figure 4 1 Mie scattering diagram: XYZ – laboratory system; k_s and k_i form scattering plane (blue triangle); E_i – incident field, E_s – scattered field; E_{i1} , E_{i1} , E_{i1} , E_{i1} ,-projections of incident/scattered field; θ - scattering angle, φ -azimuthal scattering angle;.....	46
Figure 4 2 Rayleigh scattering cross-section for 10 nm sphere a) Wavelength spectrum (blue) and power law with -4 exponent (black) b) Co-polarized in plane and out of plane components; Cross-polarized component equals to zero	50
Figure 4 3 Rayleigh-Gans scattering oscillatory behavior in cross-section for 1 μm and 2 μm spheres a) Wavelength spectra at $\theta=180^\circ$ b) Angular spectra at $\lambda=550$ nm	51
Figure 5 1 Fourier-plane formation in light scattering experiments.....	56
Figure 5 2 Angular scattering maps for 5 μm and 50 nm at $\lambda=550$ nm (see text for details)..	57
Figure 5 3 φ -differential scattering method applied to isolated 10 μm beads (a-d) and mixtures of 10 μm and 100 nm.....	60

Figure 5 4 Cross-polarized measurements at $\varphi=45^\circ$ for isolated 10 μm beads (a-d) and mixtures of 10 μm and 100 nm (c-d).....	60
Figure 5 5 Effect of size distribution on light scattering spectra a) Shape of Gaussian size distribution depending on the width values (0-2 μm) b) Wavelength spectra at $\theta=180^\circ$ for different distribution widths c) Angular spectra at $\lambda=400$ nm for different distribution widths	62
Figure 5 6 Shape of scattering spectra depending on instrument response a) Variable response in wavelength (0-30 nm) at $\theta=180^\circ$ b) Variable response in angle (0° - 2°) at $\lambda=400$ nm.....	63
Figure 5 7 Test fitting of simulated 10 μm spectra for variable initial conditions 8.5 μm and 8 μm a,c) Cross-polarized wavelength spectra at $\theta=175^\circ$ (blue-simulated data, red-fitting result) b,d) Forward scattering wavelength spectra at $\theta=5^\circ$ e,f) Error function for full range of fitting parameters diameter and standard deviation	65
Figure 5 8 Sketch of goniometric light scattering system.....	67
Figure 5 9 Light source and 4f-beam control system (top graph) Light delivery for forward and backscattering experiments (bottom graph).....	68
Figure 5 10 Emission spectrum of Xe arc lamp (marked as 6251)	69
Figure 5 11 Collection arm of the experimental system	70
Figure 5 12 Calibration of experimental system a) 2D CCD image wavelength along x-axis and angle along y-axis b) Mercury lines for wavelength calibration, slit opening of 10 μm and 750 μm width c) Angular response of experimental system -unscattered beam on the angular axis.....	73
Figure 5 13 Data normalization of 10 μm bead sample in perpendicular I_\perp in backscattering a) Raw data, color bar in CCD counts b) Background measurement (BG) in CCD counts c) 99% reflectance standard measurement in CCD counts, colorbar $\times 10^5$ d) Normalized data in 1/R99 units, colorbar $\times 10^{-3}$	74
Figure 5 14 Correction factor for forward and backscattering delivery difference in incident light wavelength shape	74
Figure 5 15 Angular calibration of light scattering system with 20 μm bead suspension in water in perpendicular, I_\perp a) Fourier plane image, slit open at 3mm, $\lambda=650$ nm b) Angular axis calibration without consideration of air-water interface effect (data –blue curve, Mie simulations – red) c) Angular axis calibration with consideration of air-water interface.....	75
Figure 5 16 Calibration verification using forward and backscattering perpendicular measurements for 10 μm bead suspension in water a) Forward scattering data at 650 nm, log scale, data-blue curve, Mie simulation-red b) Backscattering perpendicular data for 650 nm, scale 10^{-4}	76
Figure 5 17 Choosing step size in angle and wavelength for lookup table generation for forward scattering, 12 μm bead suspension a) Convolved wavelength spectrum at $\theta=10^\circ$ with convolution width between 0.3 and 3 nm b) Convolved angular spectra at $\lambda=400$ nm and convolution width of 0.01° - 0.5° c) Table of selected ranges for parameter values.....	77
Figure 5 18 Lookup table analysis of forward scattering data for 10 μm bead suspension in water a) Normalized scattering data (left), log scale -3-0.5 of 1/R99 units and best Mie theory prediction for 3 angles and 3 wavelengths log scale 1.5-5 (right) b) Wavelength spectra for	

three values of scattering angle, linear scale, (data –red and Mie theory-black) c) Angular spectra for three wavelength values, log scale.....	78
Figure 5 19 Lookup table analysis of forward scattering data for 10 μm bead suspension in oil a) Normalized scattering data (left) and best Mie theory prediction from beads in water experiment (right) b) Wavelength spectra for three values of scattering angle, linear scale (data–red and Mie theory-black) c) Angular spectra for three wavelength values, log scale, angular range is reduced according to oil-air interface	79
Figure 5 20 Lookup table analysis of backscattering perpendicular data for 10 μm bead suspension in water a) Normalized scattering data (left) and best Mie theory prediction from forward scattering b) Wavelength spectra for three values of scattering angle, linear scale (data–red and Mie theory-black) c) Angular spectra for three wavelength values, linear scale	80
Figure 5 21 Calibration with 10 μm bead suspension in oil in backscattering perpendicular a) Mie predictions for change in backscattering cross-section with reduction of relative refractive index contrast, log scale, $\theta=180^\circ$ b) Phase contrast image 20x of the bead sample c) Normalized scattering data d) Theoretical prediction based on forward scattering predictions, note difference in number of oscillations from the data.....	81
Figure 5 22 Calibration of backscattering parallel with 50 nm bead suspension in water a) Normalized scattering data b) Mie fit (blue-curve) to the wavelength spectrum (green) at $\theta=177^\circ$	81
Figure 5 23 Lookup table analysis of 10 μm and 50 nm bead suspension mixture a) Normalized mixture data in backscattering parallel, linear scale, colorbar $0-10^{-3}$ b) Normalized mixture data in backscattering perpendicular, linear scale, colorbar $0-10^{-4}$ c) Normalized mixture data in forward scattering, log scale, colorbar -3.5 to 1	82
Figure 5 24 Mie analysis of mixture data from sample 2 a) Mie prediction for angular spectrum of best fit size distribution, averaged over wavelength, minimum location (black circle) b) Wavelength spectrum of normalized mixture data at $\theta=169.8$ (black), predicted large particle contribution to the signal for two fitted values for number of large particles (red and blue), linear scale $0-6*10^{-4}$ c) Mean-centered data (red) and best Mie simulation from lookup table $d=64\pm 16$ nm(blue) d) Error value for diameter from lookup table comparison to data, y-axis – error-value in $1/R99$ units	84
Figure 5 25 Calibration of the experimental system using 5 μm bead data a) Normalized parallel backscattering data b) Wavelength scattering data at exact backscattering (red) and best Mie theory prediction (black) c) Angular scattering data at 609 nm and best Mie theory predictions	85
Figure 5 26 Application of ϕ -differential technique in backscattering to measurements of bead suspensions a) 5 μm isolated bead wavelength spectra for individual azimuthal angle values b) ϕ -differential wavelength spectra (blue) and Mie theory fit (red) to isolated 5 μm data c) 5 μm and 50 nm mixture wavelength data, power law fit to individual azimuthal spectra d) ϕ -differential signal from residuals between power law fit and the data (blue) compared to Mie fit of 5 μm (red).....	85
Figure 5 27 Experimental set-up for backscattering measurements in tissues	86

Figure 5 28 Calibration of the experimental system using 10 μm beads a) Angular-wavelength scattering map b) Wavelength scattering data at exact backscattering (black) with Mie theory (red) manual fit ($\theta=0^\circ$ corresponds to exact backscattering) c) Wavelength scattering data at exact backscattering (black) with Mie theory (red) manual fit ($\theta=2^\circ$ corresponds to 178° backscattering)..... 87

Figure 5 29 Polarization ratio $I_{||}/I_{\perp}$ for reflectance standard response a) 99% reflectance standard ratio b) BaSO4 reflectance ratio c) 5% reflectance standard..... 89

Figure 5 30 Forward scattering contamination in backscattering a) Variable incident angle geometry b) Experimental data 10 μm bead suspension for Fourier plane image at 10° incidence c) Same data with 20° incidence d) Same data with 45° incidence 90

Figure 5 31 Polarization mixing on reflection surfaces a) s- and p- polarization definition with respect to incident and scattered beams b) Ratio of reflectivities of s- and p- polarized light off of air-glass interface c) Fourier image of 10 μm bead suspension with polarization aligned with s- or p-polarization d) 45° rotation of Fourier plane from c) with polarizer-analyzer rotation, polarization e) 45° rotation of Fourier plane from c) with coherent fiber bundle 91

Figure 6 1 a) Angular scattering spectrum generated with Born approximation for 10 μm sphere, $n=1.377$, x-axis scattering angle b) Middle section of 2 μm sphere, axes dimensions are in microns c) Total accumulated phase delay for Born/Rytov approximation, axes in micron d) Total accumulated phase delay for Projection approximation, axes in micron..... 98

Figure 6 2 Angular light scattering spectra generated from Rytov approximation (blue) and Mie theory fits (black), $n(\text{media})=1.337$, $\lambda=633\text{ nm}$ a) 2 μm sphere, $n=1.347$ b) 10 μm sphere, $n=1.347$ c) 10 μm sphere, $n=1.377$ d) 20 μm sphere, $n=1.377$ 98

Figure 6 3 Processing from index tomogram to scattering spectra, 6 μm , $n=1.59$, $n_o=1.56$ a) Middle section of index tomogram, axes in microns b) Scattering field distribution in Fourier plane, axes CCD pixels c) Angular spectrum of scattering amplitude at $\phi=0^\circ$, axis in degrees d) Angular spectrum of scattering amplitude averaged over azimuthal angles 99

Figure 6 4 Comparison of approximation generated data to original scattering spectra, 6 μm beads in oil a) Angular spectrum generated with Born/Rytov approximation (blue, black) and original scattering spectrum (green) b) Projection approximation angular scattering (red) and original data (green) c) Sensitivity for inclusion or not inclusion of complex part of refractive index in Rytov approximation 100

Figure 6 5 Reconstruction of original scattering spectra for HT29 cell index tomogram a) Middle section of index tomogram, axes in microns b) Angular scattering spectrum generated using Born approximation (blue curve) and original data (green) c) Angular scattering spectrum generated using Rytov approximation (black curve) and original data (green) d) Angular spectrum of scattering amplitude averaged over azimuthal angles..... 100

Figure 6 6 Angular scattering generated from Born approximation (blue) reproducing oscillatory pattern of the data (green), with Rytov approximation for comparison (black) ..101

Figure 6 7 Angular scattering spectra at various axes of ellipsoid and fit to Mie theory for each axes a) $\phi=0^\circ$ b) $\phi=22^\circ$ c) $\phi=45^\circ$ d) $\phi=90^\circ$ 102

Figure 6 8 Scattering pattern of an ellipsoid a) Ellipsoidal axes lengths are marked, along with two diameters of ellipsoid, not aligned with ellipsoidal axes, detector plane is parallel to XY plane b) Angular scattering map from 0° to 60° forward scattering..... 102

Figure 6 9 Averaged angular scattering spectrum of an ellipsoid over azimuthal angle (blue) and fit to Mie theory (black) 103

Figure 6 10 Manipulating an index tomogram of HT29 cell, replacing cell index distribution with an average index value (X and Y-axis - μm, colorbar –refractive index value) a) Index tomogram represents a stack of 2D sections along Z-axis b) Individual section, outline of cell border (black), colorbar –refractive index values c) Refractive index inside the area is replaced with an average refractive index value..... 104

Figure 6 11 Extracting nuclear index distribution (X and Y-axis - μm, colorbar –refractive index value) a) Outline of nuclear border inside an individual section b) Replacing nuclear index with an average of nuclear index variations c) Replacing nuclear index with randomly selected cytoplasmic indexes d) Replace cytoplasm index distribution outside the nucleus with an average index of cytoplasm 104

Figure 6 12 Angular scattering spectra of the nucleus for three different ways of extracting nuclear index 105

Figure 6 13 Analyzing cell border and extracted nuclear scattering using Mie theory for HT29 cell a) Tomogram section of the whole cell b) Tomogram section of an extracted nucleus with an averaged cytoplasm index c) Angular scattering spectrum of a cell and Mie theory on linear scale d) Angular scattering spectrum of an extracted nucleus and Mie theory on linear scale e) Angular scattering spectrum of cell and extracted nucleus with Mie fit on a log scale 106

Figure 6 14 Effect of sub-cellular structure heterogeneity on scattering a) Tomogram section of the whole cell, refractive index value b) Tomogram section of an extracted nucleus with an averaged cytoplasm index c) Tomogram section of a cell with an averaged refractive index d) Tomogram section of a nucleus with an averaged refractive index e) Angular scattering spectra at $\varphi=0^\circ$ for homogenous and heterogonous cell index distribution f) Angular scattering spectra at $\varphi=0^\circ$ for homogenous and heterogonous nuclear index distribution107

Figure 6 15 Compare cell, nucleus and index-matched cell scattering signals a) Tomogram section of an index-matched cell, where cell media is replaced with an averaged cell index b) Angular scattering spectra at $\varphi=0^\circ$ generated using Born approximation (whole cell – blue, index-matched cell – green, extracted nucleus – red) c) Angular scattering spectra at averaged φ generated using Rytov approximation (whole cell – blue, index-matched cell – green, extracted nucleus – red)..... 108

Figure 6 16 Wavelength scattering spectra generated from index tomogram using Born/Rytov/Projection (red, blue, magenta) approximations and compared to Mie theory (black), $n(\text{media})=1.337$, $\theta=5^\circ$ a) 2 μm sphere, $n=1.347$ b) 10 μm sphere, $n=1.347$ c) 10 μm sphere, $n=1.377$ d) 20 μm sphere, $n=1.377$ 109

Figure 6 18 Affect of index inhomogeneous on scattering spectra in wavelength, homogeneous index distribution (blue) and heterogeneous (red) index distribution a1-c1) cell index tomograms a2-c2) nuclear index tomograms 110

Figure 6 17 Wavelength scattering spectra from index tomogram of cell (a1-c1) and extracted nucleus (a2-c2) (blue) with Mie theory fits (black). Diameter d is the best fit value	110
Figure 6 19 Wavelength scattering of whole cell tomogram, index-matched cell and extracted nucleus (blue, green and red) a1-c1) Born approximation a2-c2) Rytov approximation	111
Figure 6 20 Size distribution of cell size and nuclear size projection onto a single axis a) Phase contrast of HT29 cell monolayer b) Histogram of cell section projection distributions c) Phase contrast of HT29 cell suspension d) Histogram of nuclear section projection distributions.....	112
Figure 7 2 Simulated forward scattering for HeLa (blue) and T84 (red), use HT29 index contrast $n=1.3644$ a) Angular spectrum at 450 nm, log scale b) Wavelength spectrum at 2° , linear scale.....	115
Figure 7 1 Simulated forward scattering of HT29 cell suspension in water, $n=1.3644$, $14.74 \pm 2.5 \mu\text{m}$ a) Angular spectra for three wavelengths, log scale b) Wavelength spectra for three angles, linear scale.....	115
Figure 7 3 Variation of scattering intensity with change in cell suspension density, HT29 cell suspension a) Phase contrast image of the highest density cell suspension b) Phase contrast image of 1/8.4 diluted sample c) Angular spectra of three dilutions scaled by change in concentration (black – highest density, green – medium, blue – lowest), $\lambda=450 \text{ nm}$, linear scale d,e) Wavelength spectra of three dilutions scaled by change in concentration for two values of scattering angle, linear scale	116
Figure 7 4 Variation of scattering intensity with change in cell suspension density, HeLa cell suspension a) Phase contrast image of the highest density cell suspension b) Phase contrast image of 1/9.7 diluted sample c) Angular spectra for two dilutions scaled by change in concentration (black – highest density, blue – lowest), $\lambda=450 \text{ nm}$, linear scale d,e) Wavelength spectra of three dilutions scaled by change in concentration for two values of scattering angle, linear scale	117
Figure 7 5 Choosing step size in angle and wavelength for lookup table generation for forward scattering of cell suspensions, $15 \mu\text{m}$ bead suspension, $m=1.05$ a) Convolved wavelength spectrum at $\theta=5^\circ$ with convolution width between 0.1 and 30 nm b) Convolved angular spectra at $\lambda=400 \text{ nm}$ and convolution width of 0.01° - 0.5° c) Table of selected ranges for parameter values	118
Figure 7 6 Scattering data used for Mie look-up-table simulations a) Dense HeLa sample scattering data, oscillatory feature around 2° b) Sections in scattering angle and wavelength for further analysis (blue lines).....	118
Figure 7 7 Mie look-up-table approach best result to fit wavelength data of HeLa cell suspension a) Mean-centered wavelength spectra and best simulation Mie theory for three values of scattering angle b) Mean-centered angular spectra (log scale) and best simulation Mie theory for three values of incident wavelength.....	119
Figure 7 8 Effect of index-matching with phase contrast microscopy a) Before index matching, media PBS b) After index matching, PBS+BSA	120
Figure 7 9 Index-matching effect on forward scattering from HeLa cell suspension a) Scattering data from HeLa in PBS b) Scattering data after index-matching HeLa in	

PBS+BSA c) Angular scattering spectrum change at 525 nm before (black) and after (red) index-matching d) Change in Mie prediction for size distribution of $d=16\pm 1.6 \mu\text{m}$ and theoretically predicted index drop before (black) and after (red)..... 121

Figure 7 11 Angular and wavelength sections' analysis in the index-matching experiment (black – before index matching, red – after, green – before index matching minus change in Mie signal for cell border) a) Angular scattering spectra, parallel polarization, at 525 nm b) Wavelength spectra, parallel polarization at 178° c) Angular scattering spectra perpendicular polarization at 525 nm d) Wavelength spectra perpendicular polarization at 178° 122

Figure 7 10 Index-matching effect on backscattering from HeLa cell suspension a) Scattering data for parallel in PBS, linear scale $0-6*10^{-4}$ b) Scattering data for parallel after index-matching HeLa in PBS+BSA, linear scale $0-6*10^{-4}$ c) Scattering data for parallel in PBS, linear scale $0-1.5*10^{-4}$ d) Scattering data for cross-polarized after index-matching HeLa in PBS+BSA, linear scale $0-1.5*10^{-4}$ 122

Figure 7 12 Predicted whole cell backscattering vs. system sensitivity, HeLa cell distribution and index from forward scattering measurements a) Mie prediction for cell scattering signal in PBS for parallel polarization, colorbar - $\times 10^{-5}$ b) Wavelength scattering in parallel polarization (black) vs. system sensitivity level (blue), scale $\times 10^{-5}$ c) Angular scattering spectrum in parallel polarization (black) vs. system sensitivity level (blue), scale $\times 10^{-5}$ d) Mie prediction for cell scattering signal in PBS for perpendicular polarization, colorbar - $\times 10^{-6}$ e) Wavelength scattering in perpendicular polarization (black) vs. system sensitivity level (blue), scale $\times 10^{-6}$ f) Angular scattering spectrum in parallel polarization (black) vs. system sensitivity level (blue), scale $\times 10^{-6}$ 123

Figure 7 13 Application of θ -differential data to reduce background signal in perpendicular polarization for HeLa cell suspension in PBS a) Angular scattering spectrum at 450 nm (black – original data and θ -differential data, green – Mie theory prediction), scale $\times 10^{-5}$ b) Wavelength data at exact backscattering (magenta) and 178.8° (black), scale $\times 10^{-5}$ c) θ -differential signal scattering data (black) vs. Mie theory prediction for cell border (green), $\times 10^{-6}$ 124

Figure 7 14 System sensitivity established with 50 nm bead suspension a) Perpendicular scattering data, colorbar $0-2*10^5$ b) Wavelength data at exact backscattering and 178.8° , scale $\times 10^{-5}$ c) θ -differential signal scattering data (blue) vs. Mie theory prediction for cell border (green), scale $\times 10^{-5}$ 125

Figure 7 15 θ -differential in perpendicular applied to cell monolayer data a) HT29, Wavelength data at exact backscattering (green) and 178.8° (red), scale $\times 10^{-4}$ b) HeLa, Wavelength data at exact backscattering (green) and 178.8° (red), scale $\times 10^{-4}$ c) T84, Wavelength data at exact backscattering (green) and 178.8° (red), scale $\times 10^{-5}$ d) θ -differential residual signal for HT29 (black), HeLa (blue), T84 (magenta), scale $\times 10^{-5}$ 126

Figure 7 16 ϕ -differential signal from HT29 cell monolayer compared to system sensitivity a) Wavelength data at 176.8° for two azimuthal angles $\phi=90^\circ$ (red) and $\phi=0^\circ$ (red), power law fits to the data , scale $\times 10^{-3}$ b) ϕ -residual signal for HT29 cell monolayer data, scale $\times 10^{-5}$ c) ϕ -residual signal for 50 nm bead suspension, scale $\times 10^{-5}$ d) ϕ -residual signal for 50 nm bead suspension, scale $\times 10^{-5}$ 127

Figure 7 17 Analyzing wavelength spectra in backscattering, power law fits at $\phi=45^\circ$ (black – data, red – power law fit) a) HeLa b) T84 c) HT29 and $\phi=0^\circ$, $\phi=90^\circ$ (solid lines – data, dashed lines – fits) d) HeLa e) T84 f) HT29 128

Figure 7 18 Summary of power law exponent values for light scattering measurements a) ϕ -azimuthal experiment power law exponents b) $\phi=45^\circ$ experiment power law exponents..... 128

Figure 7 19 Sensitivity of power law exponent to DC-offset a) HT29 cell monolayer data at $\phi=45^\circ$ (black1 – original, blue2 - 7.7% offset, green3 – 23% offset) and power law fits (red) b) Summary of power law exponents for latest experiment with HT29 cell monolayer at $\phi=45^\circ$ 129

Figure 7 20 Discrete particle analysis of power laws in cell monolayers a) Universal curve of backscattering cross-section vs. ratio of wavelength to diameter b) HT29 cell monolayer data at $\theta=178^\circ$ (black), 20 nm sphere data, 100 nm sphere, 200 nm sphere (all blue), power law fits (red and black), second number is amplitude scaling (except for data), third parameter power law exponent, c) Wavelength spectrum HT29 cell monolayer data at $\theta=178^\circ$ (black) and power law fit (red) 130

Figure 7 21 Properties of scattering from power law in size distribution a) Change in wavelength scattering spectrum with the change in lower cut-off diameter of power law distribution, $\beta=4.5$ for all spectra, log-log scale b) Asymptotic behavior of exponent of power law fit ($\gamma=\beta-3$) for different values of lower cut-off diameter for 4 values of β -exponent c) Change in relative particle weight in power law size distribution with decrease of exponent β 132

Figure 7 22 Compare backscattering spectra generated from Foster’s paper [9] distributions and power law scattering from cell monolayer experiments a) (©OSA [9] Reproduced with permission) product of size distribution times total scattering cross-section from the paper b) Reproduced product of size distribution times total scattering cross-section using paper information c) Wavelength backscattering spectra at $\theta=178^\circ$ (ref. two exponential distributions – red, ref. two log-normal distributions – blue, power law size distribution – green) 133

Figure 7 23 Product of size distributions and backscattering cross-section a) Scattering cross-section vs. particle diameter, compare total and backscattering, log scale b) Size distributions, 2-exponential (red), 2 log-normal (blue), power law distribution (green), log scale c) Product of backscattering cross-section at 633nm, $\theta=178^\circ$ and size distributions vs. particle diameter, power law distribution (green), 2 exponential (red), 2 log-normal (blue), normalized to maximum value..... 133

Figure 7 24 Properties of the cross-section distribution times backscattering cross-section a) Power law wavelength spectra for three values of exponent ($\gamma=0.5$ – brown, $\gamma=1.02$ – green, $\gamma=1.5$ - magenta) b) Product of power law size distributions and backscattering cross-section at 633 nm c) Product of power law size distributions and backscattering cross-section at 433 nm 134

Figure 7 25 Continuous models of power law in backscattering a) HT29 wavelength backscattering (black) and power law fit (red) b) Spatial features spectrum according to Born approximation c) HT29 wavelength backscattering (black) and von Karman model fit (red) 135

Figure 8 2 Tissue correction factor a vs. measurement number	140
Figure 8 1 Extracting polarized residual in backscattering (a). Polarized signal from normal rat esophagus tissue, $I_{ }$ (solid line) and I_{\perp} (dashed) (b) Polarized residual signal for various values of correction parameter, a . (c) Polarized residual signal for $a=0.88$ (green) with power law fit in wavelength (black)	140
Figure 8 3 Analyzing power law in wavelength for Control and NMBA-treated groups a) Rat spectra with normal diagnosis (colored lines) and power law fits to them (black lines) b) Same for dysplastic rat spectra c) Summary for power law exponents for normal (blue) and dysplastic (red) rats. Circled are rats with normal diagnosis from NMBA-treated group. d) Summary of residual signal amplitudes at 475 nm.....	141
Figure 8 4 Difference between polarized residual spectra and power law fit a) Normal rat samples b) Dysplastic rat samples	142
Figure 8 5 Analysis of power laws for Curcumin and NMBA-curcumin rats a) Power law fits to Curcumin group spectra (data –color spectra and fits – black) b) Same as a) for NMBA-curcumin group c) Summary of power law exponents. Circled sample of NMBA-curcumin group diagnosed as normal on histology (blue – normal diagnoses, red – dysplastic) d) Summary of residual spectra amplitudes values at 475 nm	143
Figure 8 6 Analysis of power laws for epithelial data a) Intensity of individual polarization signals for epithelium, $I_{ }$ (solid line) and I_{\perp} (dashed) b) Residual signal using correction factor of 1 and 0.857s c) Normal epithelial residual data (colored lines) and power law fits (black lines) d) Same as c) for dysplastic epithelial residuals	144
Figure 8 7 Analysis of power laws for epithelial data a) Summary of power law exponents for Normal (blue), NMBA-treated (red) and NMBA—curcumin (black) epithelial data. Blue circle – sample diagnosed normal; Red circle-no corresponding tissue b) Summary of signal amplitudes for epithelial data, same data groupings c) Photograph of a normal epithelial sample, showing significant optical thickness of the sample.....	145
Figure 8 8 Effect of tissue thickness on diagnostics and power exponents a) Summary of tissue thicknesses, T , with respect to pathology Normal (blue), NMBA-treated (red) and NMBA—curcumin (black) epithelial data. b) Correlation of power law exponents to tissue thickness c) Sample histology at 20x of normal tissue and corresponding epithelium sample, demonstrating change in epithelial thickness.....	146
Figure 8 9 Polarized residual signal (averaged over 450-750 nm) vs. optical density. (Reproduced with permission from IEEE Journals ref. [1])	147
Figure 8 10 Measured polarized residual signal vs. optical density effect a) 10 μm data. Black lines mark signal at $\tau=1$ and $\tau=2$ c) 3 μm data. Black lines mark signal at $\tau=1$ and $\tau=2$	148
Figure 8 11 Power spectrum generation from phase contrast image a) (©OSA [11], Reproduced with permission) Phase contrast image of rat liver tissue section, binary scale, 100x b) (©OSA [11], Reproduced with permission) Spatial frequency power spectrum on a log-log scale, data for three magnifications (markers) plotted against von Karman function fit (solid line)	149
Figure 8 12 Limits of wavelength spectrum of von Karman function and parameter sensitivity a) Residual signal intensity vs. wavelength on log-log scale Von Karman curve (blue) vs. Fractal power law (black) vs. Rayleigh prediction (red). b) Backscattering spectrum of von	

Karman signal intensity vs. wavelength (300-800 nm). Fix fractal exponent at 1.64. Three values of fractal outer scale 0.01 μm (green data), 0.2 μm (blue) and 10 μm (red). Fit to power law in wavelength (black).....	150
Figure 8 13 Deviation from power law spectra in residual signal vs. wavelength on a log-log scale a) NMBA dysplastic data (color data) vs. power law fits (black), red circle - deviation from power law b) same as a) for Curcumin-control group, selected spectra c) NMBA-curcumin dysplastic spectra. Red region – no deviation from power law behavior.....	151
Figure 9 1 Mie predictions for backscattering of HT29 cells a) Wavelength prediction, from interferometry reference [9] using size distribution and refractive index contrast from the reference b) Angular spectra with same set of parameters c) Wavelength prediction based on reference size distribution and single cell measured refractive index contrast d) Angular spectra with same set of parameters	165
Figure 9 2 Enhancement ratio for ΔI of 22 and 0.4 μm for two values of azimuthal angle $\varphi=0^\circ, 45^\circ$	166
Figure 9 3 Analyses of backscattering power law in wavelength in ref. [25] a) Fit of the ref. data to power law in wavelength b) Comparison of the extracted power law size distribution to reported size distribution c) Product of the power law size distribution and backscattering cross-section at 650 nm, compared with reported size distribution	170
Figure 9 4 Figures are taken from reference [37, Figures 5-7], ©OSA reproduced with permission. Analysis of low-coherence interferometry measurements a) Raw experimental results and Fourier-filtered data b) Fourier-filtered data and low-order polynomial fit c) Data vs. Mie fit, low order polynomial is subtracted from both.....	173

List of tables

Table 3 1 Summary of measured nuclear size distributions in the ellipsoidal approach for three cell monolayers under investigation. Equivalent sphere diameter distribution is considered. Data are compared with size distribution from normal colon.....	36
Table 3 2 Summary of rat tissue histological grading by group	42
Table 5 1 Summary of mixture data analysis for sample1 and sample2	82
Table 6 1: Summary of Mie fitting for tomogram scattering generated using Born, Rytov and Projection approximations	97
Table 7 1 Summary of cell monolayer residual data with residual signal amplitude, nuclear size distribution and maximum refractive index.....	126
Table 9 1 Summary of cell monolayer residual data with residual signal amplitude, nuclear size distribution and maximum refractive index.....	158

Chapter 1:

Introduction

Light scattering spectroscopy has emerged as a valuable tool for cancer diagnosis in the past ten years. The interaction of light with cellular structures at a sub-micron level brings out information about morphological changes accompanying malignancy at early stages, when it can be treated most easily. The exact solution of the inverse scattering problem required for extracting tissue morphological information from scattering data, is not currently possible due to the high complexity of the sample and non-uniqueness of the scattering data. Therefore, the extracted information often strongly depends on the selection of the specific model of the cell/tissue scattering and constraints from prior knowledge about the sample.

Using a novel set of experimental methods and theoretical approaches, the present work advances understanding of the cellular light scattering, re-interprets and clarifies some of the previous results, and provides a connection between single cell and tissue scattering. Specifically, the goals of this project are to:

- (1) Establish primary scatterers at a sub-cellular level in a single cell model,
- (2) Understand scattering of cell monolayers and cell suspensions, by studying them directly and by extrapolating single cell results, and
- (3) Extract diagnostic scattering parameters from *ex vivo* tissue model and relate them to tissue morphology and single/multi-cell results.

At this time, it should be noted, that the numerical order of goals stated above is not in line with the chronological order in which the experiments were done, with the tissue experiments preceding both cell monolayer experiments and single cell studies. Thus, some of the advancements from single cell/cell monolayer work could be applied retrospectively to explaining results of the tissue experiments. Therefore, the structure of the thesis follows the layout of the goals in logical order, but the state of the system calibration and theoretical modeling in the tissue study is presented chronologically.

Chapter 2 of the thesis will elaborate on the significance of this work. Chapter 3 will be devoted to the description of cellular and tissue morphology of the investigated samples. In Chapter 4, several models of light scattering are presented, which are used to interpret cell/tissue scattering. Chapter 5 describes the principles and specifics of the instrumentation

used for the studies. Chapters 6-8 cover single cell, cell monolayer and cell suspension, and tissue studies. In Chapter 9, the connection between the results of the three studies is discussed, followed by an overall summary and conclusions for the project and discussion of the future directions. Finally, the appendix contains a short discussion of the application of nuclear model to interpretation of tissue backscattering.

Chapter 2:

Background and significance

This chapter starts with a short definition of cancer diseases and the importance of early diagnosis. In the following, diagnostic techniques are discussed with a narrower focus on light-based methods. Finally light scattering is introduced with a review of its applications to cell study/cancer diagnosis.

2.1 Light scattering spectroscopy and cancer diagnosis

Light scattering spectroscopy has recently emerged as a non-invasive technique for early cancer diagnosis in epithelial tissues [1-6]. In light scattering, the angular and spectral distribution of scattered light depends on the refractive index and size of the scattering particle [7-9]. The cornerstone of the light scattering technique for cancer diagnosis is the assumption that the changes in cells and tissues that are correlated with the development of cancer are expressed in changes of light scattering spectra in wavelength or angle.

It is currently believed that cancer can originate from mutations in the growth control cycle of a single cell, caused by external agents (tobacco, viruses) and inherent genetic factors (errors in DNA reproduction), followed by further growth and uncontrolled division of that cell (cloning), creation of additional blood supply (angiogenesis) and spread from place of origin into circulatory system (blood and lymph nodes) into other organs (metastasis) [10]. Thus, the early diagnosis is related to the ability of characterizing single or several cancerous cells and their difference from surrounding normal tissue. The current “gold” standard of cancer diagnosis at the cellular level is histopathology [11].

Histopathology has been the “gold standard” for cancer diagnosis at all stages for well over 100 years. Histopathology is a microscopic study of thin, chemically-processed tissue sections prepared from biopsy of suspicious organ sites with the goal of identifying the disease state of the tissue [11]. From the point of view of histopathology, the disease state of the tissue is associated with a specific pattern in its microscopic image, which is different from a healthy one. In Figure 2.1, the histological section of a human cervix stained with Hematoxylin and Eosin (H&E) is presented, showing a developing pre-cancerous condition called dysplasia (earliest morphological pre-cursors of cancer development) [11, 12]. For

H&E staining, the nucleic acids (such as the nuclear DNA material) stain blue, while basic macromolecules such cytoplasmic proteins and stromal collagen fibers stain pink [13].

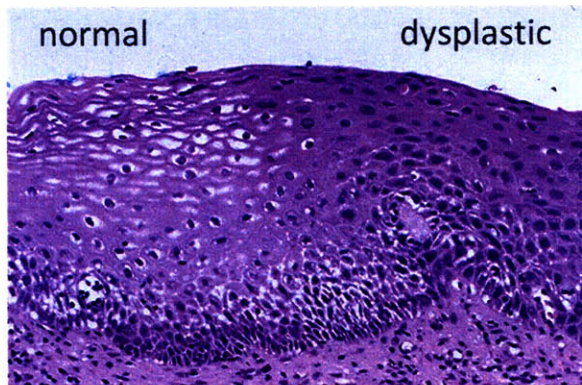


Figure 2.1 H&E stained image of human cervix

In Figure 2.1, comparison of the left side (normal appearing) with the right side (dysplastic), shows some common features associated with dysplasia, including loss of cell differentiation/cell maturity, higher cell density, pleomorphism (increase variability of sizes and shapes of cells and their nuclei), higher nucleus-to-cytoplasm ratio and hyperchromaticity (change in the intra-nuclear density distribution of DNA material). Histopathological diagnosis of tissue poses three major drawbacks: invasiveness – tissue needs to be removed from the body; alteration – tissue is chemically processed (dehydrated and stained); and intra and inter-observer diagnostic variability – the image interpretation depends and varies greatly with a specific pathologist' experience and background [14, 15].

Light scattering methods are claimed to overcome the above limitations by detecting dysplasia via quantification of changes in nuclear size distribution and refractive index variations quantitatively, non-invasively and *in vivo* [1, 16]. At the same time, light scattering spectroscopy may itself be of limited value as it represents an indirect measurement technique, thus the extracted information depends strongly on the assumed model of the scatter. In the next section, we discuss the light scattering models of the cell.

2.2 Light scattering from cells and tissues

2.2.1 Sub-cellular structural basis for light scattering

Modeling of light scattering from tissue has taken two approaches that are, to a certain extent, complementary: macroscopic, where tissue is described by a couple of bulk parameters, such as scattering and absorption coefficients [17-20], and microscopic, where an

assumption is made about the major components of cell scattering at the sub-cellular level [1, 2]. Since cells are generally weakly scattering objects, microscopic contributions are often established in studies of homogenous populations of cells in order to increase the signal levels. These typically include cell monolayers (single layers of intact, adherent cells) and cell suspensions (high-density collection of individual cells in a liquid medium).

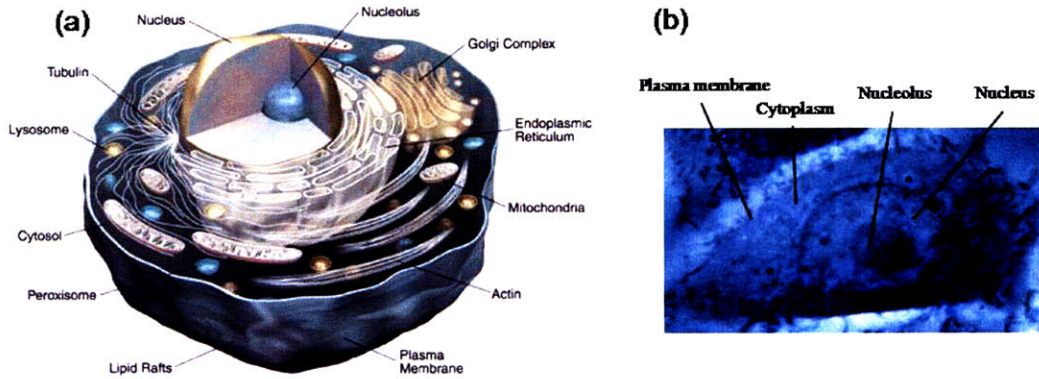


Figure 2.2 Sub-cellular structure a) Schematic representation of cellular organelles b) Phase contrast image of SiHa cell sample

The known cellular microstructure plays an important role in determining models for light scattering by sub-cellular components. Most of the fine cellular microstructure shown in a 3D-cartoon on Figure 2.2.a has been uncovered and described using transmission electron microscopy, which has a nanometer-scale resolution and measures scattering and absorption of an electron beam in a fixed and stained sample [13, 21]. The diameter of the cell can be assumed to be about 10-15 μm in order to compare the relative sizes of different components. For scattering studies, the size of the particle relative to the wavelength is of crucial importance [7]. Thus, one can conclude that relative to the visible light wavelength of 0.5 μm , the cell and the cell nucleus are large structures, while the nucleolus, the Golgi apparatus, mitochondria and endoplasmic reticulum are comparable to wavelength, and the rest, such as ribosomes, peroxisomes, lysosomes and all of the proteins (not shown) are small or very small compared to a wavelength. Some of these structures (mainly the ones on the order of or larger than the visible light wavelength) can also be visualized using phase contrast microscopy (Figure 2.2.b), which uses refractive index variations in the cell as the source of contrast, similar to light scattering spectroscopy [21]. Although changes in phase contrast image intensity reflect only qualitative changes in refractive index, one can notice that the strongest changes are at the cell border, the nuclear border with cell cytoplasm and at

the nucleolar border within the nucleus. The above information about sub-cellular structure is the basis for essentially all light scattering models as detailed below.

2.2.2 Modeling light scattering from cells

A significant number of light scattering models are based on the assumption that scattering is due to some distribution of spherical scatterers, representing the distribution of major subcellular elements described above [6, 22-33]. The reason for this widely used assumption is that the scattering problem for a sphere under plane wave illumination has an exact numerical solution, which can be reasonably easily implemented to extract structural information from scattering spectra [7-9]. The solution depends on relative refractive index of the particle to the surrounding media ($m=n_{\text{part}}/n_{\text{media}}$), the size of the particle, d , relative to the wavelength λ , and varies with respect to scattering angle θ , which is the angle between the directions of incident and scattered light. The simplest model (resembling “spherical cow in a vacuum”) consists of spherical nuclei with refractive index n_1 swimming in a continuous

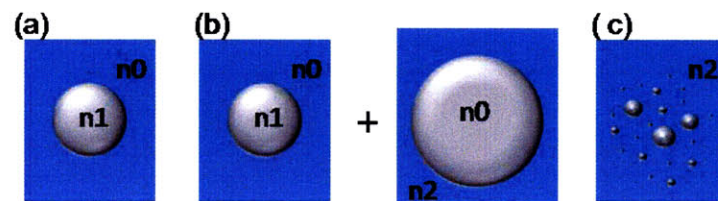


Figure 2.3 Modeling cell structure from a scattering standpoint a) Nucleus with index n_1 surrounded by cytoplasm n_0 b) Nucleus in an average refractive index of cell n_0 plus cell n_0 in the media n_2 c) Collection of small spheres

sea of cytoplasm with refractive index n_0 (Figure 2.3.a). This model has been originally developed in our laboratory and applied to explaining scattering signals from cell monolayers and tissues [1, 2, 22, 34]. A somewhat more complicated model involves another player – scattering of the cell as an independent spherical scatterer with refractive index n_0 in the outside media with index n_2 (Figure 2.3.b). This model has been applied to explaining scattering from cell suspensions [35, 36]. Others have studied scattering contributions of smaller organelles, such as mitochondria or lysosomes, which are also assumed to be spherical in shape [24-26, 31, 37, 38]. The scattering has been also assumed to come from a broad distribution of spherical sizes with the majority of particles below $1 \mu\text{m}$ in size, with index n_1 in the outside medium with index n_2 (Figure 2.3.c) [28, 32, 33, 39, 40]. Some papers combine the above models to explain observed scattering signals [32, 40].

The publications cited above differ not only by the scattering model used, but also in the way the scattering signal is detected, with one notable difference arising from the range of detected scattering angle θ . Studies at small scattering angles (forward scattering), reveal information about larger structures [40, 41]. With an increase in angle (side scattering), smaller scatterers dominate the signal [25, 28, 33, 40]. The most intriguing and diagnostically relevant region is very large scattering angles (backscattering), since these scattering signals could come directly from the intact tissue and potentially carry diagnostically significant information [6, 22, 23, 30, 31, 34, 42].

2.2.3 Contribution of cells to tissue scattering

The contribution of cells of interest may be relatively small to the overall tissue scattering. Various experimental and modeling methods have been developed to extract scattering signatures of interest from intact tissue. Polarization gating, ϕ -differential technique and diffuse scattering modeling are examples of such methods [6, 22, 30, 43]. In all of these experiments, scattering signals of interest are reported to be at the level of 1-10% of the total signal. Given the variability of interpretations in simple cell scattering cited above, selection of a specific model for cell scattering to explain a unique part of the total scattering signal from tissue seems unjustified, unless the model has been experimentally validated.

2.3 Current work motivation and significance

A method, combining detection of backscattering signals and a model of spherical nuclei as the dominating source of scattering, has been originally developed in our laboratory by Perelman and Backman [30]. This method was validated using large polystyrene spheres and cell monolayers as nuclear phantoms, placed on a highly scattering substrate to mimic tissue background signal [22, 23, 30]. Finally, the method was applied to diagnose pre-cancerous changes in a variety of tissues with reported very high degree of accuracy [1]. These findings served as a starting point of the work presented in this thesis, which was originally intended to expand on the previous results. Yet, as the present project evolved, experimental results did not connect with the previous work. Specifically, the nuclei did not seem to have a significant contribution to the backscattering signal as originally proposed. Moreover, in parallel to our work, other researchers, including the authors of original idea,

have attributed their detected backscattering signatures to smaller sub-cellular structures or other sources [31, 32, 44]. Even within the results of the original studies, there appears to be significant uncertainty in the extracted parameters. For example, the relative refractive index of T84 cell monolayer nuclei reported in three different studies had a range of $m=1.03-1.06$ [22, 23, 34]. Usually, the quoted relative refractive index for sub-cellular structures is between 1.02 and 1.1, so the spread is more than a third of the possible variation range.

The nuclear refractive index in many of the previous scattering measurements is an assumed value based on a very old study [45]. There have been a few more recent attempts to quantify refractive index variations and their effect on scattering inferred from qualitative measurements [29, 46, 47]. In the meanwhile, scattering of single cell phantoms has been modeled to understand effects of shape on scattering signals [48-51]. Most importantly, a new tomography technique was recently developed in our laboratory that allows direct measurement of the refractive index of a single cell in 3D [52]. Thus, we now have a unique piece of information about the true distribution of the refractive index inside the cell, which was not available at the time of previous light scattering studies. By combining carefully calibrated and optimized traditional intensity-based light scattering methods presented here and direct refractive index measurements enabled by Choi *et al.* [52], we aim to create a more accurate picture of light scattering from cells and assess validity of light scattering as a diagnostic tool.

References

- [1] Backman V, Wallace MB, Perelman LT, Arendt JT, Gurjar R, Muller MG, Zhang Q, Zonios G, Kline E, McGillican T, Shapshay S, Valdez T, Badizadegan K, Crawford JM, Fitzmaurice M, Kabani S, Levin HS, Seiler M, Dasari RR, Itzkan I, Van Dam J, Feld MS. Detection of preinvasive cancer cells. *Nature* 2000;406:35.
- [2] Gurjar RS, Backman V, Perelman LT, Georgakoudi I, Badizadegan K, Itzkan I, Dasari RR, Feld MS. Imaging human epithelial properties with polarized light-scattering spectroscopy. *Nature Medicine* 2001;7:1245.
- [3] Roy HK, Kim YL, Wali RK, Liu Y, Koetsier J, Kunte DP, Goldberg MJ, Backman V. Spectral Markers in Preneoplastic Intestinal Mucosa: An Accurate Predictor of Tumor Risk in the MIN Mouse. *Cancer Epidemiol Biomarkers Prev* 2005;14:1639.
- [4] Mourant JR, Bocklage TJ, Powers TM, Greene HM, Bullock KL, Marr-Lyon LR, Dorin MH, Waxman AG, Zsemlye MM, Smith HO. In vivo light scattering measurements for detection of precancerous conditions of the cervix. *Gynecologic Oncology* 2007;105:439.
- [5] Ramachandran J, Powers TM, Carpenter S, Garcia-Lopez A, Freyer JP, Mourant JR. Light scattering and microarchitectural differences between tumorigenic and non-tumorigenic cell models of tissue. *Optics Express* 2007;15:4039.
- [6] Sokolov K, Drezek R, Gossage K, Richards-Kortum R. Reflectance spectroscopy with polarized light: is it sensitive to cellular and nuclear morphology. *Opt. Express* 1999;5:302.

- [7] Hulst H. Light scattering by small particles. New York: Dover Publications, 1981.
- [8] Bohren CF, Huffman HR. Absorption and scattering of light by small particles: John Wiley & Sons, Inc., 1998.
- [9] Mishchenko M, Hovenier J, Travis L. Light scattering by nonspherical particles: theory, measurements, and applications: Academic Press, 2000.
- [10] Hanahan D, Weinberg RA. The hallmarks of cancer. *Cell* 2000;100:57.
- [11] Kumar V, Abbas A, Fausto N. Pathologic basis of disease: Saunders, 2005.
- [12] Weinberg RA. How cancer arises. *Scientific American* 1996;275:62.
- [13] Ross M, Pawlina W. Histology: A text and atlas. Hagerstown, MD: Lippincott Williams & Wilkins, 2006.
- [14] Robertson AJ, Anderson JM, Beck JS, Burnett RA, Howatson SR, Lee FD, Lessells AM, McLaren KM, Moss SM, Simpson JG. Observer variability in histopathological reporting of cervical biopsy specimens. *J Clin Pathol* 1989;42:231.
- [15] Tan P, Ho B, Selvarajan S, Yap W, Hanby A. Pathological diagnosis of columnar cell lesions of the breast: are there issues of reproducibility? *Journal of Clinical Pathology* 2005;58.
- [16] John WP, Kevin JC, Jeffrey DB, Justin K, Thomas DA, Marcia G, Frank G, Adam W. In situ detection of nuclear atypia in Barrett's esophagus by using angle-resolved low-coherence interferometry. *Gastrointestinal endoscopy* 2007;65:487.
- [17] Nilsson AMK, Berg R, Anderssonengels S. Measurements of the optical-properties of tissue in conjunction with photodynamic therapy. *Applied Optics* 1995;34:4609.
- [18] Germer CT, Roggan A, Ritz JP, Isbert C, Albrecht D, Muller G, Buhr HJ. Optical properties of native and coagulated human liver tissue and liver metastases in the near infrared range. *Lasers in Surgery and Medicine* 1998;23:194.
- [19] Bargo PR, Prah SA, Goodell TT, Steven RA, Koval G, Blair G, Jacques SL. In vivo determination of optical properties of normal and tumor tissue with white light reflectance and an empirical light transport model during endoscopy. *Journal of Biomedical Optics* 2005;10.
- [20] Holmer C, Lehmann KS, Wanken J, Reissfelder C, Roggan A, Mueller G, Buhr HJ, Ritz JP. Optical properties of adenocarcinoma and squamous cell carcinoma of the gastroesophageal junction. *Journal of Biomedical Optics* 2007;12.
- [21] Murphy D. Fundamentals of light microscopy and electronic imaging: Wiley-IEEE, 2002.
- [22] Backman V, Gurjar R, Badizadegan K, Itzkan L, Dasari RR, Perelman LT, Feld MS. Polarized light scattering spectroscopy for quantitative measurement of epithelial cellular structures in situ. *Ieee Journal of Selected Topics in Quantum Electronics* 1999;5:1019.
- [23] Backman V, Gopal V, Kalashnikov M, Badizadegan K, Gurjar R, Wax A, Georgakoudi I, Mueller M, Boone CW, Dasari RR, Feld MS. Measuring cellular structure at submicrometer scale with light scattering spectroscopy. *Ieee Journal of Selected Topics in Quantum Electronics* 2001;7:PII S1077.
- [24] Wilson JD, Bigelow CE, Calkins DJ, Foster TH. Light scattering from intact cells reports oxidative-stress-induced mitochondrial swelling. *Biophysical Journal* 2005;88:2929.
- [25] Wilson JD, Foster TH. Mie theory interpretations of light scattering from intact cells. *Optics Letters* 2005;30:2442.
- [26] Wilson JD, Foster TH. Characterization of lysosomal contribution to whole-cell light scattering by organelle ablation. *Journal of Biomedical Optics* 2007;12.
- [27] Mourant JR, Canpolat M, Brocker C, Esponda-Ramos O, Johnson TM, Matanock A, Stetter K, Freyer JP. Light scattering from cells: the contribution of the nucleus and the effects of proliferative status. *Journal of Biomedical Optics* 2000;5:131.

- [28] Mourant JR, Johnson TM, Carpenter S, Guerra A, Aida T, Freyer JP. Polarized angular dependent spectroscopy of epithelial cells and epithelial cell nuclei to determine the size scale of scattering structures. *Journal of Biomedical Optics* 2002;7:378.
- [29] Drezek R, Dunn A, Richards-Kortum R. Light scattering from cells: finite-difference time-domain simulations and goniometric measurements. *Applied Optics* 1999;38:3651.
- [30] Perelman LT, Backman V, Wallace M, Zonios G, Manoharan R, Nusrat A, Shields S, Seiler M, Lima C, Hamano T, Itzkan I, Van Dam J, Crawford JM, Feld MS. Observation of periodic fine structure in reflectance from biological tissue: A new technique for measuring nuclear size distribution. *Physical Review Letters* 1998;80:627.
- [31] Georg S, Edward V, Philip H, Caitlin OC-R, Daniel P, Lev TP. Optical spectroscopy noninvasively monitors response of organelles to cellular stress. *Journal of Biomedical Optics* 2005;10:051404.
- [32] Claudia Mujat CG, Amy Baldwin, Jonathan M. Levitt, Fenghua Tian, Lee A. Stucenski, Martin Hunter, Young L. Kim, Vadim Backman, Michael Feld, Karl Menger, Irene Georgakoudi. Endogenous optical biomarkers of normal and human papillomavirus immortalized epithelial cells. *International Journal of Cancer* 2008;122:363.
- [33] Bartlett M, Huang G, Larcom L, Jiang HB. Measurement of particle size distribution in mammalian cells in vitro by use of polarized light spectroscopy. *Applied Optics* 2004;43:1296.
- [34] Graf R, Wax A. Nuclear morphology measurements using Fourier domain low coherence interferometry. *Opt. Express* 2005;13:4693.
- [35] Xu M. Superposition rule for light scattering by a composite particle. *Optics Letters* 2006;31:3223.
- [36] Wu TT, Qu JY, Xu M. Unified Mie and fractal scattering by biological cells and subcellular structures. *Optics Letters* 2007;32:2324.
- [37] Fang H, Ollero M, Vitkin E, Kimerer LM, Cipolloni PB, Zaman MM, Freedman SD, Bigio IJ, Itzkan I, Hanlon EB, Perelman LT. Noninvasive sizing of subcellular organelles with light scattering spectroscopy. *Ieee Journal of Selected Topics in Quantum Electronics* 2003;9:267.
- [38] Wilson JD, Cottrell WJ, Foster TH. Index-of-refraction-dependent subcellular light scattering observed with organelle-specific dyes. *Journal of Biomedical Optics* 2007;12.
- [39] Schmitt JM, Kumar G. Optical scattering properties of soft tissue: a discrete particle model. *Applied Optics* 1998;37:2788.
- [40] Xu M, Wu TT, Qu JY. Unified Mie and fractal scattering by cells and experimental study on application in optical characterization of cellular and subcellular structures. *Journal of Biomedical Optics* 2008;13:024015.
- [41] Brunsting A, Mullaney PF. Differential Light Scattering from Spherical Mammalian Cells. *Biophysical Journal* 1974;14:439.
- [42] Wax A, Yang C, Backman V, Badizadegan K, Boone CW, Dasari RR, Feld MS. Cellular Organization and Substructure Measured Using Angle-Resolved Low-Coherence Interferometry. *Biophysical Journal* 2002;82:2256.
- [43] Yu CC, Lau C, Tunnell JW, Hunter M, Kalashnikov M, Fang-Yen C. Assessing epithelial cell nuclear morphology by using azimuthal light scattering spectroscopy. *Optics Letters* 2006;31:3119.
- [44] Roy HK, Liu Y, Wali RK, Kim YL, Kromine AK, Goldberg MJ, Backman V. Four-dimensional elastic light-scattering fingerprints as preneoplastic markers in the rat model of colon carcinogenesis. 2004. p.1071.
- [45] Barer R. Refractometry and Interferometry of Living Cells. *J. Opt. Soc. Am.* 1957;47:545.

- [46] Schmitt JM, Kumar G. Turbulent nature of refractive-index variations in biological tissue. *Optics Letters* 1996;21:1310.
- [47] Drezek R, Dunn A, Richards-Kortum R. A pulsed finite-difference time-domain (FDTD) method for calculating light scattering from biological cells over broad wavelength ranges. *Optics Express* 2000;6:147.
- [48] Chen ZG, Taflove A, Backman V. Equivalent volume-averaged light scattering behavior of randomly inhomogeneous dielectric spheres in the resonant range. *Optics Letters* 2003;28:765.
- [49] Li X, Chen ZG, Taflove A, Backman V. Euphase-sphere approximation for analysis of light scattering by arbitrarily shaped nonspherical particles. *Applied Optics* 2004;43:4497.
- [50] Keener JD, Chalut KJ, Pyhtila JW, Wax A. Application of Mie theory to determine the structure of spheroidal scatterers in biological materials. *Opt. Lett.* 2007;32:1326.
- [51] Giacomelli MG, Chalut KJ, Ostrander JH, Wax A. Application of the T-matrix method to determine the structure of spheroidal cell nuclei with angle-resolved light scattering. *Opt. Lett.* 2008;33:2452.
- [52] Choi W, Fang-Yen C, Badizadegan K, Oh S, Lue N, Dasari RR, Feld MS. Tomographic phase microscopy. *Nature Methods* 2007;4:717.

Chapter 3:

Characterization of biological samples: rat esophagus cancer model and cell lines

This chapter is devoted to description and characterization of the biological samples. The chapter is divided into two major parts – part one is devoted to cell culture samples based on HT29, HeLa and T84 cell lines, and part two is devoted to description of the rat esophagus cancer model used in tissue experiments. Each part starts with a brief motivation for the selection of specific types of samples, followed by an explanation of sample preparation and characterization.

3.1 Cell lines: HT29, HeLa, T84

3.1.1 Cell line selection

Cell lines are created from cells extracted from mammalian tissue and subsequently grown *in vitro* for multiple generations, which are phenotypically and genotypically similar to their ancestor. Most often cells from advanced metastasized tumors grow into successful immortalized cell lines due to acquired changes during cancer development [1]. Thus, study of cell lines provides a good test for determining features common to cancerous cells in a relatively well controlled and reproducible system.

Human and animal cell lines have been used extensively in light scattering studies [2-6]. In our work, light scattering properties of three cell lines are studied: HeLa, HT29 and T84, all of which are grown in our cell culture facility. HeLa is the first and most widespread human cell line derived from a cervical adenocarcinoma [7, 8]. HeLa cells are known for relatively high growth rate (8 h. population doubling), undemanding growth conditions, and high viability. HT29 cell line is a human colon cancer cell line derived from a primary colonic tumor [9]. T84 cell line is also a colon cell line, but it is derived from a metastasis to the lung [10]. T84 and HT29 cell lines have been previously studied using light scattering techniques and size distribution and refractive index contrast of the nuclei has been reported [5, 11-13]. Backman *et. al.* studied scattering of T84 cells on top of highly scattering media, while Wax *et. al.* studied cell monolayer (single confluent cell layer) [11-13]. These studies

report three different results for refractive index contrast $m=1.02-1.03$, 1.04 and 1.06 , yet the agreement on morphological estimation of nuclear size distribution is quite remarkable in each case. Wax *et. al.* also studied HT29 cell monolayer and report another index contrast value of $m=1.066$ [5]. We target our cell line studies to enhance signals from the nuclei in order to better quantify their contribution to specific backscattering signals, put out better estimate on refractive index contrast and test limits of light scattering signal sensitivity to nuclear size measurements.

3.1.2 Cell sample growth and preparation

Cell monolayers were grown in the in-house cell culture facility using standard procedures for epithelial cell growth [14]. Original stocks of HeLa, HT29 and T84 cells and the corresponding culture protocols were a gift of the Harvard Digestive Diseases Center. HeLa and HT29 cells were grown with the same high-glucose Dulbecco's modified Eagle medium supplemented with 10% fetal calf serum, 5% penicillin and streptomycin mixture, while T84 used a 1:1 mixture of and Ham's F12 medium and the above medium (all products from Gibco , Invitrogen Cell Culture). Cells were incubated in 75 mm^2 and 25 mm^2 culture flask (Falcon) at 37° C in a humidified atmosphere of 5% CO_2 in the air. Cells were passaged upon reaching confluency (fully grown single layer of cells), which happened every 3 days for HeLa cells, every 4-5 days for HT29 and every 7 days for T84 cells. Trypsin at 0.25% mixed with EDTA (Gibco Invitrogen Cell Culture) was used to remove cells from substrate and break inter-cellular junctions. The trypsinized media was removed after centrifugation and cells were re-suspended in the growth media. Cells were re-seeded at densities of 1:6 for HeLa, 1:3 for HT29, and 1:2 for T84 cells for the experiments.

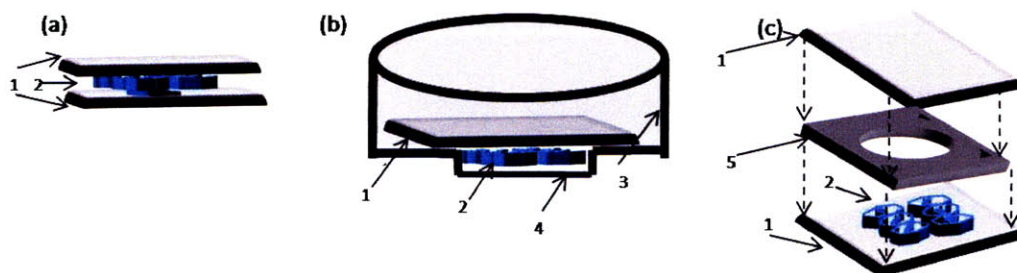


Figure 3 1 Cell holder geometries a) Two #1 thickness coverslips (1), cells (2) are in-between **b)** Plastic dish ((3), $\text{Ø}50 \text{ mm} \times 7 \text{ mm}$ height) with glass bottom ((4) $\text{Ø}25 \text{ mm}$, #0), cells (2) on top of glass bottom covered by #1 glass coverslip (1) **c)** Two #0 thickness coverslips (1), cells (2) on the bottom coverslip, sticky insert ((5), $\text{Ø}20 \text{ mm}$)

For light scattering measurements, cell media was replaced through 3-cycle centrifugation and rinsing with optically clear Hanks Balanced Salt Solution (HBSS) or Phosphate Buffer Solution (PBS from Gibco, Invitrogen Cell Culture). We conducted experiments with cells suspended in buffer solutions as well as cell monolayers attached to the substrate.

Three different sample holders were designed and optimized for the specific experiments (Figure 3.1). In the simplest design geometry cells in the media (2) were placed between two #1 or #0 glass coverslips (Electron Microscopy Sciences) (Figure 3.1.a). Glass coverslips are optically transparent in the visible range of wavelengths. Minimal commercially available thickness (0.1-0.7 mm) was used to minimize background scattering effects. A limitation of this geometry was that culture media was held only by capillary action with the glass, thus thickness of the sample could be changing with evaporation and there was a risk of cell de-hydration during long experiments. In addition, cells had to be grown on the fragile coverslip and submerged in culture media, resulting in frequent glass fracture during handling and transfer to the experimental chamber. Two other geometries were designed to address these problems. Glass-bottom dish (3, Mattek Corp., Ashland, MA) is a plastic dish, where bottom was replaced with #1 coverslip (4), which allowed cells to be easily grown and sampled in the same holder. Although optimal for cell growth, plastic dish is significantly bulkier than coverslips with 7 mm sidewalls and 50 mm² bottom (Figure 3.1.b). Larger sample holder could be a source of additional scattering background. Compromise between two sample geometries was achieved using double-sided adhesive inserts (5, GraceBio-Labs Inc., Oregon). Two centimeter diameter opening of an insert allows clear transmission of light (Figure 3.1.c). An insert has low thickness of 0.2 mm. Due to the double adhesive layer, there is no de-hydration of the sample. However, fragility still stays an issue. The adhesive insert geometry allowed microscopic evaluation of the site to be done during the light scattering experiment, while with other sample holders, the sample grown in parallel with the experimental one had to be assessed.

For single cell measurements, cells can be kept in the media because these measurements are largely insensitive to media absorption and fairly short (<10s) [15]. After removal from culture flask surface, cells were diluted to decrease cell concentration to about 1 cell per 50 μm² and placed in a dish with a 50 mm² #1 thickness coverslip on the bottom. Cells were given 4-5 h to settle and attached to the coverslip surface, then the coverslip was

removed from the dish and a second #1 coverslip is placed on top of the cells, as in the simplest cell sample geometry (as in Figure 3.1.a).

3.1.3 Cell sample characterization

Morphological information about our cells can be extracted using conventional phase contrast and fluorescence microscopy. We used the combined fluorescence and transmission upright microscope from Zeiss microscope with 5-40x magnification coupled to CCD camera to take images of the samples. In order to study nuclear size distribution, cells are stained with a DAPI DNA-stain (Sigma Aldrich), which binds DNA and causes fluorescence above 425 nm of the binding sites, highlighting the nucleus [16]. Composite images of the three cell monolayer types are shown in Figure 3.2.

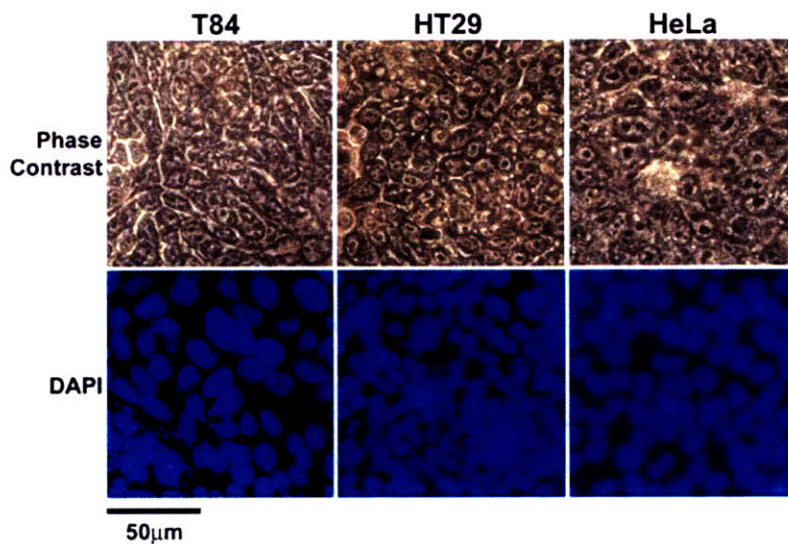


Figure 3.2 Phase contrast and fluorescence images for three cell monolayers at 40x

HT29 cells appear most uniform morphologically, while T84 cells show the greatest variation. Size distribution of the nuclei was established by Dr. K. Badizadegan in representative samples, and the data are summarized in Table 3.1. Length corresponds to the longest dimension of the nucleus and breadth is measured at the point perpendicular to the longest dimension.

Notice that the aspect ratio of major-to-minor axes varies between 1.35 and 1.5, which indicates that nucleus has an ellipsoidal shape, with the equivalent sphere diameter distribution also given. When compared to normal colon cells, HT29 and T84 cells have a larger mean nuclear diameter (by 40-80%), a larger variation in nuclear diameter from the

mean (14% and 20% vs. 7%) and a larger nucleus-to-cytoplasm ratio (60% and 85% vs. 20%) [17, 18].

Cell type	Equiv. Sphere Distribution, μm	Major axis, μm	Minor axis, μm
HT29	10.32 \pm 1.45	12.74 \pm 2.54	8.77 \pm 1.36
HeLa	12.78 \pm 2.19	15.42 \pm 2.94	11.31 \pm 2.14
T84	14.6 \pm 2.65	17.92 \pm 3.66	12.52 \pm 2.51
Normal Colon [12, 13]		9.1 \pm 0.68	

Table 3 | Summary of measured nuclear size distributions in the ellipsoidal approach for three cell monolayers under investigation. Equivalent sphere diameter distribution is considered. Data are compared with size distribution from normal colon

We also characterized cell suspension samples in the ways similar to our analysis of the cell monolayers above. The phase contrast of a typical cell suspension is presented in Figure 3.3. The bright edges are due to a high index contrast gradient between cell border and the media. For cell suspensions, we mainly characterize cell diameter distribution.

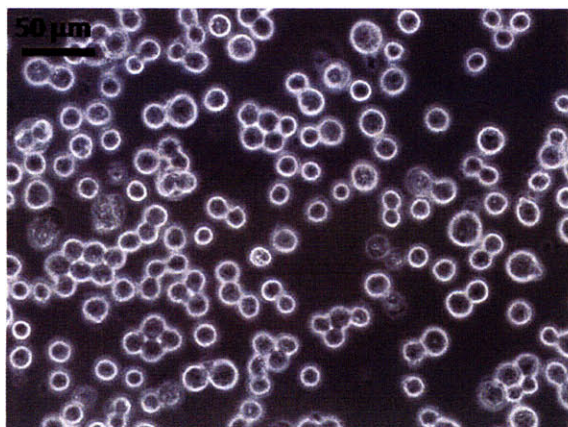


Figure 3 3 Phase contrast image of HT29 cell suspension, 20x

In single cell studies, high resolution brightfield microscopy images and phase images of a specific cell were obtained during the measurement with resolution of about 150 nm [15]. Morphological information was extracted directly along with the processing of scattering data and both processes are described alongside in chapter 6.

3.2 Rat Esophageal Cancer Model

3.2.1 Animal Model Selection

Epithelium is a tissue lining outer surfaces and inner cavities of the body, and it is estimated that about 85% of cancers are epithelial in origin [19]. Originating from the esophageal lining epithelium, squamous cell carcinoma represents about 90% of all esophageal cancers worldwide [20]. Epithelial dysplasia is a pre-cursor state of squamous cell carcinoma, which is characterized in microscopic examination by accumulation of atypical cells with nuclear hyperchromasia, abnormal chromatin and loss of polarity. Dysplasia is believed to develop from mild into severe forms, followed by carcinoma in-situ and invasive carcinoma. Several nitrosamine-compounds in the diet have been linked in epidemiological studies to high incidence of squamous cell carcinoma, although the exact mechanism of carcinogenesis has not been studied in humans.

One of the nitrosamine compounds, methylbenzyl nitrosamine (NMBA), is able to induce esophageal dysplasia in rats with similar molecular mechanism and microscopical manifestation to human disease [20, 21]. The model has been used extensively to study chemopreventive mechanisms of suppressing NMBA-induced dysplasia in rat esophagus [20, 22-24]. NMBA would induce methylation of guanine adducts in DNA, causing mutation in amino-acid groups of oncogenes *ras* and p53. Moreover, a quantitative study of microscopic tissue images demonstrates ability to assess severity of dysplasia based on absolute intensity and local distribution of staining of nuclei, given information about their number density and degree of nuclei atypia [25]. Around the same time, light scattering techniques were being tested for diagnostic capabilities in a variety of human epithelial cancers in a limited number of *in vivo* experiments including ones for oral cavity, esophagus, colon, and cervix [12, 26, 27]. In these studies, changes in average nuclear size, size variation, and nuclear density and refractive index variations correlated with histopathological evaluation of normal and cancerous tissues. Thus, we postulated that it may be possible to apply light scattering to NMBA rat esophagus carcinogenesis model in order to predict the degree of dysplasia in *ex vivo* tissues without the use of any exogenous agents, and to use tissue scattering signatures as potential biomarkers in a chemopreventive agents study.

3.2.2 Rat esophagus study protocol

Our experimental work in rat esophageal cancer studies was conducted in collaboration with the research group of Dr. Gary Stoner in Ohio State University [22, 25, 28, 29], with proven expertise in applying of the NMBA-carcinogen model to study of chemopreventive agents. The goal of the study was to diagnose NMBA-induced dysplasia in Fisher 344 rats and to test the use of curcumin as a chemopreventive agent.

Animal protocol. All of the experimental protocols were in accordance with the NIH guidelines and were approved by the Institutional Animal Care and Use Committees of the Massachusetts Institute of Technology and Ohio State University. Male F344 rats were obtained from Harlan Sprague Dawley (Indianapolis, IN) at 5–6 weeks of age. All rats were fed a modified AIN-76A diet consisting of 20% casein, 0.3% DL-methionine, 52% cornstarch, 13% dextrose, 5% corn oil, 5% Alphacel, 3.5% AIN mineral mixture, 1% AIN vitamin mixture, and 0.2% choline bitartrate. The rats were maintained under standard conditions (20±2°C temperature, 50±10% relative humidity; 12/12-h light-dark cycle). After transfer to the Massachusetts Institute of Technology, rats were under acclimatization for a 2-week period.

Carcinogen and chemopreventive administration. NMBA, from Ash Stevens (Detroit, MI), was administered subcutaneously 3 times per week for 5 weeks in the dose of 0.25 mg/ml. A dose of 0.5 mg/ml would induce dysplasia in 100% of the rats by the 5th week of post-carcinogen treatment [25]. The solvent for NMBA is 20% DMSO:H₂O, and the injection volume is 0.2 ml. Chemopreventive curcumin was purchased from LKT Laboratories (St. Paul, MN). The chemopreventive was administrated through diet beginning a week after the end of NMBA treatment until the time of the actual measurement.

3.2.3 Tissue sample preparation, registration and grading

At 20 weeks after beginning of carcinogen treatment, animals were euthanized using CO₂, and their esophagi were immediately excised, longitudinally opened and two 1 cm-long sections cut out starting at about 5 mm from the top of the esophagus. One of the sections was laid out flat, epithelial side-up, onto a #1 glass coverslip, submerged into HBSS, covered with another coverslip on top and taken for light scattering experiment (Figure 3.4.a). The second section underwent chemical processing to physically isolate epithelium from underlying connective tissue and muscle. An enzyme (dispase II, extracted from bacteria

neutral protease) had been previously used to separate epithelia from underlying connective tissue and to disperse cells in cell culture, depending on concentration and length of application [30]. We used concentration of 1 U/ml of dispase II (Sigma-Aldrich, US) in HBSS and 30 minute incubation time to loosen epithelial-stromal junction, thereafter separating epithelium gently with forceps. Extracted epithelium was placed in the sample holder. Efforts were made to keep epithelium polarity the same as in tissue experiments (Figure 3.4.b).

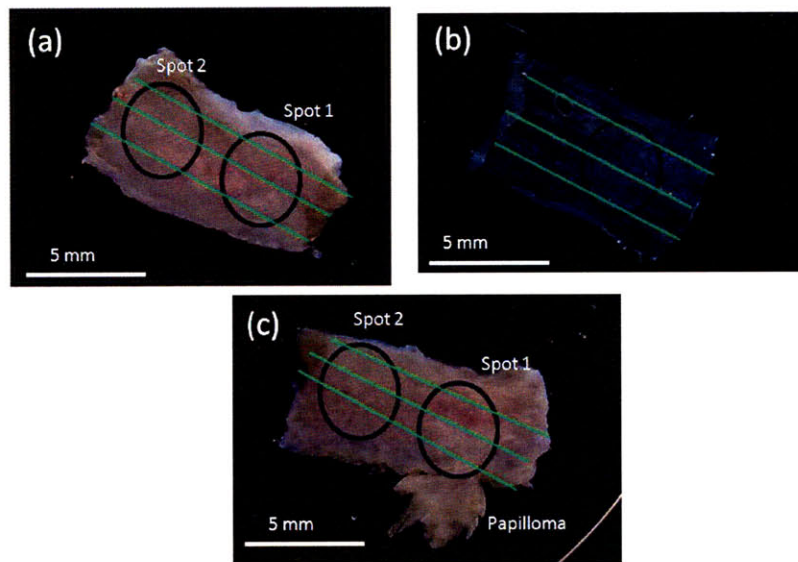


Figure 3.4 Camera photographs of various rat samples in a sample holder. Measurement spots are marked (black circles). Histopathological section sites are marked (green lines). a) Normal rat tissue sample b) Extracted epithelium of a normal sample c) Dysplastic rat tissue sample with papilloma

Upon gross examination, there was little difference between normal and dysplastic samples, except for the presence of papillomas (abnormal outgrowth of epithelium into esophageal lumen) (Figure 3.4.c). Papillomas represent benign proliferative lesions of the epithelial surface, in contrast to invasive carcinomas which invade the supporting connective tissues underlying the epithelium. The presence and number of papillomas in the previous studies correlated with the development of dysplasia [20, 21]. Papillomas were avoided during light scattering measurements to make the field of measurement more uniform. Two locations (22mm^2 each) were studied for each rat tissue sample and one location for each rat epithelial sample. There were 5 rats sacrificed for each of the following study groups: (i) Normal; (ii) Curcumin-treated control group; (iii) NMBA-treated; and (iv) NMBA- and curcumin-treated rats. Each measurement area was marked with black ink for grading and

sample polarity identification. Immediately after the measurement, tissue was fixed in formalin for histopathological grading. Intact tissue samples were fixed in approximately 50 minutes from the time of excision, while isolated epithelia were fixed in approximately 85 minutes from the time of excision.

For histopathological evaluation, three longitudinal cross-sections of the sample (5 μm thick) were taken from the middle of the marked measurement area and closer to the edges (green lines on Figure 3.4, not to scale). Cross-sections were stained with H&E (MIT Division of Comparative Medicine) and evaluated under upright microscope (Axioscope, Zeiss) at 4x, 20x and 40x magnification. In addition to the regular eyepiece, the microscope was equipped with a secondary arm, in which the eyepiece had been replaced by a CCD light detector. The image viewed in eyepiece was registered on a CCD detector and transferred to computer for further analysis.

The tissue was graded under the guidelines of an experienced pathologist (Dr. Charles Boone). Combination of high and low magnification images gave information about local microstructure and its consistency throughout the section length. Normal esophageal epithelium in the rat contains stratified (layered) squamous epithelium consisting of three distinct layers: basal cell layer, intermediate cell layer and keratin layer [14] (Figure 3.5.a). Basal cell layer (B) consists of single layer of cells proliferation and differentiation of which has created and controlled epithelium. Basal cells differentiate into prickle cells, which form an intermediate layer (I) 2-6 cells thick. Basal cells usually stain darker than prickle cells. Finally, differentiated prickle cells should lose their nuclei and form keratin layer (K). Under microscopic examination several key features pertinent to dysplasia are identified: increase in cellular density of basal cell layer (1), increase in density of intermediate layer (2), thickening of keratin (3), overall thickening of epithelium (compare side bars), and increase in variability in all of these parameters (Figure 3.5.b).

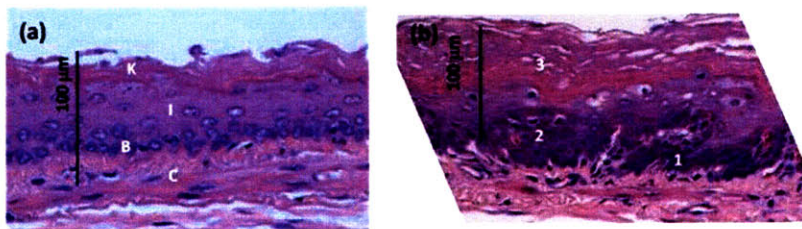


Figure 3.5 H&E histological sections of rat esophageal tissue at 20x a) Normal section: three epithelium sub-layers, K-keratin, I-intermediate, B-basal, and connective tissue C. b) Dysplastic tissue and it's properties: increase in cellular density of basal cell layer (1), increase in density of intermediate layer (2), thickening of keratin (3)

Quality of our H&E stained images does not allow for conclusive results about basal cell nuclei size distribution due to combined effects of H&E sectioning, relatively small size of basal cells ($\sim 5\text{-}6\ \mu\text{m}$) and low magnification of a microscope, given resolution of $0.25\ \mu\text{m}$ per CCD pixel. Overall normal epithelium thickness is anywhere between 60 and $90\ \mu\text{m}$ for different samples with a uniform behavior throughout. Dysplastic epithelium has an increase in local thickness and greater variation on lower magnification images (Figure 3.6, 10x).

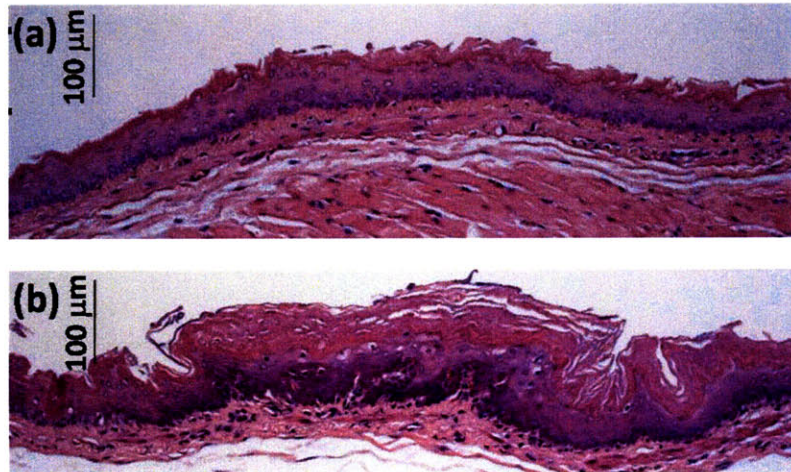


Figure 3.6 H&E histological sections of rat esophageal tissue at 10x a) Uniformity of normal tissue section b) Variability of dysplastic tissue sample

Extracted epithelium is a very difficult sample to handle. Extracted epithelium has a lower thickness ($20\text{-}40\ \mu\text{m}$ lower for normal samples) than when it is intact and attached to the stroma. This possibly happens due to epithelial-stromal junction keeping epithelium under tension. Fragility due to low thickness makes it subject to tear, flipping and bunching up, which most often happens during process of fixation and histological processing and on rare occasions before light scattering experiments. We did take a note of the samples, which bunch before light scattering experiments to keep an eye for abnormal outcomes. In addition, although most of the epithelium isolated pretty well from the connective tissue, there was a significant loss of basal cell layer – samples have variation anywhere between 10% and 60% of basal layer being preserved (Figure 3.7). Epithelium light scattering data were analyzed along with tissue data. The grading of epithelium by itself is very hard, as it breaks up during processing due to fragility. Therefore, in most cases the grade is inferred from the grade of the original tissue sample.

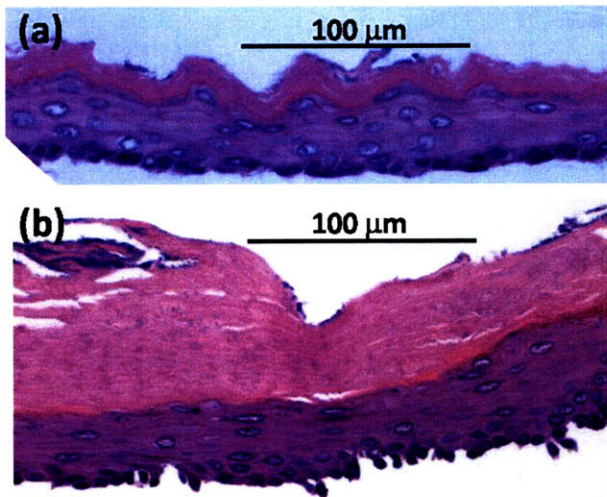


Figure 3.7 H&E histological sections of rat esophageal epithelium a) Normal section b) Dysplastic section

According to the histopathologic analysis, all tissue was divided into two diagnostic groups: normal and dysplastic. A third group (“not counted”) consisted of samples in which scattering was not analyzed due to experimental errors. The grading results are summarized in Table 3.2, in which the rat tissue of each study group is sorted into the three diagnostic categories. Out of 20 tissue samples we used for the experiment, 4 samples were not analyzed due to experimental errors. One sample from normal group had epithelium smaller than incident beam diameter, hence it had direct stroma contribution to the signal. One sample from chemopreventive control group dropped and flipped epithelium side down during re-positioning in the sample holder. Stromal contribution was detected instead of epithelial in this case. One sample from NMBA treated group had a polyp throughout measurement areas. One sample of NMBA-chemopreventive group was disregarded since water was used in the experiment instead of buffer solution.

Rat Group/Diagnosis	Normal	Dysplastic	Not counted
Control	4	0	1
Curcumin	4	0	1
NMBA	1	3	1
NMBA+curcumin	1	3	1

Table 3.2 Summary of rat tissue histological grading by group

Thickness measurements of rat esophagus tissue are summarized together with scattering data in section 8.2.4, where connection between tissue thickness and scattering measurements is established. To summarize, description of biological samples selection and

preparation for light scattering experiments is given in this chapter. Also, a baseline for light scattering experiment interpretation is established by providing morphometric characterization of cells and pathological grading of tissue samples.

References

- [1] Masters JRW. Human cancer cell lines: fact and fantasy. *Nature Reviews Molecular Cell Biology* 2000;1:233.
- [2] Mourant JR, Hielscher AH, Eick AA, Johnson TM, Freyer JP. Evidence of intrinsic differences in the light scattering properties of tumorigenic and nontumorigenic cells. *Cancer Cytopathology* 1998;84:366.
- [3] Wilson JD, Bigelow CE, Calkins DJ, Foster TH. Light scattering from intact cells reports oxidative-stress-induced mitochondrial swelling. *Biophysical Journal* 2005;88:2929.
- [4] Xu M. Superposition rule for light scattering by a composite particle. *Optics Letters* 2006;31:3223.
- [5] Wax A, Yang C, Backman V, Badizadegan K, Boone CW, Dasari RR, Feld MS. Cellular Organization and Substructure Measured Using Angle-Resolved Low-Coherence Interferometry. *Biophysical Journal* 2002;82:2256.
- [6] Backman V, Gopal V, Kalashnikov M, Badizadegan K, Gurjar R, Wax A, Georgakoudi I, Mueller M, Boone CW, Dasari RR, Feld MS. Measuring cellular structure at submicrometer scale with light scattering spectroscopy. *Ieee Journal of Selected Topics in Quantum Electronics* 2001;7:PII S1077.
- [7] Gey GO, Coffman WD, Kubicek MT. Tissue culture studies of the proliferative capacity of cervical carcinoma and normal epithelium. *Cancer Res* 1952;12.
- [8] Masters JR. HeLa cells 50 years on: the good, the bad and the ugly. *Nature Reviews Cancer* 2002;2:315.
- [9] Fogh J. *Human tumor cells in vitro*. New York: Plenum Press, 1975.
- [10] Murakami H, Masui H. Hormonal-control of human-colon carcinoma cell-growth in serum-free medium. *Proceedings of the National Academy of Sciences of the United States of America-Biological Sciences* 1980;77:3464.
- [11] Perelman LT, Backman V, Wallace M, Zonios G, Manoharan R, Nusrat A, Shields S, Seiler M, Lima C, Hamano T, Itzkan I, Van Dam J, Crawford JM, Feld MS. Observation of periodic fine structure in reflectance from biological tissue: A new technique for measuring nuclear size distribution. *Physical Review Letters* 1998;80:627.
- [12] Backman V, Gurjar R, Badizadegan K, Itzkan L, Dasari RR, Perelman LT, Feld MS. Polarized light scattering spectroscopy for quantitative measurement of epithelial cellular structures in situ. *Ieee Journal of Selected Topics in Quantum Electronics* 1999;5:1019.
- [13] Graf R, Wax A. Nuclear morphology measurements using Fourier domain low coherence interferometry. *Opt. Express* 2005;13:4693.
- [14] Wise C. *Epithelial cell culture protocols*: Humana Press, 2002.
- [15] Choi W, Fang-Yen C, Badizadegan K, Oh S, Lue N, Dasari RR, Feld MS. Tomographic phase microscopy. *Nature Methods* 2007;4:717.
- [16] Kapuscinski J. DAPI: a DMA-specific fluorescent probe. *Biotechnic and Histochemistry* 1995;70:220.
- [17] Tipoe GL, White FH, Pritchett CJ. A morphometric study of histological variations during cellular-differentiation of normal human colorectal epithelium. *Journal*

of Anatomy 1992;181:189.

- [18] P.W. Hamilton. A combination of cytological and architectural morphometry in assessing regenerative hyperplasia and dysplasia in ulcerative colitis. *Histopathology* 1990;17:59.
- [19] Kumar V, Abbas A, Fausto N. *Pathologic basis of disease: Saunders*, 2005.
- [20] Stoner GD, Gupta A. Etiology and chemoprevention of esophageal squamous cell carcinoma. *Carcinogenesis* 2001;22:1737.
- [21] Pozhariski K. *Tumors of the Esophagus*. Lyons, France: IARC Scientific Publications, 1990.
- [22] Boone CW, Stoner GD, Bacus JV, Kagan V, Morse MA, Kelloff GJ, Bacus JW. Chemoprevention with theaflavins of rat esophageal intraepithelial neoplasia quantitatively monitored by image tile analysis. *Cancer Epidemiology Biomarkers & Prevention* 2000;9:1149.
- [23] Li Z, Shimada Y, Kawabe A, Sato F, Maeda M, Komoto I, Hong T, Ding YZ, Kaganoi J, Imamura M. Suppression of N-nitrosomethylbenzylamine (NMBA)-induced esophageal tumorigenesis in F344 rats by JTE-522, a selective COX-2 inhibitor. *Carcinogenesis* 2001;22:547.
- [24] Wargovich MJ, Woods C, Eng VWS, Stephens LC, Gray K. Chemoprevention of n-nitrosomethylbenzylamine-induced esophageal cancer in rats by the naturally-occurring thioether, diallyl sulfide. *Cancer Research* 1988;48:6872.
- [25] Boone CW, Stoner GD, Bacus JV, Kagan V, Morse MA, Kelloff GJ, Bacus JW. Quantitative grading of rat esophageal carcinogenesis using computer-assisted image tile analysis. *Cancer Epidemiology Biomarkers & Prevention* 2000;9:495.
- [26] Backman V, Wallace MB, Perelman LT, Arendt JT, Gurjar R, Muller MG, Zhang Q, Zonios G, Kline E, McGillican T, Shapshay S, Valdez T, Badizadegan K, Crawford JM, Fitzmaurice M, Kabani S, Levin HS, Seiler M, Dasari RR, Itzkan I, Van Dam J, Feld MS. Detection of preinvasive cancer cells. *Nature* 2000;406:35.
- [27] Sokolov K, Drezek R, Gossage K, Richards-Kortum R. Reflectance spectroscopy with polarized light: is it sensitive to cellular and nuclear morphology. *Opt. Express* 1999;5:302.
- [28] Gupta A, Nines R, Rodrigo KA, Aziz RA, Carlton PS, Gray DL, Steele VE, Morse MA, Stoner GD. Effects of dietary N-(4-hydroxyphenyl)retinamide on N-nitrosomethylbenzylamine metabolism and esophageal tumorigenesis in the Fischer 344 rat. *Journal of the National Cancer Institute* 2001;93:990.
- [29] Morse MA, Kresty LA, Steele VE, Kelloff GJ, Boone CW, Balentine DA, Harbowy ME, Stoner GD. Effects of theaflavins on N-nitrosomethylbenzylamine-induced esophageal tumorigenesis. *Nutrition and Cancer-an International Journal* 1997;29:7.
- [30] Gipson IK, Grill SM. A technique for obtaining sheets of intact rabbit corneal epithelium. *Investigative Ophthalmology & Visual Science* 1982;23:269.

Chapter 4:

Theoretical modeling of light scattering

In this chapter we cover some of the basic theoretical approaches to light scattering. These approaches are used to connect structural information about scattering particle, such as size and more generally refractive index distributions, with scattering variations in angle and wavelength. First, Mie theory solution is introduced for scattering of a plane polarized wave on a homogenous sphere. Mie theory gives an exact numerical solution and is used extensively in analysis of light scattering data. Rayleigh and Rayleigh-Gans are analytical approximations to Mie theory and are discussed next. In Born and Rytov approximations, Fourier transform of refractive index distribution and scattering field are related. Fourier transform is a linear operation. The solution of an inverse problem, getting structural information from scattering data, is unique in these approximations. Both Born and Rytov approximations can only be applied under certain conditions, but for any particle shape.

4.1 Mie theory for spherical scatterer

4.1.1 Mie theory solution

Mie theory gives an exact numerical solution to far-field scattering of a plane wave on an isotropic homogenous dielectric sphere. Formal derivation of the formula can be found in the literature [1]. Below, we describe the results of the solution targeted to intensity-based experiments based on the formalism of Dr. Vadim Backman with minor corrections [2].

Electromagnetic wave in a time-averaged experiment is characterized by its direction of propagation in space described by wave vector \mathbf{k} , ($|\mathbf{k}| = 2\pi/\lambda$, where λ - wavelength of light in the media). Scattering is described within a scattering plane, which is defined by the \mathbf{k}_i , incident light wave-vector, and \mathbf{k}_s , scattered light wave-vectors (Figure 4.1, blue triangle). Parallel and perpendicular projections of incident field \mathbf{E}_i , and scattered field, \mathbf{E}_s , on a scattering plane are denoted, accordingly, $\mathbf{E}_{i\parallel}$, $\mathbf{E}_{i\perp}$ and $\mathbf{E}_{s\parallel}$, $\mathbf{E}_{s\perp}$. Scattered field is related to incident field through amplitude scattering matrix without time-dependent part of the field (van de Hulst),

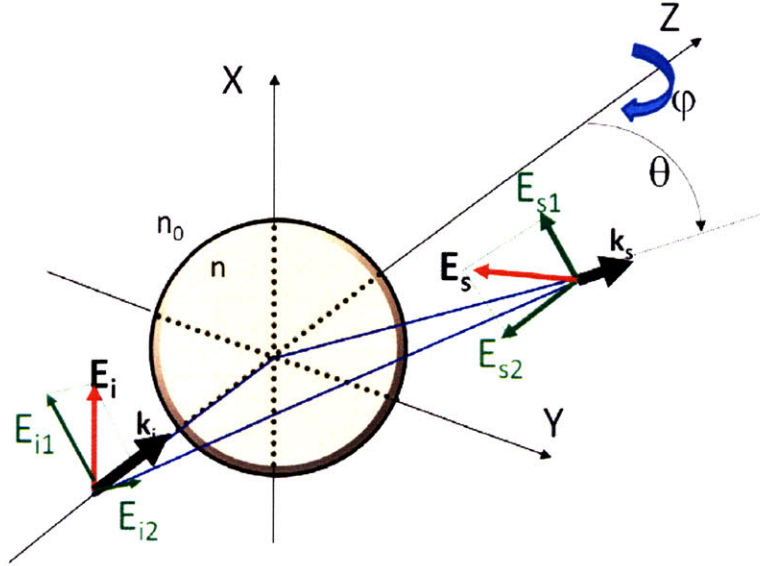


Figure 4.1 Mie scattering diagram: XYZ – laboratory system; k_s and k_i form scattering plane (blue triangle); E_i – incident field, E_s – scattered field; E_{i1} , E_{i2} , E_{s1} , E_{s2} – projections of incident/scattered field; θ – scattering angle, ϕ – azimuthal scattering angle;

$$\begin{pmatrix} E_{s1} \\ E_{s2} \end{pmatrix} = \frac{e^{-ikr}}{ikr} \begin{pmatrix} S2 & 0 \\ 0 & S1 \end{pmatrix} \begin{pmatrix} E_{i1} \\ E_{i2} \end{pmatrix} \quad (4.1)$$

Where,

$$S1 = \sum_{n=1}^{\infty} \frac{2n+1}{n(n+1)} \{a_n \pi_n(\cos \theta) + b_n \tau_n(\cos \theta)\} \quad (4.1.2)$$

$$S2 = \sum_{n=1}^{\infty} \frac{2n+1}{n(n+1)} \{b_n \pi_n(\cos \theta) + a_n \tau_n(\cos \theta)\}$$

Where,

$$a_n = \frac{\varphi'_n(mx)\varphi_n(x) - m\varphi_n(mx)\varphi'_n(x)}{\varphi'_n(mx)\zeta_n(x) - m\varphi_n(mx)\zeta'_n(x)} \quad (4.1.3)$$

$$b_n = \frac{m\varphi'_n(mx)\varphi_n(x) - \varphi_n(mx)\varphi'_n(x)}{m\varphi'_n(mx)\zeta_n(x) - \varphi_n(mx)\zeta'_n(x)}$$

$$\pi_n(\cos \theta) = \frac{1}{\sin \theta} P_n^1(\cos \theta)$$

$$\tau_n(\cos \theta) = \frac{d}{d\theta} P_n^1(\cos \theta)$$

Where $m = n/n_0$ is the relative refractive index ratio of sample(n)-to-media(n_0), $x = k \cdot a$, so called size parameters, is the product of wave-vector amplitude and particle radius, θ is a scattering angle between \mathbf{k}_i and \mathbf{k}_s . φ_n and ζ_n are Ricatti-Bessel functions, and P_n^1 are Legendre polynomials of the first kind, all of which can be calculated numerically [3]. **Therefore, according to Mie theory, scattering of a spherical particle depends on the scattering angle θ , relative refractive index contrast m , and ratio of particle radius to wavelength a/λ .**

In a laboratory system, the incident field has to be projected into scattering plane and scattered field is projected back onto laboratory axis \mathbf{E}_{ix} and \mathbf{E}_{iy} . Using standard formulas for vector projection and matrix rotation, the expression for the fields for geometry given on Figure 4.1 becomes [2]:

$$\begin{pmatrix} \mathbf{E}_x \\ \mathbf{E}_y \end{pmatrix} = \begin{pmatrix} \cos(\theta) \cos(\varphi) & \sin(\theta) \sin(\varphi) \\ \cos(\theta) \sin(\varphi) & \sin(\theta) \cos(\varphi) \end{pmatrix} \begin{pmatrix} S_2 & 0 \\ 0 & S_1 \end{pmatrix} \begin{pmatrix} \cos(\varphi) \\ \sin(\varphi) \end{pmatrix} |E_o| \frac{e^{-ikr}}{ikr} \quad (4.2)$$

where, $0 < \varphi < 2\pi$ is the angle of rotation around axis Z in XY-plane.

Intensity of scattered light equals to the square of the field. Taking complex conjugate and conducting matrix multiplication, we get:

$$I_x = (|S_2|^2 \cos^2(\theta) \cos^4(\varphi) + |S_1|^2 \sin^4(\varphi) - 2\text{Re}(S_1 S_2^*) \cos(\theta) \cos^2(\varphi) \sin^4(\varphi)) \frac{I_o}{k^2 r^2} \quad (4.3)$$

$$I_y = (|S_2|^2 \cos^2(\theta) + |S_1|^2 - 2\text{Re}(S_1 S_2^*) \cos(\theta)) \cos^2(\theta) \cos^2(\varphi) \sin^2(\varphi) \frac{I_o}{k^2 r^2}$$

Intensities I_x and I_y in our notation are intensities measured with linear polarizer behind the sample parallel and perpendicular to the incident beam polarization. They are denoted as I_{\parallel} and I_{\perp} . On-axis amplitude of $I_{\perp}(\varphi=0^\circ, 90^\circ)$ equals to zero. Note, that fields \mathbf{E}_x and \mathbf{E}_y are linear combinations of the scattered fields $\mathbf{E}_{s,\parallel}$ and $\mathbf{E}_{s,\perp}$ calculated with respect to the scattering plane. Parallel and perpendicular notation in the referenced scattering books, such as van de Hulst or Bohren and Huffman, is set with respect to scattering plane, thus, it is different from the current work, where parallel and perpendicular are set with respect to laboratory frame. Therefore, care should be taken in using scattering formulas from the volumes (see example in 4.1.3). The following notation is chosen because it has direct relevance to the experimentally measured parameters.

4.1.2 Definition of scattering parameters

Various parameters are used to describe scattering from specific samples and relate microscopic and macroscopic scattering properties. In this section, we give definition for some of the most widely used ones in the literature.

Measured quantity in our experiments is differential scattering cross-section $\sigma(\theta, \varphi)$:

$$\sigma(\theta, \varphi) = r^2 * \frac{I}{I_0} = \frac{F(\theta, \varphi)}{k^2} \quad (4.4)$$

Differential scattering cross-section has units of area and denotes the amount of light scattered in a unit solid angle by unit incident irradiance [1, 3]. Function $F(\theta, \varphi)$ is called scattering phase function (nothing to do with phase of the wave). It equals to the square of the scattering amplitude matrix times all the angular transformations (compare Eq. 4.4. and 4.3). Phase function is dimensionless quantity describing probability of scattering in a unit solid angle, thus the integral of phase function over all solid angle equals to 1:

$$\int_{4\pi} F(\theta, \varphi) d\Omega = 1 \quad (4.5)$$

Total scattering cross-section is an integral of differential cross-section over scattering angles θ and azimuthal angle φ [3]:

$$\sigma_{TOTAL} = \int_0^\pi \int_0^{2\pi} \sigma(\theta, \varphi) \sin \theta d\theta d\varphi \quad (4.6)$$

When no absorption is present in the sample, total scattering cross-section equals to particle extinction coefficient C_{ext} , which describes amount of energy removed from original beam by the sample and is expressed in terms of forward scattering through extinction theorem [[1], p. 127]:

$$C_{ext} = \frac{4\pi}{k^2} Re(S(\theta = 0)) \quad (4.7)$$

Scattering extinction normalized by particle geometrical cross-section area is scattering efficiency, which is a dimensionless parameter:

$$C_{ext} = \frac{4\pi}{k^2} Re(S(\theta = 0)) \quad (4.8)$$

Total scattering cross-section and extinction are parameters connecting macroscopic and microscopic properties of scatterers. These parameters quantify with a single value

scattering of particle in a large ensemble of other structures producing a lot of scattering events. Another parameter playing a similar role is g , an asymmetry factor. Asymmetry factor equals to an average cosine of the scattering angle, defined through phase function:

$$g = \langle \cos \theta \rangle = \int_{4\pi} F(\theta, \varphi) \cos \theta \, d\Omega \quad (4.9)$$

If $g=0$, particle scatters isotropically, while $g>0$, means that light scatters mostly forward with respect to the incident beam, and $g<0$, describes the opposite direction of scattered beam propagation.

In case of many independent scatterers, scattering cross-section (and all similar parameters) is weighted by probability density distribution, $N(d)$:

$$\sigma_{distrib} = \int_0^{\infty} \sigma(d) * N(d) \, dd, \quad (4.10)$$

where $\int_0^{\infty} N(d) \, dd = 1$

Macroscopic description of an ensemble of particles is done through scattering coefficient μ_s , which is a product of total scattering cross-section and particle volume density, thus it has units of inverse length:

$$\mu_s = \rho(d) \sigma_{TOTAL}(d) \quad (4.11)$$

For many-particle simulation, such as Monte-Carlo, the likelihood of scattering in a certain direction is important, thus reduced scattering coefficient is introduced by combining scattering coefficient and anisotropy factor:

$$\mu_s' = \mu_s * g \quad (4.12)$$

As mentioned above, in our studies, we describe scattering in multi-cell and tissue work using differential scattering cross-section. In single cell work, we measure scattering phase function. Comparison of our results to other works in the field requires interpretation of our results in terms of other scattering parameters defined above.

4.1.3 Describing properties of Mie solution: Analytical approximations

Analytical approximations to Mie theory, though limited in the applicability range, give an insight into properties of Mie solution, otherwise buried in an expression of complex spherical harmonic functions. Depending on the diameter of the particles, we consider two approximations, Rayleigh and Rayleigh-Gans.

Rayleigh approximation of a scattering by point particles (dipole) is valid, when diameter, d , of the particle is much smaller than the wavelength of illumination λ . In the language of Mie solution $x \ll 1$ is very small and so is $m \cdot x \ll 1$. In this case differential scattering cross-section takes the following form, in scattering plane (SP) [1]:

$$\begin{aligned}\sigma_{\parallel sp} &= \left(\frac{m^2 - 1}{m^2 + 2}\right)^2 * a^6 * \lambda^{-4} * (\cos \theta)^2 \\ \sigma_{\perp sp} &= \left(\frac{m^2 - 1}{m^2 + 2}\right)^2 * a^6 * \lambda^{-4}\end{aligned}\quad (4.13)$$

And in laboratory frame (Eq. 4.3 and 4.4)

$$\begin{aligned}\sigma_{\parallel}(\varphi = 0^\circ) &= \left(\frac{m^2 - 1}{m^2 + 2}\right)^2 * a^6 * \lambda^{-4} * (\cos \theta)^4 \\ \sigma_{\parallel}(\varphi = 90^\circ) &= \left(\frac{m^2 - 1}{m^2 + 2}\right)^2 * a^6 * \lambda^{-4} \\ \sigma_{\perp}(\varphi = 90^\circ, 0^\circ) &= 0\end{aligned}\quad (4.14)$$

In order to not repeat lengthy expressions of Eq. 4.3, the two representative φ -angles are considered. According to Rayleigh formula, wavelength and angular dependence are decoupled from each other, particle diameter and refractive index contrast m . Scattering in wavelength follows λ^{-4} behavior characteristic of Rayleigh scatterer (Figure 4.2.a). Scattering in angle θ is uniform for $\varphi=0^\circ$ and follows $\cos(\theta)$ dependence for $\varphi=90^\circ$ component (Figure 4.2.b). There is no scattering with polarization perpendicular to incident beam at $\varphi=0^\circ$ or $\varphi=90^\circ$.

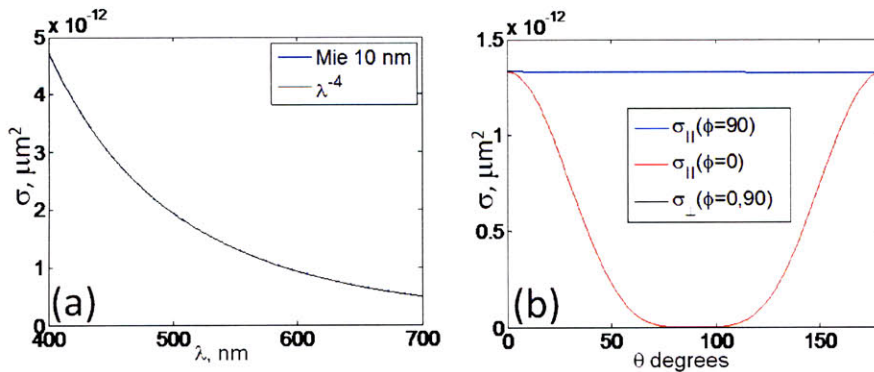


Figure 4.2 Rayleigh scattering cross-section for 10 nm sphere a) Wavelength spectrum (blue) and power law with -4 exponent (black) b) Co-polarized in plane and out of plane components; Cross-polarized component equals to zero

Under Rayleigh-Gans approximation, scattering particle is assumed to be an ensemble of Rayleigh scatterers, which interfere at the point of observation. The range of validity is

determined by matching two conditions: refractive index contrast of the particle should be small $|m-1| \ll 1$, and product of size parameter and refractive index contrast should be small $x * |m-1| \ll 1$. Both are related to the fact that incident field is unperturbed by the particle. Rayleigh-Gans theory is a particular case of Born approximation (see section 4.2) applied to spherical particles. Rayleigh-Gans formula for scattering has the following form:

$$\sigma_{II}(\varphi=0^\circ) = \left(\frac{m^2-1}{m^2+2}\right)^2 * a^6 * \lambda^{-4} * (\cos \theta)^4 * \frac{9}{u^6} (\sin u - u * \cos u)^2$$

$$\sigma_{II}(\varphi=90^\circ) = \left(\frac{m^2-1}{m^2+2}\right)^2 * a^6 * \lambda^{-4} * \frac{9}{u^6} (\sin u - u * \cos u)^2 \quad (4.15)$$

Scattering becomes a non-linear combination of sine and cosine functions, and gains an oscillatory component, determined by parameter $u=2x*\sin(\theta/2)$. Contributions of angle, wavelength and diameter are entangled in the body of oscillating function much like in Mie solution, but refractive index contrast m is not. Data are presented for wavelength variation at exact backscattering ($\theta=180^\circ$) and angular variation at $\lambda=550$ nm for σ_{II} at $\varphi=0$ for two diameters of the particle, 1 μm and 2 μm , and refractive index contrast $m=1.002$ (Figure 4.3.a-b). The conditions of applicability are observed, since $|m-1|=0.002$ and $x*|m-1|=0.061$. Notice, that frequency of the oscillations in angle or wavelength is increasing with increase in particle diameter.

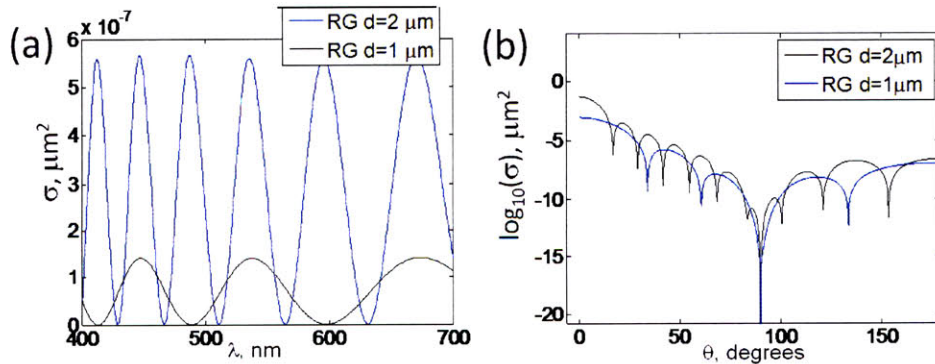


Figure 4.3 Rayleigh-Gans scattering oscillatory behavior in cross-section for 1 μm and 2 μm spheres a) Wavelength spectra at $\theta=180^\circ$ b) Angular spectra at $\lambda=550$ nm

Rayleigh and Rayleigh-Gans demonstrate scattering trends for scattering for very small sizes and also presence of oscillatory behavior. Properties of the exact Mie solution applied to scattering ranges of interest for the present work will be discussed in section 5.2.

4.2 Born approximation of weak scattering

Born approximation is based on the assumption that field scattered by a particle is much weaker than the incident field. The scalar wave equation for scattered field $U^{(s)}$,

$$(\nabla^2 + n_o^2 k^2)U^{(s)}(\vec{r}, w) = -4\pi F(\vec{r}, w)U^{(T)}(\vec{r}, w) \quad (4.16)$$

can be represented by the integral form [4].

$$U^{(s)}(\vec{r}, w) = \int_V F(\vec{r}', w)G(\vec{r}-\vec{r}', w)U^{(T)}(\vec{r}', w)d^3\vec{r}' \quad (4.17)$$

In the formula,

$U^{(T)} = U^{(i)} + U^{(s)}$, relation between total, scattered and incident fields,

$$F(\vec{r}, w) = -\frac{1}{4\pi} * k^2 (n^2(\vec{r}, w) - n_o^2) \quad (4.18)$$

scattering potential, characterizing sample, with $n(\vec{r}, w)$, index distribution in the sample, and n_o - index of the media,

$$G(\vec{r}-\vec{r}', w) = \frac{e^{i\vec{k}_s \cdot (\vec{r}-\vec{r}')}}{|\vec{r}-\vec{r}'|} \quad (4.19)$$

Green's function, characterizing propagation of the scattering field from each point in the sample,

$$U^{(i)}(\vec{r}, w) = e^{i\vec{k}_i \cdot \vec{r}}$$

incident field, which is a plane wave in our case. Note, that integral is taken over sample volume and is zero outside. In the first Born approximation the total field inside the particle equals to the incident field,

$$U^{(T)}(\vec{r}, w) \cong U^{(i)}(\vec{r}, w) = e^{i\vec{k}_i \cdot \vec{r}} \quad (4.20)$$

thus we get a closed-form solution for wave equation in integral form

$$U^{(s)}(\vec{r}, w) = \int_V F(\vec{r}', w)G(\vec{r}-\vec{r}', w)U^{(i)}(\vec{r}', w)d^3\vec{r}' \quad (4.21)$$

Applicability range of Born approximation can be most generally determined according to the maximum phase change $2 * \pi / \lambda * (n(\vec{r}, w) - n_o)$ through the sample being lower, than π [5]. Therefore, applicability of Born approximation would depend on physical dimensions of the particle, and would be more often applicable to smaller (compared to wavelength) size particles or particles with very low index contrast. If particles are spherical,

then the limit is transformed into well-known limit for Rayleigh-Gans approximation, of $k*d*(m-1) < 1$. For incident light wavelength of $\lambda=550$ nm, particle diameter of $d=1$ μm , relative refractive index contrast of $m=1.03$, the maximum phase change equals to 0.46. In this case, particles below 1 μm are within the range of Born approximation.

Higher order Born approximations ($n>1$) can be obtained by recursively adding scattered fields of the order of ($n-1$) to the incident field into the formula (4.21).

Substituting expression for Green's function in the far-field approximation

$$G(\vec{r}-\vec{r}', \omega) = \frac{e^{i\vec{k}_s \cdot (\vec{r}-\vec{r}')}}{|\vec{r}-\vec{r}'|} \cong \frac{e^{-ikr}}{r} e^{-i\vec{k}_s \cdot \vec{r}'} \quad (4.22)$$

and re-arranging terms

$$U^{(S)}(\vec{r}, \omega) = \frac{e^{-ikr}}{r} \int_V F(\vec{r}', \omega) e^{-i(\vec{k}_s - \vec{k}_i) \cdot \vec{r}'} d^3\vec{r}' \quad (4.23)$$

we obtain scattered field proportional to a Fourier transform of the scattering potential. The integral part of the expression is defined as scattering amplitude function

$$f^{(S)}(\vec{k}_s, \vec{k}_i) = \int_V F(\vec{r}', \omega) e^{-i(\vec{k}_s - \vec{k}_i) \cdot \vec{r}'} d^3\vec{r}' \quad (4.24)$$

The difference between scattered and incident wave vector defines scattering momentum q , with absolute value $|q| = k*\sin(\theta/2)$.

4.3 Rytov approximation of weak change in phase

In Rytov approximation it is assumed, that gradient of the phase changes slowly over distances comparable to wavelength of incident light. Rytov introduced a complex phase, φ , such, that the field is defined by

$$U(\vec{r}) = e^{\varphi(\vec{r})} \quad (4.25)$$

and scattered, total and incident phases are related through

$$\varphi^{(T)}(\vec{r}) = \varphi^{(i)}(\vec{r}) + \varphi^{(s)}(\vec{r}) \quad (4.26)$$

The wave equation then takes the following form

$$(\nabla^2 + n_o^2 k^2) U^{(i)}(\vec{r}) * \varphi^{(s)}(\vec{r}) = -4\pi U^{(i)}(\vec{r}) * \left\{ F(\vec{r}) + \left(\nabla \varphi^{(s)}(\vec{r}) \right)^2 \right\} \quad (4.27)$$

and corresponding integral form will be [4]

$$U^{(i)}(\vec{r}) * \varphi^{(s)}(\vec{r}) = \int_V G(\vec{r}-\vec{r}') U^{(i)}(\vec{r}') * \{F(\vec{r}') + (\nabla\varphi^{(s)}(\vec{r}'))^2\} d^3\vec{r}' \quad (4.28)$$

The right side of the integral will take the same form as in the first Born approximation, if

$$F(\vec{r}') + (\nabla\varphi^{(s)}(\vec{r}'))^2 \cong F(\vec{r}') \quad (4.29)$$

That condition is called first Rytov approximation and can be explicitly written out as [5]:

$$(n^2 - n_o^2) \gg (\nabla\varphi^{(s)}(\vec{r}') \frac{\lambda}{2\pi})^2 \quad (4.30)$$

Therefore, Rytov approximation is sensitive to the phase gradient inside the sample being smaller than relative refractive index contrast, in other words, phase changes slowly inside the sample. Applicability of Rytov approximation depends strongly on the structure of the sample, while overall sample dimension plays less crucial role than in the case of Born approximation.

Higher order Rytov approximations ($n > 1$) can be obtained by recursively substituting complex scattered phases of the order of $(n-1)$ into integral equation. In the first Rytov approximation, Fourier transform equals to the product of incident field and complex scattered phase function:

$$U^{(i)}(\vec{r}) * \varphi^{(s)}(\vec{r}) = \frac{e^{-ikr}}{r} \int_V F(\vec{r}', \omega) e^{-i(\vec{k}_s - \vec{k}_i) \cdot \vec{r}'} d^3\vec{r}' \quad (4.31)$$

References

- [1] Hulst H. Light scattering by small particles. New York: Dover Publications, 1981.
- [2] Backman V. Early diagnosis of cancer with light scattering spectroscopy. HST PhD Thesis. Cambridge: Massachusetts Institute of Technology, 2001.
- [3] Bohren CF, Huffman HR. Absorption and scattering of light by small particles: John Wiley & Sons, Inc., 1998.
- [4] Born M, Wolf E. Principles of Optics. Cambridge: Cambridge University Press, 2005.
- [5] Slaney M. Imaging with diffraction tomography. PhD Thesis: Purdue University, 1985.

Chapter 5:

Design principles and calibration of light scattering instruments

This chapter is devoted to the description of the design and calibration of light scattering instruments based on theoretical predictions from Mie theory. First, intensity-based Fourier plane and field-based image plane detection schemes for light scattering are discussed. Mie theory numerical implementation is introduced for prediction of light scattering and its implementation in solving an inverse scattering problem from cells and tissues. A Mie-based optimization is applied to determine favorable experimental geometries of light scattering instruments for cell/tissue experiments. Finally, the light scattering instruments used for tissue, multi-cell and single cell experiments are described, along with their detailed calibration.

5.1 Principles of Fourier-plane and Image plane light scattering spectroscopy

5.1.1 Fourier-plane imaging

Generation of angular scattering maps is presented schematically in Figure 5.1. An incident plane wave with given linear polarization is scattered in the sample (FP1). The sample plane is in the focus of the lens L1. All parallel rays of light scattered at a given scattering angle θ in the sample plane are collected into the same point $P(\theta, \varphi)$ of a detector plane (FP2), which is in the second focal plane of lens L1. Angle φ is an azimuthal scattering angle determined with respect to the axis parallel and perpendicular to the polarization of the incident light. The union of points $P(\theta, \varphi)$ forms an angular scattering map. If wavelength frequency of the incident source is varied, the intensity of sample response at given $P(\theta$ -fixed, φ -fixed, λ) changes. Thus angular scattering at detector plane is a function of three parameters θ , φ and λ . Since most of the conventional detectors are 2D, at most 2 of the light scattering parameters can be measured at any given time, and the third has to be scanned in some way. All of our intensity-based systems measure angular scattering maps directly in a

detector plane. We use intensity-based methods in tissue, cell monolayer and cell suspension measurements.

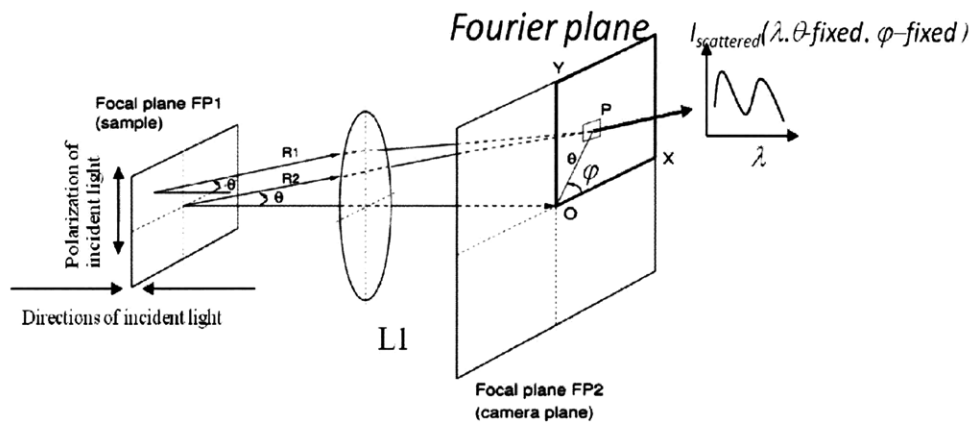


Figure 5 1 Fourier-plane formation in light scattering experiments

Mathematically, lens L1 creation of angular scattering map is equivalent to a Fourier transform operation on the sample plane [1]. Specifically, it transforms spatial distribution of a scattered field at the sample plane into spatial frequency distribution in a detector plane. Thus, the detector plane is also called Fourier plane. A field-based light scattering technique developed by Dr. Wonshik Choi in our laboratory is based on measuring spatial distribution of a scattered field in the sample plane, and then mathematically transforming that distribution into angular scattering using Fourier transform operation [2]. The field-based light scattering spectroscopy (LSS) system is used for the measuring of single cell scattering and generation of 3D-index tomograms of single cells.

5.2 Numerical simulations and instrument optimization using Mie theory

5.2.1 Numerical implementation of Mie theory

Mie theory solution has been implemented into the geometry of a light scattering instrument using a code by Barber and Hill [3]. Fortran 95 is used, as one of the fastest languages for scientific calculations (about 30 times faster, than Matlab ver. 6.5 on the same machine). Amplitude scattering matrix elements are calculated in the main body of the program according to Eq. 4.1.2. The main numeric load is in recursive calculation of these elements. The number of iterations for convergence of the light scattering calculation is scaling up proportional to the power of the size parameter x . Thus, more calculations are

required for larger diameters and shorter wavelengths. The main code is adapted to calculate differential scattering cross-section according to Eq. 4.3. and 4.4. User defined parameters include scattering angles θ and φ , refractive index of the media n_0 and that of the sample, n , scattering wavelength λ in vacuum, and sphere diameter, d . Calculations can be performed for a single particle diameter, d , or for a probability density distribution of diameters, $N(d)$. $N(d)$ can be a delta-function, Gaussian or power law distribution.

5.2.2 Mie-optimized detection of large and small particles in angle

Particle-size discrimination capability is key for the development of light scattering experimental methods. In order to optimize detection for various sizes of sub-cellular structures in cells and tissue, Mie modeling is used. Scattering is compared from particles larger than wavelength (whole cells and cell nuclei) vs. smaller than wavelength (small sub-cellular structures) for various values of scattering parameters λ , θ , and φ .

In particular, Mie spheres of $5\ \mu\text{m}$ and $50\ \text{nm}$ in size are used to mimic scattering of sub-cellular structure larger and smaller than wavelength of visible light in the Fourier plane (Figure 5.2). We are looking for ways to enhance larger particle signals over the smaller ones. Once optimal angular ranges of observation are found, we can expand the data in wavelength λ . Three pairs of Fourier plane angular maps $\sigma(\theta, \varphi, \lambda=550\text{nm}, n_0=1.337, n=1.4)$ are covering most of our detection range of interest in scattering angle. Scattering angle is defined with respect to an incident beam, which means 0° is light scattered directly forward. Forward

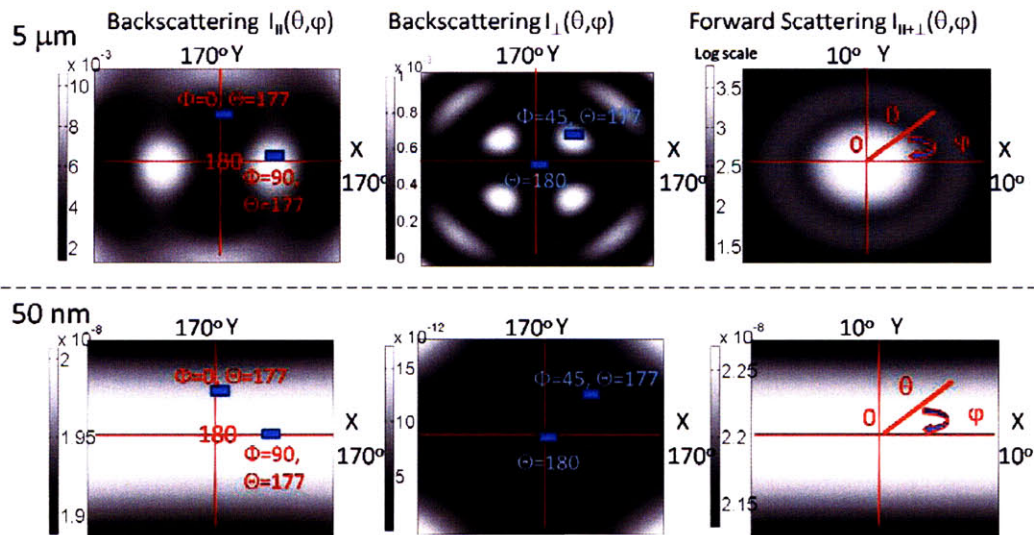


Figure 5.2 Angular scattering maps for $5\ \mu\text{m}$ and $50\ \text{nm}$ at $\lambda=550\ \text{nm}$ (see text for details)

scattering is described at least up to 10° away from the forward scattering direction at all values of azimuthal angle φ . The same goes for backscattering, except scattering angle θ is changing between 180° and 170° . Backscattering parallel (I_{\parallel}) and perpendicular (I_{\perp}) are defined with respect to linear polarizer orientation on the scattered beam parallel or perpendicular to the incident beam polarization. Backscattering perpendicular (I_{\perp}) is zero on the axis and reaches maximum near $\varphi=45^\circ$. Forward scattering is on a log scale, while backscattering data are on a linear scale. Brighter areas have a higher scattering cross-section, then the darker areas relative to a specific image colorbar.

Difference in the ratio of signal amplitudes. Amplitude of the signal of an individual $5\ \mu\text{m}$ sphere is many orders of magnitude higher than that of a $50\ \text{nm}$ particle, but the density of smaller particles in cells is greater (see section 1.2). Therefore, we are looking for relative enhancement of various size particles. Greatest difference in amplitude between two bead cross-sections is in the forward scattering geometry ($>10^{11}$) for most of the scattering map. Thus, forward scattering is greatly favorable to the larger structures. Backscattering parallel has the strongest overall contribution of small particles relative to the large ones according to the amplitude scale ($\sim 1:10^6$). Backscattering perpendicular has the smallest amplitude of a large particle signal (10^{-3} vs. 10^{-2} vs. 10^3), but higher than parallel ratio to small particles ($\sim 10^8:1$).

Difference in shape of angular scattering distributions. In addition to overall maximum amplitude ratios, small and large particles have quite different variation of the amplitude across angular scattering maps. While small particles are characterized by a uniform angular distribution (variation within 10% for forward and backscattering I_{\parallel}), large particles exhibit an oscillatory behavior of scattering cross-section [4]. Based on this difference, a couple of differential methods have been developed in our laboratory. Phi-differential technique has been developed by Dr. C.C. Yu and C. Lau for the detection of scattering from cell nuclei in tissue [5]. Their method is based on studying wavelength variation of the backscattering parallel σ_{\parallel} at a fixed scattering angle θ (for example, 177°) and two scattering angles φ of 0° and 90° . For these angles Mie oscillations are out-of-phase with each other. If one takes the difference between data at two azimuthal angles, $\Delta I_{\varphi 0-\varphi 90} = I_{\parallel}(\theta=177^\circ, \varphi=0^\circ) - I_{\parallel}(\theta=177^\circ, \varphi=90^\circ)$, the small particle contribution will be greatly suppressed due to its uniformity, while the difference in oscillatory phase of large particle should produce significant residual. The amplitude of the residual signal will be proportional to the amplitude of oscillatory component of large particle scattering. The author of this thesis has

developed an alternative to the phi-differential technique. The alternative method is based on detecting cross-polarized geometry to suppress small particle contribution to backscattering. There are several benefits to this method. There is a larger ratio of amplitudes between small and large particles in angle, 10^8 vs. 10^6 . All of our intensity-based measurements are for fixed azimuthal angle ϕ , while wavelength λ and, often, scattering angle θ are varied. Therefore, phi-perpendicular is a single shot technique, unlike phi-differential parallel, which requires two measurements, which doubles acquisition time and can introduce more experimental error. Although the amplitude of a large particle signal I_{\perp} is about 10 times lower, than in I_{\parallel} , both the DC and AC components of the large particle signal are preserved in I_{\perp} , while only the AC component is preserved in the I_{\parallel} .

To summarize, larger structures are best observed in forward scattering. In the case, when forward scattering is not accessible, as in most tissue experiments, phi-differential and cross-polarization method can be used to enhance the scattering signal from large particles. Smaller structures are best observed in the backscattering parallel I_{\parallel} .

5.2.3 Implementation of Mie optimization in wavelength

Experimental systems for an intensity-based light scattering, used in this thesis work, measure intensity of scattered light varying with respect to incident wavelength, λ , and scattered angle, θ , for fixed azimuthal angle ϕ . Thus, the scattering intensity can be represented as a 2D-map with respect to angle θ and wavelength λ . Angular enhancements of larger structure scattering, determined in previous section, can be expanded to wavelength. 2D-maps of scattering cross-section for 100 nm and 10 μm spheres are presented on a 2D-color plots, where axes represent angle, θ , and wavelength, λ , and colorbar is scattering cross-section in μm^2 . Refractive index of the media is fixed at $n_0=1.337$ and that of the sample at $n=1.42$, giving an m-value of 1.061. The scattering angle range and wavelength range are selected to encompass experimental ranges.

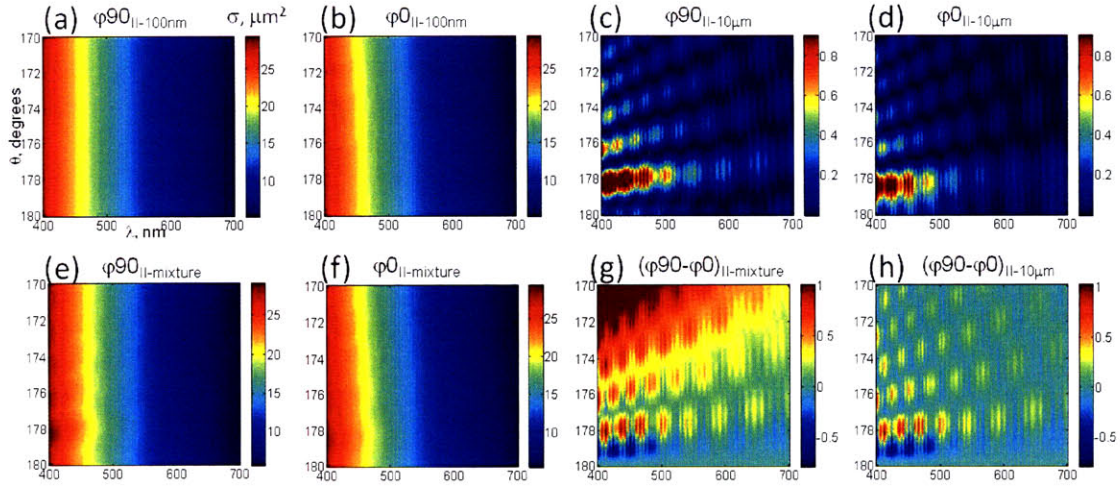


Figure 5.3 ϕ -differential scattering method applied to isolated 10 μm beads (a-d) and mixtures of 10 μm and 100 nm

Individual cross-sections for two azimuthal angles $\phi=0, 90$ are represented in Figures 5.3.a-d. In a real biological sample, there are many more small structures than the larger ones. Thus the difference in the differential scattering cross-section is offset by the number of structures. To mimic this situation, the 100 nm sphere differential cross-section is weighted by the ratio of total scattering cross-sections for 10 μm and 100 nm particles, thus making their contributions to total scattering equal. The sum of the two cross-sections in ϕ_{\parallel} -geometry is dominated by weighted 100 nm sphere cross-section (Figure 5.3.e-f compare to 5.3.a-b and 5.3.c-d). Phi-differential method enhances 10 μm sphere contribution and is dominated by the 10 μm near exact backscattering (around 178°), as the scattering angle increases the oscillatory pattern of the differential signal remains similar, but it is riding on the slope from 100 nm particles residual signal (angles greater than 176°) (Figure 5.3.g-h). The angle of the clearest 10 μm scattering signature is going to vary with the particle size, also the signal of interest (10 μm) is riding on a large background signal of 100 nm particles.

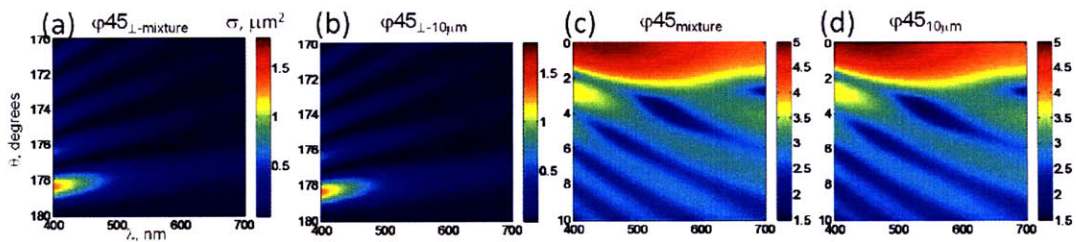


Figure 5.4 Cross-polarized measurements at $\phi=45^\circ$ for isolated 10 μm beads (a-d) and mixtures of 10 μm and 100 nm (c-d)

By comparison, both perpendicular- ϕ -45° and forward scattering have 10 μm signal dominating scattering in equi-scattering mixture (Figure 5.4.a vs. b, and 5.4.c vs. d). This behavior is independent of angle or wavelength in relevant ranges and it can be readily applied to the observation of large particle signal at all angles and wavelengths without additional data manipulation. The perpendicular- ϕ -45° has most of the oscillatory structure in angle, and less in wavelength. Also absolute magnitude in variation of the perpendicular signal (difference between maximum and minimum value) is lower than the differential signal for ϕ -parallel (~3 times). Forward has the strongest (log scale) and the clearest light scattering signal from 10 μm particle. Its only drawback in the detection of large structures is that it cannot be applied to tissue. Thus, forward scattering in the considered angular-wavelength ranges is best used for observing larger structures. In case when forward is not accessible, perpendicular- ϕ -45° or ϕ -parallel differential can be used. Smaller structures are best observed in ϕ -parallel geometry.

5.2.3 Simulating experimental data

Scattering spectra in real measurements are usually associated with the broadening of the above single particle features. In order to closely simulate and correctly analyze scattering data, broadening should be taken into account. The sources of broadening included in simulations are experimental system's instrument response in angle, wavelength and size distribution of scattering particles.

The size distribution is presented in any of the multi-particle samples used in the intensity-based studies. Biological samples have a very wide and non-uniform distribution of sizes (see section 2.2). Size distribution of some particles, for example nuclei, is often assumed to be Gaussian, characterized by mean and standard deviation (see section 3.1.3). The most straight-forward is the effect of the size distribution in wavelength, since variation in size is equivalent to spectrum shifting along the wavelength axis (scattering depends on λ/d ratio). If shift is equivalent to half-a-period of an oscillation, then the oscillatory pattern will be most diminished.

The effect of size distribution is demonstrated on the scattering cross-section for 4 Gaussian distributions with 10 μm mean and standard deviations of 0 μm , 0.1 μm , 1 μm and 2 μm (Figure 5.5.a). Mean \pm two times standard deviation generally characterize 95% of the area under the distribution curve. A Gaussian distribution standard deviation multiplied by a

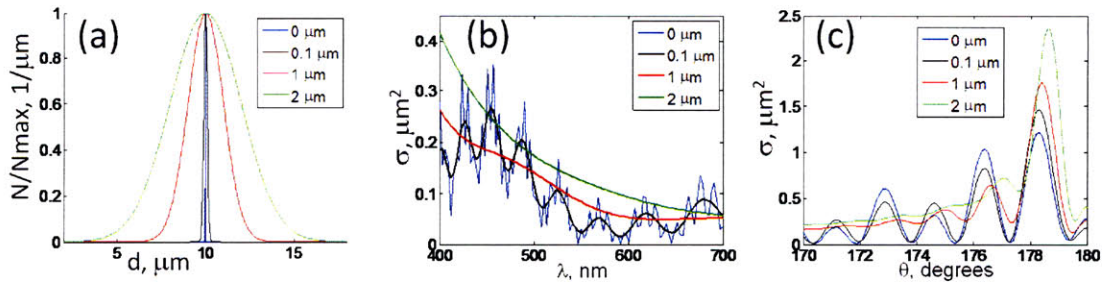


Figure 5.5 Effect of size distribution on light scattering spectra a) Shape of Gaussian size distribution depending on the width values (0-2 μm) b) Wavelength spectra at $\theta=180^\circ$ for different distribution widths c) Angular spectra at $\lambda=400\text{ nm}$ for different distribution widths

factor $2 \cdot (2 \cdot \ln(2))^{0.5}$ describes FWHM (Full Width of Gaussian curve at Half Maximum). Note that in the calculation, the areas under all distributions are made equal to one. In order to show the difference in widths, distributions are plotted normalized to a maximum value. The rest of the scattering parameters are fixed at $\theta=180$, $n_0=1.337$ and $n=1.42$.

First, the highest frequency oscillations disappear even for low standard deviation (1%) (Figure 5.5.b). With about 10% standard deviation, the low frequency envelope is significantly distorted along with the disappearance of second to highest frequency oscillations. Finally, with a 20% standard deviation only the general slope of the data are preserved. In angle, dependence on the size variation cannot be interpreted as simply, as in wavelength, but can still be qualitatively described (Figure 5.5.c). Wavelength is fixed at 400 nm. The absence of the very high frequency oscillations even in the single particle spectra explains relative insensitivity for small standard deviation values. Higher standard deviations of 10% and 20% cause the loss of most of the angular structure, similar to the wavelength case, except for the peak closest to exact backscattering, which shifts in frequency, but is preserved for the most part. Thus size distribution is associated with the loss of oscillatory structure, and larger size distributions also affect the overall slope of the data. A single oscillation is preserved in angular, even for larger standard deviations.

A finite resolution of various components of the experimental system results in the uncertainty of determination of the exact values of angle and wavelength, $\Delta\theta$ and $\Delta\lambda$. Point spread function (PSF) of an imaging system measures spatial blurring of an image of a point on a detector plane [6], Similarly, a light scattering instrument can be characterized with an instrument response, which is a cumulative effect of light generation, propagation and detection. While PSF is a function of space, instrument response is a function of angle and wavelength, and it can be determined by the measurement of an unscattered beam profile on

the detector in Fourier plane. Scattering signal in the linear experimental system is defined by the convolution theorem, where scattering of the sample is convolved with the instrument response (IR) for a measured variable according to (in wavelength and angle):

$$I_{detected}(\theta, \lambda) = \int \int_{-\infty}^{+\infty} I_{sc}(\Theta, \Lambda) * IR(\theta - \Theta, \lambda - \Lambda) d\Theta d\Lambda \quad (5.1)$$

The exact shape of an IR-function can vary, but it commonly assumes Gaussian-like shape. In both wavelength and angle, an increase in the width of the instrument response leads to a loss of oscillatory features, similar to the effect of size distribution (Figure 5.6.a-b). Wavelength distribution degrades data faster than size distribution of equivalent width as per ratio variation of λ/d . Increase in width of the angular response reduces oscillations evenly across measured angular range, while effect of size distribution is less for angles near exact backscattering.

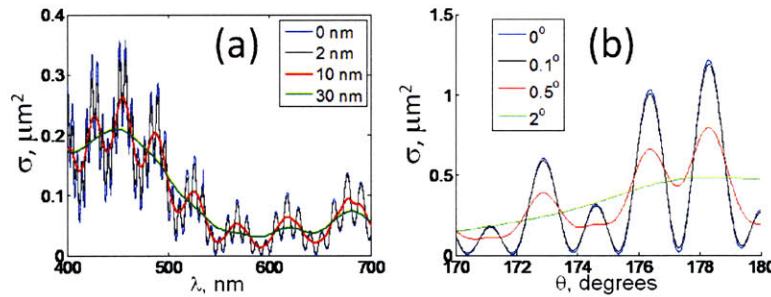


Figure 5.6 Shape of scattering spectra depending on instrument response a) Variable response in wavelength (0-30 nm) at $\theta=180^\circ$ b) Variable response in angle (0° - 2°) at $\lambda=400$ nm

An optimally designed experimental system has maximum width of an instrument response, which increases the signal level and reduces the data acquisition time, while preserving main features of the signal. For an accurate comparison with experimental data, Mie generated 2D-distribution of cross-section with the size distribution already included, is convolved with a 2D –instrument response. There are numerical algorithms, such as Wiener or Lucy-Richardson, which perform de-convolution of experimental data from instrument response [7]. Wiener is a linear algorithm requiring separation of signal and noise, which is hard in complex data. Lucy-Richardson is a non-linear iterative algorithm, relying on the accuracy of numerical solution. Thus a direct convolution of the theoretical prediction is the least convoluted way of comparing experiment to theory.

5.2.4 Analyzing experimental data

Three different approaches can be used in analyzing scattering data using Mie theory: manual fitting, non-linear least squares fitting and lookup table approach. Advantages, disadvantages and uses of these approaches are discussed below.

Manual fitting is, according to the name, a manual variation of model parameters to best match the data. The visual inspection is most often used as the matching criteria. It is very useful at the early stages of alignment and calibration of experimental systems and generally when significant distortions of unknown origin are present, which can easily fool a fitting routine. A good example would be an initial calibration of the scattering angle. Take a single spectrum in wavelength created by scattering from particles, whose size distribution and refractive index contrast are known. Scattering angle is the only parameter varied in this case. The angular scattering is symmetrical around $\theta=180^\circ$ or $\theta=0^\circ$, therefore the position of exact forward or exact backscattering can be determined easily. Once it is determined, at least a linear assumption about an angular range can be made with one more angle determined from manually comparing data and Mie theory for different angles.

The second approach is a non-linear least squares minimization routine [8, 9]. Assume, $I_n(\lambda_n)$ are n – measurements of scattering intensity at n -wavelengths. Theoretical Mie prediction $f_n(\lambda_n, p_1, \dots, p_m)$ is calculated as a function of n -wavelengths and m -parameters (angle, size, refractive index) for each wavelength. The goal of the routine is to minimize the square of the residual $\Delta_n = I_n(\lambda_n) - f_n(\lambda_n, p_1, \dots, p_m)$ summed over n measured points. The minimum is reached when the gradient of the function equals to 0, thus:

$$2 \sum_{i=1}^n \Delta_n \frac{\partial \Delta_n}{\partial p_m} = 0 \quad (5.2)$$

The function $(\partial \Delta_n)/(\partial p_m)$ is generally non-linear, and the solution comes from its linearization using Taylor expansion for Δ :

$$\Delta(\lambda^s) \approx \Delta(\lambda^s) + J_n(\lambda^s) \delta \lambda \quad (5.3)$$

where J stands for Jacobian matrix of partial derivatives, $J_{ij} = -(\partial \Delta_n)/(\partial p_m)$, and parameters $\lambda^s = \lambda^{s-1} + \lambda^0$ are changed iteratively from initial value λ^0 . In this case problem $\delta \lambda$ satisfies the following equation:

$$(J_\Delta^T J) \delta \lambda = -J_\Delta^T * \Delta \quad (5.4)$$

The biggest advantage of the non-linear least squares is that it does not assume a specific function form and can be used with any reasonable function with valid partial derivatives. On the other hand, the outcome strongly depends on the iterative procedure of parameter selection. Thus it is very sensitive to initial selection of parameters, when local minima of Δ are present. The later point is demonstrated on the example of fitting two simulated data with the following parameters $\sigma_{\perp}(\lambda, \theta=175^{\circ}, \varphi=45^{\circ}, d=10 \mu\text{m}, \Delta d=0.1 \mu\text{m}, m=1.19)$ and $\sigma_{\text{forw}}(\lambda, \theta=5^{\circ}, \varphi=45^{\circ}, d=10 \mu\text{m}, \Delta d=0.1 \mu\text{m}, m=1.19)$. The fit is across wavelengths, and only to the shape of the data, since the data and Mie theory are normalized to the mean value across the spectrum. The fit is for Gaussian size distribution, and the fitting parameters are allowed to vary between $8 \mu\text{m} < d < 12 \mu\text{m}$ and $0 \mu\text{m} < \Delta d < 0.4 \mu\text{m}$. Two initial starting values of particle diameter are considered: $d=8.5 \mu\text{m}$ and $d=8 \mu\text{m}$ (Figure 5.7.a-b and 5.7.c-d accordingly). For the initial condition of $8 \mu\text{m}$, σ_{\perp} , non-linear least squares fitting returns true distribution, at the same time σ_{forw} does not return original distribution, but rather a distribution of $8 \mu\text{m}$ and a standard deviation of $0.003 \mu\text{m}$. For an initial condition of $d=8.5 \mu\text{m}$, both cases are resolved correctly. The difference in fitting results becomes obvious, if error function Δ^2 is plotted for difference between the simulated data and Mie predictions, as a function of diameter and standard deviation (Figure 5.7.e and 5.7.f). There is only a single minimum for σ_{\perp} , making the solution global for the chosen ranges of parameters. For σ_{forw} , besides the global minimum at $d=10 \mu\text{m}$, there are local minima at $8 \mu\text{m}$ and $12 \mu\text{m}$, and the $8 \mu\text{m}$ minimum is discovered with $8 \mu\text{m}$ initial condition.

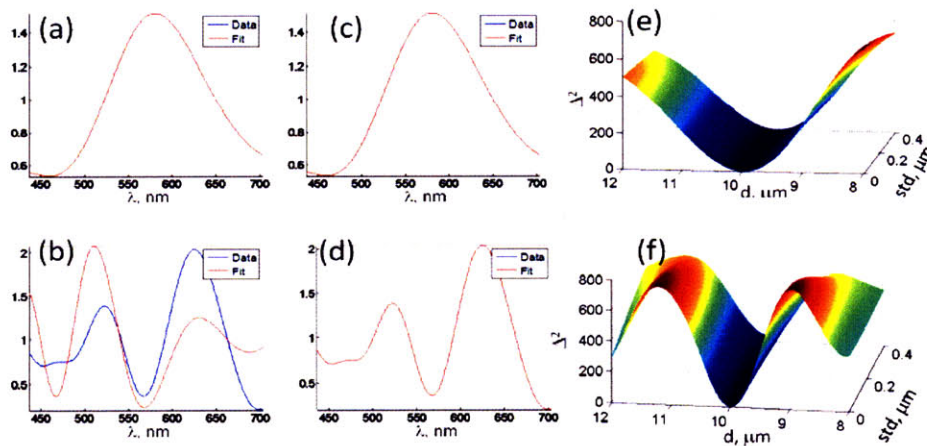


Figure 5.7 Test fitting of simulated $10 \mu\text{m}$ spectra for variable initial conditions $8.5 \mu\text{m}$ and $8 \mu\text{m}$ a,c) Cross-polarized wavelength spectra at $\theta=175^{\circ}$ (blue-simulated data, red-fitting result) b,d) Forward scattering wavelength spectra at $\theta=5^{\circ}$ e,f) Error function for full range of fitting parameters diameter and standard deviation

Therefore, even in a simulated case and a limited range of parameters, the fitting routine can be fooled by local minima. If fitting is to be used, the initial condition randomization becomes a necessary step in fitting the scattering data, even if only a single parameter is varied. The slowest part of the calculation is generation of Mie spectra. Due to the repetitive nature of Mie spectra generation for the same values of parameters, the fitting routine even for a single spectrum becomes quite inefficient. For example, to fit a single spectrum in wavelength for fixed angles, for each step of parameter change, a theoretical Mie spectrum has to be generated for a given size distribution, refractive index and angle. Besides that, given the presence of an instrument response in angle, a range of spectra needs to be generated for angles to cover instrument response width, centered on the angle of interest. Although, if standard deviation of a size distribution is changed from values $0.1 \mu\text{m}$ to $0.11 \mu\text{m}$, Mie spectra will need to be re-generated for the full width of size distribution, not only to cover the difference between standard deviations. An analysis of multiple spectra from different samples requires a repeated generation of the same Mie spectra with all the caveats above. At the end of calculation, the result can still be off due to the presence of the local minima.

Given issues listed above, the more efficient way of data analysis using Mie theory is a lookup table approach. It requires a one-time generation of Mie spectra covering the full possible range of parameters. Experimental data are then compared to all Mie spectra from lookup table, and N-dimensional error function is created similar to the ones plotted on (Figure 5.7.e-f). In this case a true global minimum will be found. The main drawback of the lookup table approach is in the time needed for a lookup table generation. For example, a realistic lookup table to analyze a contribution of a cell border in the cell suspension data takes 92 hours on a 1.7 MHz Pentium M machine. Even this time can be considered short, since the steps in the scattering parameters are maximized to optimize the table generation time.

5.3 Instruments for intensity-based light scattering measurements: Forward/Backscattering at $\phi=45^\circ$ combined instrument

Three versions of experimental system are used for intensity-based measurements. They differ in the way the light is collimated. The collection ranges of scattering angles and

extent of system calibration. First, the latest version of experimental system is described. It is the most complete example of how a light scattering system can be designed, built and calibrated. Also in addition to backscattering, it is capable of collecting light scattered in forward direction. This system is used in studies of cell suspensions and cell monolayers. Studies are conducted using θ -differential and forward scattering, as large particle enhancement methods. The goal is to establish relative contributions of large and small sub-cellular structures to scattering. In the following sections (section 5.4 and 5.5), the two other systems, used in cell monolayers experiments and tissue studies are described briefly.

The construction of experimental set-up consists of the following steps:

- Design of experimental system guided by Mie predictions,
- Instrument alignment, and
- Bead calibration.

5.3.1 Experimental system design

In general, two types of experimental designs are used for light scattering experiments: stationary and goniometric. In a goniometric system, either one of the light delivery, sample or light collection, is placed on a rotary stage. The rotation of the stage gives variation in collected scattering angle (Figure 5.8). Most commonly scattering intensity is measured as a function of angle for a fixed wavelength, since monochromatic lasers are used as a source of light. Photodiode is used as a detector in this case [10-12]. Some of the systems use broadband illumination, which allows for wavelength variation of scattered intensity to be measured as well [13].

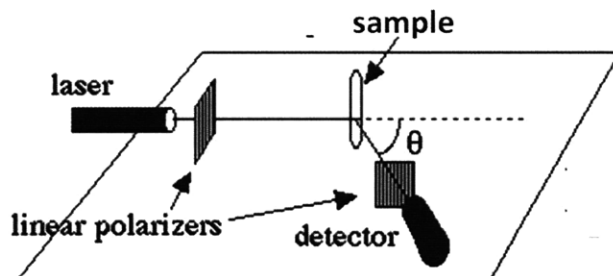


Figure 5.8 Sketch of goniometric light scattering system

Main advantage of a goniometric system is in the wide range of measured scattering angles. On the downside, due to the system geometry, angles near exact backscattering are inaccessible and on-site measurements, such as inside human body can be difficult. In our

laboratory, stationary systems are used from the time of initial experiments in which the main focus is on measuring scattered light on or near exact backscattering direction [14-16]. Thus the two modalities can be considered complimentary in the type of scattering information they collect.

The current experimental system is constructed to collect light near exact forward and backscattering directions. First, the light source and the light delivery part of the system are discussed (Figure 5.9).

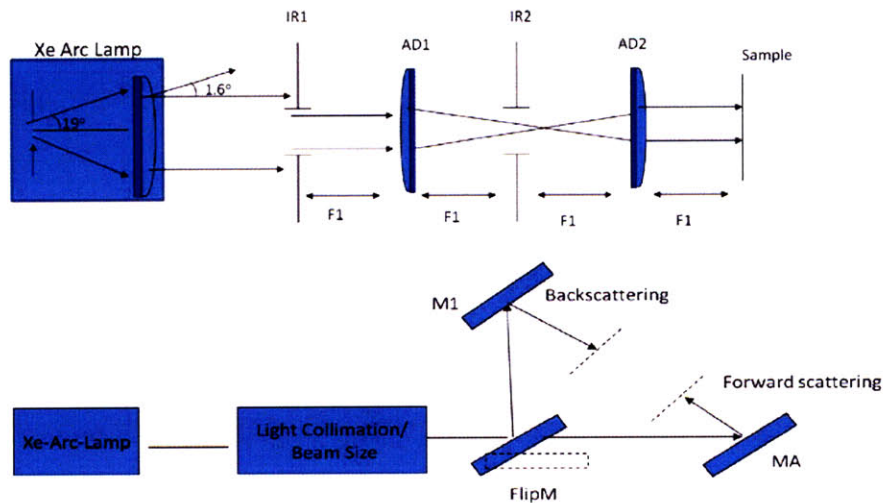


Figure 5.9 Light source and 4f-beam control system (top graph) Light delivery for forward and backscattering experiments (bottom graph)

The selection of the source for the light scattering experiment is guided by several criteria. Since cells are weak scatterers and scattering is a linear effect, the signal is proportional to the incident light intensity, thus more intense sources are desired. A higher divergence degrades features in the scattering spectrum (Figure 5.6), therefore the beam collimation should be of a high quality. Finally, the decrease in a beam diameter increases the specificity in sampled area of tissue or cells. Lasers sources perfectly fit the above criteria with high power, high collimation and with small diameter beams, but they are mostly monochromatic, thus the wavelength distribution of scattered light cannot be measured. There are broadband tunable laser sources, such as OPO, but instability in an output pulse energy variation makes them less of a choice than broadband incoherent white light sources. The original source for light scattering experiments – Xe arc lamp from Oriel Instruments, is used in all experimental set-ups described in this chapter [16]. The optical extent equality states, that for a rotationally symmetric beam, a product of beam height and divergence, is

constant throughout the system $h_i\theta_i=h_o\theta_o$ [17]. If the ratio is not observed, then the beam energy will be lost. The 100W Xe arc lamp is the best choice of arc lamps, with the highest intensity per source area, which translates into a highest possible energy in the beam of a given divergence and diameter. Also Xe-type lamp is preferred to other arc lamps, such as mercury, because of its relatively uniform spectrum in a visible range of wavelengths (Figure 5.10, dotted spectrum).

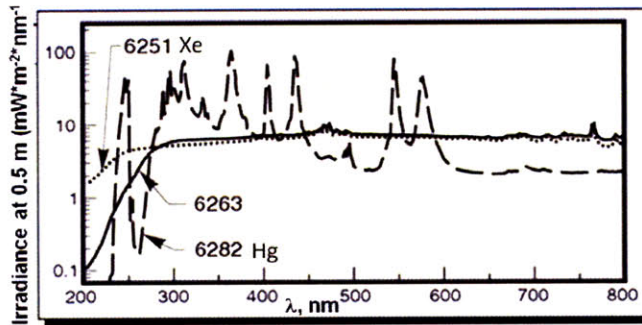


Figure 5.10 Emission spectrum of Xe arc lamp (marked as 6251)

Light from an arc lamp is collimated into a slowly diverging beam with a half-angle of 1.6° . In order to control the beam divergence and diameter, the 4f-imaging block is constructed with two achromatic doublets ($F=30$ cm, $D=1$ inch, ThorLabs, Inc) and two calibrated irises, IR1 and IR2 from ThorLabs, Inc. (Figure 5.9.top). The beam at the entrance of iris IR1 will be imaged onto a sample surface. Iris IR1 controls the beam diameter between 1 and 11 mm. Iris IR2 is in a Fourier plane centered on the exact forward direction. It controls the contribution of various angular components to the beam, thus the beam divergence can be adjusted between 0.1 and 0.6 degrees half-angle.

The same beam is used for backscattering and forward scattering experiments (Figure 5.9.bottom). The beam is directed for the backscattering experiment by a flip mirror FlipM. Six degrees of freedom are needed to control the beam propagation in space (coordinates of 2 points in space). Six tilt angles comprised of mirrors FlipM and M1, control the beam delivery for backscattering, and the two-mirror assembly MA controls the beam for the forward scattering experiments. The mirrors are 1-inch broadband dielectric mirrors from ThorLabs, Inc.

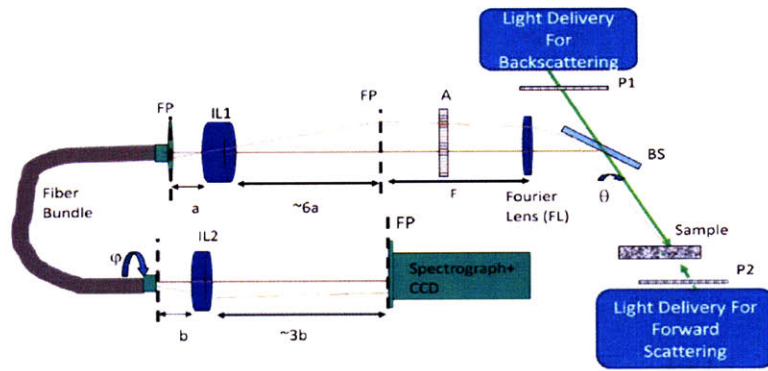


Figure 5.11 Collection arm of the experimental system

For backscattering, an incident beam is polarized with a calcite linear polarizer P1 (10 mm square, Mells Griot, Inc.), and delivered through a broadband beam splitter BS (50/50, 50 mm square, Mells Griot Inc.) at 45° onto the surface of the sample (Figure 5.11). For forward scattering, a broadband dichroic linear polarizer P2 (1.5 inch, round, Edmund Optics) is used, and the light is delivered to the bottom of the sample. The forward and backscattering beams are directed by mirror adjustments on the same path in the opposite directions of incidence (Figure 5.11, green arrows). Thus the 0° forward scattering coincides with the direction of 180° backscattering. The backscattered (forward scattered) light is directed by a beam splitter into the collection arm of the system. A broadband achromatic doublet ($F=75$ mm, $D=40$ mm, Newport inc) creates a Fourier plane FP with a distribution of scattered angles. Light is analyzed with a dichroic linear polarizer A (1.5 inch, round, Edmund Optics). For forward scattering experiments in a Fourier plane, there is a beam stop (small black absorber glued to the center of a glass window) on a flip mount that prevents unscattered light from saturating the detector. Fourier plane is demagnified and mapped by the camera lens IL1 ($F=35$ mm, $F=50$ cm, Canon) onto an input of coherent imaging fiber bundle (4 mm square, 160000 fibers, SchottGlass, Inc.). Input of a fiber bundle is centered on a 360° rotation mount. The other end of the fiber bundle is fixed in height on top of a 2D translation stage adjusting lateral and longitudinal positions of the fiber output in space. The output of the fiber is magnified and imaged through an achromatic two lens assembly (manufacturer unknown) onto an input slit of the spectrograph (10 mm slit height, $10\ \mu\text{m}$ -3 mm width, Acton Pro SP150, Princeton Instruments). The spectrograph output is a 2D distribution of scattered light intensity in wavelength along the height of the slit, and it is imaged onto a 2D nitrogen cooled CCD detector (512×512 diode matrix, $25\ \mu\text{m}^2$ pixel area, Princeton Instruments). Various beam stops and beam blocks are used throughout the system to diminish background light effects.

5.3.2 *Experimental system alignment*

The experimental system is aligned element-by-element from the source to detector. Lenses are used to focus light to a point, collimate light coming from a point or image point-to-point. The focal distances can be measured from the manufacturer's specs. The 4F-beam control unit is placed on a rail (50 inch length, Newport, Inc.), allowing for an accurate adjustment of axial position and lateral centering of the optics. The Iris IR2 position coincides with the sharp image of the arc of Xe-lamp. The sample position is determined by placing a semi-transparent grid in the center of the iris IR1. The sharp image of the grid on the output of the 4F-system points at the sample position. FlipM has weak transmission of the incident light, while delivering backscattering. If a backscattering excitation beam is propagated through the sample, it should go through a forward scattering mirror assembly back into the delivery path and overlap the weakly transmitted beam through a flip mirror FlipM.

The Beamsplitter BS is aligned in a way that reflected beam and incident beam form a plane perpendicular to the optical table surface. The focal distance of the Fourier lens on the sample side is determined from focusing a HeNe laser beam from the detection side on a sample plane. On the other side the focal distance is determined from focusing of a forward scattering beam. The beam stop on a flip mount is placed on a Fourier plane.

A 99% reflectance standard, R99, (Labsphere Inc.) is placed in a sample plane, and scatters most of the incident light almost (see section 5.5.3) uniformly in a 2π hemisphere. Thus the full range of scattering angles allowed by the beamsplitter and Fourier lens apertures is created in Fourier plane. The output of the fiber bundle is illuminated with a flashlight, and the input end of the fiber bundle and the imaging lens IL1 are adjusted in 3D, so that the image of the fiber grid is focused on a Fourier plane and the grid image covers the illuminated area of a Fourier plane. If the input of the fiber bundle is illuminated, the axial positions of a fiber bundle output and the imaging lens assembly IL2 can be determined by focusing a fiber grid image on a spectrograph entrance slit. The input end of a fiber bundle can be rotated, to change azimuthal angles ϕ of the Fourier plane centered on a spectrograph slit. Ideally the axis of fiber rotation and 0° , 180° centers of scattering map should overlap, so that rotation of the fiber input does not shift its lateral position of the center of the scattering map on the spectrograph slit. Experimentally, it is hard to achieve. Instead, the position of the fiber output is adjusted laterally to compensate for the shift in position of the center of the

scattering map on the slit and values of the shift are tabulated. More accurate centering is done with the help of polystyrene bead suspensions below.

A spectrograph with a closed slit is illuminated with a white light and zero order grating reflection (all wavelengths of light are focused in the same point on the output of the spectrograph) is placed on a CCD. CCD is shifted axially to obtain physical dimensions of the slit width on a CCD chip.

5.3.3 Measuring instrument response and calibration

Quality of system alignment and the degree of system sensitivity is judged by a comparison of the data for polystyrene sphere solutions in water/oil to Mie theory. In order to make a direct comparison to Mie theory, one has to take into account the following:

- Determine values of collected scattering angles and wavelengths,
- Determine broadening of a single angle/wavelength in the system,
- Determine illuminated area,
- Remove background light contributions (light not coming from the sample),
and
- Remove spectrum of various systems components, such as wavelength variations in the source spectrum.

According to Mie predictions in section 5.2.2, large structures are best observed in forward scattering and backscattering perpendicular geometries $I_{BS_{\perp}}$ at $\varphi=45^\circ$ and small structures are best observed in backscattering parallel. Thus, for the described system an azimuthal angle φ is fixed, and CCD collects scattering intensity at various values of scattering angle θ and wavelength λ .

CCD measures wavelength components of light along the height of a spectrograph slit (Figure 5.12.a). X-axis is wavelength λ , and Y-axis is scattering angle θ , both measured in CCD pixels. The colorbar represents intensity of the detected signal in CCD counts.

Wavelength axis calibration from pixels to nanometers and width of wavelength response is measured using Hg mercury with known spectral line positions (Figure 5.12.b). The width of atomic mercury lines is narrower than the spectrograph resolution determined by the width of the opened slit, thus the broadening of the atomic lines is due to instrument response in wavelength. For a given system (Figure 5.12.b, red curve), the width of the spectral response is about 20 nm (38 pixels, 0.52 nm per pixel) and the wavelength range is between 436.7 and

710 nm. Angular response of the system in pixels and position of 0° forward scattering is measured by profiling a forward unscattered beam on the “slit” axis of the CCD (Figure 5.12.c). Roughly, a position of exact backscattering can be defined by placing a mirror in a sample plane and aligning the reflected beam with the incident beam, thus creating a 180° scattering. Rough angular range (more accurately determined with bead spectra, below) of the system in air can be determined by rotation of the mirror causing change in angle and a respective beam position on a CCD detector. For a given system, angular range in air is approximately 15.5° . A beam diameter for the described system is set to 5 mm by iris IR1 and on the sample, due to 45° incidence, it is ellipsoidal in shape with a 5 mm minor axis and a ~ 7 mm major axis.

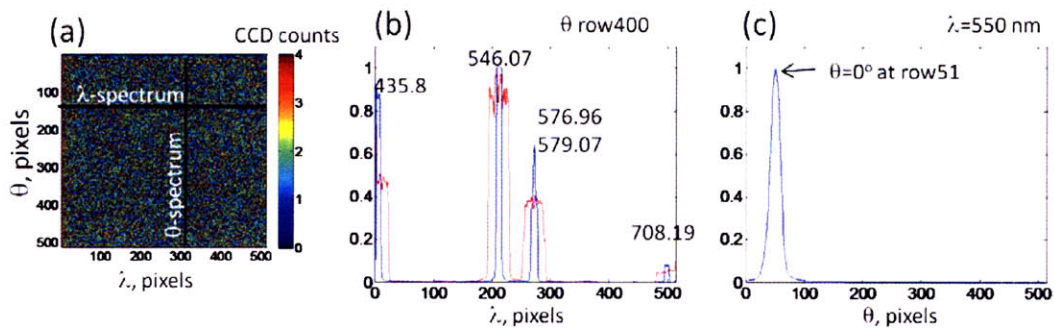


Figure 5.12 Calibration of experimental system a) 2D CCD image wavelength along x-axis and angle along y-axis b) Mercury lines for wavelength calibration, slit opening of $10\ \mu\text{m}$ and $750\ \mu\text{m}$ width c) Angular response of experimental system -unscattered beam on the angular axis

Before being compared to Mie theory, the bead signal undergoes a process known as normalization: $(I_{\text{beads}} - I_{\text{background}}) / R_{99}$ for given polarization settings (Figure 5.13). The presented raw bead spectral counts image in backscattering perpendicular is created from a suspension of polystyrene beads in water ($10\ \mu\text{m}$ mean diameter, 1% standard deviation in diameter, Duke Scientific) with the 45 second acquisition time (Figure 5.13.a). The beads are placed in-between two coverslips with an insert (sample configuration 2, see section 3.1.2 for details). Background signal I_{bg} is measured with the sample having only media without the beads, and it's a measure of non-sample related contributions to the detected signal (Figure 5.13.b). The strongest background signal is around exact backscattering/forward scattering directions due to scattering of the incident beam on beamsplitter (BS) surfaces, which is collected by the CCD detector. In the cross-polarized geometry, this background is diminished. Background signal collection time should equal to data collection time. The R99 reflectance standard (Labsphere, Inc., North Sutton, NH) has a flat response in wavelength and almost Lambertian uniform behavior in angle (more on R99 in section 5.5.3). When R99

is placed instead of the sample, all detected spectral variations in angle or wavelength of R99 intensity are due to spectral variations in optical components and source spectrum (Figure 5.13.c). The R99 signal is collected in a shorter time than the backscattering data and is usually scaled to the data acquisition time (1 sec for backscattering perpendicular). By dividing measured signal by the R99 measurement, the system variations can be removed. Scattering signals are usually presented with respect to the reflectance standard intensity measured for the same amount of time in 1/R99 units (Figure 5.13.d). For absolute reflectance measurement, the reflectance units are calibrated with known bead concentration.

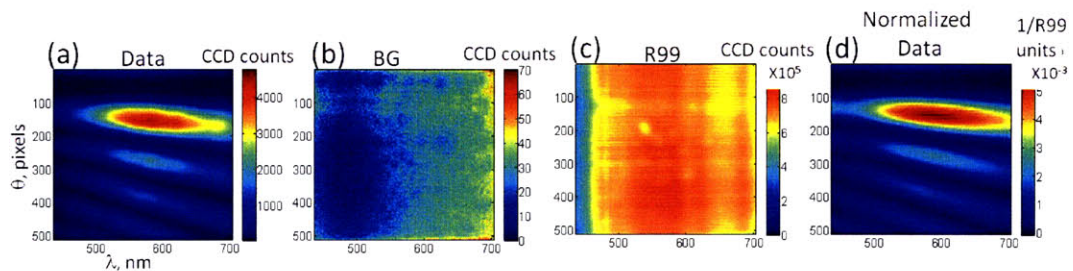


Figure 5.13 Data normalization of 10 μm bead sample in perpendicular I_{\perp} in backscattering **a)** Raw data, color bar in CCD counts **b)** Background measurement (BG) in CCD counts **c)** 99% reflectance standard measurement in CCD counts, colorbar $\times 10^5$ **d)** Normalized data in 1/R99 units, colorbar $\times 10^{-3}$

For forward scattering, incident beam travels on a different path from the one taken by a backscattering incident beam between mirror FlipM and the sample. To account for that difference in normalization, the difference in shape between no sample measurement in forward scattering and the R99 reflectance standard measurement in backscattering at 0° forward scattering can be studied (Figure 5.14). The mean-centered ratio of two signals can be used as the wavelength normalization correction factors for R99 reflectance standard to normalize forward scattering data.

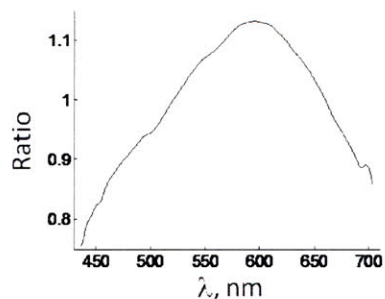


Figure 5.14 Correction factor for forward and backscattering delivery difference in incident light wavelength shape

If a spectrograph slit is open wide and the wavelength of illumination is fixed, for example, if white light from the arc lamp is filtered using a bandpass filter, then the actual Fourier plane image is created on a CCD detector within the width of a spectrograph slit opening. 20 μm beads' (Duke Scientific) data are taken with a 10 nm bandpass filter centered at 650 nm, and compared to Mie theory, in order to accurately determine angular range (Figure 5.15.a). 20 μm beads are used instead of 10 μm due to higher oscillatory content, which helps to determine angular range and position of exact backscattering.

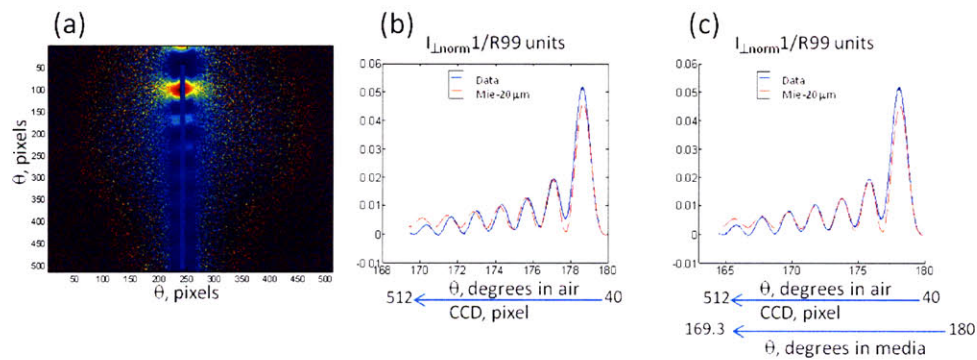


Figure 5.15 Angular calibration of light scattering system with 20 μm bead suspension in water in perpendicular, I_{\perp} a) Fourier plane image, slit open at 3mm, $\lambda=650$ nm b) Angular axis calibration without consideration of air-water interface effect (data –blue curve, Mie simulations – red) c) Angular axis calibration with consideration of air-water interface

Mie prediction angular range is adjusted to match the peak positions in CCD pixels, while angle in the media is converted to angle in air. Because of air-water interface, the range of scattering angles in media corresponds to a wider angular range in air, as an inverse sin of ratio of indexes according to the Snell's law [17]. Not taking into account the interface effect, leads to disagreement between Mie theory and the data at larger angles away from backscattering direction (Figure 5.15.b). Although, due to a 45° angle to the surface of exact backscattering, the angular spacing is changing non-linearly as various angle beams coming out from the interface (Figure 5.15.c). The total angular range in backscattering is 10.7° , with approximately 0.02 degrees per pixel. Backscattering is centered at row 40, 10 rows above the center of forward scattering, which gives approximately 0.22° extra in angle for the forward. Calculated ranges are used to plot Mie theory against data for 10 μm in backscattering perpendicular and for 10 μm in forward scattering (Figure 5.16). After angular calibration, the system divergence can be calculated from forward scattering, and measures at 0.5° (from Figure 5.12.c).

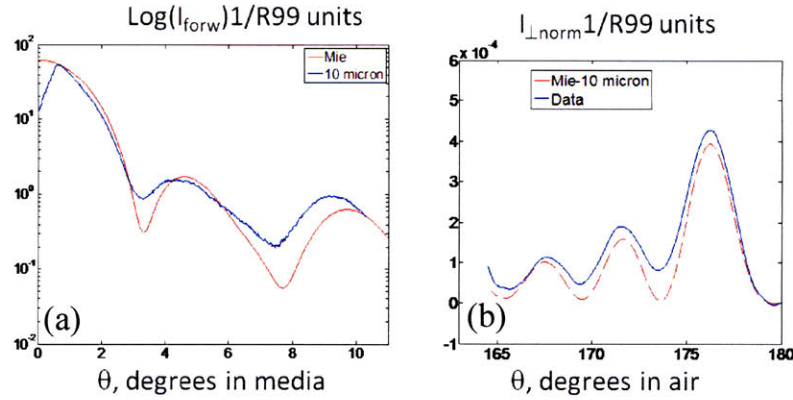


Figure 5.16 Calibration verification using forward and backscattering perpendicular measurements for 10 μm bead suspension in water a) Forward scattering data at 650 nm, log scale, data-blue curve, Mie simulation-red b) Backscattering perpendicular data for 650 nm, scale 10⁻⁴

5.3.4 Forward scattering Mie analysis of bead suspensions

10 μm beads suspensions (Duke Scientific) in water and oil are used for calibration of the forward scattering data. The data are processed with a lookup table approach. The lookup table has three varying parameters: wavelength λ , scattering angle θ and scatterers diameter d . Refractive indexes of beads, water and oil, are known along with their dispersion curves for beads ($n_{\text{beads}}(\lambda, \mu\text{m}) = 1.5663 + 0.00785/\lambda^2 + 0.000334/\lambda^4$, Duke Scientific), water ($n_{\text{water}}(\lambda, \mu\text{m}) = 1.31279 + 0.015763/\lambda - 0.004382/\lambda^2 + 0.0011455/\lambda^4$, Invitrogen Inc.) and oil ($n_{\text{oil}}(\lambda, \mu\text{m}) = 1.5283 + 0.012736/\lambda^2 - 0.00052098/\lambda^4$, Cargille oil). Not accounting for the dispersion of refractive indexes will lead to a deviation of Mie calculation from the data. Since the exact bead diameter is well known, the lookup table for fitting can be limited to the diameters around the size of interest between 8 and 12 μm. In order to determine steps in wavelength and angle, Mie simulated data are created for three steps in angle and three steps in wavelength. These Mie predictions are convolved with instrument response in angle and wavelength accordingly (Figure 5.17.a-b). From these simulations, it follows, that a 1 nm step in wavelength and a 0.1° step in scattering angle are sufficient for an accurate representation of Mie spectra. Lookup table parameters are described in table in Figure 5.17.c.

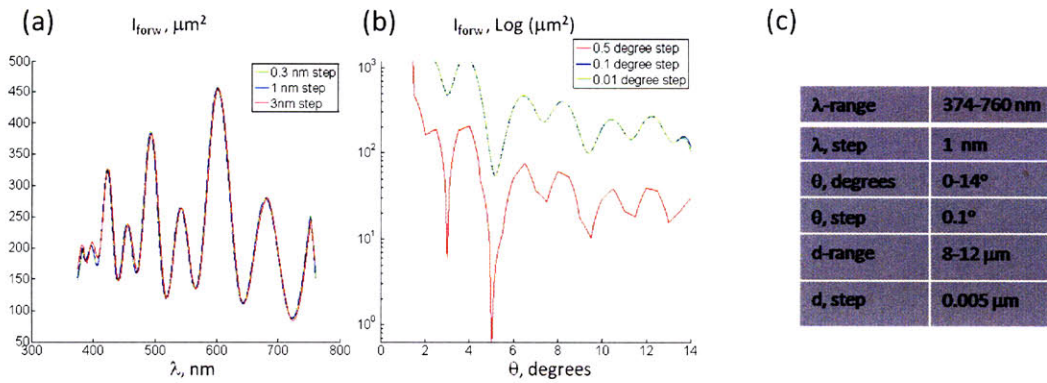


Figure 5.17 Choosing step size in angle and wavelength for lookup table generation for forward scattering, 12 μm bead suspension **a)** Convolved wavelength spectrum at $\theta=10^\circ$ with convolution width between 0.3 and 3 nm **b)** Convolved angular spectra at $\lambda=400$ nm and convolution width of 0.01° - 0.5° **c)** Table of selected ranges for parameter values

The data for beads in water forward scattering is presented in Figure 5.18.a. The data are collected for 50 ms per measurement (1 measurement of data, 1 measurement of background, and 1 measurement of R99 reflectance standard for 200 ms). The first 0.5° from exact forward scattering are blocked by a beam stop. The lookup table is searched for the size distribution, which best fit the spectra at 3 fixed angles (1.9, 3.8, 8.3) and 3 fixed wavelengths (450 nm, 550 nm, 650 nm) simultaneously. Due to a very large dynamic range, the angle data are analyzed on a log scale, otherwise the first peak heavily outweighs the rest of the data.

Excellent agreement is obtained for the bead size distribution of $9.92 \pm 0.14 \mu\text{m}$ (compared to the bottle size distribution of 10.1 ± 0.045) (Figure 5.18.b-c). A conversion factor is calculated between Mie theory and the data through the following equation:

$\rho_{\text{conversion}} \cdot \text{data}_1 / \text{R99_units} = N_{\text{beads}} \cdot M_{\text{ic}}(d=9.92, 0.14) \cdot \sigma_{\text{Mie}}(d=9.92, 0.14)$. Area under the size distribution for Mie theory is normalized to one, and it has to be scaled up by the number of beads N_{beads} in a beam area counted under a microscope. The conversion factor equals to $4 \cdot 10^7$ for forward scattering data.

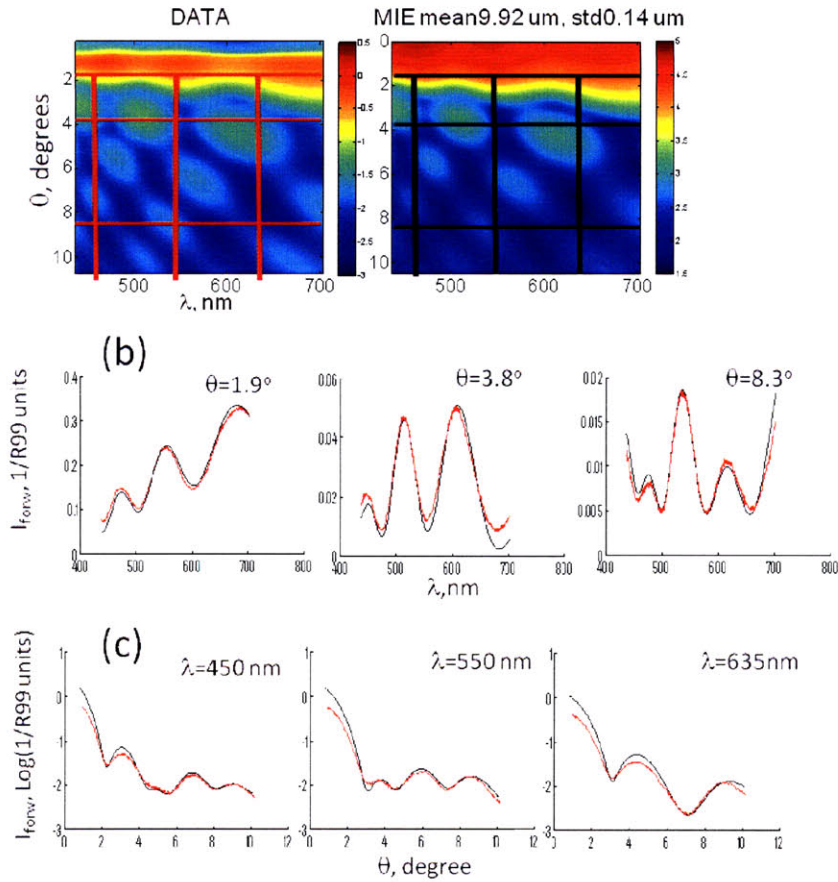


Figure 5.18 Lookup table analysis of forward scattering data for 10 μm bead suspension in water a) Normalized scattering data (left), log scale -3-0.5 of 1/R99 units and best Mie theory prediction for 3 angles and 3 wavelengths log scale 1.5-5 (right) b) Wavelength spectra for three values of scattering angle, linear scale, (data –red and Mie theory-black) c) Angular spectra for three wavelength values, log scale

The data for bead suspension in oil from the same stock is presented in Figure 5.19.a. The data are collected for the same 50 ms per measurement. Angular range is adjusted in accordance with change of media refractive index from water to oil. A very good agreement between Mie theory and the data are obtained, if the bead distribution from beads in water is used (Figure 5.19.b-c).

According to the above data, refractive index contrast does not significantly affect the amplitude of the data in forward direction in agreement with Mie theory, thus very strong signals are expected even from such weak scatterers as cells. Forward scattering is well calibrated for the detection of large particle signal, which should dominate scattering according to Mie theory predictions.

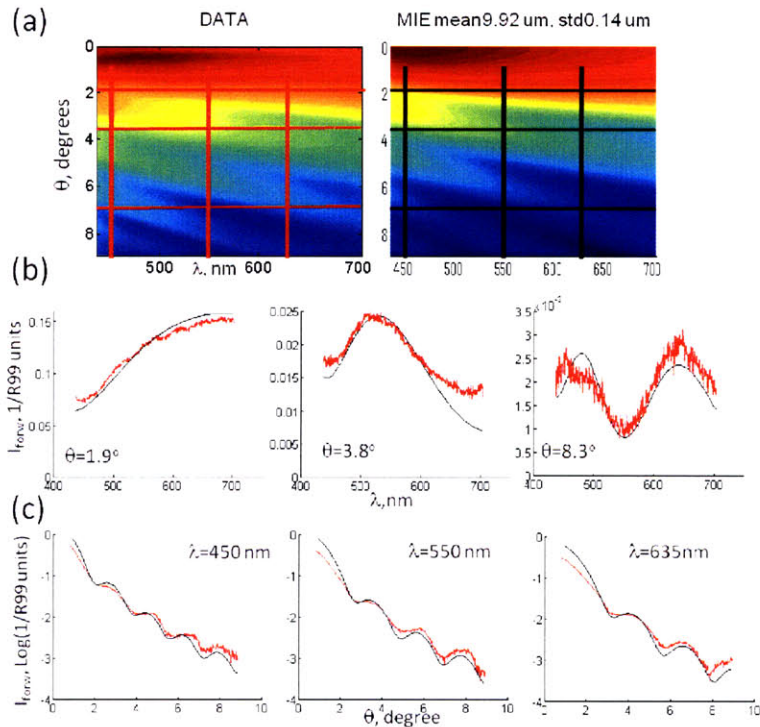


Figure 5.19 Lookup table analysis of forward scattering data for 10 μm bead suspension in oil **a)** Normalized scattering data (left) and best Mie theory prediction from beads in water experiment (right) **b)** Wavelength spectra for three values of scattering angle, linear scale (data—red and Mie theory—black) **c)** Angular spectra for three wavelength values, log scale, angular range is reduced according to oil-air interface

5.3.5 Backscattering Mie analysis of beads

Backscattering geometry is calibrated for detection of large particles in the backscattering perpendicular as well as small particles in backscattering particle. Same stock of 10 μm beads is used for calibration of backscattering perpendicular as well as for forward calibration. Scattering data for beads in water are presented on Figure 5.20.a. Mie theory is again in good agreement with the data for a given size distribution. The conversion factor between data and Mie theory is $4 \cdot 10^6$.

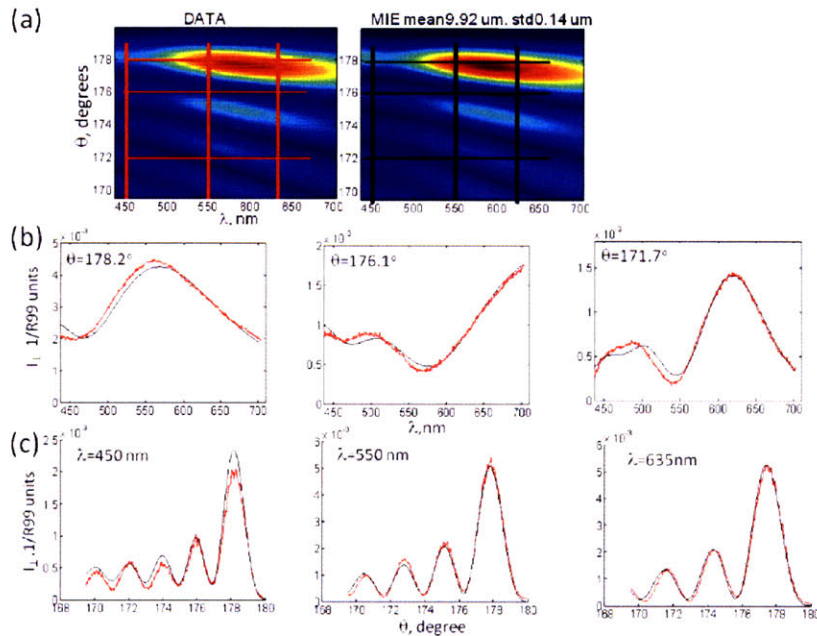


Figure 5.20 Lookup table analysis of backscattering perpendicular data for 10 μm bead suspension in water a) Normalized scattering data (left) and best Mie theory prediction from forward scattering b) Wavelength spectra for three values of scattering angle, linear scale (data–red and Mie theory–black) c) Angular spectra for three wavelength values, linear scale

Mie theory predicts a significant drop in the signal for backscattering with the drop of refractive index (Figure 5.21.a). Thus, in order to preserve similar signal level for beads in oil, concentration has to be increased significantly. Concentration increase is achieved through evaporating water from the bead suspension and re-suspension of the beads in small amounts of oil. Beads aggregate during water evaporation. Due to high density of oil (which is a direct consequence of increased refractive index), beads separation is not possible despite extensive sonication (>40 min.) (Figure 5.21.b). The aggregate spectrum is very different from the expected bead spectrum, which can be seen in presence of the peak at 180° backscattering, and different frequency period of the oscillations (count oscillatory peaks in angle) between Mie theory and the data (Figure 5.21.c-d). Though the behavior of an aggregate of beads compared to that of an isolated bead sample is an interesting topic for an investigation, it is a poor sample for calibration purposes. Therefore, one has to be careful in choosing, preparing and monitoring calibration samples, since even a relatively simple sample can give misleading results.

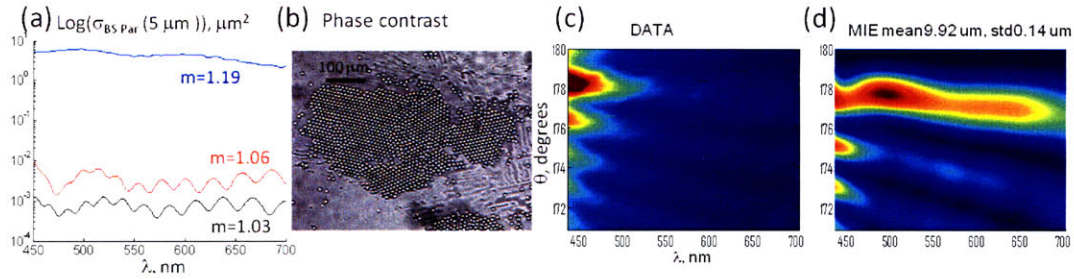


Figure 5 21 Calibration with 10 μm bead suspension in oil in backscattering perpendicular a) Mie predictions for change in backscattering cross-section with reduction of relative refractive index contrast, log scale, $\theta=180^\circ$ b) Phase contrast image 20x of the bead sample c) Normalized scattering data d) Theoretical prediction based on forward scattering predictions, note difference in number of oscillations from the data

Backscattering parallel is calibrated for detection of small particle signals with solution of 50 nm beads in water (Duke scientific). Bead data are presented on Figure 5.22.a. These data show a behavior characteristic for small particles with relatively uniform distribution of scattering along the scattering angle and power-law like behavior in wavelength. Excellent agreement between Mie theory and the data is obtained for size distribution of 60 ± 15 nm, given bottle specification 45 ± 10 nm (Figure 5.22.b). Due to very small size beads could not be counted for density determination under light microscope. In the absence of microscopy measurement, the manufacturer density is used, which appears in excellent agreement with the density obtained through Mie theory and data comparison using conversion factor for backscattering parallel (data - $1.05 \cdot 10^{10}$ particles, manufacturer - $1.25 \cdot 10^{10}$ particles).

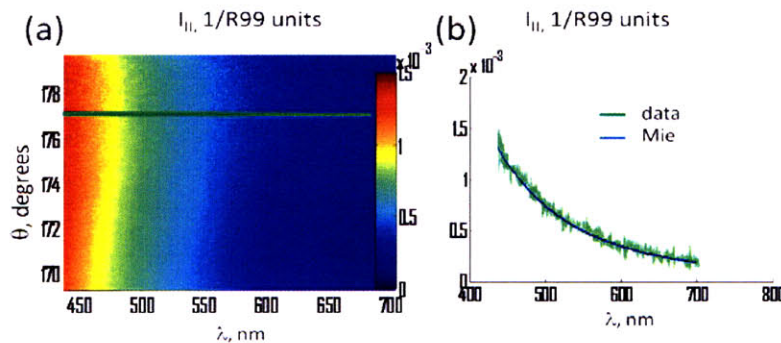


Figure 5 22 Calibration of backscattering parallel with 50 nm bead suspension in water a) Normalized scattering data b) Mie fit (blue-curve) to the wavelength spectrum (green) at $\theta=177^\circ$

In conclusion, backscattering is well calibrated with beads in water in case of small and large particles. Beads in oil do not provide a good calibration due to aggregation in the process of sample preparation.

5.3.6 Bead mixtures

To show power of enhancement techniques, we study mixtures of small and large beads, and analyze mixture data with lookup table approach. Two different mixtures of 10 μm and 50 nm beads are prepared in a blind study, where concentration of large beads is unknown and concentration of smaller particles is kept constant. Data are collected for the three modalities calibrated above at $\varphi=45^\circ$, I_{forw} , I_{\parallel} and I_{\perp} . Data for sample with lower density (sample2) of large particles, according to the shape of the signal in I_{\parallel} and amplitude of the signal in I_{forw} and I_{\perp} , are presented on Figure 5.23.

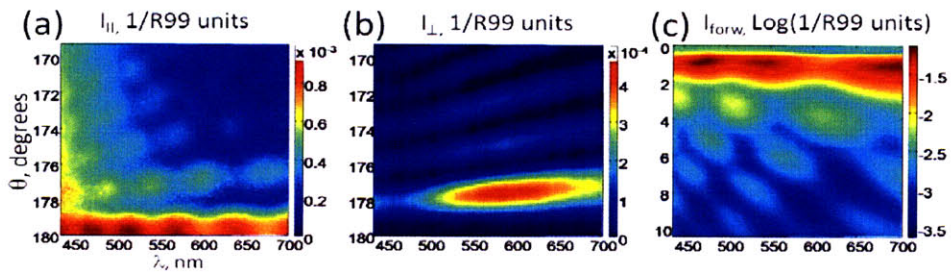


Figure 5.23 Lookup table analysis of 10 μm and 50 nm bead suspension mixture a) Normalized mixture data in backscattering parallel, linear scale, colorbar $0-10^{-3}$ b) Normalized mixture data in backscattering perpendicular, linear scale, colorbar $0-10^{-4}$ c) Normalized mixture data in forward scattering, log scale, colorbar -3.5 to 1

The I_{forw} and I_{\perp} signals are dominated by large particle contribution, while I_{\parallel} is an obvious mixture of the two signals, having a decay at longer wavelengths due to small particle cross-section. Lookup table approach is used to analyze perpendicular and forward data in wavelength (for fixed $\theta=175^\circ$ and 4.6°) and in angle (for fixed $\lambda=537\text{ nm}$) for both sample2 and sample1. Lookup tables are searched for diameters 8-12 μm and standard deviation 0-0.4 μm . The best prediction and results are summarized in table 5.1.

	$I_{\parallel}(\lambda)$, d, μm	$I_{\text{forw}}(\lambda)$, d, μm	$I_{\perp}(\lambda)$, d, μm	$I_{\text{forw}}(\theta)$, d, μm	$I_{\perp}(\theta)$, d, μm	I_{\perp} , N, Particles (dilution)	I_{forw} , N, Particles (dilution)	Microscpe, N, Particles (dilution)	Dilution
Sample2	d=0.064 $\Delta d=0.01$ $\epsilon=6$	d=9.89 $\Delta d=0.2$ $\epsilon=50$	d=9.86 $\Delta d=0.025$ $\epsilon=12$	d=10.14 $\Delta d=0.005$ $\epsilon=153$	d=10.24 $\Delta d=0.005$ $\epsilon=13$	380 (1/39)	900 (1/16)	700 (1/21)	1/14
Sample1		d=9.86 $\Delta d=0.4$ $\epsilon=8$	d=9.81 $\Delta d=0.03$ $\epsilon=4$	d=10.14 $\Delta d=0.005$ $\epsilon=108$	d=10.17 $\Delta d=0.255$ $\epsilon=6$	140 (1/105)	400 (1/36)	280 (1/55)	1/29

Table 5.1 Summary of mixture data analysis for sample1 and sample2

Both, the perpendicular and the forward, produce very close angle and wavelength mean diameters to the expected ones. Distribution in mean diameters within the wavelength and within the angular data is less than 1%. Although there is roughly a 3% difference

between the angular and the wavelength means, which points at a slight potential difference in calibration or normalization. The lookup table results are much less sensitive for the distribution of standard deviation values. The number of beads in the beam area is calculated using perpendicular data, forward data and microscopy data, and then compared to original stock dilution with known concentration of stock. Forward scattering data are closest in reported number of particles to microscopy and to the original dilution values. Perpendicular data are much lower in reported numbers. All of the data report a similar ratio of concentration difference between sample1 and sample2. Thus, the mixture results are reporting a correct mean particle diameter, and they are not as sensitive to particle distribution. They also report a correct change in concentration between sample1 and sample2, although perpendicular is somewhat off in particle number.

Given the mixed nature of the signal in I_{II} , a pre-determined large bead distribution can be used to extract small particle contribution. Based on the results of lookup table, Mie scattering map of the best fit size distribution ($9.85 \pm 0.024 \mu\text{m}$) can be generated for backscattering parallel. The map is summed across all wavelengths. Minimal position of the sum in angle (169.8°) identifies the smallest contribution of large particles to the signal (Figure 5.24.a). An absolute value of large particle signal at the given angle is calculated and compared to the signal of the mixture in sample2 (Figure 5.24.b). Given, the oscillatory content of the mixture signal, the 140-particle signal seems more reasonable, than a 400-particle one. In this case, large particle contribution is considered small enough, so that the original data can be used to search small particle lookup table (2 nm to 1.3 μm). The resultant diameter is $64 \pm 16 \text{ nm}$ is close to the stock specification for mean diameter distribution of $45 \pm 10 \text{ nm}$ with 1% standard deviation (Figure 5.24.c). A condition is placed to find a minimal-error solution for which the standard deviation would not be greater than 25% of mean diameter. Otherwise there is little distinction in difference between Mie and the small diameter between 10 nm and 120 nm (Figure 5.24.d)

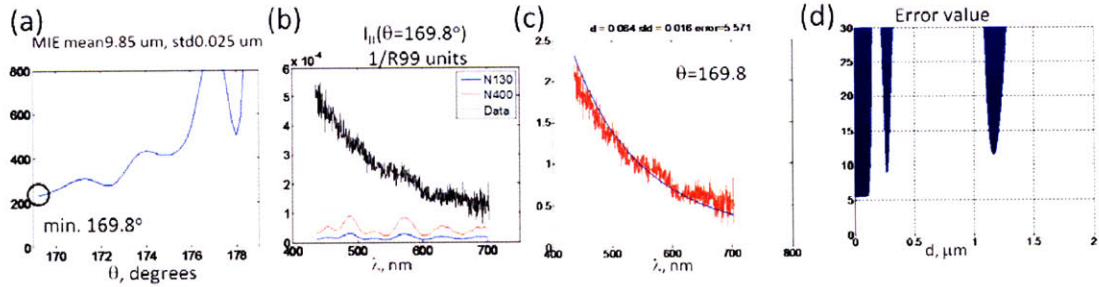


Figure 5.24 Mie analysis of mixture data from sample 2 a) Mie prediction for angular spectrum of best fit size distribution, averaged over wavelength, minimum location (black circle) b) Wavelength spectrum of normalized mixture data at $\theta=169.8$ (black), predicted large particle contribution to the signal for two fitted values for number of large particles (red and blue), linear scale $0-6 \times 10^{-4}$ c) Mean-centered data (red) and best Mie simulation from lookup table $d=64 \pm 16$ nm (blue) d) Error value for diameter from lookup table comparison to data, y-axis – error-value in $1/R99$ units

5.4 Instruments for intensity-based light scattering measurements: Phi-differential backscattering parallel

5.4.1 Experimental system, alignment and calibration

The early version of the described above system (without a forward scattering arm and with less extensive calibration) is used in ϕ -differential experiments with cell monolayers. The goal of the experiments is to establish relative contributions of large and small sub-cellular scatterers in cell monolayers. Five μm beads (Duke scientific) are used for system calibration. Angular range is determined through a manual fitting of selected spectra in wavelength and angle. The spectrograph slit is closed, thus a fine oscillatory structure is present (Figure 5.25.a). First, since there is no ambiguity about the position of exact backscattering (center of the peak), the bead data are fit there to determine bead size distribution by accurately matching peak positions and Mie theory shape to the data (Figure 5.25.b). Angular range is then determined by comparing a Mie spectrum in angle for fixed wavelength (609 nm) to the data (Figure 5.25.c). Although, the angular axis is scaled linearly, and the air-water interface is not accounted for, the angles of interest for ϕ -differential experiment are close to exact backscattering ($\theta: 176^\circ-178^\circ$), therefore, the angular position of interest is determined fairly accurately.

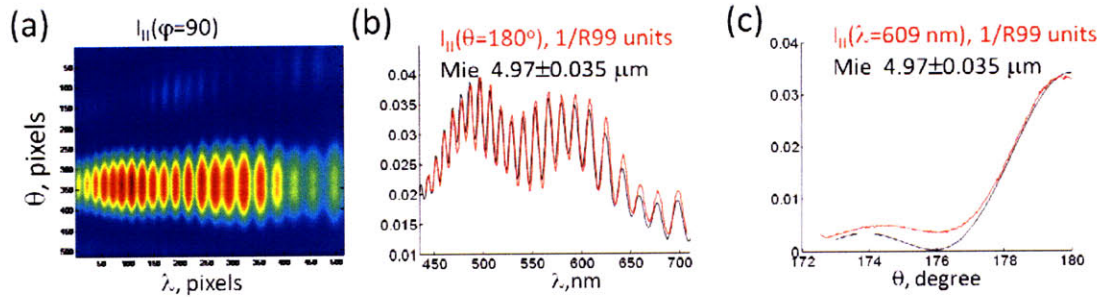


Figure 5.25 Calibration of the experimental system using 5 μm bead data a) Normalized parallel backscattering data b) Wavelength scattering data at exact backscattering (red) and best Mie theory prediction (black) c) Angular scattering data at 609 nm and best Mie theory predictions

After the angular range is determined, the system is re-aligned so that 180° backscattering is centered on a Fourier lens, thus the geometric center of system collection is fairly close to the center of the scattering map. As the collection ranges for $\phi 0^\circ$ and $\phi 90^\circ$ are made similar, the collected range is reduced from the one shown on Figure 5.25.c .

5.4.2 Bead mixtures

To show the power of enhancement techniques, we again study mixtures of small and large beads. The data are collected for 45 seconds, and the wavelength spectra at $\theta=176.8^\circ$ are analyzed. Individual spectra of 5 μm for $\phi 0$ and $\phi 90$ are out of phase (Figure 5.26.a). The

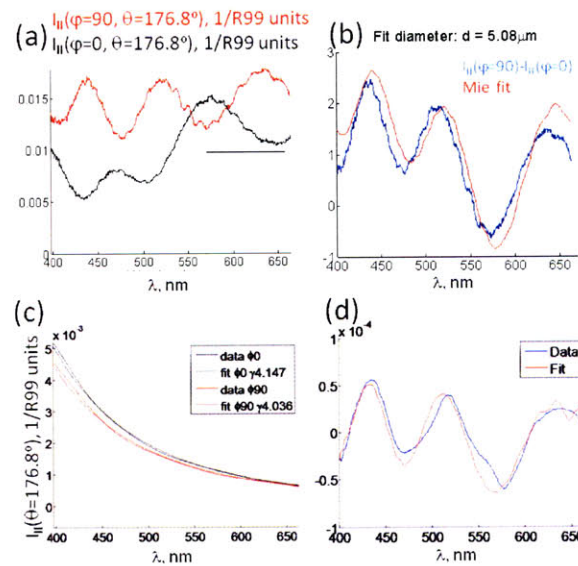


Figure 5.26 Application of ϕ -differential technique in backscattering to measurements of bead suspensions a) 5 μm isolated bead wavelength spectra for individual azimuthal angle values b) ϕ -differential wavelength spectra (blue) and Mie theory fit (red) to isolated 5 μm data c) 5 μm and 50 nm mixture wavelength data, power law fit to individual azimuthal spectra d) ϕ -differential signal from residuals between power law fit and the data (blue) compared to Mie fit of 5 μm (red)

difference between the two spectra is normalized to the mean and fitted with an automated routine to Mie theory, which is also normalized to the mean (Figure 5.26.b). The fit diameter is very close to bead diameter.

The spectra from the mixture of 5 μm and 50 nm beads are dominated by a power-law like shape of 50 nm bead scattering (Figure 5.26.c). There is an amplitude shift between the data at $\phi 0$ and $\phi 90$, which may be partially due to normalization inaccuracy. In order to remove the effect of the shift, each of mixture spectra is fit with a power law. Then, the power law fit is subtracted from the data and the difference between the two residual signals is taken. The difference is shown in Figure 5.26.d. Mie spectra undergo the same procedure, in which 5 μm Mie generated spectra are fit to the power law, and the difference between the residuals is taken. A very good fit is obtained for a diameter value of 5 μm . Thus, the system is well calibrated for applying ϕ -differential method at 176.8°.

5.5 Instruments for intensity-based light scattering measurements: Polarization gating for backscattering

5.5.1 Experimental system description

The system used in the tissue study is a modification of the original system described in [16]. The goal of the system is to collect parallel and perpendicular polarization of scattered light near exact backscattering for polarization-gating experiment (see more in section 8.1). Instead of the combination of the filter wheel and CCD in a Fourier plane, another arm of the system is added with a spectrograph in a Fourier plane and CCD on spectrograph output, similar to the system described in previous sections (Figure 5.27).

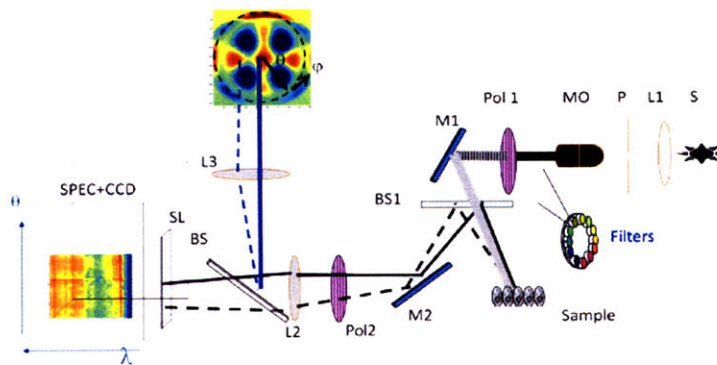


Figure 5.27 Experimental set-up for backscattering measurements in tissues

Also, in a delivery part 10x microscope objective with 100 μm pinhole is used for a tight fixed beam divergence of 0.2° . Iris is placed on the beam path to reduce beam size to 3 mm in diameter on the sample.

5.5.2 Bead calibration

The system is calibrated with a 10 μm bead suspension. The spectra in wavelength for I_{\parallel} are fit manually in for two rows in angle with 0° degree corresponding to 180° degree backscattering (Figure 5.28.a). An agreement in wavelength spectra is obtained between the data and Mie theory for both angles (Figure 5.28.b-c).

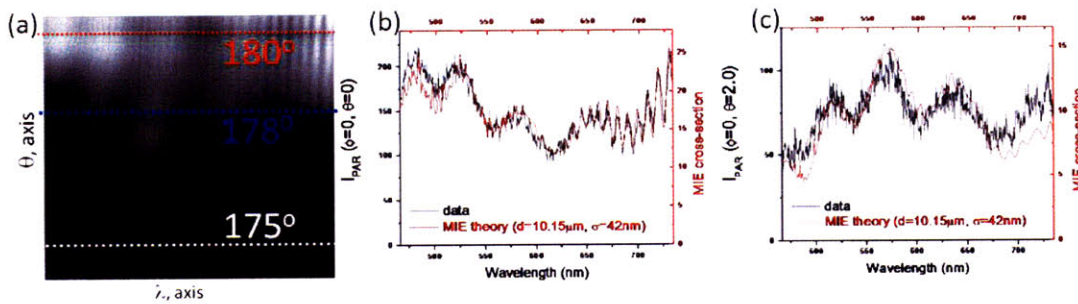


Figure 5.28 Calibration of the experimental system using 10 μm beads a) Angular-wavelength scattering map b) Wavelength scattering data at exact backscattering (black) with Mie theory (red) manual fit ($\theta=0^\circ$ corresponds to exact backscattering) c) Wavelength scattering data at exact backscattering (black) with Mie theory (red) manual fit ($\theta=2^\circ$ corresponds to 178° backscattering)

5.5.3 R99 correction factor

The R99 spectralon reflectance standard is used for normalization of scattering data for each polarization. Although the R99 diffuse reflectance standard is supposed to be polarization insensitive in angle, it is not tested for linear polarization insensitivity. For example, in a simple experiment a HeNe laser beam is sent on a surface of the reflectance standard and the backreflection is analyzed with polarization parallel and perpendicular to the incident beam on a photodiode detector within a few degrees of exact backscattering. The data are showing about 15% difference between the two beams. Moreover, for a spectralon standard with reflectivity of 20% (R20), this ratio is a factor of 4 greater photon count in I_{\parallel} compared to I_{\perp} . R20 was originally used for some of the early experiments due to dynamic range issues with high reflectivity of R99, but it is not used in any of the experiments described in this work. The prime hypothesis is that, R99 has a particle structure (the exact

structure is proprietary, but there are particles of 10 μm dimension). Therefore, it has a certain amount of single scattering, which is polarization preserving to a large extent, and providing additional scattering into parallel polarization according to polarization gating [15]. This hypothesis also agrees with an increased ratio of parallel to perpendicular signal in a R20 spectralon with high absorption, due to a lower proportion of diffuse light coming back, and, accordingly, a larger proportion of singly scattered light coming back.

$$I_{II}(\varphi 0)= I_{II_delivery}(\varphi 0)*RR99_{II}(\varphi 0)*R_{II_detection}(\varphi 0) \quad (5.5.1)$$

$$I_{\perp}(\varphi 0)= I_{II_delivery}(\varphi 0)*RR99_{\perp}(\varphi 0)*R_{\perp_detection}(\varphi 0) \quad (5.5.2)$$

$$I_{II}(\varphi 90)= I_{II_delivery}(\varphi 90)*RR99_{II}(\varphi 90)*R_{\perp_detection}(\varphi 0) \quad (5.5.3)$$

$$I_{\perp}(\varphi 90)= I_{II_delivery}(\varphi 90)*RR99_{\perp}(\varphi 90)*R_{II_detection}(\varphi 0) \quad (5.5.4)$$

The correction method is developed to account for the difference in R99 polarizability. It uses four measurements of R99 reflectance at two orthogonal polarizations and two values of azimuthal angle $\varphi 0$ and $\varphi 90$. Measured intensity on the detector consists of three components – the intensity profile of delivery $I_{delivery}$, the spectralon response RR99 and the collection part of the system response $I_{detection}$ (Eq.5.5.1-5.5.4). There are four measurable quantities and 12 variables. First, taking the ratio of Eq. 5.5.1 to Eq. 5.5.2 and Eq. 5.5.3 to Eq. 5.5.4, removes all terms related to $I_{delivery}$, reducing to two equations with eight variables. It is fair to assume, that a reflectance standard does not have azimuthal variation in scattering angle, thus $R99_{II}(\varphi 0)= R99_{II}(\varphi 90)$ and $R99_{\perp}(\varphi 90)=R99_{\perp}(\varphi 0)$. For detection, the axes of polarization and azimuthal axes are interchangeable $R_{II_detection}(\varphi 0)=R_{\perp_detection}(\varphi 90)$ and $R_{II_detection}(\varphi 90)=R_{\perp_detection}(\varphi 0)$. Then, the number of variables is reduced to four for two equations. If the ratio of equation ratios is taken, then finally the following formula is obtained:

$$I_{II}(\varphi 0)/ I_{\perp}(\varphi 0) *I_{II}(\varphi 90)/ I_{\perp}(\varphi 90)] =(RR99_{II}(\varphi 0)/RR99_{\perp}(\varphi 0))^2 \quad (5.5.5)$$

Four measurable quantities are on the left side of the equation, and the squared ratio of polarization responses of R99 reflectance standard is on the right. Note, that this technique does not allow measuring an absolute value of spectralon reflectance at each polarization, just relative values. This method is applied to three standards, previously used in calibration of light scattering instruments: R99 [15], R20, and barium sulfate BaSO₄ [18]. Results are summarized on Figure (5.29).

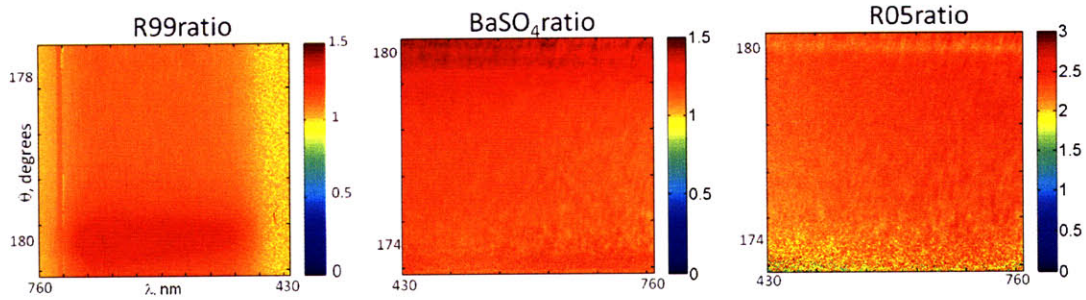


Figure 5.29 Polarization ratio $I_{||}/I_{\perp}$ for reflectance standard response a) 99% reflectance standard ratio b) BaSO₄ reflectance ratio c) 5% reflectance standard

All of the samples exhibit variation in angle in the ratio between the two polarizations. In addition, wavelength dependence is present in barium sulfate sample and in a gray spectralon. Polarizability is strongest at or near exact backscattering at about 25% of R99 and 35% of BaSO₄. The R99 polarizability drops to about 15% by 179.5 degrees and stays at a similar level up to 178 degrees. Polarizability of barium sulfate drops from 35% to 22% at 179 degrees to approximately 18% at 178 degrees, and it varies with wavelength.

Thus due to the overall shape, R99 would be a preferable depolarizer for scattering system calibration, although barium sulfate performs sufficiently well. Gray standard spectralon has, in addition to significant ratio in polarizations, a significant variation in wavelength, larger than in two other standards. Note, that instead of spectralon, there could be a real sample, whose true ratio of signal for two polarizations will be measured.

5.5.4 Effect of incidence angle

The usual condition on the incidence angle in backscattering collection geometry is in order to avoid specular reflection (~4% of incident light) from the front glass surface of the sample holder [15, 19]. Approximately 15° tilt from the normal, in incidence beam towards collection direction tilts reflection 15° away from collection. This should be sufficient for near backscattering collection. However, in optically thin samples, such as bead suspensions or cell monolayers, significant amount of incident light reflects off the bottom coverslip. Thus, approximately 4% of the beam returns back to the sample, propagating in the direction of $2*\theta_{incidence}$ away from the incident beam. If glass-reflected beam is scattered forward or to the side by the sample, it can scatter back into the detector. To demonstrate this effect, a Fourier plane scattering for a thin layer of 10 μm beads is measured for three different incidence angles – 10°, 20° and 45° (Figure 5.30.a).

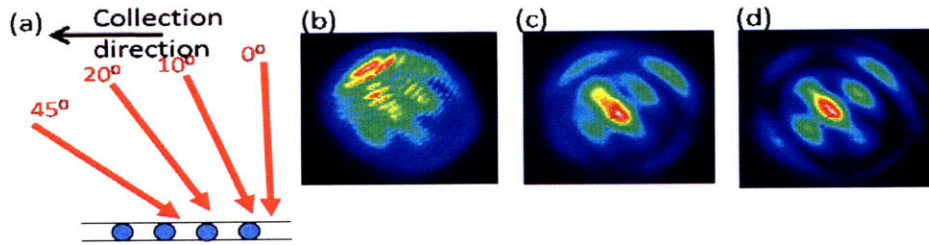


Figure 5.30 Forward scattering contamination in backscattering a) Variable incident angle geometry b) Experimental data 10 μm bead suspension for Fourier plane image at 10° incidence c) Same data with 20° incidence d) Same data with 45° incidence

High frequency oscillatory features represent the backscattering signal contamination (Figure 5.30.b-c). There is no observable contamination of the backscattering signal for incidence angle of 45° (90° side scattering) (Figure 5.30.d). This behavior follows the behavior of scattering cross-section: in exact forward direction, it is many orders of magnitude higher ($\sim 10^3$ - 10^6) than backscattering, thereafter it drops off to minimum (zero for some geometries) at 90°. One of the solutions is to have incidence at 45° minimizing the contribution of side scattering. That is implemented in the design of all of the systems presented above. Another solution is to put a sample on top of the absorptive optical density filter with a very high absorptivity while matching the refractive index between the slide and the filter with an index matching oil. This approach is the only usable approach for suppression of reflection, when incidence angles are close to normal. It creates physical difficulties for subsequent analysis of the sample, for example under a microscope, due to an oil present on the bottom slide.

5.5.5 Rotating Fourier Plane

Polarization properties of reflective optical elements, such as mirrors and beam splitters, are usually described in terms of s- and p- polarization components, defined as parallel and perpendicular polarization components with respect to the plane formed by incoming and reflected beams (Figure 5.31.a). Mirrors and beam splitters that are usually optimized (give 50%-s/50%-p) for normal or for 45° incidence, otherwise reflect with different efficiencies or s- and p- polarized light. For example, glass-air interface, which is a front or back surface of some optical components, has a significantly different dependence on polarization reflection depending on incident angle (Figure 5.31.b).

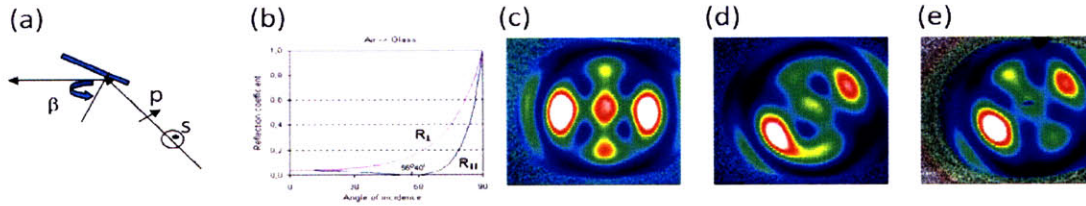


Figure 5.31 Polarization mixing on reflection surfaces a) s- and p- polarization definition with respect to incident and scattered beams b) Ratio of reflectivities of s- and p- polarized light off of air-glass interface c) Fourier image of 10 μm bead suspension with polarization aligned with s- or p-polarization d) 45° rotation of Fourier plane from c) with polarizer-analyzer rotation, polarization e) 45° rotation of Fourier plane from c) with coherent fiber bundle

To avoid distortion effects, the incoming polarization should be either parallel or perpendicular to the surface of the reflector (either 100% s or 100% p). For the systems described above, the following argument applies with respect to the reflections, which take place between the analyzer and polarizer. Before a polarizer or after an analyzer system, all of the light is propagated or detected independently of polarization. The elements discussed are a single beam splitter in case of the first instrument, and the beam splitter plus two mirrors in case of the second. These scattering elements aligned in such a way that the incident beam is polarized with s- (or p-) polarization. Thus the original scattering map of I_{II} , for example, does not have distortions (Figure 5.31.c). The originally suggested mean of changing an azimuthal angle on the spectrograph slit was to rotate the polarizer and the analyzer by the same angle, thus rotating the axis determining the Fourier plane. Due to polarization mixing on reflective elements, it leads to distortion of the scattering pattern (Figure 5.31.d). To avoid these distortions, the Fourier plane should be rotated after the analyzer. This problem is solved by introducing a coherent fiber bundle (described in the latest experimental system) which rotates the Fourier plane after scattering is put through an analyzer (Figure 5.31.e).

Intensity-based light scattering systems used in the current work are described. Extensive calibration for correct representation of wavelength/angular features and concentration of polystyrene microspheres is presented, showing that all of the instruments are well calibrated. The necessary components for making correct theoretical predictions of the data with Mie theory are discussed. The reasons for a specific design of the stationary (non-goniometric) light scattering system are given, including source selection, non-uniformity of reflectance standard and effect of the incident angle. Finally, the discussion of systems' sensitivities is delayed until the actual application of the instruments is discussed in Chapters 7 and 8.

References

- [1] Papulis A. Theory of systems and conversions in optics. Moscow: Mir, 1971.
- [2] Sung Y, Choi W, Fang-Yen C, Badizadegan K, Dasari RR, Feld MS. Optical diffraction tomography for high resolution live cell imaging. *Opt. Express* 2009;17:266.
- [3] Barber PW, Hill SC. Light scattering by particles: computational methods. Singapore: World Scientific Publishing Co. Pte. Ltd, 1990.
- [4] Hulst H. Light scattering by small particles. New York: Dover Publications, 1981.
- [5] Yu CC, Lau C, Tunnell JW, Hunter M, Kalashnikov M, Fang-Yen C. Assessing epithelial cell nuclear morphology by using azimuthal light scattering spectroscopy. *Optics Letters* 2006;31:3119.
- [6] Goodman J. Introduction to Fourier optics: Roberts and Company Publishers, 2005.
- [7] Liu YH, Liang YM, Mu GG, Zhu XN. Deconvolution methods for image deblurring in optical coherence tomography. *Journal of the Optical Society of America a-Optics Image Science and Vision* 2009;26:72.
- [8] Bates DM, Watts DG. Nonlinear regression analysis and its applications: Wiley, 1988.
- [9] Weisstein EW. Nonlinear least squares fitting. *MathWorld--A Wolfram Web Resource*.
- [10] Mourant JR, Canpolat M, Brocker C, Esponda-Ramos O, Johnson TM, Matanock A, Stetter K, Freyer JP. Light scattering from cells: the contribution of the nucleus and the effects of proliferative status. *Journal of Biomedical Optics* 2000;5:131.
- [11] Mourant JR, Johnson TM, Carpenter S, Guerra A, Aida T, Freyer JP. Polarized angular dependent spectroscopy of epithelial cells and epithelial cell nuclei to determine the size scale of scattering structures. *Journal of Biomedical Optics* 2002;7:378.
- [12] Wilson JD, Bigelow CE, Calkins DJ, Foster TH. Light scattering from intact cells reports oxidative-stress-induced mitochondrial swelling. *Biophysical Journal* 2005;88:2929.
- [13] Wu TT, Qu JY. Assessment of the relative contribution of cellular components to the acetowhitening effect in cell cultures and suspensions using elastic light-scattering spectroscopy. *Applied Optics* 2007;46:4834.
- [14] Perelman LT, Backman V, Wallace M, Zonios G, Manoharan R, Nusrat A, Shields S, Seiler M, Lima C, Hamano T, Itzkan I, Van Dam J, Crawford JM, Feld MS. Observation of periodic fine structure in reflectance from biological tissue: A new technique for measuring nuclear size distribution. *Physical Review Letters* 1998;80:627.
- [15] Backman V, Gurjar R, Badizadegan K, Itzkan L, Dasari RR, Perelman LT, Feld MS. Polarized light scattering spectroscopy for quantitative measurement of epithelial cellular structures in situ. *Ieee Journal of Selected Topics in Quantum Electronics* 1999;5:1019.
- [16] Backman V, Gopal V, Kalashnikov M, Badizadegan K, Gurjar R, Wax A, Georgakoudi I, Mueller M, Boone CW, Dasari RR, Feld MS. Measuring cellular structure at submicrometer scale with light scattering spectroscopy. *Ieee Journal of Selected Topics in Quantum Electronics* 2001;7:PII S1077.
- [17] Hecht E. *Optics*: Pearson Education, 2001.
- [18] Sokolov K, Drezek R, Gossage K, Richards-Kortum R. Reflectance spectroscopy with polarized light: is it sensitive to cellular and nuclear morphology. *Opt. Express* 1999;5:302.
- [19] Schuele G, Vitkin E, Huie P, O'Connell-Rodwell C, Palanker D, Perelman LT. Optical spectroscopy noninvasively monitors response of organelles to cellular stress. *Journal of Biomedical Optics* 2005;10:051404.

Chapter 6:

Sub-cellular contributions to single cell scattering and index tomogram manipulation

In previous studies [1, 2], our group developed a method to map the 3D distribution of refractive index in single live cells. Since the index map is a source function of light scattering, we can quantitatively characterize the contribution of cellular components to light scattering. The approach is to manipulate the 3D index tomogram of a single cell in order to extract relative contributions of various cellular components to cell scattering. The feasibility of fitting Mie theory to light scattering of cellular components is validated. A brief description of tomogram acquisition process is followed by testing Born and Rytov approximation in reproducing original scattering data and matching Mie theory in phantom samples. Then, the direct scattering problem is solved for original cell index tomogram, and for tomogram manipulated in order to minimize scattering of the cell border, nucleus or heterogeneity of sub-nuclear or sub-cellular structures. Finally, the influence of a single cell study on the multi-cellular studies is discussed.

6.1 Optical diffraction tomography using Born/Rytov approximations

Optical diffraction tomography is first introduced to explain how to create 3D index tomogram of a single live cell from experimental measurements of scattered fields. It provides solutions for the inverse scattering problems based upon Born or Rytov approximation. The following description is based upon the previous work of our group [2].

According to Born approximation (Chapter 4.2), Fourier transform of spatial distribution of scattering potential equals to scattered field distribution in real space (Eq. 4.23). If Fourier transform of both sides is taken, then Eq. 4.23 takes the following form, known as Fourier diffraction theorem [3]:

$$\frac{ik_z}{\pi} \hat{U}^{(S)}(k_x, k_y, z^+ = 0) = \hat{F}(K_x, K_y, K_z) \quad (6.1)$$

This expression connects 3D-Fourier transform of scattering potential and 2D Fourier transform of the scattered field at the detector plane. Scattered fields' $U^{(s)}$ spatial frequencies k_x and k_y are related to the object spatial frequencies (K_x, K_y, K_z) through the following relations which also include incident beam spatial frequency (k_{x0}, k_{y0}, k_{z0}):

$$K_x = k_x - k_{x0}, K_y = k_y - k_{y0}, K_z = k_z - k_{z0}, \text{ where } k_z = (k_0^2 - k_x^2 - k_y^2)^{1/2} \quad (6.2)$$

The last expression follows from preservation of momentum, which states that absolute value of the wave-vector does not change during scattering. Thus, spatial frequencies of the fields correspond to a hemisphere surface in object spatial frequency space, this shape is called an Ewald's sphere (in particular example, only half of it is calculated). By varying the angle of the incident beam, the incident k_0 -vector is varied, thus object frequency space will be filled with various orientations of Ewald's spheres. Full, 4π , illumination should give complete frequency spectrum of the object, and inverse Fourier transform should reconstruct a true complex refractive index spatial distribution of the object. In the case of the field-based light scattering spectroscopy (LSS) system, the range of incident scattering angles changes from $-\pi/3$ to $\pi/3$ along single planar azimuthal angle, revealing object's spatial frequencies responsible for scattering in forward direction.

In Rytov approximation scattered field $U^{(s)}$ in Fourier diffraction theorem is replaced with the following expression [4]:

$$U^{(s)}(\vec{r}) = U^{(i)}(\vec{r}) * \varphi^{(s)}(\vec{r}) \quad (6.3)$$

where $U^{(i)}$ is an incident field and $\varphi^{(s)}$ is a complex phase defining scattered field in Rytov approximation through:

$$U^{(s)}(\vec{r}) = e^{\varphi^{(s)}(\vec{r})} \quad (6.4)$$

Comparison of Born and Rytov approximations used for reconstruction of $6 \mu\text{m}$ polystyrene bead refractive index distribution in index-matching oil medium shows, that Rytov approximation reconstructs bead index distribution more accurately [5]. For the rest of this chapter, we work with 3D-index tomograms generated by the Rytov approximation from forward scattered data measured by field-based LSS system. Since our samples, polystyrene beads and cells, are non-absorbing, only the real part of a refractive index tomogram is important.

6.2 Solving direct scattering problem using Born/Rytov/Projection approximation in angle

6.2.1 Obtaining angular scattering from tomogram using Born/Rytov approximations

With Dr. Wonshik Choi, who lead the previous study of reconstructing 3D index map of single live cells, we developed a method to calculate light scattering distribution of cellular components from index tomograms. The algorithm calculates light scattering distribution from 3D index map. This is the opposite of optical diffraction tomography in which the 3D index map is reconstructed from light scattering distribution. Below is the detailed description of the algorithm.

First, 3D refractive index tomogram is converted into the scattering potential:

$$F(x, y, z) = \frac{1}{4\pi} * k^2 (n^2(x, y, z) - n_o^2) \quad (6.5)$$

3D-Fourier transform of the scattering is then mapped out to 2D scattering transform of the scattered field $U^{(s)}$ according to Eq. 6.1 and 6.2. As a result, Fourier transform of the field $U^{(s)}$ is a Born-scattered field in a Fourier plane. The angular distribution of scattered light is mapped out according to the following expressions [4]:

$$\theta = \text{asin} \left(\frac{\sqrt{k_x^2 + k_y^2}}{n_0} * \lambda \right), \quad \varphi_{\text{angle}} = \text{atan} \left(\frac{k_x}{k_y} \right) \quad (6.6)$$

For Rytov approximation, the inverse Fourier transform is taken to extract field $U^{(s)}$. Field $U^{(s)}$ is transformed into Rytov field according to Eq. 6.3, 6.4, incident field $U^{(i)}$ is assumed to be unity. Fourier transform of $U_R^{(s)}$ gives field in the Fourier plane, which is mapped according to (Eq. 6.6) onto angular space.

Besides Rytov and Born approximations, we also consider Projection approximation. In this approximation, only total phase accumulation along incident beam propagation direction through the sample is taken into account (incident beam is assumed to propagate along z-axis of the laboratory system), thus the field in projection approximation equals to:

$$U_p^{(s)} = \exp(i * 2\pi / \lambda \int_{z_{\min}}^{z_{\max}} (n(x, y, z) - n_o) dz) \quad (6.7)$$

Here, n_0 is the refractive index of medium. Angular scattering is obtained from Fourier transform of the projection field with slightly different angular mapping from the cases in Born and Rytov approximations:

$$\theta = 2 * \text{asin} \left(\frac{\sqrt{k_x^2 + k_y^2}}{n_0} * \lambda \right), \quad \varphi_{\text{angle}} = \text{atan} \left(\frac{k_x}{k_y} \right) \quad (6.8)$$

Exact applicability criteria of each of the approximations are not well established and need to be determined depending on constraints of a specific problem [6]. In general, Born approximation is usually limited by maximum phase accumulation in the wave propagation through the sample ($\Delta\varphi < \pi/2$), while Rytov is more sensitive to the maximum gradient of the phase change [7]. Projection approximation is likely to be inaccurate for smaller and complex index objects [5]. We establish applicability of these approximations by means of comparing the calculated scattering fields of the spherical samples with those from Mie theory. Another way to validate these approximations is to compare the calculated scattering fields with original scattering data which are used to create the 3D index map.

6.2.2 Validation of Rytov/Born approximations using Mie theory

Phantom index tomograms of spheres are created using Matlab software. For our studies, we choose three different scatterer diameters, 2, 10 and 20 microns, and two different index values, 1.347 and 1.377. Index of the media was assumed to be 1.337 (water, cell media), and wavelength is fixed at 633 nm (He-Ne laser). Thus, our relative refractive index contrast is, if recorded as ratio, $m_1=1.0015$ and $m_2=1.03$, and, if recorder as difference, $\delta n_1=0.01$ and $\delta n_2=0.04$. Spheres of 10 and 20 micron diameters are selected to model cell nucleus and cell body. Limitation of Born approximation due to phase accumulations across the sample is tested. A small sphere with a diameter of 2 microns is used to model small organelles such as nucleoli and is supposed to be well within limits of the Born approximation validity. We digitize our spheres in a $0.0036 \mu\text{m}^3$ volume unit cube with side of 153 nm, corresponding to the diffraction limit of imaging system used in the experiment. Exact diameter of the sphere is defined from tomogram section through the center of the sphere. Maximum phase delay $\Delta\varphi$ and gradient of phase, $\max(\Delta\varphi_1-\Delta\varphi_2)$, is determined from phase images of scattered fields in units of π . Scattering spectrum at azimuthal angle $\varphi=0$ is fit to a table of Mie sizes between 1 and 21 μm for 60° angular range on logarithmic scale. Note, that logarithmic scale gives a higher weight to higher angle scattering while fitting with

a linear scale would be dominated by small angle forward scattering especially for sub-wavelength particles.

d, μm	1.96	9.89	9.89	19.86
n, particle	1.347	1.347	1.377	1.377
d_Mie, μm	2.04 (R) 2.04 (B) 1.99 (P)	9.9 (R) 9.89 (B) 9.9 (P)	9.75 (R) 9.82 (B) 9.75 (P)	19.74 (R) 19.68 (B) 19.66 (P)
$\Delta\phi$, π	0.0209 (R&B) 0.0242 (P)	0.306 (R&B) 0.314 (P)	1.238 (R&B) 1.257 (P)	2.13 (R&B) 2.53 (P)
$\max(\Delta\phi_1 - \Delta\phi_2)$, π	0.0624 (R&B) 0.0628 (P)	0.0362(R&B) 0.0532 (P)	0.146 (R&B) 0.212 (P)	0.1675 (R&B) 0.33 (P)
Error (Mie), a.u.	19.2 (R) 21.5 (B)	10.2 (R) 23 (B)	11.6 (R) 40.2 (B)	8.5 (R) 60 (B)

Table 6.1 Summary of Mie fitting for tomogram scattering generated using Born, Rytov and Projection approximations

All three approximations give diameter through Mie theory fitting within few percent of the true diameter (Table 6.1). The least-squares error of Born approximation fitting to Mie progressively increases with increase of maximum phase delay, mainly due to depth of oscillatory structure and difference in slope from Mie theory (Figure 6.1.a). Projection approximation is at most 20% different in the maximum phase delay from Born/Rytov (Figure 6.1.c vs. d). It performs better than or similar to the Born approximation for larger diameters and slightly worse for smallest diameter, possibly due to higher curvature of a particle. All three approximations perform slightly worse for smallest diameter particle, largely due to digitization issue (Figure 6.1.b).

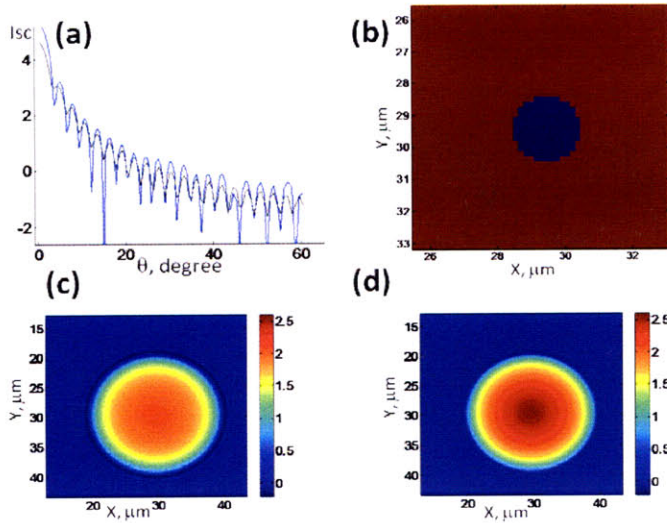


Figure 6 1 a) Angular scattering spectrum generated with Born approximation for 10 μm sphere, $n=1.377$, x-axis scattering angle b) Middle section of 2 μm sphere, axes dimensions are in microns c) Total accumulated phase delay for Born/Rytov approximation, axes in micron d) Total accumulated phase delay for Projection approximation, axes in micron

Rytov approximation gives the best results overall for various sizes and refractive index contrasts, confirming that its sensitivity to maximum phase delay is not significant, while the gradient of phase change is small enough for approximation to be valid up to approximately 40° . Light scattering distributions in angle calculated from Rytov approximation are shown in Fig. 6.2 and those from Mie theory are also presented for comparison.

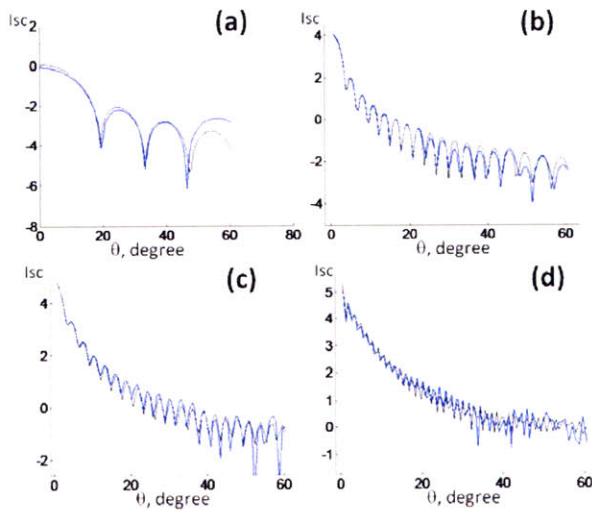


Figure 6 2 Angular light scattering spectra generated from Rytov approximation (blue) and Mie theory fits (black), $n(\text{media})=1.337$, $\lambda=633\text{ nm}$ a) 2 μm sphere, $n=1.347$ b) 10 μm sphere, $n=1.347$ c) 10 μm sphere, $n=1.377$ d) 20 μm sphere, $n=1.377$

6.2.3 Validity of Rytov/Born/Projection approximation in reproducing original scattering data

From experimentally recorded field images at various angles of illuminations, original index tomogram is generated using Rytov approximation. When it comes to calculation of the light scattering distribution, Rytov approximation is expected to be the best in reproducing original scattering data. For test samples, we have chosen index tomograms of 6 μm polystyrene beads in index matching oil $n=1.56$ and HT29 cell in cell media ($n=1.337$).

Center section of 6 μm bead tomogram is presented on Figure 6.3.a. Because of the relatively high noise on the signal, data are averaged over azimuthal angle (Figure 6.3.b). The averaged spectrum carries much clearer oscillatory information of a bead scattering (Figure 6.3.c and d).

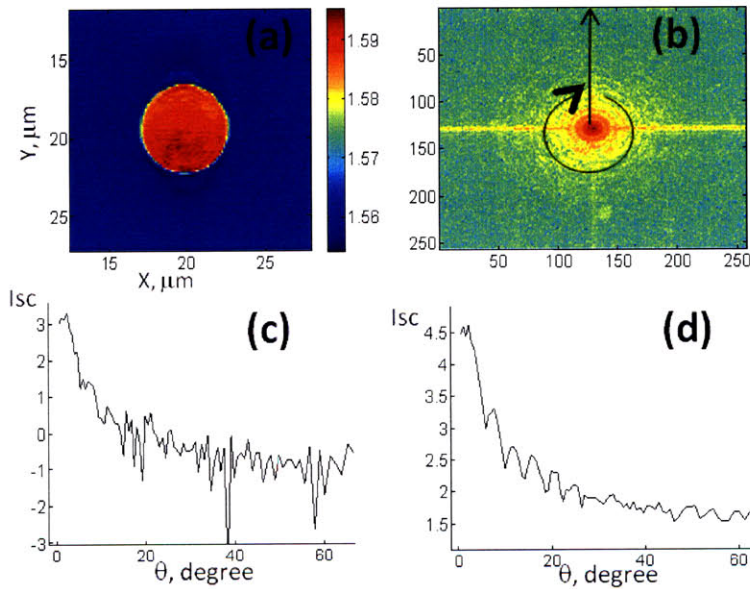


Figure 6.3 Processing from index tomogram to scattering spectra, 6 μm , $n=1.59$, $n_0=1.56$ a) Middle section of index tomogram, axes in microns b) Scattering field distribution in Fourier plane, axes CCD pixels c) Angular spectrum of scattering amplitude at $\varphi=0^\circ$, axis in degrees d) Angular spectrum of scattering amplitude averaged over azimuthal angles

Comparison of original scattering spectra at normal beam incidence to the spectra calculated from an index tomogram indicates that Born and Rytov approximations show equally good matches, while projection approximation is marginally worse to about 30° and shows much more erratic behavior thereafter (Figure 6.4.a-b). The goodness of all of the approximations can be seen through maximum phase delay values, $\Delta\varphi=0.5$ (R&B) and 0.56 (P), and maximum gradient of phase, $\max(\Delta\varphi_1-\Delta\varphi_2)=0.068$ (R&B) and 0.057 (P), well within the goodness of all of the approximations. Original scattering spectrum is acquired at normal

incidence, while tomogram is generated from multiple incident directions. Thus tomogram has more information and represents sample scattering more accurately. Bead sample has no absorption, yet due to some errors in reconstruction, the extracted tomogram has a complex component. The inclusion of this component has relatively minor influence on spectra, also it should have no effect on Projection approximation data (Figure 6.4.c).

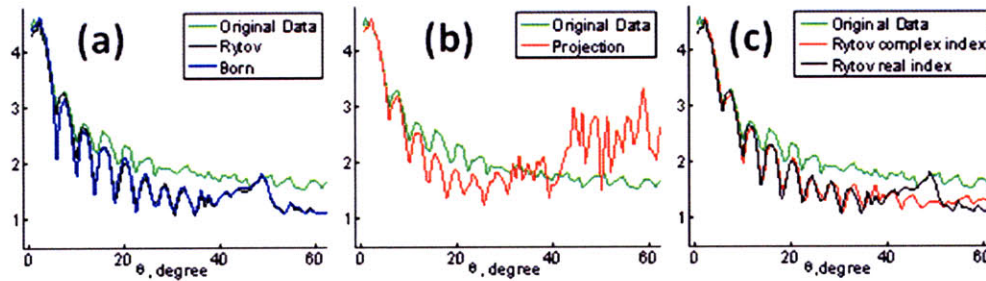


Figure 6.4 Comparison of approximation generated data to original scattering spectra, 6 μm beads in oil a) Angular spectrum generated with Born/Rytov approximation (blue, black) and original scattering spectrum (green) b) Projection approximation angular scattering (red) and original data (green) c) Sensitivity for inclusion or not inclusion of complex part of refractive index in Rytov approximation

Next, we check the validity of approximations for biological cells. We take index tomogram of single HT29 cells, and calculate light scattering distribution from the measured tomogram. Cells are usually larger than 6 μm , in addition the sub-cellular index distribution

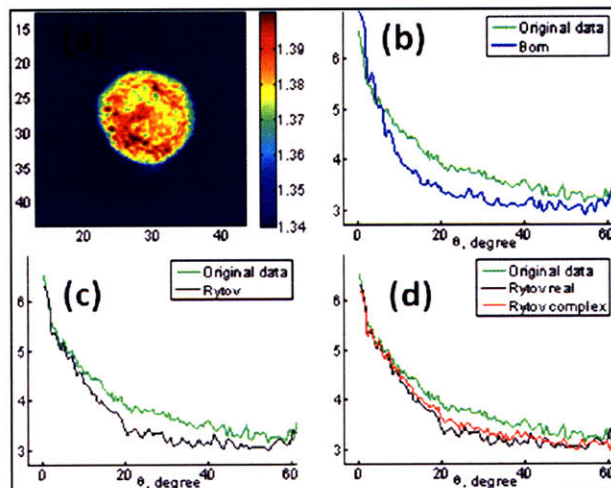


Figure 6.5 Reconstruction of original scattering spectra for HT29 cell index tomogram a) Middle section of index tomogram, axes in microns b) Angular scattering spectrum generated using Born approximation (blue curve) and original data (green) c) Angular scattering spectrum generated using Rytov approximation (black curve) and original data (green) d) Angular spectrum of scattering amplitude averaged over azimuthal angles

is heterogeneous (Figure 6.5.a). At this point we exclude Projection approximation, as it does not seem to offer much advantage over Rytov approximation. Since maximum phase delay

has increased significantly to $\Delta\varphi=1.56$ (R&B) [1.644 (P)] and maximum phase gradient, $\max(\Delta\varphi_1-\Delta\varphi_2)=0.15$ (R&B) [0.16 (P)], more deviation is expected and seen from Born approximation (Figure 6.5.b vs. c). Complex contribution to refractive index has little influence on cell scattering spectra as well as beads (Figure 6.5.d).

Thus, when scattering data are summed over azimuthal angle, Born approximation shows worse fit to original scattering distribution than Rytov approximation does. Born approximation enhances the correct oscillation frequency of the original data for scattering angles $\theta < 10^\circ$, if data are considered over single azimuthal angle φ (Figure 6.6). This feature

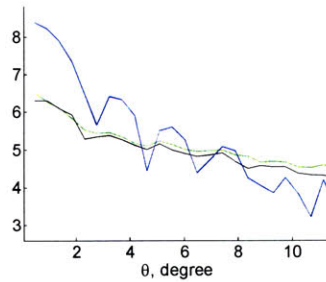


Figure 6.6 Angular scattering generated from Born approximation (blue) reproducing oscillatory pattern of the data (green), with Rytov approximation for comparison (black)

is essential for our analysis of manipulated tomogram in section 6.3. For most of the section 6.3 Born approximation will be used to analyze the oscillatory frequency of scattering from manipulated index tomogram, with some of the conclusions confirmed by Rytov approximation.

6.2.4 Effect of shape on Mie interpretation of scattering from tomogram

General shape of cells and nuclei is non-spherical. Thus the extracting size of them using Mie theory is limited. Now that we have an algorithm to deal with any shape of object for calculating scattering distribution, we validate the use of Mie theory for non-spherical particles. We use ellipsoidal particles to study the effect of shape on Mie theory analysis of scattering data. The shape of an ellipsoid is determined by lengths of its three semi-axis (a,b,c) and space inside ellipsoid is defined by:

$$\frac{x^2}{a^2} + \frac{y^2}{b^2} + \frac{z^2}{c^2} \leq 1 \quad (6.9)$$

We assume that the three semi-axis of ellipsoid are $a=3$, $b=6$ and $c=5$ in μm , respectively. The incident wave propagates along Z-axis and detector is located in XY plane. Refractive index of the media is set to 1.337 and that of ellipsoid to 1.357 (Figure 6.7.a). The semi-axis lengths are chosen in order to model rather an extreme aspheric shape of the nuclei in cell monolayers (see section 3.1.3, Table 3.1). We use Born approximation to calculate angular scattering spectra out of the ellipsoidal phantom. Angular scattering spectra are

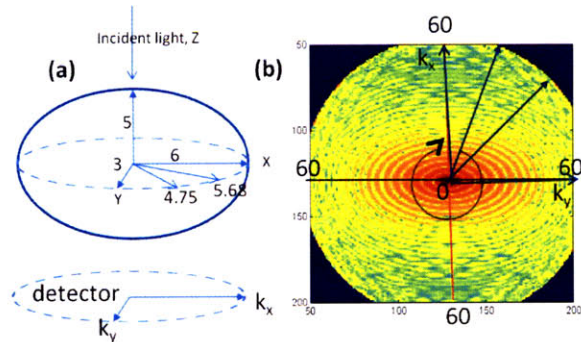


Figure 6.8 Scattering pattern of an ellipsoid a) Ellipsoidal axes lengths are marked, along with two diameters of ellipsoid, not aligned with ellipsoidal axes, detector plane is parallel to XY plane b) Angular scattering map from 0° to 60° forward scattering

analyzed, corresponding to two axis of ellipsoid X and Y, as well as two angles in-between (Figure 6.7.b). We find that the spectra of each individual axis in XY plane of the ellipsoid correspond to a Mie spectrum of a sphere with radius equal to radius of an ellipsoidal axis (Figure 6.8). Note, that the true length of ellipsoidal axis along X is $5.94 \mu\text{m}$, not $6 \mu\text{m}$, due to digitization (Figure 6.8.d). In general, the difference between the true size of ellipsoidal axis and the one determined through Mie theory is less than 10%.

In the experiment, samples are randomly oriented with respect to the observation axis. In order to account for orientation effect, one should sum the data over all azimuthal

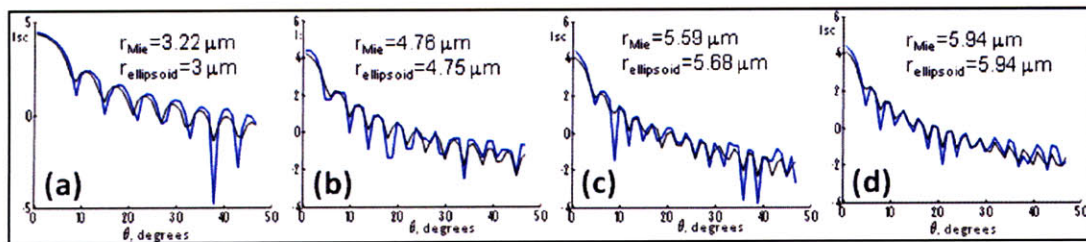


Figure 6.7 Angular scattering spectra at various axes of ellipsoid and fit to Mie theory for each axes a) $\varphi=0^\circ$ b) $\varphi=22^\circ$ c) $\varphi=45^\circ$ d) $\varphi=90^\circ$

angles, as in section 6.2.3 (Figure 6.3.b). Then a distribution of different-sized spheres, not a single-diameter sphere, corresponds to observed scattering spectrum. The oscillatory

component of that spectrum is dominated by smaller dimensions of an ellipsoid. The larger the diameter is, the finer the oscillations become in angle. Thus, the scattering signal from large diameters tends to average out (Figure 6.9). Note that low frequency spectral component is flatter in the shape, then corresponding single size Mie spectrum, which is similar to the effect of a size distribution of multiple cell data. But, that effect is not equivalent to introducing cell size distribution (further discussion will be given in the end of the chapter).

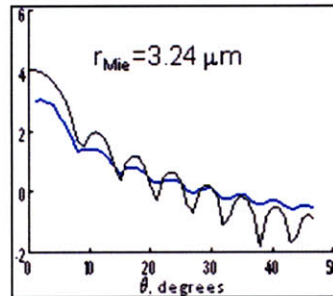


Figure 6.9 Averaged angular scattering spectrum of an ellipsoid over azimuthal angle (blue) and fit to Mie theory

6.3 Extracting the contribution of sub-cellular components to the scattering distribution

6.3.1 Manipulating cell index tomogram

Contrast responsible for scattering comes from index variations inside the cell. In order to estimate contribution of various sub-cellular components to scattering spectrum, we modify the 3D index tomogram of the cell. We remove specific organelle in the measured tomogram and calculate light scattering distribution resulted from the modified tomogram. By comparing this distribution with the original scattering distribution, the contribution of that specific organelle can be determined. We match the index of that organelle to its surroundings, thus reducing its scattering contribution. The index tomogram can be represented as a stack of images in XY plane along Z-axis with thickness corresponding to our resolution of $0.153 \mu\text{m}$ (Figure 6.10.a). For our calculations, we assumed incident light along Z-axis. We can highlight an area of interest in XY section and extract coordinates for its index values using Matlab. Section belongs to a real HT29 cell tomogram, with an outline of a cell border (Figure 6.10.b). The selected index values can be replaced with values of our choice, in a particular example with the average index of the selected area (Figure 6.10.c).

Replacing selected area in each XY-section, we recreate a 3D index tomogram with new refractive index distribution.

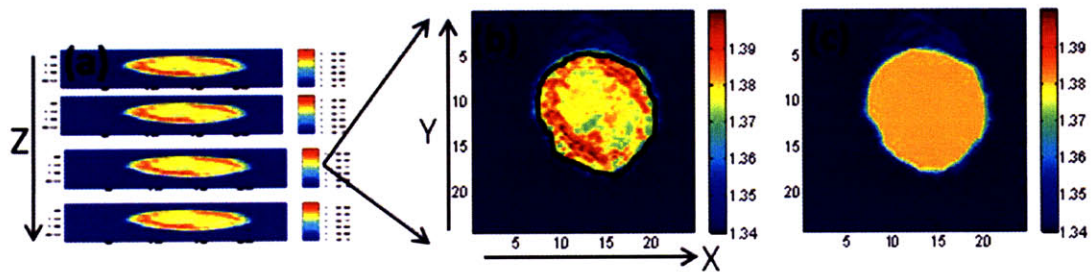


Figure 6 10 Manipulating an index tomogram of HT29 cell, replacing cell index distribution with an average index value (X and Y-axis - μm , colorbar –refractive index value) a) Index tomogram represents a stack of 2D sections along Z-axis b) Individual section, outline of cell border (black), colorbar –refractive index values c) Refractive index inside the area is replaced with an average refractive index value

Next, we study the effect of the nucleus on the angular scattering spectrum. We outline the border of a nucleus in all of the X-Y images (Figure 6.11.a). The region of the cell outside of the outlined area is cytoplasm. Due to index heterogeneity inside the cell, the border of the nucleus cannot be perfectly matched to that of the cytoplasm. We devise three different ways of matching the nucleus border, each of them giving quite similar results, judging by scattering spectra. In case I, nucleus is replaced by an averaged index of cytoplasm (Figure 6.11.b). In case II, nucleus is filled with randomly selected indices from a certain area of cytoplasm (Figure 6.11.c). In case III, nucleus can be extracted directly from cell tomogram and surrounded by an average index of cytoplasm as the media (Figure 6.11.d). One can notice that in all three cases nuclear border is still visible.

To determine scattering of the nucleus in case-III, scattering can be calculated directly from the modified tomogram. For cases I-II, nucleus can be extracted by taking a difference between original and modified tomograms' scattering fields. Scattering fields are squared to generate scattering intensity distributions.

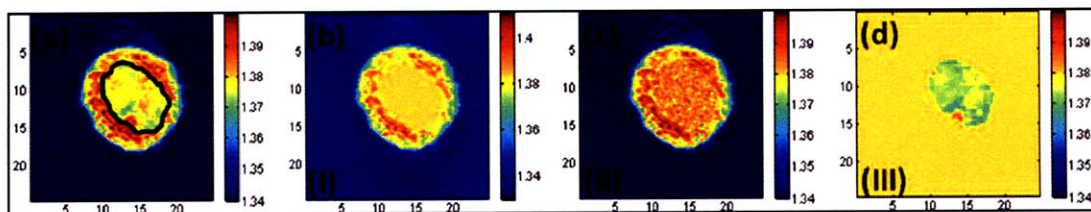


Figure 6 11 Extracting nuclear index distribution (X and Y-axis - μm , colorbar –refractive index value) a) Outline of nuclear border inside an individual section b) Replacing nuclear index with an average of nuclear index variations c) Replacing nuclear index with randomly selected cytoplasmic indexes d) Replace cytoplasm index distribution outside

Scattering spectra at single azimuthal angle are generated using Born approximation (Figure 6.12). While all of the spectra show quite similar behavior, certain differences can be attributed to slight differences in refractive index distributions in the samples. Note that this is the first time to our knowledge to deterministically characterize the scattering distribution of the cell nucleus. Our approach is based on the real index tomogram of live cells not on any specific model of nucleus.

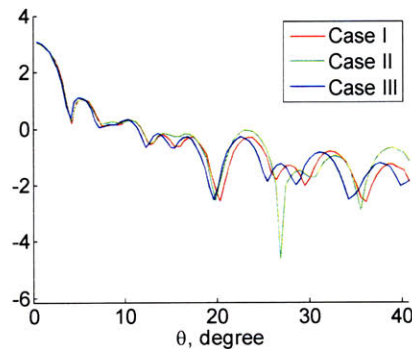


Figure 6.12 Angular scattering spectra of the nucleus for three different ways of extracting nuclear index

6.3.2 Mie analysis of Born approximation scattering from manipulated tomograms

Mie theory can be used to identify relation between scattering and originating structure. At the same time we can test the applicability of Mie theory to analysis of single cell scattering data. We choose to analyze scattering from single cell tomogram of HT29 cell, as well as tomogram of cell nucleus of the same cell from case-III (Figure 6.13.a-b). Our Mie analysis is based on searching a lookup table for particle diameter scattering spectrum (range of sizes 1-19 μm), which, in shape, is closest to the data. The index of refraction of the cell media is 1.337, and nucleus is surrounded by an average cytoplasmic index of 1.38. An important assumption is made for Mie theory, that scattering of the cell and nucleus will be modeled as uniform sphere with index of the cell equal to an average cell index of 1.3644, and for nucleus – 1.3744. As it is mentioned in section 6.2.2, analysis on a linear scale enhances the small angle forward scattering. Thus, more than 90% of the signal is in the first 4° (Figure 6.13.c-d). Mie fitting on a linear scale give sizes of 13.4 μm for cell and 9.4 μm for nucleus with an excellent reproducibility of data shape. On a log scale, larger angles are given more weight in the fitting (Figure 6.13.e).

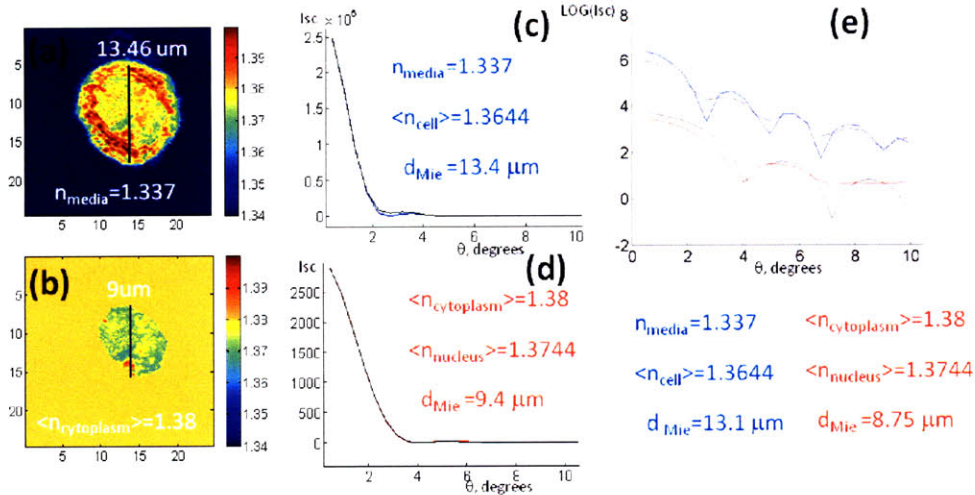


Figure 6.13 Analyzing cell border and extracted nuclear scattering using Mie theory for HT29 cell a) Tomogram section of the whole cell b) Tomogram section of an extracted nucleus with an averaged cytoplasm index c) Angular scattering spectrum of a cell and Mie theory on linear scale d) Angular scattering spectrum of an extracted nucleus and Mie theory on linear scale e) Angular scattering spectrum of cell and extracted nucleus with Mie fit on a log scale

The extracted sizes are 13.1 μm and 8.75 μm for nucleus. On a log scale Mie adequately reproduces shape and relative amplitude of the oscillatory structure of the signal. By comparing with actual physical dimension of cell and nucleus at the largest section, we can conclude that the main contributor to scattering signal extracted either on linear or log scales is the outer border of the object, in either case of cell or nucleus.

6.3.3 Cell boundary or nucleus boundary versus heterogeneous structures in the cell

Mie theory can be used to identify relation between scattering and originating structure. In the previous section, we established that the scattering data processed with Born approximation can be analyzed with Mie theory. In section 6.2.3, we established that Rytov approximation by nature of tomogram generation algorithm reproduces original data more closely. We use both Born and Rytov approximation to compare scattering signals of an individual cell, its extracted nucleus, as well as index-matched cell. The index-matched cell is supposed to mimic an intact tissue, where cell border contrast is lowered, in comparison to individual cell in the medium.

First, we study the overall effect of cell structure heterogeneity on the scattering in comparison with that of cell boundary to the surrounding medium. We replace nucleus and other inner structures' index variations with a single-valued index, 1.3744, which is an average index of the cell (Fig. 6.14 c). There is little change in scattering between homogeneous and heterogeneous cases (Figure 6.14.e). Because the index contrast between

cell border and the media is relatively high, it is responsible not only for most scattering below $<10^\circ$, but also for a large portion of scattering at larger angles, where original oscillation frequency and amplitude are preserved.

Same analysis is made for the nucleus. The inner structure of nucleus is removed and filled with a single-valued index, 1.3744 (Fig 6.14.d). The nucleus border contrast is much lower, thus the effect of inner structure starts to be significant even at angles below 10° (Figure 6.14.f). The oscillations of nuclear border are convoluted with the inner structure response, which suppresses the obvious oscillator structure and alters amplitude of the scattering spectra.

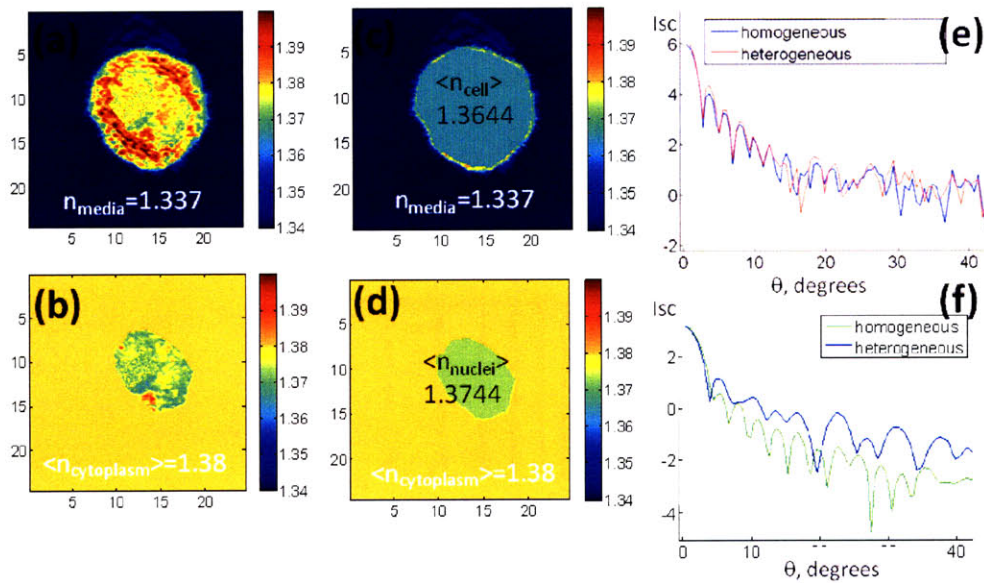


Figure 6.14 Effect of sub-cellular structure heterogeneity on scattering a) Tomogram section of the whole cell, refractive index value b) Tomogram section of an extracted nucleus with an averaged cytoplasm index c) Tomogram section of a cell with an averaged refractive index d) Tomogram section of a nucleus with an averaged refractive index e) Angular scattering spectra at $\varphi=0^\circ$ for homogenous and heterogonous cell index distribution f) Angular scattering spectra at $\varphi=0^\circ$ for homogenous and heterogonous nuclear index distribution

Finally, we compare the scattering spectra from whole cell, extracted cell nucleus and whole cell with outside index equal to an average cell index to minimize effect of cell border (Figure 6.15.a). This comparison is done for both, Born approximation with scattering calculated at single azimuthal angle and Rytov approximation, where scattering is calculated over an averaged azimuthal angle (Figure 6.15.b and c). In either case the scattering from whole cell (blue line), which is dominated by cell border according to Born approximation-Mie comparison, is about 2 orders of magnitude higher than the nuclei scattering (red line) for scattering angles $<10^\circ$. When the cell border is matched to an average cell index, scattering spectrum (green) still constitutes a significant part of oscillatory component of the

cell border, but now it is affected by the sub-cellular structures. Sub-cellular structures do include nucleus, but nuclear contribution is only 10% of the total scattering signal, and has a different shape.

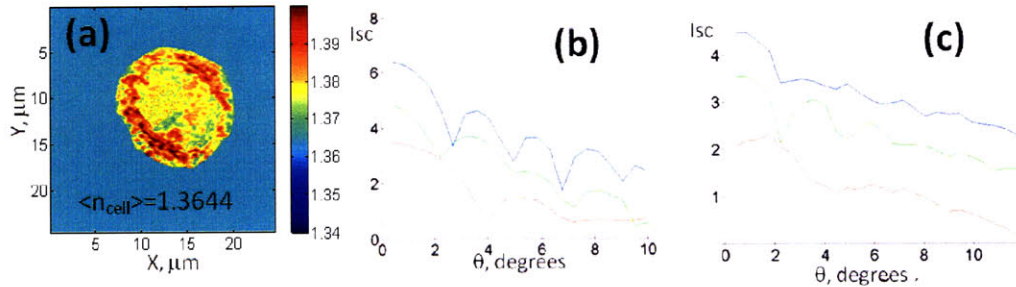


Figure 6.15 Compare cell, nucleus and index-matched cell scattering signals a) Tomogram section of an index-matched cell, where cell media is replaced with an averaged cell index b) Angular scattering spectra at $\varphi=0^\circ$ generated using Born approximation (whole cell – blue, index-matched cell – green, extracted nucleus – red) c) Angular scattering spectra at averaged φ generated using Rytov approximation (whole cell – blue, index-matched cell – green, extracted

6.4 Study single cell scattering in wavelength

In many light scattering studies, scattering is measured as a function of wavelength [8-11, for example] as well as a function of angle. Expanding the single cell study results for angular scattering into wavelength will be meaningful to understand scattering in wavelength for multi-cellular samples. This study, however, requires creating a tomogram from wavelength-dependent scattering data. Index tomogram measured at single wavelength, 633 nm in our experiment, can be used for calculation of scattering as a function of wavelength if index dispersion is negligible. This assumption is reasonable in biological cells. Proteins and nucleic acids, main chemical constituents of cells, have resonance absorption at around 280 nm and 250 nm, respectively. Visible wavelengths are quite far from these resonances, and index dispersion is thus minor. The goal of wavelength calculation is to qualitatively observe relations between wavelength components of scattering from index tomograms used in angular study and compare to results above.

Four simulated index tomograms of spheres (size and index: 2 μm and 1.347; 10 μm and 1.347; 10 μm and 1.377; 20 μm and 1.377), same as in Section 6.2.2, are used to check applicability of Born, Rytov and Projection approximations. For each wavelength λ defining the magnitude of incident wave-vector k_0 , forward problem (section 6.2.1) is solved and 2D angular scattering map is calculated. The wavelength variation is created from combining

data of 2D maps for fixed values of scattering angle θ and azimuthal angle φ . The wavelength spectra for simulated tomograms are presented for $\theta=5^\circ$ and $\varphi=0^\circ$ (Figure 6.16).

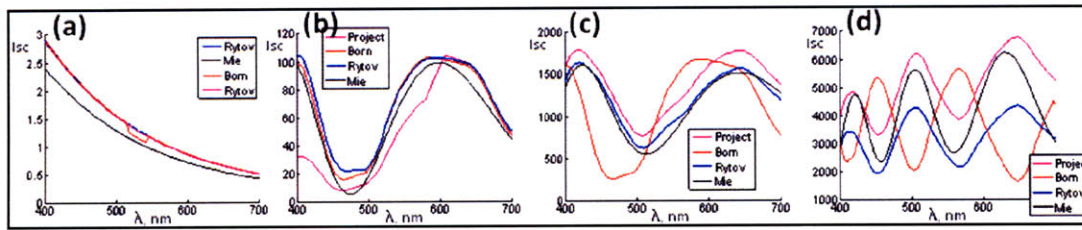


Figure 6.16 Wavelength scattering spectra generated from index tomogram using Born/Rytov/Projection (red, blue, magenta) approximations and compared to Mie theory (black), $n(\text{media})=1.337$, $\theta=5^\circ$ a) $2 \mu\text{m}$ sphere, $n=1.347$ b) $10 \mu\text{m}$ sphere, $n=1.347$ c) $10 \mu\text{m}$ sphere, $n=1.377$ d) $20 \mu\text{m}$ sphere, $n=1.377$

Spectra are plotted for the three approximations (Born, Rytov and projection) and Mie theory. Each of the spectra is normalized with wavelength-dependent factor of $2.8/\lambda^2$. All of the approximations show identical result for $2 \mu\text{m}$ particle and closely reproduce the shape of Mie theory spectra with slight shift in amplitude (Figure 6.16.a). The lower index contrast $10 \mu\text{m}$ data show good agreement between Mie theory, Born and Rytov approximations, while Projection approximation is somewhat off in shape (Figure 6.16.b). The higher index $10 \mu\text{m}$ data have a good agreement between Mie, Rytov and Projection approximation, while Born approximation is deviating, as expected for higher index contrast values (Figure 6.16.c). Finally, in the case of high index contrast and large diameter of $20 \mu\text{m}$ all approximations deviate from Mie theory significantly, but Rytov and projection preserve correct frequency of oscillations. Same spectral behavior is reproduced for two other scattering angles θ of 2° and 9° degrees. Overall, similar to section 6.2.1, Rytov approximation provides best agreement to Mie theory for simulated tomograms.

Two index tomograms, one of the HT29 cell and one of the extracted nucleus, used in section 6.2.3 (Figure 6.13.a-b) are analyzed for agreement between Born-generated scattering spectra and Mie theory. Scattering spectra at $\theta=2^\circ$, 5° and 9° , and $\varphi=0^\circ$ are fit with Mie theory, and best fit diameter is determined (Figure 6.17.a-c). Spectra at $\theta=2^\circ$ and 5° are well fit with the sizes close to the size of cell border and cell nucleus (Figure 6.17.a1, b1 and a2,b2). At 9° , extracted size from Mie theory is consistently lower, than expected structure size.

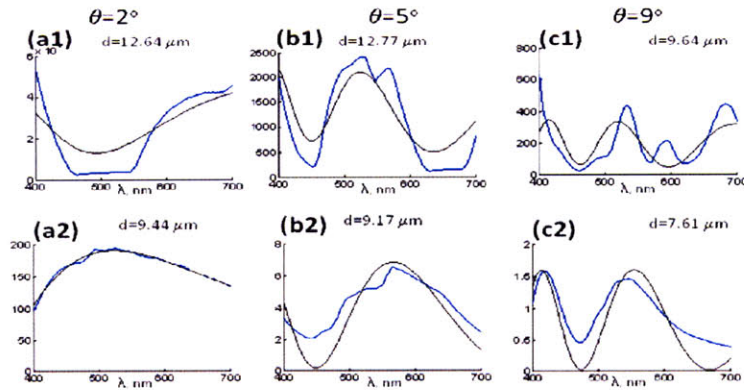


Figure 6.17 Wavelength scattering spectra from index tomogram of cell (a1-c1) and extracted nucleus (a2-c2) (blue) with Mie theory fits (black). Diameter d is the best fit value

In section 6.3.3, the effect of inner structure on the scattering of whole cell and extracted nucleus is studied, and the absolute amplitudes of scattering in angle of whole cell, index-matched cell and nuclear scattering are compared. Same calculations can be conducted in wavelength.

Using Born approximation the effect on the wavelength spectrum of the whole cell and nucleus are compared for same three scattering angles used in Mie fitting. Cell scattering is mainly due to the effect of the cell border, thus, the effect of the inner structure is fairly small (Figure 6.18.a1-c1). Nuclear scattering is a combined effect of the border and inner structure especially towards larger angles (Figure 6.18.a2-c2).

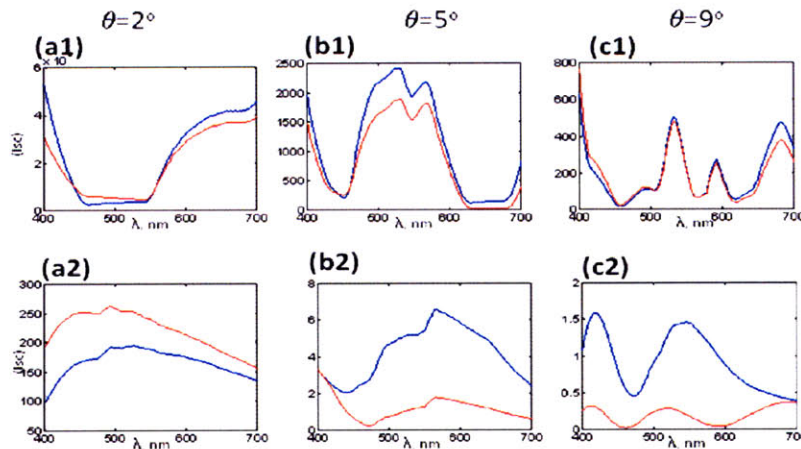


Figure 6.18 Affect of index inhomogeneous on scattering spectra in wavelength, homogeneous index distribution (blue) and heterogeneous (red) index distribution a1-c1) cell index tomograms a2-c2) nuclear index tomograms

Finally, relative contributions of the whole cell, index-matched cell border and whole nucleus can be compared in wavelength (Figure 6.19.a-c). Data are summed over azimuthal angle ϕ , according to calculation in angle (section 6.3.3). Calculations through Born

approximation (Figure 6.19.a1-c1) and Rytov approximation (Figure 6.19.a2-c2) give similar results: whole cell signal is an order of magnitude higher than index-matched cell and about 2 orders of magnitude higher than nuclear signal. The shape of index-matched cell is still significantly different from the shape of the nuclear signal. Thus, wavelength and angular data provide consistent information about scattering of various components of a single cell.

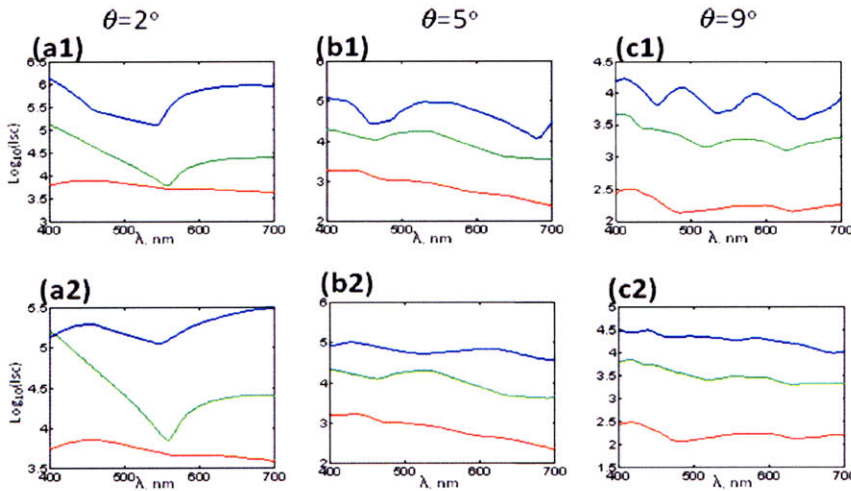


Figure 6.19 Wavelength scattering of whole cell tomogram, index-matched cell and extracted nucleus (blue, green and red) a1-c1) Born approximation a2-c2) Rytov approximation

6.5 Extrapolation of single cell study to multi-cellular systems

Biological systems are composed of multiple cells. For light scattering instrument to be useful as a diagnostic tool, it is important to extend our understanding on light scattering to multi-cellular system. As long as the interference of scattering from different cells is negligible, which is the case with biological cells, individual cell in multi-cellular system such as cell monolayers and cell suspensions can be treated independently. Thus, single cell study should be directly scalable to multi-cellular systems. However, size distribution of cells and sub-cellular components need to be taken into consideration.

Combining results of 6.3.2 and 6.2.4, we conclude that scattering of cell/nuclear border along a selected axis can be analyzed using Mie theory. In many studies, including ours, Gaussian distribution is assumed for scattering from cells/nuclei. From single cell measurements, it follows that the validity of this assumption depends on whether distribution of projections of cells on a selected detection axis is Gaussian. To test this assumption we have chosen a phase contrast image of a cell monolayer and cell suspension and measure projection distribution on detection axis (Figure 6.20.a-c). We measure projection distribution

of 103 cells for cell suspensions, and 40 nuclei for cell monolayer. The histogram of sizes of nuclei can be approximately represented with Gaussian distribution with mean diameter 8.45 μm and standard deviation of 1.94 μm , while cells have mean diameter 10.73 μm and standard deviation 1.73 μm (Figure 6.20.b-d). Thus, the single Gaussian Mie fitting should apply to analysis of small forward angle scattering data from cell suspensions. Nuclei scattering can also be analyzed using single Gaussian Mie, if an actual nuclear signal is extracted.

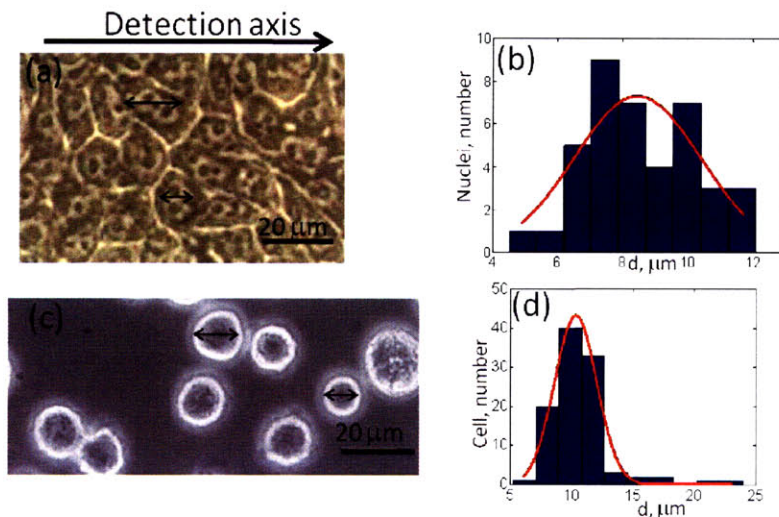


Figure 6.20 Size distribution of cell size and nuclear size projection onto a single axis a) Phase contrast of HT29 cell monolayer b) Histogram of cell section projection distributions c) Phase contrast of HT29 cell suspension d) Histogram of nuclear section projection distributions

As shown in section 6.3.3 and 6.4, nuclear signal amplitude is only 1% of cell suspension signal in small angle forward scattering and about 10% of the signal in cell-border-index matched case. Even when cell border is matched, the main component of the scattering signal carries more information about cell border and overall sub-cellular structure heterogeneity, rather than the nucleus. This has a direct impact on multi-cellular data, since per cell number of nuclei is not going to change.

Backscattering of single cell could not be studied due to lack of experimental data for tomogram. Note that the index tomogram is reconstructed from the forward scattering data. Without exact measurements, it is difficult to extrapolate single cell study to backscattering, which is directly pertinent to tissue studies and intensity-based cell monolayer/suspension measurements. If one considers Mie picture in section 4.1 to qualitatively represent scattering of nucleus, the small angle forward scattering has the largest enhancement of nuclear signal. Thus, the results of this study point out that observation of nuclear signal in backscattering, at

least for specific cell monolayer types, is not necessarily meaningful. The ability to observe cell border has been studied in combination of forward and backscattering using intensity-based methods and is described in following chapter.

In Projection approximation, scattering is a direct function of momentum change, thus angular and wavelength information are equivalent. In Born and Rytov approximation, the connection is similar, and results of wavelength study fully confirm results of angular study. Since index dispersion is a function of wavelength, more accurate solution requires generation of index tomograms at different wavelengths. Finally, the index distribution may be cell/tissue specific. Thus, to make the single cell conclusion more general, detailed study of multiple cell types is needed.

References

- [1] Choi W, Fang-Yen C, Badizadegan K, Oh S, Lue N, Dasari RR, Feld MS. Tomographic phase microscopy. *Nature Methods* 2007;4:717.
- [2] Choi W, Yu C-C, Fang-Yen C, Badizadegan K, Dasari RR, Feld MS. Field-based angle-resolved light-scattering study of single live cells. *Opt. Lett.* 2008;33:1596.
- [3] Wolf E. Three-dimensional structure determination of semi-transparent objects from holographic data. *Optics Communications* 1969;1.
- [4] Devaney AJ. Inverse-scattering theory within the Rytov approximation. *Opt. Lett.* 1981;6:374.
- [5] Sung Y, Choi W, Fang-Yen C, Badizadegan K, Dasari RR, Feld MS. Optical diffraction tomography for high resolution live cell imaging. *Opt. Express* 2009;17:266.
- [6] Born M, Wolf E. *Principles of Optics*. Cambridge: Cambridge University Press, 2005.
- [7] Chen BQ, Stamnes JJ. Validity of diffraction tomography based on the first Born and the first Rytov approximations. *Applied Optics* 1998;37:2996.
- [8] Xu M, Wu TT, Qu JY. Unified Mie and fractal scattering by cells and experimental study on application in optical characterization of cellular and subcellular structures. *Journal of Biomedical Optics* 2008;13:024015.
- [9] Georg S, Edward V, Philip H, Caitlin OC-R, Daniel P, Lev TP. Optical spectroscopy noninvasively monitors response of organelles to cellular stress. *Journal of Biomedical Optics* 2005;10:051404.
- [10] Sokolov K, Drezek R, Gossage K, Richards-Kortum R. Reflectance spectroscopy with polarized light: is it sensitive to cellular and nuclear morphology. *Opt. Express* 1999;5:302.
- [11] Hunter M, Backman V, Popescu G, Kalashnikov M, Boone CW, Wax A, Gopal V, Badizadegan K, Stoner GD, Feld MS. Tissue self-affinity and polarized light scattering in the Born approximation: A new model for precancer detection. *Physical Review Letters* 2006;97.

Chapter 7:

Experiments with cell monolayers and suspensions

This chapter summarizes results of light scattering experiments in multi-cellular samples, such as cell suspension and cell monolayers of three types of cells: HeLa, HT29 and T84. According to single cell results and refractive index measurements, the strongest scattering comes from cell border-media interface. Moreover, this component has oscillatory Mie-analyzable features, even for non-spherical cell shapes. Thus, initial multi-cellular measurements are conducted with cell suspensions in forward scattering. Measurements are then combined with backscattering results through an index-matching experiment in a cell suspension. Analysis of large structure contribution to backscattering is conducted using large particle enhancement methods developed in experimental Chapter 5. A major component of the backscattering signal from cell monolayers is determined to be a power law in wavelength. Power laws are analyzed using continuous and discrete particle size distributions.

7.1 Forward and backscattering of cell suspensions

7.1.1 Expanding single cell results to multi-cellular systems

Signal from individual non-spherical cells has a Mie-like oscillatory component. The frequency of the oscillations corresponds to the frequency of a scattering spectrum from a Mie sphere. This sphere has an average refractive index of the whole cell and diameter equal to length of the cell projection on the detection axes. Therefore, Mie theory can be used to predict Mie component of the signal for the size distribution of cells.

In section 3.1.3, equivalent nuclear diameter distributions are listed for three cell monolayers of interest. According to these size distributions of the nuclei, standard deviation is ~17% of the mean diameter. The nuclear-to-cytoplasm diameter ratio is about 70% (13 μm vs. 9 μm , HT29 cell, see section 6.3.2). Combining these facts, the distribution of HT29 cells is $14.74 \pm 2.5 \mu\text{m}$. Assuming similar ratios for other two cell types, their cell diameter distributions are T84 - $20.85 \pm 3.54 \mu\text{m}$, and HeLa - $18.25 \pm 3.1 \mu\text{m}$.

Combining size distribution predictions with the average index value of 1.3644 for HT29 cells, the expected wavelength and angular scattering distributions can be calculated using Mie theory. Mie theory prediction is generated in the range of wavelengths and angles detected by an intensity-based experimental system ($450 < \lambda < 710$ nm and $0.5^\circ < \theta < 10^\circ$, Chapter 5). The wavelength spectra are calculated at the same angles as for single cells ($2^\circ, 5^\circ, 9^\circ$), and angular spectra are calculated at three wavelengths (450 nm, 550 nm, 633 nm) (Figure 7.1).

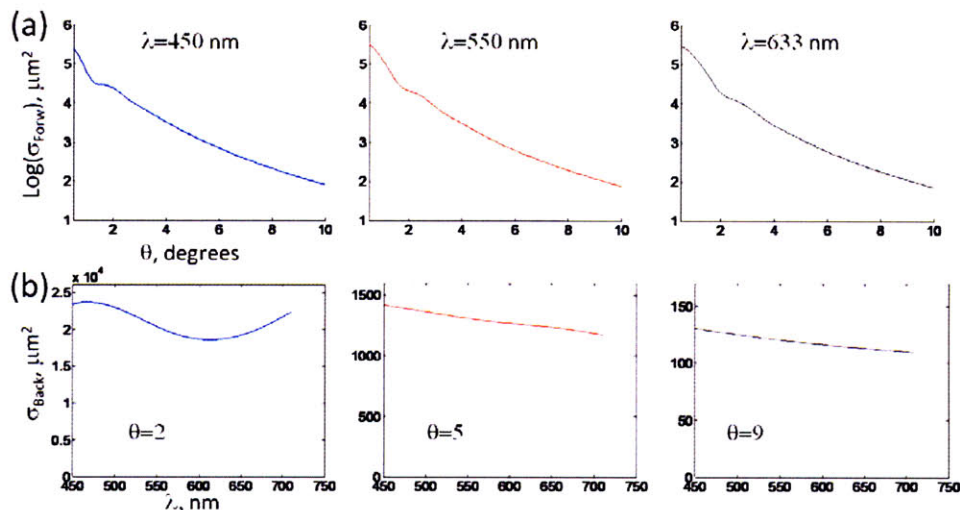


Figure 7.1 Simulated forward scattering of HT29 cell suspension in water, $n=1.3644$, $14.74 \pm 2.5 \mu\text{m}$ a) Angular spectra for three wavelengths, log scale b) Wavelength spectra for three angles, linear scale

Angular spectra are plotted on a log scale, while wavelength spectra are on a linear scale. The only prominent feature in all of the spectra is a peak near 2° in angular spectrum, which degrades from 450 nm to 633 nm. The feature also manifests itself in wavelength at 2° , if HeLa or T84 spectra can also be plotted (Figure 7.2.a-b).

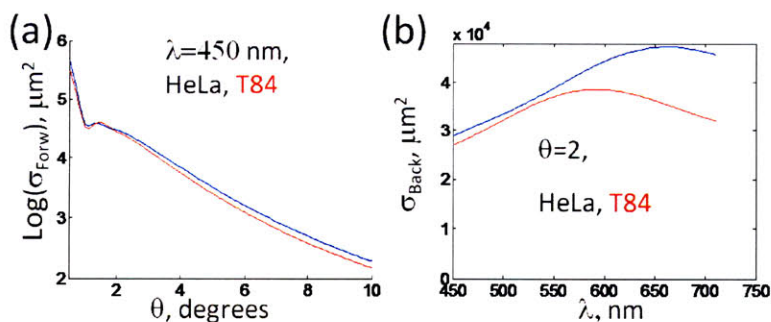


Figure 7.2 Simulated forward scattering for HeLa (blue) and T84 (red), use HT29 index contrast $n=1.3644$ a) Angular spectrum at 450 nm, log scale b) Wavelength spectrum at 2° , linear scale

7.1.2 Measurements of HT29 and HeLa cell suspensions in forward scattering

Forward scattering of suspensions of HT29 and HeLa cells is measured by an intensity-based light scattering instrument. Details of cell growing and sample preparation are discussed in section 3.1.2. In brief, cells are removed from the surface of the culture dish and placed in an optically transparent buffer solution, such as PBS. About 90 μl of cell suspension are sandwiched between two #1 coverslips with a 0.1 mm-thick insulator in between (the insulator opening diameter is 20 mm). After the scattering experiment, the area of interest (5 x 7 mm) is marked and can be studied under the microscope.

Of the two cell types, HT29 cells have stronger inter-cellular junctions. As a consequence, a significant percentage of HT29 cells is clumped. The same degree of clumping is preserved even when cells are diluted from the relatively dense suspension of 21000 cells in the measurement area to 2100 cells as can be seen in phase contrast images (Figure 7.3.a-b). The angular scattering spectrum for a fixed wavelength of 450 nm and wavelength spectra at two angles of 1.1° and 3.4° are plotted (Figure 7.3.c-e). Lower concentration spectra (blue and green lines) are scaled by concentration change (8.4 and 123) to plot on the largest concentration scale. Because of clumping, scattering spectra are changing in shape/amplitude in greater proportion than could be explained by change in concentration alone. These changes can be seen in angle (Figure 7.3.c) and wavelength (Figure 7.3.d-e).

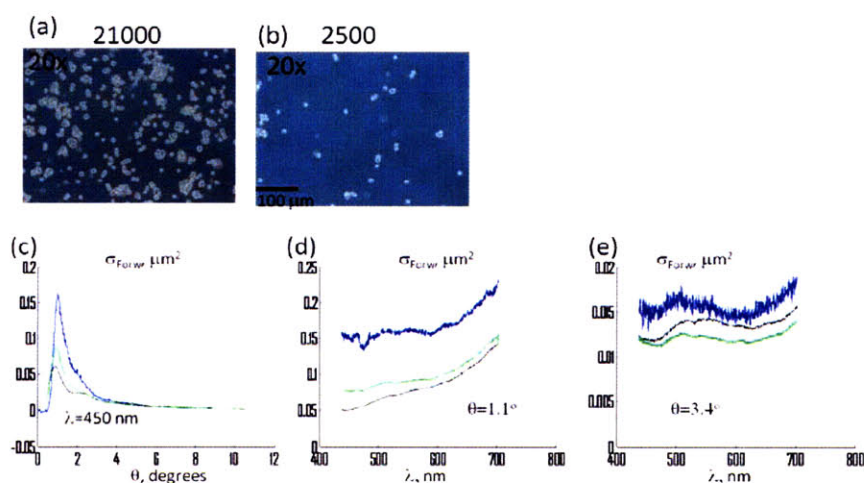


Figure 7.3 Variation of scattering intensity with change in cell suspension density, HT29 cell suspension **a)** Phase contrast image of the highest density cell suspension **b)** Phase contrast image of 1/8.4 diluted sample **c)** Angular spectra of three dilutions scaled by change in concentration (black – highest density, green – medium, blue – lowest), $\lambda=450 \text{ nm}$, linear scale **d,e)** Wavelength spectra of three dilutions scaled by change in concentration for two values of scattering angle, linear scale

Another possible explanation is that the non-linear scaling of the signal could be due to the significant proportion of multiply scattered light. This would be true for a sample with the high value of the optical density. Optical density can be estimated from the product of the total scattering cross-section of HT29 cell distribution and the number of cells. Estimated optical density τ equals 0.57 for the 21000-cell sample, and it is a factor of 8.4 smaller in the 2500 cell sample. Thus, multiple scattering should not be significant in either of the samples, supporting the clumping issue.

HeLa cells with a similar optical density τ of 0.35 for a 9700-cell sample exhibit a much lower degree of clumping (Figure 7.4.a-b). HeLa scattering spectra overlap accurately in angle or wavelength when scaled by the ratio of concentrations (Figure 7.4.c-e). HeLa scattering measurements are more accurate due to lower amount of clumping, and as such are processed with Mie theory (see below).

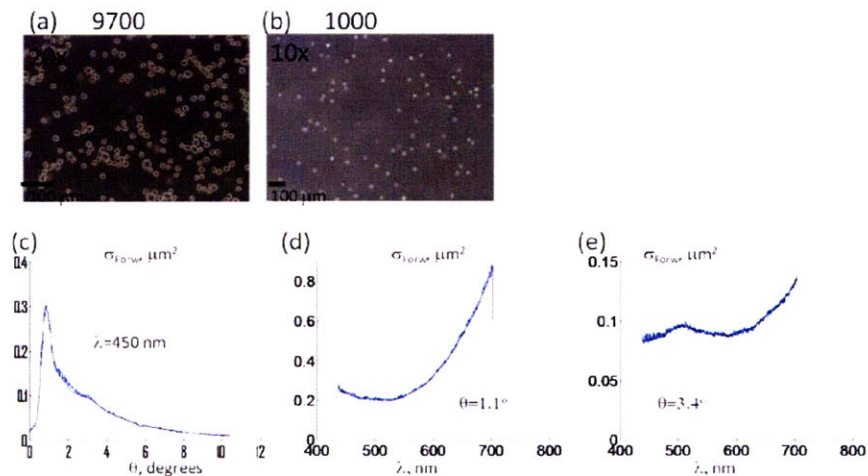


Figure 7.4 Variation of scattering intensity with change in cell suspension density, HeLa cell suspension a) Phase contrast image of the highest density cell suspension b) Phase contrast image of 1/9.7 diluted sample c) Angular spectra for two dilutions scaled by change in concentration (black – highest density, blue – lowest), $\lambda=450 \text{ nm}$, linear scale d,e) Wavelength spectra of three dilutions scaled by change in concentration for two values of scattering angle, linear scale

7.1.3 Analyzing HeLa cell suspension data

Analysis of HeLa cell suspension scattering data is performed using a lookup table approach. In lookup table generation, a 4-th parameter is added: refractive index. Compared to bead calibration in Chapter 5, the range of diameter has to be increased. In order to check the step size in scattering parameters, a 15 μm diameter particle with refractive index contrast

of $m=1.05$ is considered. Spectra in angle at 400 nm and wavelength at 5° are convoluted with the angular and wavelength response of the system (Figure 7.5.a-b).

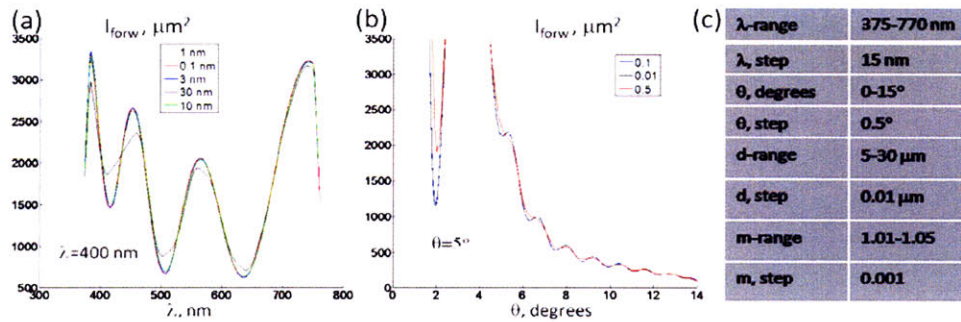


Figure 7.5 Choosing step size in angle and wavelength for lookup table generation for forward scattering of cell suspensions, $15\text{ }\mu\text{m}$ bead suspension, $m=1.05$ a) Convolved wavelength spectrum at $\theta=5^\circ$ with convolution width between 0.1 and 30 nm b) Convolved angular spectra at $\lambda=400\text{ nm}$ and convolution width of 0.01° - 0.5° c) Table of selected ranges for parameter values

Since little change was seen in scattering spectra in wavelength for step sizes below 30 nm , a step of 15 nm is chosen. Similarly, angle step of 0.5° is used, as there is little change in scattering spectra. Step size in diameter is increased from 5 nm to 10 nm , which has little effect given the wide size distributions of cell/nuclear sizes. The lookup table parameters are listed in Figure 7.5.c.

The denser of the two HeLa cell samples is analyzed, since the shape is identical, but signal level is higher (Figure 7.6.a). The main detectable feature, as predicted by Mie calculations, is around 2° . Thus, the analysis is focused on this feature. Wavelength spectra at 1.34° , 2.14° and 2.96° are analyzed, along with angular spectra at 450 , 550 and 633 nm (Figure 7.6.b).

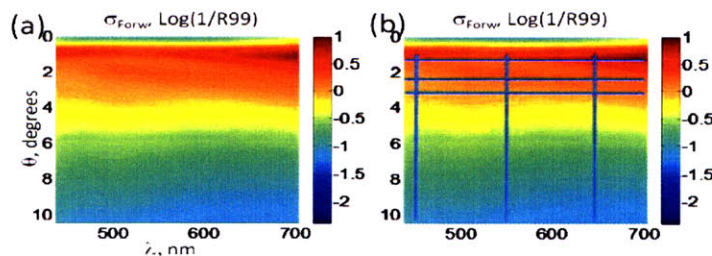


Figure 7.6 Scattering data used for Mie look-up-table simulations a) Dense HeLa sample scattering data, oscillatory feature around 2° b) Sections in scattering angle and wavelength for further analysis (blue lines)

Three parameters are varied: size ($5:0.1:30\text{ }\mu\text{m}$), relative refractive index (1.01 - 1.05) and width of size distribution ($0.1:0.1:3.5\text{ }\mu\text{m}$), where distribution has a single Gaussian shape. First, the spectra in wavelength are mean-centered, and the shapes at three angles are analyzed for best simultaneous match to Mie theory. The best match is determined at three

values of parameters $d=16\pm 1.6\ \mu\text{m}$ and $m=1.027$ (Figure 7.7.a). Then, the same parameters are used to generate a Mie prediction for angular data (Figure 7.7.b).

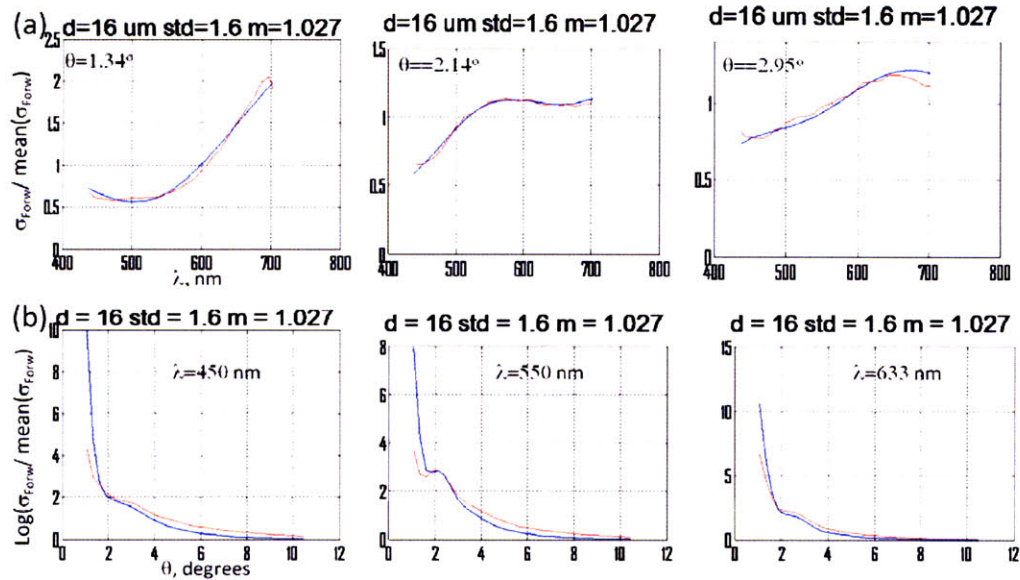


Figure 7.7 Mie look-up-table approach best result to fit wavelength data of HeLa cell suspension a) Mean-centered wavelength spectra and best simulation Mie theory for three values of scattering angle b) Mean-centered angular spectra (log scale) and best simulation Mie theory for three values of incident wavelength

Therefore, pure Mie behavior is extracted around the significant feature at 2° . Deviation from Mie behavior is observed at other angles (Figure 7.7.b). This deviation is similar to the deviation of Born approximation from true cell scattering data observed in single cell experiments (see section 6.2.3). Mean cell diameter is about 14% lower, then predicted in section 7.1.1. This cell distribution is predicted based on fluorescence measurements of nuclei in cell monolayers, where the transverse dimension is elongated and the longitudinal is shortened due to attachment of cells to the substrate. The relative refractive index contrast of 1.027 is a fairly reasonable value, since averaging of single cell indices of the HT29 cell predicts 1.02. The difference in relative index values can be due to the difference in cell types. Also, a lookup table is generated for the media refractive index of 1.36, which is assumed to be the refractive index of the cytoplasm in some studies [1, 2]. The media refractive index with respect to the cell border is just a cell media index of 1.337. Since Mie depends on the ratio of the wavelength in the media to particle diameter, the mean diameter is increased by the ratio of indexes $1.36/1.337$ to $16.3\ \mu\text{m}$. Therefore, according to the analysis of forward scattering data, a major feature of the signal is related to cell-media

interface and can be fitted to Mie theory predictions with a single Gaussian distribution of whole cell sizes and an average relative index contrast value for the whole cell.

7.1.4 Index-matching experiment in forward scattering

Quality of the above analysis relies on how well Mie model matches the scattering data. An experimental approach, suggested by Dr. Wonshik Choi, is used to determine whether the scattering signals are coming from the cell border. Cell media is mixed with a higher index substance, bovine serum albumin (BSA), which is a purified protein fraction. BSA is 100% water soluble and is available in crystallized form. BSA has been previously used to index-match cell cytoplasm [3, 4]. The addition of BSA changes the refractive index according to the following formula: $n=n_{\text{cell_media}}+\alpha*C$, where C is the concentration of solid BSA in grams per milliliter of solution and $\alpha=0.000185$. BSA is added to the cell suspension until the cell border contrast is visibly diminished in phase microscopy images (Figure 7.8.a-b).

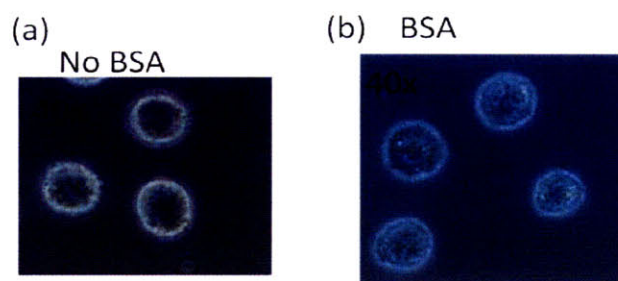


Figure 7.8 Effect of index-matching with phase contrast microscopy a) Before index matching, media PBS b) After index matching, PBS+BSA

Scattering is measured in two samples, with and without BSA. The former has 13500 cells, and the latter, 21800 cells. The intensity data are scaled in the analysis according to the difference in concentrations. One can see a clear distinction between index matched and non-index matched scattering data due to the disappearance of the 2^o feature and the increase in scattering near the forward direction (compare Figures 7.9.a-b). For further comparison, angular spectra at 525 nm are considered, which again show the disappearance of an oscillatory feature and an increase in near-forward scattering (Figure 7.9.c). For given concentration of BSA, the refractive index of the media is increased from 1.337 to 1.3663. Therefore, the relative refractive index changes from $m=1.027$ (according to the Mie fitting in the previous section) to $m=1.005$. Mie theory simulations are conducted using the size distribution $d=16\pm 1.6 \mu\text{m}$ (determined in the forward scattering experiment) and the two

values of relative refractive index contrast (Figure 7.9.d). Mie spectra behavior is consistent with the data: the oscillatory feature at 2° disappears, and near forward scattering increases. Note that the ratio of the maxima between BSA and noBSA spectra is similar for Data and Mie theory, both differ by a factor of three between index-matched and non index-matched, case.

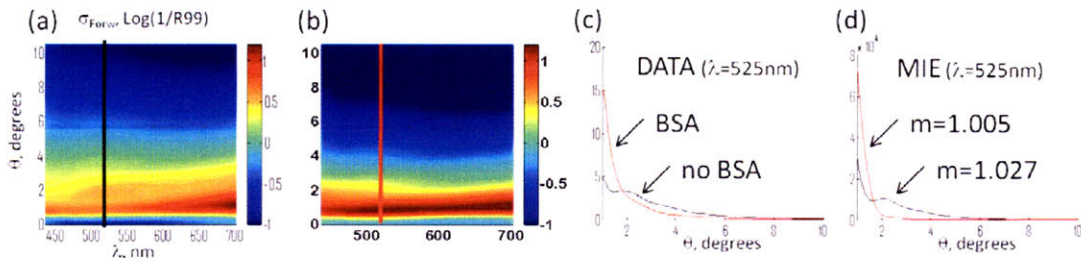


Figure 7.9 Index-matching effect on forward scattering from HeLa cell suspension a) Scattering data from HeLa in PBS b) Scattering data after index-matching HeLa in PBS+BSA c) Angular scattering spectrum change at 525 nm before (black) and after (red) index-matching d) Change in Mie prediction for size distribution of $d = 16 \pm 1.6 \mu\text{m}$ and theoretically predicted index drop before (black) and after (red)

As indicated by the cell border index matching experiment, when pure cell media is used, the majority of the scattering signal is due to the cell-media interface. Data and Mie spectra become featureless, with a smooth drop-off in intensity of the index-matched scattering data. Mie has a faster drop-off than the data spectrum, which means that other scatterers also contribute to the signal. At the same time, analyses of the signal structure will be significantly impaired by the lack of features.

7.1.5 Index-matching experiment in backscattering

The highest index contrast achievable in the cell occurs at the cell-media interface. The interface contributes to the majority of the signal in forward scattering from cell suspension. The question with backscattering is whether the cell border will still contribute significantly to backscattering signal. Same samples, as in forward scattering, are measured in backscattering. Parallel and perpendicular polarization geometries are used at $\varphi = 45^\circ$ (Figure 7.10). The scale for parallel data is $0 - 6 \cdot 10^{-4}$ (Figure 7.10.a-b). For perpendicular data, the scale is $0 - 1.5 \cdot 10^{-4}$ (Figure 7.10.c-d).

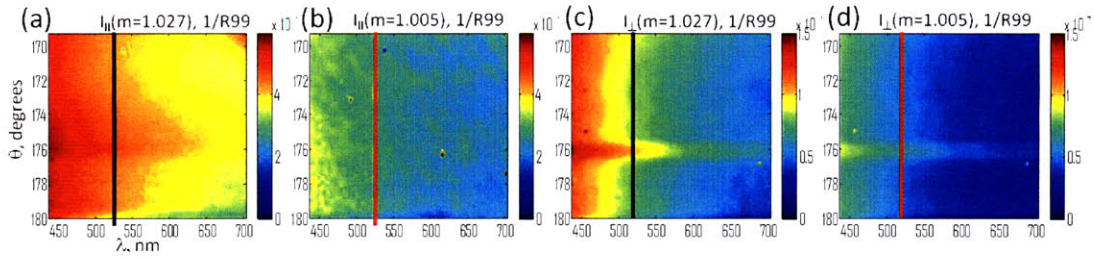


Figure 7.10 Index-matching effect on backscattering from HeLa cell suspension **a)** Scattering data for parallel in PBS, linear scale $0-6 \cdot 10^{-4}$ **b)** Scattering data for parallel after index-matching HeLa in PBS+BSA, linear scale $0-6 \cdot 10^{-4}$ **c)** Scattering data for parallel in PBS, linear scale $0-1.5 \cdot 10^{-4}$ **d)** Scattering data for cross-polarized after index-matching HeLa in PBS+BSA, linear scale $0-1.5 \cdot 10^{-4}$

Angular spectra at 525 nm and wavelength spectra at 178° are considered (Figure 7.11). The observed change in average signal intensity for angular spectra is a factor of 1.5 for parallel geometry and 1.2 for perpendicular between index-matched and non index-matched cases (Figure 7.11.a and c, compare black and red curves). According to Mie theory, which uses the size distribution determined from forward scattering, the backscattering intensity in wavelength should drop with decrease in relative refractive index contrast by a factor of 30 in parallel and factor of 5000 in perpendicular. Therefore, the expected drop of the signal is 1-3 orders of magnitude higher than observed, and the majority of the signal is not due to cell diameter distribution. Similarly, the wavelength spectra do not show much change (Figure 7.11.b and d).

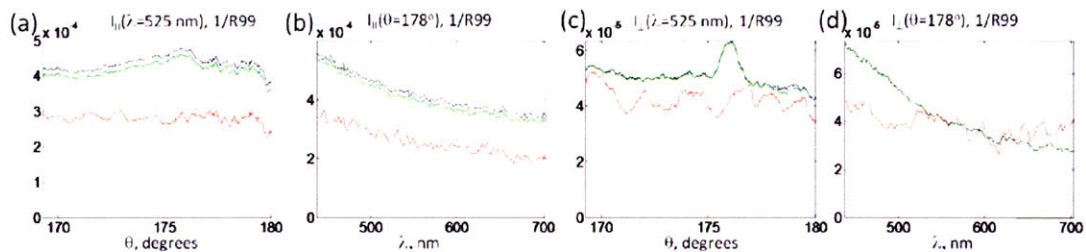


Figure 7.11 Angular and wavelength sections' analysis in the index-matching experiment (black – before index matching, red – after, green – before index matching minus change in Mie signal for cell border) **a)** Angular scattering spectra, parallel polarization, at 525 nm **b)** Wavelength spectra, parallel polarization at 178° **c)** Angular scattering spectra perpendicular polarization at 525 nm **d)** Wavelength spectra perpendicular polarization at 178°

Given the number density of cells and highest relative refractive index contrast of $m=1.027$, the absolute value of the signal of cell diameter distributions is small compared to the total signal. In the Figure 7.11, the green curve is the difference between total backscattering signal and backscattering Mie prediction for cell size distribution. According to the amplitude of expected signal, all of the observed features (e.g., variations in angle and wavelength) are part of errors in normalization and signal correction. The ability to detect

small contributions to backscattering signal is determined by system sensitivity discussed in next section.

7.1.6 Backscattering system sensitivity and cell-media interface scattering

Theoretical limitations of system sensitivity are determined by photon shot noise (with the signal-to-noise ratio defined as the number of photons over the square root of the number of photons). Actual system sensitivity is worse than the shot noise limit and can be determined by calibration measurements. Two measurements are used to define limits of system sensitivity. In one, the difference is taken between two background measurements, rather than real sample measurements. The scattering maps of Mie predictions for cell distribution are presented in Figure 7.12.a-b in R99 units. In parallel, Mie theory predicts a light scattering signal with a large DC component ($3-4 \times 10^{-5}$) and small amplitude variations (2×10^{-6}). These variations are small compared to background variations of $0.5-2 \times 10^{-5}$ (Figure 7.12.b-c). Therefore, in parallel orientation the cell-media interface scattering has only a DC component. This component lacks features above system sensitivity, and its analysis would be quite complicated.

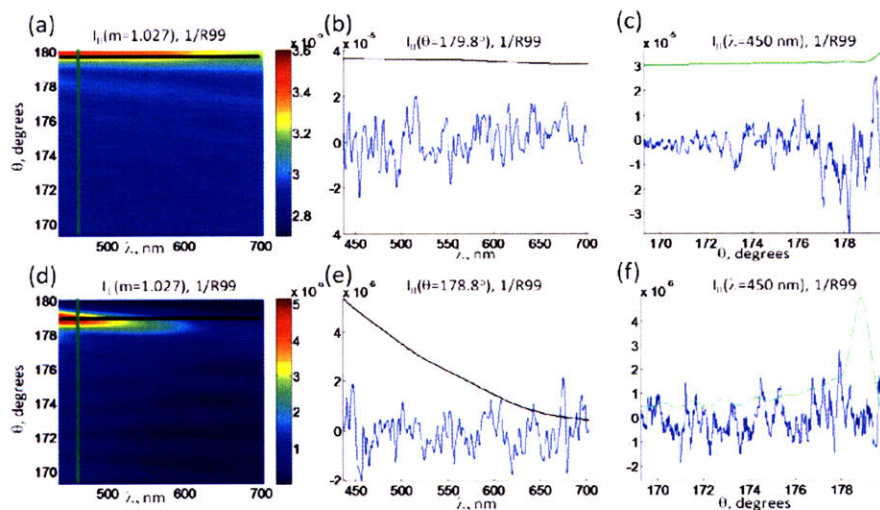


Figure 7.12 Predicted whole cell backscattering vs. system sensitivity, HeLa cell distribution and index from forward scattering measurements a) Mie prediction for cell scattering signal in PBS for parallel polarization, colorbar - $\times 10^{-5}$ b) Wavelength scattering in parallel polarization (black) vs. system sensitivity level (blue), scale $\times 10^{-5}$ c) Angular scattering spectrum in parallel polarization (black) vs. system sensitivity level (blue), scale $\times 10^{-5}$ d) Mie prediction for cell scattering signal in PBS for perpendicular polarization, colorbar - $\times 10^{-6}$ e) Wavelength scattering in perpendicular polarization (black) vs. system sensitivity level (blue), scale $\times 10^{-6}$ f) Angular scattering spectrum in parallel polarization (black) vs. system sensitivity level (blue), scale $\times 10^{-6}$

For the perpendicular polarization case, the signal is above system sensitivity for a maximum cross-section peak close to exact backscattering (178.8°). For all other angles, the

signal is at system sensitivity level of $1-1.5 \times 10^{-6}$. Even at the peak angle, the wavelength drops below system sensitivity at 600 nm.

Note that for exact backscattering in cross-polarized geometry, large particle scattering is zero for a perfectly collimated beam. The only signal observed is due to an instrument response at the angle of about 0.5° , and is 5-15 times smaller than the signal at all other angles. Therefore, the signal at exact backscattering can be subtracted from the rest of the signal defining the maximum possible amplitude of large particle contribution within 20%. This can be thought of as a perpendicular θ -differential technique ($I_{\perp}(\varphi=45^\circ, \theta \neq 180^\circ) - I_{\perp}(\varphi=45^\circ, \theta=180^\circ)$). Note that this method can be used to subtract any angularly uniform contribution to scattering, for example to remove diffuse scattering contribution from tissue scattering signals (see Section 8.2.5). If this method is applied to the cell data above, the shape of the residual signal in angle stays the same, with only an amplitude drop to about 2×10^{-5} , which is still significantly bigger than Mie predicted signal (Figure 7.13.a). Upon subtraction, the wavelength shape changes significantly from a power law-like component in wavelength to a DC-like signal which is still bigger than the Mie-predicted cell interface contribution (Figure 7.13.b and c). Also, the actual fluctuations of the residual scattering signals from cell data are equal or greater than variations predicted by Mie theory.

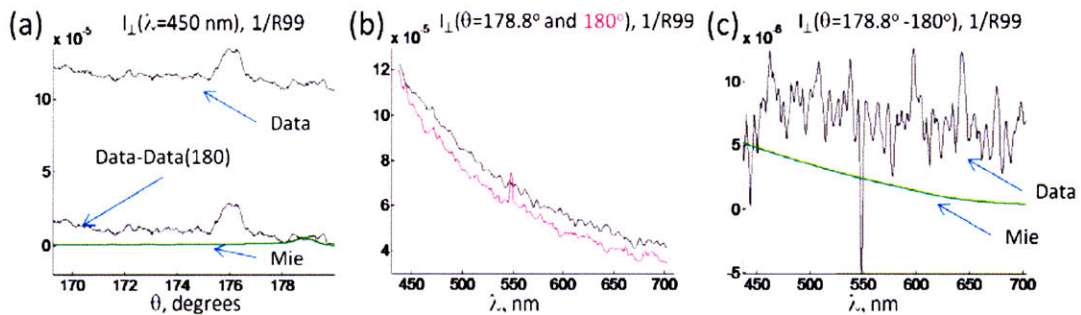


Figure 7.13 Application of θ -differential data to reduce background signal in perpendicular polarization for HeLa cell suspension in PBS a) Angular scattering spectrum at 450 nm (black – original data and θ -differential data, green – Mie theory prediction), scale $\times 10^{-5}$ b) Wavelength data at exact backscattering (magenta) and 178.8° (black), scale $\times 10^{-5}$ c) θ -differential signal scattering data (black) vs. Mie theory prediction for cell border (green), $\times 10^{-6}$

50 nm beads can also be used to establish system sensitivity limits. In section 5.3.5, 50 nm beads are used to calibrate parallel polarization, and the measured signal closely follows Mie theory predictions in shape and amplitude. Cross-polarized signal of the same sample is also measured (Figure 7.14.a). The θ -differential signal can be calculated and compared to Mie prediction for the given sample (Figure 7.14.b-c). Since Mie prediction is on the level of 10^{-10} of R99 units, most of the signal is system-related uncertainties. Their

amplitude of $1-1.5 \times 10^{-5}$ is comparable to the θ -differential signal from cells, making further analysis of the cell signal unreasonable.

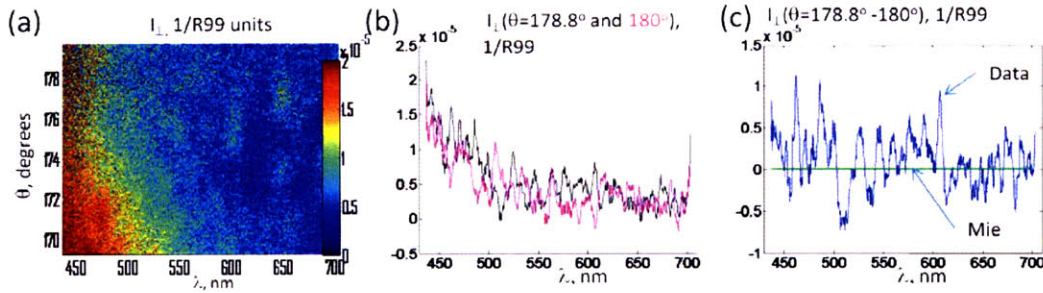


Figure 7.14 System sensitivity established with 50 nm bead suspension a) Perpendicular scattering data, colorbar $0-2 \times 10^5$ b) Wavelength data at exact backscattering and 178.8° , scale $\times 10^{-5}$ c) θ -differential signal scattering data (blue) vs. Mie theory prediction for cell border (green), scale $\times 10^{-5}$

To conclude section 7.1, the cell-media interface is a major scatterer in near forward direction scattering below $<10^\circ$ degrees. An approximate cell size distribution can be established based on Mie model analysis for angles near 2° and cell-border index matching experiments in which the cell border contribution is reduced. In backscattering, the cell-media interface (which has the strongest index contrast of all cell components) contributes relatively little to the total backscattering signal ($<10\%$ in parallel and $<5\%$ in perpendicular). Even when all other contributions are minimized through θ -differential technique in perpendicular geometry system sensitivity is still an issue. In order to interpret Mie variations of the signal, system sensitivity has to be better than 10^{-6} in 1/R99 units, which is close to an order of magnitude improvement on current system sensitivity levels.

7.2 Backscattering from cell monolayers

7.2.1 Large particle signal through enhancement methods

The previous chapter's results clearly indicate that even the cell-media interface contributes very little to the backscattering signal. According to single cell refractive index measurements, nuclear index contrast with cytoplasm will be even lower ($m=1.0042$ vs. 1.027) As a result, the absolute magnitude of the nuclear signal is smaller (at least by an order of magnitude), and nuclear contributions to backscattering are going to be negligible, requiring at least a two-fold increase in system sensitivity. At the same time, the inner structure has even more of an impact on the signal than for the case of the cell-media

interface, so even if the experimental system is sensitive enough, signals may be difficult to interpret.

Based on the single cell and cell suspension results, the probability of seeing nuclei in cell monolayer experiments is fairly negligible, but such experiments were still conducted to illustrate this point using actual measurements. Three types of cell monolayers were studied using the θ -differential technique at $\phi=45^\circ$. The normalized signals for perpendicular polarization at $\theta=177^\circ$ and $\theta=180^\circ$ are presented on Figure 7.15. Signal amplitudes are of the same order as in the case of cell suspension signal ($3 \times 10^{-5} - 2 \times 10^{-4}$ in 1/R99 units).

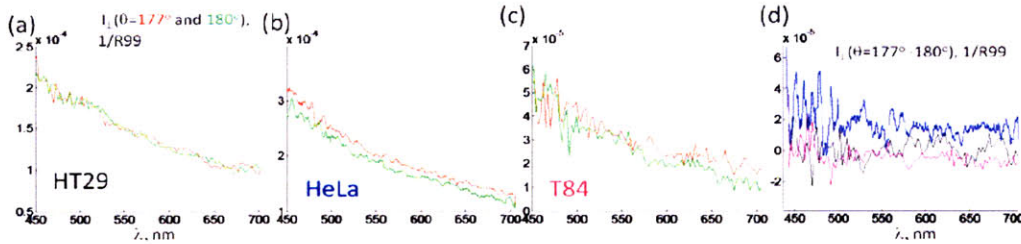


Figure 7.15 θ -differential in perpendicular applied to cell monolayer data a) HT29, Wavelength data at exact backscattering (green) and 178.8° (red), scale $\times 10^{-4}$ b) HeLa, Wavelength data at exact backscattering (green) and 178.8° (red), scale $\times 10^{-4}$ c) T84, Wavelength data at exact backscattering (green) and 178.8° (red), scale $\times 10^{-5}$ d) θ -differential residual signal for HT29 (black), HeLa (blue), T84 (magenta), scale $\times 10^{-5}$

All the residual signals and variations in them are at, or below, the level of system sensitivity (Figure 7.15.d). If one only uses intensity-based results, the residual signal amplitude can be set as an upper limit on the possible scattering signal amplitude coming from nuclei. Since size distribution of the nuclei is measured, the only parameter, which can vary freely, is the relative refractive index contrast. Results are summarized in Table 7.1.

Cell type	ΔI	Nuclear size, μm	Max(m)
T84	$<3 \times 10^{-6}$	14.6 ± 2.65	1.025
HT29	10^{-5}	12.8 ± 2.19	1.034
HeLa	$<2 \times 10^{-5}$	10.3 ± 1.45	1.033

Table 7.1 Summary of cell monolayer residual data with residual signal amplitude, nuclear size distribution and maximum refractive index

Note that the relative refractive index contrast is much higher than one measured in single cell experiments. The reason is that contribution to the scattering by cell-media interface and other cell components is not included in interpretation of differential signal

amplitude. Even given these approximations, the reported values are still lower than some of those previously reported in the literature [5, 6].

The ϕ -differential method, described in section 5.4.2, has been applied to study scattering from HT29 cell monolayers. Signals in each individual ϕ -angle configuration are comparable to the ones detected at $\phi=45^\circ$ (Figure 7.16.a). The residual signal is on the level of 6×10^{-5} (Figure 7.16.b). System sensitivity limits are established at the level of 4×10^{-5} in background measurements and in 50 nm beads measurement (Figure 7.16.c-d). Therefore, most of the residual signal amplitude and all of the residual signal variations are below system sensitivity limits.

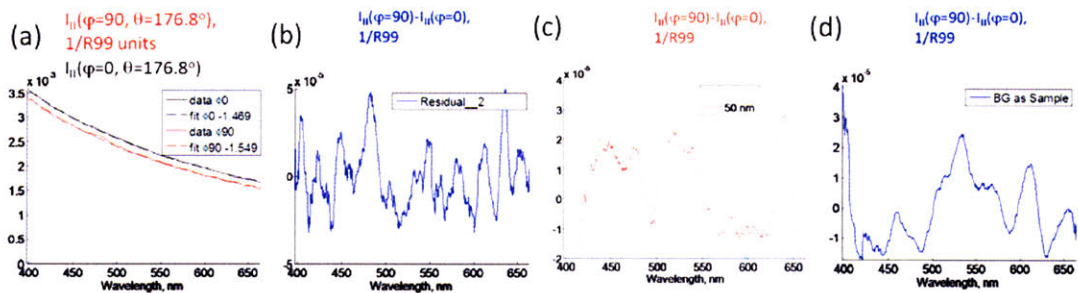


Figure 7.16 ϕ -differential signal from HT29 cell monolayer compared to system sensitivity a) Wavelength data at 176.8° for two azimuthal angles $\phi=90^\circ$ (red) and $\phi=0^\circ$ (red), power law fits to the data, scale $\times 10^{-3}$ b) ϕ -residual signal for HT29 cell monolayer data, scale $\times 10^{-5}$ c) ϕ -residual signal for 50 nm bead suspension, scale $\times 10^{-5}$ d) ϕ -residual signal for 50 nm bead suspension, scale $\times 10^{-5}$

To summarize, the nuclear signal does not make a significant and detectable contribution to backscattering of cell monolayers and cell suspensions. The next section is devoted to the interpretation of the main component in backscattering: smooth power law decay.

7.2.2 Measuring power law in backscattering of cell monolayers

The clearest spectral feature of the backscattering signals from the cell monolayer experiments is a power law decay of scattering intensity with wavelength $I(\lambda) \sim \lambda^{-\gamma}$. It has been detected in all the measurement configurations in the three different types of cell monolayers. The scattering intensity at $\phi=45$ follows power law behavior with three different exponents for three different cell types (Figure 7.17.a-c). Similarly, each individual azimuthal angle configuration in $\phi=0$ and $\phi=90$ has a spectrum that follows power law behavior (Figure 7.17.e-f). The variation of exponents between individual azimuthal components is smaller than the difference between different cell types.

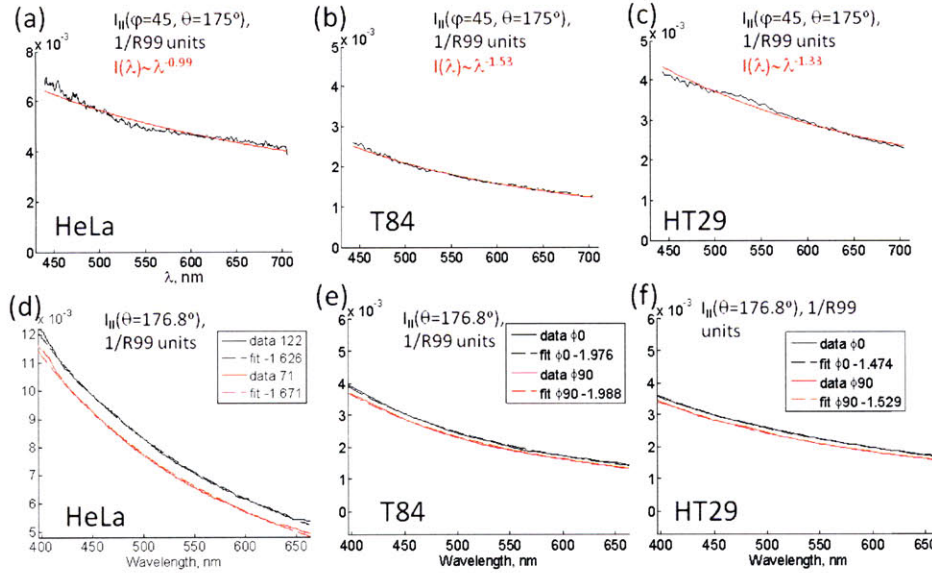


Figure 7.17 Analyzing wavelength spectra in backscattering, power law fits at $\phi=45^\circ$ (black – data, red – power law fit) a) HeLa b) T84 c) HT29 and $\phi=0^\circ, \phi=90^\circ$ (solid lines – data, dashed lines – fits) d) HeLa e) T84 f) HT29

Several measurements for each of the system configurations are summarized in Figure 7.18. The γ -values cluster for different cell monolayer types, with average values for HT29 and HeLa cells very close to each other, and T84 clearly separated from both. In $\phi=45$ experiments, the generated γ -distributions are 1.21 ± 0.08 (HT29), 1.27 ± 0.13 (HeLa), and 1.54 ± 0.1 (T84) (Figure 7.18.a). In the ϕ -azimuthal experiment, the following γ -distributions are observed: 1.47 ± 0.11 (HT29), 1.47 ± 0.2 (HeLa), 1.92 ± 0.19 (T84) (Figure 7.18.b). Relative to the mean value, the biggest variation is in the exponents of HeLa cell distributions. Although relative behavior of the extracted exponents is consistent with the degree of variation of the mean value, the absolute value has a shift of about 0.25-0.38 between $\phi=45$ and ϕ -differential measurements.

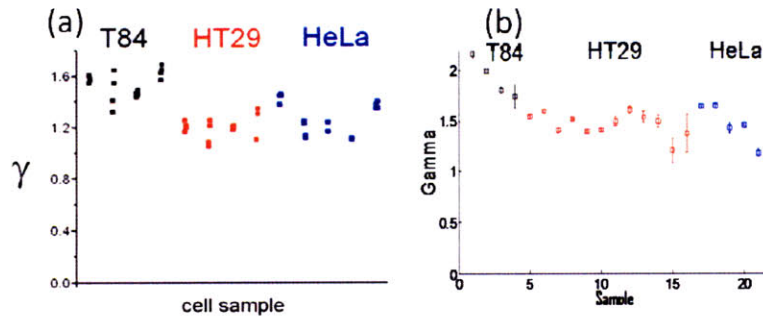


Figure 7.18 Summary of power law exponent values for light scattering measurements a) ϕ -azimuthal experiment power law exponents b) $\phi=45$ experiment power law exponents

One reason for the shift could be the presence of a DC component in $\phi=45^\circ$ data. DC component can be due to background or a real cell scattering signal. If a DC component is present, then the actual power law exponent will be lower than the true exponent. To illustrate this point real scattering data are taken for HT29 cell monolayers. Data are fit to power law in wavelength with exponent value of 1.57 (Figure 7.19.a, data 1). Then, a DC component with the amplitude of 7.7% and 23% of the original mean of the signal is added to the data (Figure 7.19.a, data 2 and 3). Again, data are fit to power law, and the exponent of power law fit decreases with the increase of the additional DC component from 1.57 to 1.46 to 1.27. Therefore, one has to be mindful of the possible DC contributions to the signal affecting the exponent of the power law decay. Moreover, the latest experiments in HT29 cell monolayers yield 1.51 ± 0.07 as the distribution of exponents, which is closer to the one measured in ϕ -differential system (Figure 7.19.b).

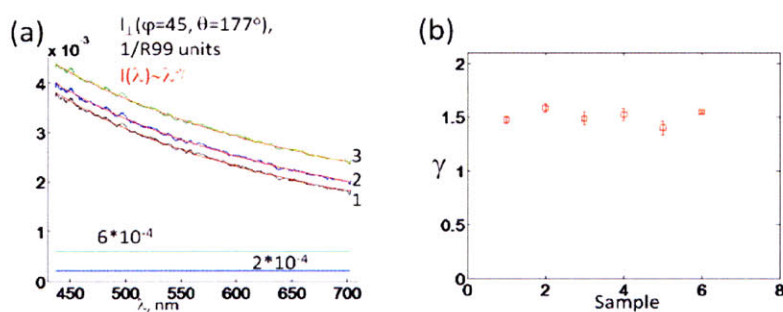


Figure 7.19 Sensitivity of power law exponent to DC-offset a) HT29 cell monolayer data at $\phi=45^\circ$ (black1 – original, blue2 - 7.7% offset, green3 – 23% offset) and power law fits (red) **b)** Summary of power law exponents for latest experiment with HT29 cell monolayer at $\phi=45^\circ$

Therefore, power law behavior in cell monolayer backscattering has been established. Observed cell monolayer exponents have a range between 0.9 and 2.1, but are sensitive to signal distortions. The next section presents various interpretations of the power law signals.

7.2.3 Modeling power law in backscattering

The overall goal of model development is to correlate measured scattering intensity with parameters related to cell/tissue morphology. Most of the theoretical work reported in this section was done by my colleagues Dr. Vadim Backman and Dr. Martin Hunter. The models were developed for the interpretation of the power laws observed in rat tissue experiments described in next chapter. The overall range of power law exponents observed in tissues is 0.4-2 and encompasses most of the range for cell monolayers. Since the models are

developed for single scattering of light, which dominates the signal in cell monolayers, these models should be directly applicable to the interpretation of cell monolayer scattering.

Interpretations of power law signals can be divided into two groups: discrete particle and continuous refractive index. The simplest discrete model is that of a single size sphere or a narrow Gaussian size distribution of spheres. For fixed values of relative refractive index contrast ($m=1.027$) and scattering angle ($\theta=180^\circ$), the scattering of a sphere depends on the ratio of wavelength to sphere diameter (see Chapter 4, Figure 7.20.a). For very large values of the ratio, the sphere behaves as a point particle with power law behavior in wavelength λ^{-4} . As value of the ratio decreases, the spectrum deviates from pure power law behavior until the first oscillation appears at the value of the ratio, approximately equal to 4. For our detection range of wavelengths (450 nm -710 nm), the diameter for the product peak value is between 110 and 180 nm. For example, single sphere data of three diameters 20 nm, 100 nm and 200 nm are compared to scattering from the HT29 cell monolayer with power law spectrum in wavelength $\gamma=1.473$ (Figure 7.20.b). Mie spectra are plotted in 1/R99 units and scaled to approximately match the intensity of the data. Spectra of 20 nm and 100 nm are fit to power law, with exponents of 3.96 and 2.9, while 200 nm spectrum has an obvious deviation from a power law. Therefore, single sphere does not model scattering from cells well.

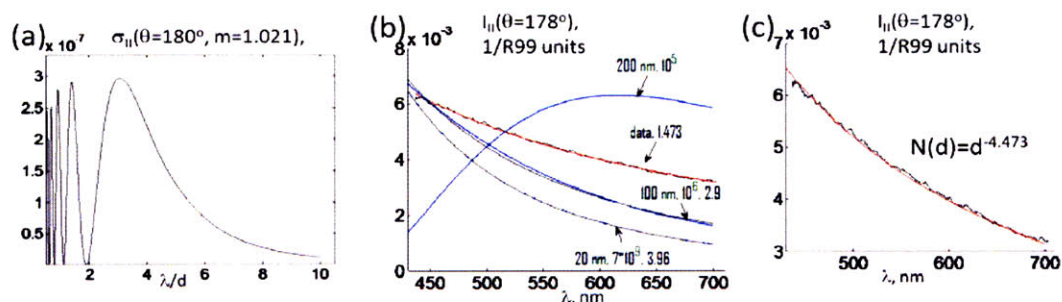


Figure 7.20 Discrete particle analysis of power laws in cell monolayers a) Universal curve of backscattering cross-section vs. ratio of wavelength to diameter b) HT29 cell monolayer data at $\theta=178^\circ$ (black), 20 nm sphere data, 100 nm sphere, 200 nm sphere (all blue), power law fits (red and black), second number is amplitude scaling (except for data), third parameter power law exponent, c) Wavelength spectrum HT29 cell monolayer data at $\theta=178^\circ$ (black) and power law fit (red)

Also a good check is to see that given the diameter and quantity of 100 nm spheres, whether their cumulative volume does not exceed the volume of the whole cell. Assuming average cell diameter at $18 \mu\text{m}$, the volume of the cell is $3.05 \times 10^3 \mu\text{m}^3$. The volume of 10^6 of 100 nm spheres is $525 \mu\text{m}^3$. Thus particles take $<17\%$ of cell volume, which is a reasonable number. At the same time, the shape of 100 nm bead scattering spectrum does not match the shape of the data.

If spheres of uniform size do not reproduce scattering data from the cell, it might be possible that a distribution of sizes would work. For example, the scattering data above can be reproduced by a power law size distribution of spheres $N(d) \sim d^{-4.473}$ (Figure 7.20.c). The formal basis of the connection is established by the work of Dr. Vadim Backman and Dr. Martin Hunter (not published). As in Chapter 6, scattering can be interpreted using Born approximation, assuming that phase delay (defined by $x^*|n-n_0|$) is small. For particle of 1 μm in size, wavelength of 550 nm, and index values of 1.337 and 1.3644, the phase delay is $0.1 \cdot \pi$, and therefore Born approximation is applicable. Through Born approximation, the scattering spectrum can be connected to the spatial distribution of the refractive index, which can be expressed as the two-point correlation function $C(\mathbf{r}) = \int \varepsilon(\mathbf{r}') \varepsilon(\mathbf{r}'+\mathbf{r}) d^3 \mathbf{r}'$ [7]:

$$C(\mathbf{r}) \propto \int I(\mathbf{q}) \exp(i\mathbf{q} \cdot \mathbf{r}) d^3 \mathbf{q} \quad (7.1)$$

The experimental finding that $I(\lambda) \sim \lambda^{-\gamma}$ implies that the above correlation function must also follow an inverse power law $C(r) \sim r^{1-\gamma}$. The correlation function can be related to the discrete particle size distribution [8]:

$$N(l) \propto \left. \frac{d}{dr} \left[\frac{1}{r} \frac{d^2 C(r)}{dr^2} \right] \right|_{r=l} \quad (7.2)$$

If the expression for correlation function extracted from scattering is substituted into Eq. 7.2, then the expression for particle size distribution becomes $N(l) \sim l^{-(3+\gamma)}$. Therefore, exponent of the size distribution $N(d) \sim d^{-\beta}$ is connected to the exponent of scattering spectrum intensity as $\beta = \gamma + 3$. Some care must be taken in considering the range of sphere diameters, d , which can be probed by this analysis. For an ideal experiment, where an angular scattering spectrum is recorded over an infinite range of wavelengths, the corresponding size distribution of scattering spheres extracted via Eq. 7.1 and Eq. 7.2 could range between $0 < d < \infty$. In practice, the finite wavelength range of spectra will limit this to a finite range of diameters, $d_{\min} < d < d_{\max}$. In order to assess the range of particle sizes whose size distribution can be inferred from light scattering spectra, one can model the spectra according to Mie theory with variable particle size limits. The β value of 4.5 is selected for size distribution (corresponds to $\gamma = 1.5$), index contrast is fixed at $m = 1.05$, and maximum diameter is set at 1 μm . By varying minimal diameter, the deviations from the relation between the exponent of the size distribution and spectral exponent are observed (deviations from straight line on log-

log plot in Figure 7.21.a). Spheres, as small as 25 nm, should be included into a distribution in order for relation to hold. Also, as exponent of size distribution is varied, the minimal diameter needed to preserve relation between exponents varies between 20 and 30 nm (Figure 7.21.b).

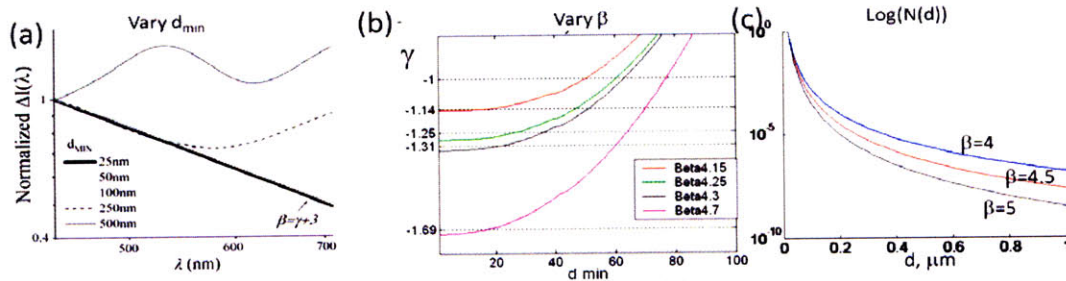


Figure 7.21 Properties of scattering from power law in size distribution a) Change in wavelength scattering spectrum with the change in lower cut-off diameter of power law distribution, $\beta=4.5$ for all spectra, log-log scale b) Asymptotic behavior of exponent of power law fit ($\gamma=\beta-3$) for different values of lower cut-off diameter for 4 values of β -exponent c) Change in relative particle weight in power law size distribution with decrease of exponent β

Given power law size distribution, relative contribution of larger scatterers is decreasing with increase of the power law exponent in scattering intensity. For example, three γ values of 1, 1.5 and 2 correspond to three β values of 4, 4.5 and 5. An increase in slope of inverse power law of size distribution means relative decrease of larger particle presence in a distribution (Figure 7.21.c).

Another representation of discrete particle analysis of scattering has been suggested in the studies by Foster *et al.* on side scattering from cell suspensions [9], and earlier in Wang *et al.* on measuring reduced scattering coefficient in soft tissues [10]. Foster's work can be directly related to current study, since angular light scattering of cell suspensions of EMT6 mouse cells was measured between 5 and 30 degrees at 633 nm. The data were fitted with combinations of two Gaussians, two exponentials or two log-normal size distributions of spheres with refractive index of the spheres at 1.4 and that of the media at 1.38. Authors claim that the products of each of the cumulative size distribution, which did fit scattering data by the total scattering cross-section, are very similar in shape. Using authors' parameters for size distributions, only two out of three data could be reproduced to give result similar to presented in the paper (Figure 7.22.a and b). The curve describing product value with respect to particle diameter is normalized to its maximum value. According to the result, side scattering is dominated by the scattering from particles between 2 and 4 μm in diameter with a smaller peak at very small particle diameters. Same size distributions are used to calculate backscattering spectra for the intensity-based experimental system, but generated spectra do

not follow power law like behavior characteristic of the cell monolayer results described in this thesis (Figure 7.22.c, compare blue and red curves to the green one). The above HT29 power law spectrum is taken as an example. The curves are normalized to the maximum cross-section value in order to compare shapes.

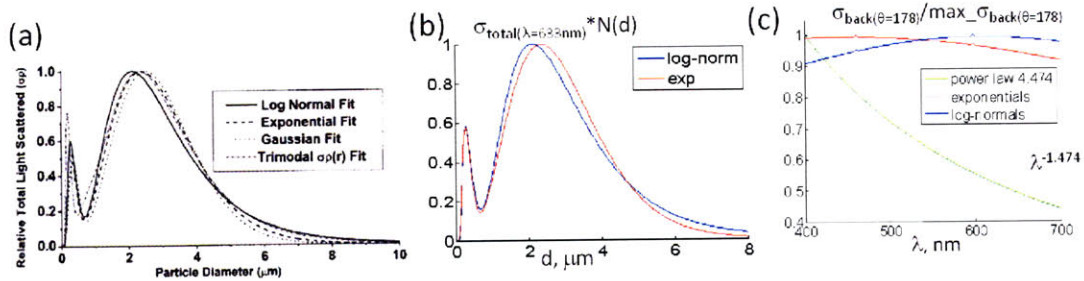


Figure 7.22 Compare backscattering spectra generated from Foster's paper [9] distributions and power law scattering from cell monolayer experiments a) (©OSA [9] Reproduced with permission) product of size distribution times total scattering cross-section from the paper b) Reproduced product of size distribution times total scattering cross-section using paper information c) Wavelength backscattering spectra at $\theta=178^\circ$ (ref. two exponential distributions – red, ref. two log-normal distributions – blue, power law size distribution –green)

Instead of creating product of total cross-section and size distribution, one can also create a product of backscattering cross-section. In backscattering cross-section of larger particles is reduced more compared to total scattering cross-section, than in the case of smaller scatterers (Figure 7.23.a). Therefore, if the same size distributions are used (Figure 7.23.b), product of the cross-section times the size distribution should shift to smaller diameters (Figure 7.23.c). The product does shift from major contribution to scattering of particles between 2 and 4 μm in diameter to major contributors in scattering from particles below 400 nm in diameter.

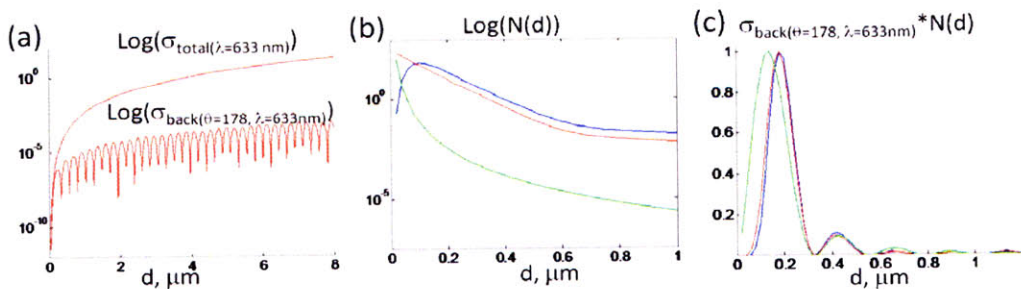


Figure 7.23 Product of size distributions and backscattering cross-section a) Scattering cross-section vs. particle diameter, compare total and backscattering, log scale b) Size distributions, 2-exponential (red), 2 log-normal (blue), power law distribution (green), log scale c) Product of backscattering cross-section at 633nm, $\theta=178^\circ$ and size distributions vs. particle diameter, power law distribution (green), 2 exponential (red), 2 log-normal (blue), normalized to maximum value

The major difference in the product values for power law distribution (green curve) and the Foster's group distributions (red and blue curves) is in the shift of the main peak from 180 nm for Foster's distributions to 140 nm for power law distribution, with both

distributions having more than 80% of backscattering signal between diameters of 2 and 400 nm.

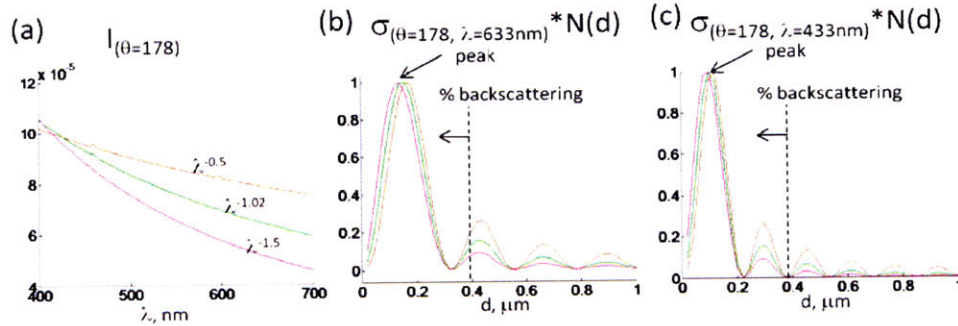


Figure 7.24 Properties of the cross-section distribution times backscattering cross-section a) Power law wavelength spectra for three values of exponent ($\gamma=0.5$ – brown, $\gamma=1.02$ – green, $\gamma=1.5$ - magenta) b) Product of power law size distributions and backscattering cross-section at 633 nm c) Product of power law size distributions and backscattering cross-section at 433 nm

Three different wavelength decays and corresponding power law size distributions are studied for the behavior of the product with change in parameters (Figure 7.24.a). The increase in power law exponent of scattering spectrum (from 0.5 to 1.5) is associated with the decrease of a major peak position (from 170 to 150 nm) and increase in the relative contribution to backscattering of 2-400 nm particles (from 64% to 91 %) (Figure 7.24.b). Since backscattering cross-section changes with wavelength, the behavior of the product is studied at another end-point wavelength of 433 nm (Figure 7.24.c). The peak positions are shifted and cover the range now (110 to 90 nm) with contribution of 2-400 nm (from 71% to 95%). Since peak position shift is due to change in cross-section, and backscattering cross-section is a function of the wavelength-to-diameter ratio, the peak position should be independent for the ratio.

Large cellular scatterers such as cell itself, nucleus or nucleoli have clearly defined borders. Therefore their size distribution can be characterized by an independent method. According to single cell index tomograms (such as the ones in Chapter 6), there are no structures inside the cell with clearly defined borders, which can be resolved by imaging techniques. Therefore, discrete particle picture does not have a good support in independent measurements. Per suggestion of Dr. Wonshik Choi, the interpretation of backscattering data is linked to interpretation of single cell scattering data in forward direction, given that Born approximation is valid. In single cell calculations, the Fourier transform of the object function generates scattering spectrum in Fourier space (see section 6.1). Scattering angle is correlated with a specific spatial frequency of the Fourier transform (Eq. 6.6). It is also shown in section

6.4, that change in wavelength can be treated in the same manner. Using well known formula for scattering momentum change between incident and scattered wave-vectors, $q = 2 * 2\pi * n_{\text{media}} / \lambda * \sin(\theta/2)$, and connection between spatial frequency and spatial dimension of $q * x = 2\pi$, the wavelength spectrum can be transformed into a relative contribution of various spatial components to the scattering spectrum. For example, for scattering angle of 180° degrees, index of the media of 1.337, in the wavelength range of 450 nm to 710 nm, x is changing between 160 and 260 nm. Therefore, wavelength scattering spectrum of cell monolayers can be transformed into relative contribution spectrum of Fourier components. As an example spectrum of HT29 cell monolayer is transformed into a spatial feature spectrum (Figure 7.25.a, b).

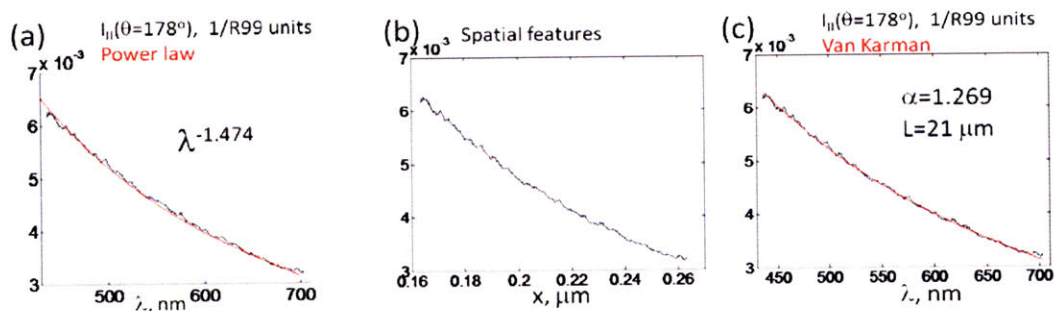


Figure 7.25 Continuous models of power law in backscattering a) HT29 wavelength backscattering (black) and power law fit (red) **b)** Spatial features spectrum according to Born approximation **c)** HT29 wavelength backscattering (black) and von Karman model fit (red)

Advantage of this interpretation compared to the discrete particle approach is that it does not rely on any assumptions about structure of the object, except for validity of Born approximation. Also, the range of diameters is within the range of diameters reported by discrete particle approach.

In an attempt to gain an insight about sub-cellular morphology using scattering data, my colleague Dr. Martin Hunter developed a model connecting light scattering of cells under Born approximation with continuous statistically fractal fluctuations of refractive index of sub-cellular structures [11]. Full description of the model is in the next chapter devoted to tissue data collection and interpretation. In brief, according to unified Born-van Karman model scattering of the sample follows

$$\Delta I(\lambda) \propto \lambda^{-4} \frac{1}{[1 + (4\pi L/\lambda)^2]^\alpha} \quad (7.3)$$

If the scattering data have a pure power law nature, then correlation length L becomes very large and scattering is described by a simplified equation of power law dependence in

wavelength $I(\lambda) \sim \lambda^{2\alpha-4}$. Same scattering data are interpreted using van Karman model (Figure 7.25.c). As predicted the correlation length, $21 \mu\text{m}$, is very large compare to wavelength of scattered light and extracted fractal exponent has value of 1.269. Therefore, all of the cell monolayer data following the power law dependence in wavelength with exponent γ can be converted into fractal exponent α , through $|\gamma| = |(4-\gamma)/2|$.

The validity of fractal model application is based on the previous work by Schmitt *et al.*, connecting van Karman function to refractive index fluctuations based on phase contrast images of cells [12]. The actual applicability of van Karman model can be now tested using refractive index information extracted from single cell measurements, but it is beyond the scope of this work.

References

- [1] Sokolov K, Drezek R, Gossage K, Richards-Kortum R. Reflectance spectroscopy with polarized light: is it sensitive to cellular and nuclear morphology. *Opt. Express* 1999;5:302.
- [2] Wu TT, Qu JY, Xu M. Unified Mie and fractal scattering by biological cells and subcellular structures. *Optics Letters* 2007;32:2324.
- [3] Barer R. Refractometry and Interferometry of Living Cells. *J. Opt. Soc. Am.* 1957;47:545.
- [4] Myakov A, Nieman L, Wicky L, Utzinger U, Richards-Kortum R, Sokolov K. Fiber optic probe for polarized reflectance spectroscopy in vivo: Design and performance. *Journal of Biomedical Optics* 2002;7:388.
- [5] Backman V, Gurjar R, Badizadegan K, Itzkan L, Dasari RR, Perelman LT, Feld MS. Polarized light scattering spectroscopy for quantitative measurement of epithelial cellular structures in situ. *Ieee Journal of Selected Topics in Quantum Electronics* 1999;5:1019.
- [6] Wax A, Yang C, Backman V, Badizadegan K, Boone CW, Dasari RR, Feld MS. Cellular Organization and Substructure Measured Using Angle-Resolved Low-Coherence Interferometry. *Biophysical Journal* 2002;82:2256.
- [7] Born M, Wolf E. *Principles of Optics*. Cambridge: Cambridge University Press, 2005.
- [8] Lembke U, Hoell A, Kranold R, Muller R, Schuppel W, Goerigk G, Gilles R, Wiedenmann A. Formation of magnetic nanocrystals in a glass ceramic studied by small-angle scattering. *Journal of Applied Physics* 1999;85:2279.
- [9] Wilson JD, Foster TH. Mie theory interpretations of light scattering from intact cells. *Optics Letters* 2005;30:2442.
- [10] Wang RKK. Modelling optical properties of soft tissue by fractal distribution of scatterers. *Journal of Modern Optics* 2000;47:103.
- [11] Hunter M, Backman V, Popescu G, Kalashnikov M, Boone CW, Wax A, Gopal V, Badizadegan K, Stoner GD, Feld MS. Tissue Self-Affinity and Polarized Light Scattering in the Born Approximation: A New Model for Precancer Detection. *Physical Review Letters* 2006;97:138102.
- [12] Schmitt JM, Kumar G. Turbulent nature of refractive-index variations in biological tissue. *Optics Letters* 1996;21:1310.

Chapter 8:

Experiments with rat esophagus tissue

This chapter summarizes the results of backscattering experiments in detecting pre-cancerous changes in rat esophagus tissue, which preceded studies described in previous chapters.

Natural extension of cell monolayer experiments would be tissue phantoms, such as multi-cell layer, or cell monolayer on highly diffusing substrate [1-4]. Such experiments would provide an insight into change of scattering behavior of cellular components and its relation to macroscopic structure, on the way of a gradual build-up to understanding of full tissue scattering. On the other hand, as samples change from large homogeneous microspheres to isolated cells to ensemble of cells, the amount of features in backscattering signals is decreasing from complex oscillatory spectrum to a smooth power law in wavelength, characterized only by two parameters: magnitude and power law exponent. Scattering in multi-cell type tissue may or may not undergo further degradation, since macroscopic properties start to affect light propagation, such as depth of penetration into tissues for various wavelengths.

Even if power law is observed in tissue scattering similar to cell monolayer results (see Chapter 7), the interpretation may not be straightforward. Dynamic range of power law exponents in cell monolayer experiments (Chapter 7) is between 0.9 and 2, and does not provide a large enough dynamic range for power laws to be unique on every occasion. Especially given that variation in exponents for a single cell type is on the level of 0.1-0.2 and variation within measurement is on the order of 0.03 of exponent units. Moreover, exponents above 3 are characteristic of single size small spheres, adding to non-uniqueness of interpretation. Therefore, the main questions to be addressed by rat esophagus tissue study are isolation of the cell-like single scattering and diagnostic power of extracted power law exponents.

First, polarization gating is described as a technique for extracting single-scattering from highly scattering sample. Differential signal is obtained from rat esophagus tissue data for normal, carcinogen-treated and chemopreventive treated rats. Exponents and amplitudes of the power law residual signal are compared and determined to be diagnostically

significant. Also scattering of isolated epithelia is measured and results are compared to whole tissue scattering, and connection between tissue thickness and scattering parameters is established. Feasibility of polarization gating is discussed again in the light of tissue results and some of the microsphere experiments. Finally, Born-von Karman model for tissue scattering is described and applied to data from rat esophagus.

8.1 Extracting power laws from rat esophagus

8.1.1 Polarization gating

Original concept of polarization gating has been developed by my colleagues Backman *et al.* [1]. In their study, tissue is modeled as a two-layer scatterer. Bottom layer of the connective tissue accounts for diffuse scattering and hemoglobin absorption. Top layer consists of singly scattering nuclei. Diffuse scattering randomizes direction of light propagation and scrambles polarization at the same time, while single-backscattering at $\theta=180^\circ$ preserves incident light polarization. In polarization gating, difference, ΔI , is taken between parallel, I_{\parallel} , and perpendicular, I_{\perp} , backscattering measurements to suppress depolarized component contribution and absorption. Scattering was measured for several sizes of microspheres 0.5-10 μm and a few refractive index contrasts. Authors measured differential signal ΔI as a function of optical density τ , which was varied with changes in physical thickness of the sample. Main conclusion is that differential signal ΔI saturates around $\tau=2$, where it has 95% percent of saturation value, as measured at $\tau=5$. If $\tau=1$, which corresponds to one scattering event per particle on average, 85% of ΔI at saturation level is detected. Then, authors conclude that even optical density of 1 had a majority of differential signal. Therefore, residual signal is not going to change if more scatterers are added.

Backman *et al.* proceeded with this method to two-layer tissue model of 5-10 μm beads with $\tau=1$ on top of mixture of human blood and highly scattering substrate. The residual signal was fit to Mie theory, and had only features of top layer beads. Polarization-gating technique was applied to measurement of three types of cell monolayers, including T84 cell monolayer used also in this thesis work. Residual signal is quoted as 1%-10% of total signal intensity. It was analyzed using lookup table approach for size distribution and relative refractive index contrast. Obtained results of $d=9.8 \mu\text{m}$, $\Delta d=1.5 \mu\text{m}$, and $n=1.04$ were within 0.1 μm of measured nuclear size distribution under the microscope. Finally, normal and cancerous colon tissues were studied. Residual spectra were again related to

nuclei distribution of $d=4.8 \mu\text{m}$, $\Delta d=0.4 \mu\text{m}$, and $n=1.035$ for normal and $d=9.75 \mu\text{m}$, $\Delta d=1.5 \mu\text{m}$, and $n=1.045$ for cancerous cells, although there was no comparison with an independent technique. Overall, polarization gating had been showing a great promise for detecting backscattering of cell nuclei in intact tissues, potentially allowing nuclear morphometry *in vivo*.

8.1.2 Polarized scattering measurements from rat tissues: Normal vs. NMBA-treated

Based on the work of Backman *et al.* described above, *ex vivo* rat esophagus tissue experiments were conducted with expectation of detecting nuclear signatures and relating them to pre-cancer development in rat tissue. Tissue model, sample preparation and characterization are described in detail in section 3.2. In short, rats were separated into four groups: control group, NMBA-group, to which carcinogen is administered, and NMBA-chemopreventive group. Small *ex vivo* sections of rat esophagus (6-10 mm thick and 1-2 cm long) were freshly excised and placed in a plastic dish with a buffer solution for a scattering measurement with epithelium side up. Also, chemical separation of epithelium was performed, and detached epithelium was examined individually. Measurements of backscattering were conducted on the instrument described in section 5.5.1, which measures backscattering with polarizations parallel and perpendicular to the incident beam. Backscattering was measured in the range of wavelengths 450-700 nm and angles 175° - 179.5° degrees. After scattering measurements, thin sections of measured sample areas were stained and graded under microscope.

There were a total of 5 rats in the control group, 5 rats in NMBA-treated group, 5 rats in chemopreventive control group and 5 rats in NMBA-chemopreventive group. There were two measurements per sample, except for one chemopreventive-group sample, where second measurement was not taken for technical reasons. Each polarization was measured in 7 minutes (total of 30 minutes/per tissue sample and 15 minutes/per epithelium sample). Some measurements were discarded due to experimental errors as described below.

Normalized scattering data at exact backscattering are presented on Figure 8.1 in units of $1/R99$ for a normal rat sample. The most significant feature in both spectra is the deep in the spectrum around 560 nm due to oxy-hemoglobin absorption and beginning of the 420 nm deep below 450 nm [5]. All blood vessels are localized below epithelium, therefore presence of hemoglobin points at the signal beyond the region of interest. Direct subtraction of parallel

and perpendicular signals does not completely remove hemoglobin absorption, even when R99 standard polarizability is taken into account (section 5.5.3) (Figure 8.1.b, red line). There may be an effect of imperfect system calibration or some sample-dependent signal. If perpendicular polarization data are scaled with a wavelength-independent scaling factor, a , then hemoglobin features are fully removed. Moreover, data exhibit power law behavior in scattering wavelength (Figure 8.1.c).

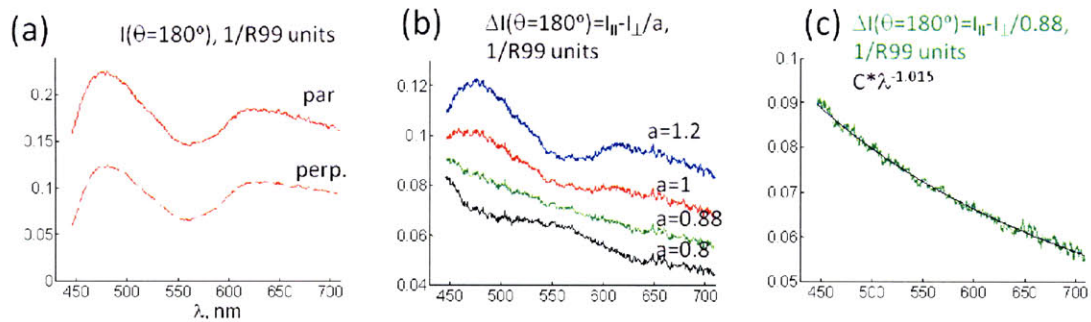


Figure 8.1 Extracting polarized residual in backscattering (a). Polarized signal from normal rat esophagus tissue, $I_{||}$ (solid line) and I_{\perp} (dashed) (b) Polarized residual signal for various values of correction parameter, a . (c) Polarized residual signal for $a=0.88$ (green) with power law fit in wavelength (black)

Note that the residual signal ΔI is on average 40% of the total parallel component and varies depending on the wavelength. Thus, rat tissue has a highly polarized scattering response in backscattering.

All of the samples normalized to fully remove hemoglobin feature are showing similar power law behavior. Therefore, procedure of scaling factor selection for best fit to power law was automated by my colleague Uzoma Orji. In this procedure, polarization gated signal, ΔI , is calculated for each value of parameter, a , between 1.3 and 0.4, fitted to power law, and the difference between power law fit and ΔI is taken. The value of scaling factor minimizing residual of the difference is then selected. The average value of α is 0.857, and it is independent of the tissue sample type (Figure 8.2).

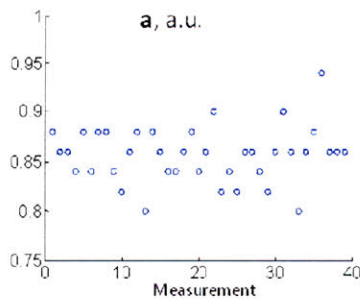


Figure 8.2 Tissue correction factor a vs. measurement number

8.2 Analysis of power laws in rat esophagus data

8.2.1 Power law exponent in wavelength of Normal vs. NMBA groups

Data for normal and NMBA rat groups with power law fits are summarized in Figure 8.3.a-b. One measurement per sample is shown for normal group data for figure clarity. All of the NMBA-treated rat measurement spectra are shown. There is a difference between normal and dysplastic samples in absolute signal amplitude and exponent of power law fits. Values of power law exponents are plotted within the 95% confidence limits with normal values distribution of $\gamma_{\text{normal}}=1.25\pm0.2$ and NMBA-treated values of $\gamma_{\text{dysplastic}}=0.72\pm0.22$ (Figure 8.3.c). Note, that two “normal” γ -values, circled out on the figured, are measured from NMBA-treated rat, which also appears normal in histopathology. The absolute amplitudes of the signals for all wavelength are compared at $\lambda=475$ nm, where hemoglobin contribution is minimized. The distributions of amplitude A-values are $A_{\text{normal}}=0.075\pm0.01$ and $A_{\text{dysplastic}}=0.101\pm0.06$ in units of 1/R99 (Figure 8.3.d).

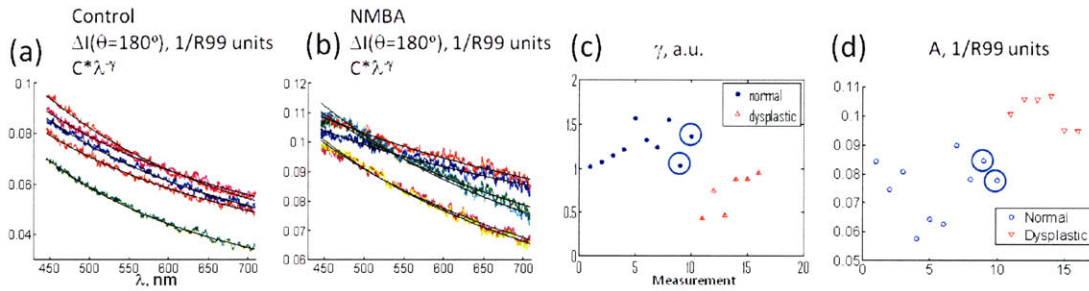


Figure 8.3 Analyzing power law in wavelength for Control and NMBA-treated groups a) Rat spectra with normal diagnosis (colored lines) and power law fits to them (black lines) b) Same for dysplastic rat spectra c) Summary for power law exponents for normal (blue) and dysplastic (red) rats. Circled are rats with normal diagnosis from NMBA-treated group. d) Summary of residual signal amplitudes at 475 nm

The statistical analysis of the data was done using two sided t-test, which checks correlation between the means of two normal distributions with unknown variances [6]. The difference in the means of γ -distributions and A-distributions for normal and dysplastic samples are both statistically significant with p value <0.001 and p value <0.0001 , respectively. Therefore, even a single wavelength measurement has enough information to separate normal and dysplastic samples in this small data set.

Contrary to expectations based on previous tissue studies, but in complete agreement with the previous chapters of this thesis, the oscillatory signature related to nuclei spectra is not observed in light scattering from rat tissues. In analogy to cell monolayer results, the

exponent values of spectral power laws can be converted into power laws of size distributions of Mie spheres, with exponents following $\beta=\gamma+3$ and diameter ranges of 25 – 1000 nm. Note that in comparison to cell monolayers, the ranges of normal rat data exponents of spectrum and size distribution are within cell monolayer range of exponents ($0.9<\gamma<2$), while dysplastic rats have lower values. The residual differences between ΔI and power law fit in wavelength are presented in Figure 8.4 for different rat samples. System sensitivity had not been evaluated to determine the degree of trust in this “residual” of residual data.

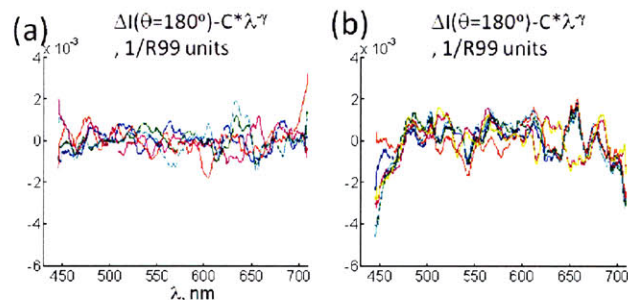


Figure 8.4 Difference between polarized residual spectra and power law fit a) Normal rat samples b) Dysplastic rat samples

Out of 20 tissue samples 4 samples are not analyzed due to experimental errors. One sample from normal group has epithelium smaller than incident beam diameter, hence has direct stroma contribution to the signal. One sample from chemopreventive control group was accidentally flipped (epithelium side down) during the experiment. One sample from NMBA-treated group has polyps in measurement areas. One sample of NMBA-chemopreventive group is disregarded since water was accidentally used in the experiment instead of the buffer solution.

8.2.2 Polarized scattering measurements from rat tissues: Chemopreventive control vs. NMBA-chemopreventive group

Same analysis is repeated to extract and analyze power law behavior in scattering spectra from chemopreventive data. First, power laws from curcumin control and NMBA-chemopreventive group spectra are extracted using hemoglobin suppression method Figure 8.5.a-b. The exponents and amplitudes of power laws are correlated with histology (Figure 8.5.c-d). Distributions of power law exponents are $\gamma_{\text{curcumin_normal}}=1.17\pm 0.22$ and $\gamma_{\text{curcumin_dysplastic}}=0.91\pm 0.14$. Distributions of amplitudes at 475 nm equal to $A_{\text{curcumin_normal}}=0.079\pm 0.01$ and $A_{\text{curcumin_dysplastic}}=0.089\pm 0.07$ in unites of 1/R99. There is one sample, in

NMBA-curcumin group (blue circle on the graphs), which showed up as normal in histological evaluation, but is closer to cancerous samples in spectroscopic parameters. One plausible explanation could be that histology probes only very thin section of tissue (see section 3.2.3), while spectroscopy surveys whole measurement volume. Therefore the dysplastic part of the sample could have been missed by histological section. Of course, there is no way to confirm, that it is not an experimental error in spectroscopic measurement.

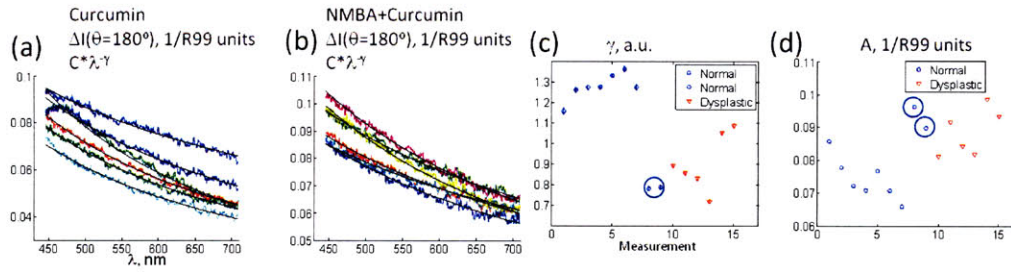


Figure 8 5 Analysis of power laws for Curcumin and NMBA-curcumin rats a) Power law fits to Curcumin group spectra (data –color spectra and fits – black) b) Same as a) for NMBA-curcumin group c) Summary of power law exponents. Circled sample of NMBA-curcumin group diagnosed as normal on histology (blue – normal diagnoses, red – dysplastic) d) Summary of residual spectra amplitudes values at 475 nm

The means of the normal and dysplastic exponents and normal and dysplastic amplitude distributions are again well separated with p-value of 0.015 and 0.04, respectively. If disputed sample is graded according to spectroscopy, then p-value drops to 0.0007 and 0.0035, respectively. Although abnormal samples of NMBA-curcumin group vs. NMBA group could not be separated histological, mean values of exponents' distributions ($\gamma_{\text{dysplastic}}=0.72\pm 0.22$ and $\gamma_{\text{curcumin_dysplastic}}=0.91\pm 0.14$) are separated with p-value of 3×10^{-5} . When mean values of exponents for control samples are compared ($\gamma_{\text{normal}}=1.25\pm 0.2$ and $\gamma_{\text{curcumin_normal}}=1.17\pm 0.22$), p-value increases to 0.41, which means that there is almost no separation in the means. Thus, there is statistically significant difference in exponents of dysplastic NMBA and NMBA-curcumin data, potentially pointing on effect of chemopreventive agent, although the data set is fairly small to say conclusively.

8.2.3 Polarized scattering measurements from rat tissues: Epithelial data

Detached epithelial data are used to study change in scattering signal with the higher structural localization. Due to nature of epithelium extraction (see section 3.2.3), which leads to some distortion of the epithelial layer, results should be considered on a qualitative, rather than quantitative basis. Twenty epithelial samples are measured, corresponding to 1 isolated epithelium for each tissue sample. Absence of hemoglobin peaks in the individual polarization measurements is an obvious difference between tissue and detached epithelium

data (Figure 8.6.a). The Hb signal is absent, since blood vessels are localized to the stroma. Detached epithelium is about 30%-70% of original tissue scattering depending on the wavelength (compare to Figure 8.1.a, same sample, but tissue). Significant perpendicular component (~40% of parallel) suggests that single scattering is generated only by part of the epithelium. Since there are no hemoglobin peaks to guide correction of polarization gating, two approaches can be used. First approach assumes that tissue correction is sample-dependent and related to stromal scattering. Therefore no correction is used in epithelial

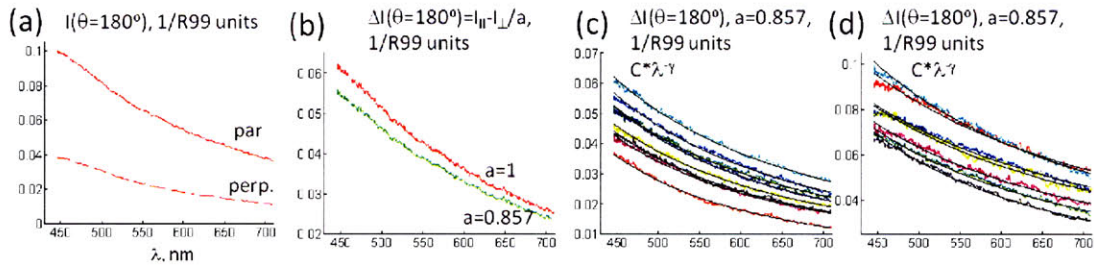


Figure 8.6 Analysis of power laws for epithelial data a) Intensity of individual polarization signals for epithelium, $I_{||}$ (solid line) and I_{\perp} (dashed) b) Residual signal using correction factor of 1 and 0.857s c) Normal epithelial residual data (colored lines) and power law fits (black lines) d) Same as c) for dysplastic epithelial residuals

samples. Second approach assumes correction to be sample-independent, in which case average correction factor for tissue ($a=0.857$) is used for all epithelial samples. Both approaches give fairly similar results with slight difference expressed in power law exponents (0.08-0.15 shift in γ -values) and signal amplitudes (Figure 8.6.b). The rest of the processing is done with the average tissue correction factor. Residual signal contribution increases to about 55%-60% of the parallel signal (almost independent of wavelength) compared to 40% in intact tissue (Figure 8.6.a-b compare to Figure 8.1.a-b).

In case of epithelium, some samples are excluded due to preparation errors. One normal and one curcumin group sample were bunched up during preparation and could not be laid out flat for experiment. One NMBA group sample had a papilloma in the center of the measurement area. Another NMBA sample did not cover the entire incident beam area. One NMBA-curcumin sample was accidentally placed in water instead of buffer solution similar to corresponding tissue sample case. The rest of the samples were processed according to average tissue correction factor of 0.857. Normal and curcumin control groups spectra are plotted together, and so are NMBA and NMBA-curcumin data (Figure 8.6.c-d).

Based on tissue results extracted parameters are split into three groups. Control and curcumin measurements, along with samples diagnosed as normal from two other groups, form group number one. Dysplastic NMBA and NMBA-curcumin samples are put into

separate groups (Figure 8.7.a-b). Average values for exponents are $\gamma_{\text{normal+curcumin}}=1.98\pm 0.19$, $\gamma_{\text{NMBA_dysplastic}}=1.36\pm 0.16$ and $\gamma_{\text{NMBA_curcumin_dysplastic}}=1.49\pm 0.19$ and amplitudes are $A_{\text{normal+curcumin}}=0.044\pm 0.008$, $A_{\text{NMBA_dysplastic}}=0.079\pm 0.01$ and $A_{\text{NMBA_curcumin_dysplastic}}=0.075\pm 0.012$. Red circle is the epithelium sample, for which the corresponding tissue sample was flipped during tissue measurement, but it is diagnosed as dysplastic in pathology. Blue circle, sample diagnosed normal with pathology, but has dysplastic exponent in tissue data, and seems to have similar result in epithelium data, therefore it is bundled together with dysplastic values.

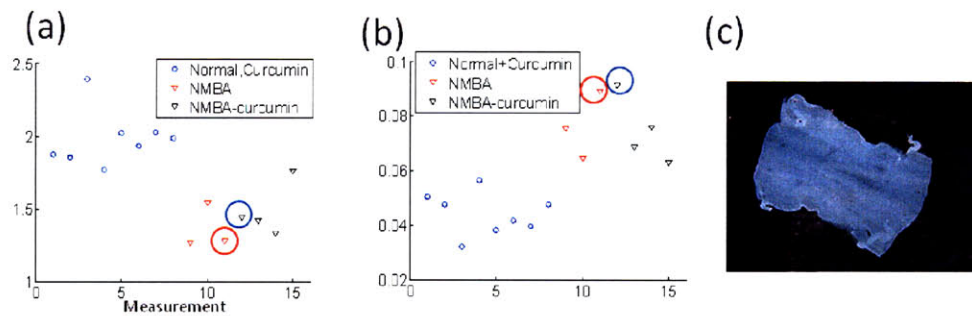


Figure 8.7 Analysis of power laws for epithelial data a) Summary of power law exponents for Normal (blue), NMBA-treated (red) and NMBA—curcumin (black) epithelial data. Blue circle – sample diagnosed normal; Red circle—no corresponding tissue **b)** Summary of signal amplitudes for epithelial data, same data groupings **c)** Photograph of a normal epithelial sample, showing significant optical thickness of the sample

Absolute values of power law exponents of epithelium are higher, than those measured in tissue. Even dysplastic values of epithelium are equal or higher than values for normal tissue. Relatively, values of power laws for normal and dysplastic epithelium data are well separated. Similarly to tissue, separation between normal and dysplastic epithelium is observed in amplitude data for 475 nm. There is almost no difference in exponents or amplitude between NMBA and NMBA-curcumin dysplastic epithelial samples.

Interestingly, there is a drop in amplitude of residual scattering signal between epithelial and whole tissue samples. The drop is 45% for normal epithelium (0.079 to 0.044) and about 15%-25% for dysplastic (1.1 or 0.9 to 0.079 or 0.075). This indicates that significant part of the polarized residual comes from the stroma, especially in the case of normal epithelium. On the other hand, in epithelial data there is a significant perpendicularly polarized component of about 40% from parallel. Although not calculated formally, epithelium optical density seems to be above 1 (Figure 8.7.c). According to polarization gating experiments described in section 8.1.1, the differential signal, ΔI , should saturate for

epithelium and almost not change for tissue, which is not the case. To resolve this seeming contradiction the bead experiments were conducted (see section 8.2.5).

8.2.4 Polarized scattering measurements from rat tissues: Correlating power law exponent and sample thickness

Tissue grading is compared against the value of average tissue thickness for 10 points, throughout histological section. Normal samples from all groups are clumped together, while NMBA and NMBA-curcumin dysplastic samples are grouped separately. Average thickness of normal tissue epithelium is $T_{\text{normal}}=90\pm 15 \mu\text{m}$ and $T_{\text{dysplastic}}=140.2\pm 34 \mu\text{m}$. Dysplastic and normal data are separated by values of full epithelium thickness, T (Figure 8.8.a).

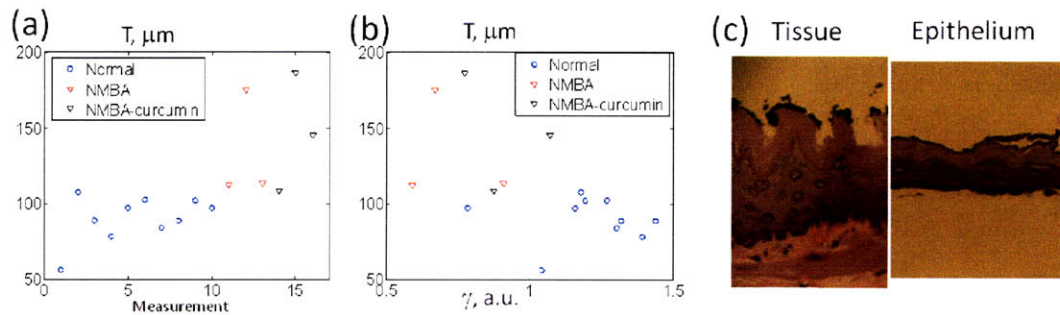


Figure 8.8 Effect of tissue thickness on diagnostics and power exponents **a)** Summary of tissue thicknesses, T , with respect to pathology Normal (blue), NMBA-treated (red) and NMBA—curcumin (black) epithelial data. **b)** Correlation of power law exponents to tissue thickness **c)** Sample histology at 20x of normal tissue and corresponding epithelium sample, demonstrating change in epithelial thickness

When thickness of epithelium is plotted against values of exponent, some degree of statistically significant correlation (p value < 0.015) can be observed (Figure 8.8.b). Therefore, sample thickness plays a role in determining exponent value. That conclusion is qualitatively confirmed with epithelial data. Epithelium is thinner than tissue sample from which it originates, partially due to loss of basal layer and partially due to stretching out of the epithelium after losing connection to stroma (Figure 8.8.c). The exponent values for epithelium from dysplastic samples, $\gamma_{\text{NMBA_dysplastic}}=1.36\pm 0.16$ (1.49 ± 0.16), are at the level of the normal tissue values, $\gamma_{\text{normal}}=1.25\pm 0.2$ (1.17 ± 0.22), while normal exponent values for epithelium, $\gamma_{\text{normal+curcumin}}=1.98\pm 0.19$, are well above all other values for tissue. These exponents are even greater, than most cell monolayer values (see section 7.2.3). As follows from Mie prediction in section 7.2.3, power law of a single size sphere can reasonably reproduce γ -values of 3 and above. Therefore, data are going to the limit, where they can be fit with a single size sphere as well as with other models. In the rat tissue, single size sphere

can have an interesting explanation, related to structure of keratin, the top layer of epithelium. Keratin consists of bundles of fibers with single filament dimension of 2.8 nm, second-order structure of 10 nm and third-order structure of 40 nm [7]. Therefore, all of keratin features are in a small particle regime with expected power laws between 3.8 and 4. This hypothesis has to be tested experimentally, as well as transition from microscopic to macroscopic effect of structure on scattering, which is not part of the presented work.

8.2.5 Testing polarization gating: Bead suspensions of varying optical density

There is a significant decrease in polarization-gated signal going from tissue to epithelium. At the same time, epithelium produces significant cross-polarized component and its optical density is at least one. In experiment by our colleagues establishing the feasibility of the polarization gating technique, residual signal intensity is studied depending on the optical density of the sample [1]. The optical density is varied by changing the thickness of the sample. Although experiments with various bead sizes and refractive index contrast values are mentioned, only one experiment is presented, where the value of differential signal intensity ΔI for 10 μm bead sample was averaged over wavelength range (Figure 8.9). Authors claim that differential signal has 85% of its saturation (saturation value measured at $\tau_{\text{saturation}}=6$) value at $\tau=1$ and 95% - at $\tau=2$. Therefore, most of polarized residual comes from optical density of 1.

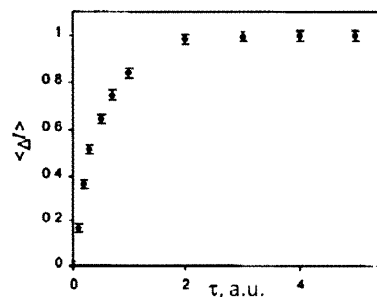


Figure 8.9 Polarized residual signal (averaged over 450-750 nm) vs. optical density. (Reproduced with permission from IEEE Journals ref [1])

The polarization gating test experiment is repeated with two single bead suspensions of 3 and 10 μm beads in water. The optical density is varied by varying the number density of beads, while keeping thickness of the sample constant. The values of optical density are calculated using Mie theory and double-checked with intensity measurements of laser beam

throughput ($I_{\text{scattered}}/I_{\text{incident}}=e^{-\tau}$). Optical density is varied between 0.1 and 6 for 10 μm sample and between 0.1 and 20 for 3 μm sample. The average values are calculated for the wavelength range of 450 to 750 nm (Figure 8.10.a-b). For 10 μm bead sample differential signal saturates at $\tau=6$ at the value of 0.26. At $\tau=1$, differential signal has 65% of saturation value and 82% of saturation value at $\tau=2$. Therefore, for 10 μm sample, optical density of 1 accounts only for 2/3 of the signal. For 3 μm sample, differential signal does not saturate even for very large values of $\tau=18$ with differential signal of 0.105. Differential signal at optical density of 1 is 38% of the signal at $\tau=18$ and 57% of density 2. Therefore, optical density saturation value changes with variation in bead diameter, increasing for smaller bead diameters. Along with that, the percentage of saturated signal at optical densities of 1 and 2 decreases with decrease in bead diameter.

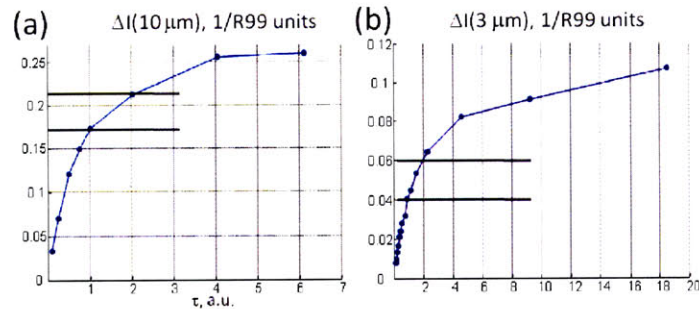


Figure 8 10 Measured polarized residual signal vs. optical density effect a) 10 μm data. Black lines mark signal at $\tau=1$ and $\tau=2$ c) 3 μm data. Black lines mark signal at $\tau=1$ and $\tau=2$

Therefore, polarization gating is more complicated to implement than it was thought originally and needs more thorough calibration. At the same time, two methods developed more recently in our laboratory may be more effective in removing polarized background. One, phi-differential method developed by my colleagues Dr. Chung-Chieh Yu and Condon Lau (described in section 5.2.2), has been applied to *ex vivo* tissue measurements [8]. An extension of this method into cross-polarized geometry has been developed by author of this thesis during experiments with cell monolayers (see section 7.1.6). Both of the above methods are advantageous to polarization gating, since they suppress diffuse scattering and small particle contribution to the light scattering signal. At the same time, one should remember that according to cell suspension and cell monolayer results of Chapter 7, none of the enhancement techniques give large particle signature, whether it is nuclei or whole cells.

8.3 Von Karman Analysis of power laws in rat esophagus

8.3.1 Von Karman-Born model

Another interpretation of rat spectra was developed by my colleague Dr. Martin Hunter, combining Born approximation for tissue scattering and fractal fluctuations of refractive index, described by von Karman correlation function [9]. Fractal behavior often characterizes the rule by which an object is created from smaller identical copies of itself [10]. Such property is called self-similarity and is characterized by a fractal dimension, D . For geometrical objects, fractal dimension is a non-integer analog of Euclidian dimension describing object's metrics. Fractal behavior can be also associated with variation in physical parameters. Since power law describes an increase of the value of a function with decrease of the parameter and is itself a self-similar curve, it is often associated with a fractal behavior of a described function.

Connection between fractal behavior and refractive index fluctuations in tissue has been established in the work by Schmitt and Kumar [11]. The phase contrast images of thin slices of mouse liver tissue were taken at various magnifications (Figure 8.11.a). Variations in gray scale intensity are converted to refractive index fluctuations. Fourier transform gives a power spectrum of refractive index fluctuations, and variation in magnification provides significant range of spatial frequencies (Figure 8.11.b).

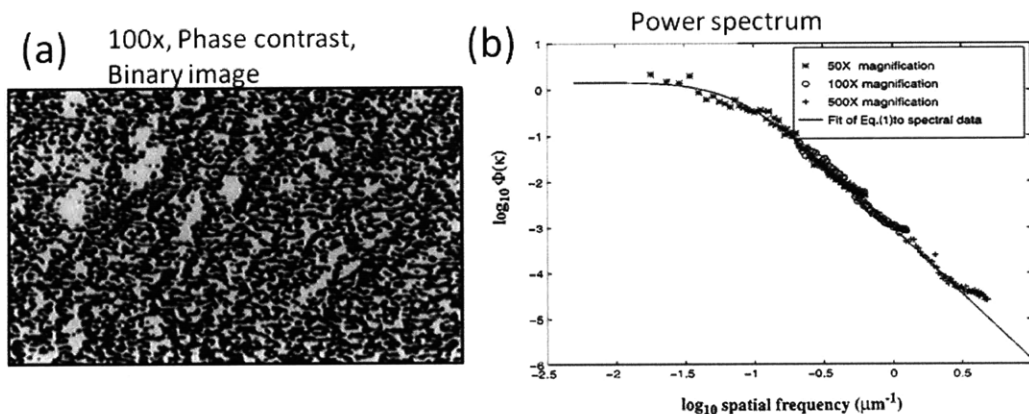


Figure 8.11 Power spectrum generation from phase contrast image a) (©OSA [11], Reproduced with permission) Phase contrast image of rat liver tissue section, binary scale, 100x b) (©OSA [11], Reproduced with permission) Spatial frequency power spectrum on a log-log scale, data for three magnifications (markers) plotted against von Karman function fit (solid line)

Power law behavior in power spectrum of spatial frequencies spans about 1.5 orders of magnitude until it levels off for very short spatial frequencies. Authors noted, that this behavior can be described by von Karman power spectrum function (©OSA [11]):

$$\Phi(\kappa) = \frac{4\pi \langle \delta n^2 \rangle L_o^2(m-1)}{(1 + \kappa^2 L_o^2)^m},$$

Parameter m is related to fractal dimension, through $D=1+1.5 \cdot D_E - m$, where D_E is Euclidean dimension [12]. L_o is an outer scale of fractal behavior and k - spatial frequency. For given images of tissue, spatial dimension is 2, fitted m equals 1.4, $L_o = 8 \mu\text{m}$, and corresponding fractal dimension equals to 2.6.

My colleague Dr. Martin Hunter has adapted von Karman model for interpretation of tissue scattering. Born approximation connects spatial frequencies and wavelength spectrum (see Chapter 6 or Chapter 7). The spatial frequency is connected to wavelength through $k=2\pi/\lambda$. Von Karman-based expression for wavelength spectrum takes the following form ($m=\alpha$):

$$\Delta I(\lambda) \propto \lambda^{-4} \frac{1}{[1 + (4\pi L/\lambda)^2]^\alpha} \quad (8.1)$$

If outer scale of fractal behavior L is much smaller than the wavelength, then von Karman spectral behavior is proportional to λ^{-4} . On the opposite end, if L is much bigger than wavelength, von Karman expression has fractal behavior of $\lambda^{-2\alpha-4}$. Value of fractal exponent of 1.64 is taken to from power law exponent average of NMBA-dysplastic rat tissue data of 0.72 and outer scale is assumed to be 200 nm. On a log-log scale, one can see the two limiting cases of fractal and Rayleigh behavior: much larger and much smaller than fractal outer scale (Figure 8.12.a).

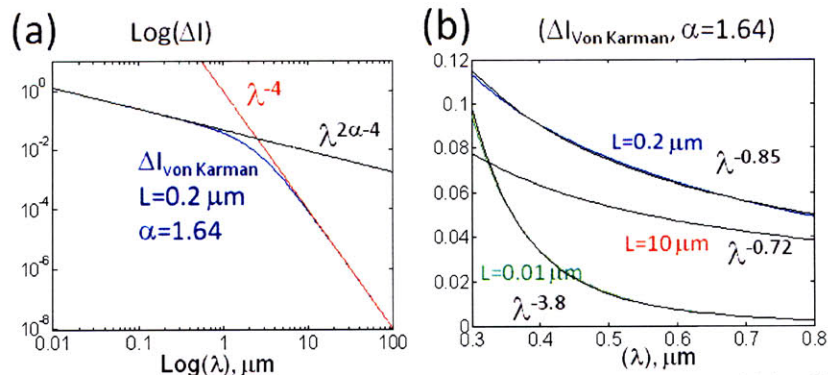


Figure 8.12 Limits of wavelength spectrum of von Karman function and parameter sensitivity a) Residual signal intensity vs. wavelength on log-log scale Von Karman curve (blue) vs. Fractal power law (black) vs. Rayleigh prediction (red). b) Backscattering spectrum of von Karman signal intensity vs. wavelength (300-800 nm). Fix fractal exponent at 1.64. Three values of fractal outer scale 0.01 μm (green data), 0.2 μm (blue) and 10 μm (red). Fit to power law in wavelength (black)

The spectrum in the wavelength range of interest is plotted for fractal outer scales of 10 nm, 200 nm and 10 and fixed fractal exponent of 1.64 (Figure 8.12.b). Data are plotted on a linear scale. Signals are scaled to see difference in shape and fitted to power law in wavelength. Notice, that instead of original power law value of 0.72, the power law exponent is 0.85. Also data deviate slightly from power law fit across wavelengths. The original exponent is extracted for outer scale much larger than wavelength. Outer scale much lower than wavelength leads to almost Rayleigh behavior with exponent of 3.8. Therefore, detecting only power law part of the curve, given finite instrument sensitivity, may not be sufficient for correct extraction of fractal exponent and outer scale.

8.3.2 Applying von Karman to rat data analysis

Originally, it was thought that von Karman function would help to explain deviations from power law behavior of the differential intensity ΔI in carcinogen-treated rats in shorter wavelength region through presence of outer scale of fractal behavior near lower wavelengths of detection (Figure 8.13.a). This would effectively indicate that for dysplastic samples the data are collected in the non-fractal regime. Upon examination of additional samples, deviations are observed in some samples of normal (curcumin control) rat group. While some of carcinogen-treated rats have excellent power law fits throughout the whole range (Figure 8.13.b-c). Moreover, these deviations can be a function of imperfect hemoglobin subtraction,

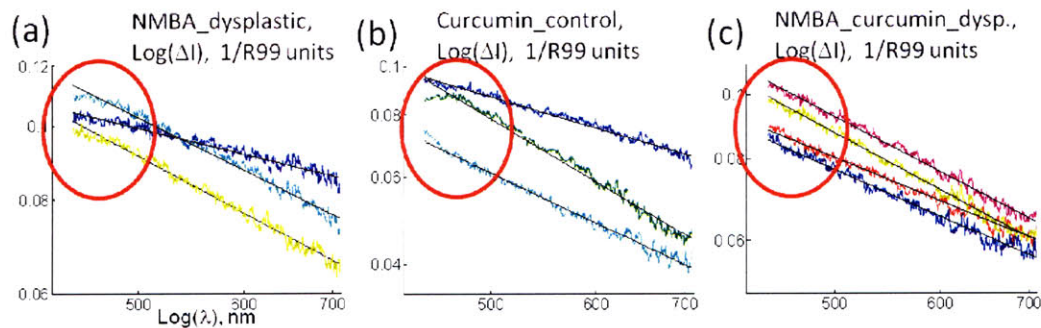


Figure 8.13 Deviation from power law spectra in residual signal vs. wavelength on a log-log scale a) NMBA dysplastic data (color data) vs. power law fits (black), red circle - deviation from power law b) same as a) for Curcumin-control group, selected spectra c) NMBA-curcumin dysplastic spectra. Red region – no deviation from power law behavior

given their location near 420 nm peak of hemoglobin absorption drop off, since beyond that area data show an excellent fit to power law. Also, if von Karman-Born scattering function is fit with power law, its deviation are fairly small compared to the whole signal amplitude, therefore, distinction between power law and von Karman function cannot be made clearly (see Figure 8.12.b above).

The range of spatial frequencies covered by our experimental methods according to Born approximation (see section 7.2.3) is between $1/0.16$ and $1/0.26 \mu\text{m}^{-1}$, which is much less than range needed to define fractal behavior. Therefore, the assumption has to be made, that tissue follows von Karman model. Then, in the case of pure power law behavior as observed in most of our rat samples, the outer scale of fractal behavior could not be observed and direct fitting to von Karman formula is not possible. Rather, a large value for fractal outer scale has to be assumed, and power law exponent would be converted directly to fractal exponent via $(4-\gamma)/2=\alpha$. Values of fractal exponents obtained from average power law exponents are $\alpha_{\text{dysplastic}}=1.64\pm 0.11$ (from $\gamma=0.72\pm 0.22$), $\alpha_{\text{curcumin_dysplastic}}=1.55\pm 0.07$, $\alpha_{\text{normal}}=1.375\pm 0.1$ and $\alpha_{\text{curcumin_normal}}=1.415\pm 0.11$.

Corresponding fractal dimension can only be extracted, if Euclidean dimension is known. Assuming, that cumulative phase through the measured area is responsible for scattering, scattering structures then become 2-dimensional with $D_E=2$. Then calculated values of fractal dimension become $D_{\text{dysplastic}}=2.36\pm 0.11$, $D_{\text{curcumin_dysplastic}}=2.45\pm 0.07$, $D_{\text{normal}}=2.625\pm 0.1$ and $D_{\text{curcumin_normal}}=2.585\pm 0.11$.

References

- [1] Backman V, Gurjar R, Badizadegan K, Itzkan L, Dasari RR, Perelman LT, Feld MS. Polarized light scattering spectroscopy for quantitative measurement of epithelial cellular structures in situ. *Ieee Journal of Selected Topics in Quantum Electronics* 1999;5:1019.
- [2] Sokolov K, Drezek R, Gossage K, Richards-Kortum R. Reflectance spectroscopy with polarized light: is it sensitive to cellular and nuclear morphology. *Opt. Express* 1999;5:302.
- [3] Sokolov K, Galvan J, Myakov A, Lacy A, Lotan R, Richards-Kortum R. Realistic three-dimensional epithelial tissue phantoms for biomedical optics. *Journal of Biomedical Optics* 2002;7:148.
- [4] Bartlett M, Huang G, Larcom L, Jiang HB. Measurement of particle size distribution in mammalian cells in vitro by use of polarized light spectroscopy. *Applied Optics* 2004;43:1296.
- [5] Hooper B, Splinter R. *An Introduction To Biomedical Optics*: Taylor & Francis Group, 2007.
- [6] P. Armitage, Geoffrey Berry, Matthews JNS. *Statistical methods in medical research* Blackwell Science, 2002.
- [7] Norlen L, Al-Amoudi A. Stratum Corneum Keratin Structure, Function, and Formation: The Cubic Rod-Packing and Membrane Templating Model. *J Investig Dermatol* 2004;123:715.
- [8] Yu CC, Lau C, Tunnell JW, Hunter M, Kalashnikov M, Fang-Yen C. Assessing epithelial cell nuclear morphology by using azimuthal light scattering spectroscopy. *Optics Letters* 2006;31:3119.

- [9] Hunter M, Backman V, Popescu G, Kalashnikov M, Boone CW, Wax A, Gopal V, Badizadegan K, Stoner GD, Feld MS. Tissue self-affinity and polarized light scattering in the Born approximation: A new model for precancer detection. *Physical Review Letters* 2006;97.
- [10] Mandelbrot B. *The Fractal Geometry of Nature*: Macmillan, 1982.
- [11] Schmitt JM, Kumar G. Turbulent nature of refractive-index variations in biological tissue. *Optics Letters* 1996;21:1310.
- [12] Sheppard CJR. Scattering by fractal surfaces with an outer scale. *Optics Communications* 1996;122:178.

Chapter 9:

Impact of the current work on modeling scattering from cells and tissues

In this chapter, the conclusions of four experimental chapters are summarized together in section 9.1. These conclusions are placed in the unified model of backscattering/forward scattering from cells near exact forward/backward directions in section 9.2. The model and experimental techniques are discussed from the point of view of previous works, with in-depth discussion of selected publications. Conclusions of the current work and future directions are discussed in section 9.3.

9.1 Summary of experimental methods, single cell, cell monolayer/suspension and rat tissue results

9.1.1 Experimental methods

Experimental methods are described in Chapter 5. Mie theory simulations are used extensively to develop and test signal enhancement techniques for various particle sizes and geometries with the focus on enhancing the signal from large particles, such as nuclei. An original polarization-gating method for single scattering extraction and suppression of diffuse background is used in rat tissue studies: $\Delta I = I_{\parallel}(\lambda, \theta=180^\circ) - I_{\perp}(\lambda, \theta=180^\circ)$ [1]. Polarization-gating does not differentiate between large and small particle single scattering. Therefore, if small particle single scattering dominates the backscattering, large particle signal may not be seen. For cell monolayer studies, two new methods are developed to enhance large particle signal over diffuse background and small particle signal.

The Φ -differential technique is developed by my colleagues Dr. Chung-Chieh Yu and Condon Lau: $\Delta I = I_{\parallel}(\lambda, \theta \sim 178^\circ, \varphi=90^\circ) - I_{\parallel}(\lambda, \theta \sim 178^\circ, \varphi=0^\circ)$ [2]. This method utilizes a non-uniform behavior of large particles in azimuthal angle φ , when for some scattering angles near backscattering, wavelength spectra at azimuthal angles, $\varphi=90^\circ$ and, $\varphi=0^\circ$ will be out of phase. At the same time, diffuse background or small particles are generally uniform in azimuthal angle. The drawback of this method is the sensitivity to exact θ -location of the out-of-phase signal, which requires collection of two azimuthal angles, wavelength spectra and a range of θ -angles requiring at least two-step collection on a 2D detector. Also, the DC

component of the signal is removed and on a large DC of small particle scattering and diffuse scattering signal, the oscillatory residual has to be detected.

To tackle some of these drawbacks in the course of this thesis work, the θ -differential technique was developed in cross-polarized geometry: $I = I_{\perp}(\lambda, \theta \neq 180^{\circ}, \varphi = 45^{\circ}) - I_{\perp}(\lambda, \theta = 180^{\circ}, \varphi = 45^{\circ})$. This technique is based on the fact that small particle cross-section is many orders of magnitude smaller in cross-polarized than in co-polarized geometries. Therefore, the small particle signal is naturally suppressed and subtraction of the scattering angle θ allows for suppression of diffuse scattering. As such, not only the AC, but also the DC component of the large particle signal is detected. All of the necessary measurements can be performed in a single shot on a 2D detector. The drawback of this method is that scattering cross-section drops faster with decrease in index-contrast for cross-polarized than for co-polarized geometries, and therefore signals may be too small to detect compared to the system sensitivity. Finally, in forward scattering, large particles generally dominate the signal in angle and wavelength, and therefore forward scattering geometry is used in cell suspension experiments. Optimal geometry for detecting small particle scattering is at $\varphi = 45^{\circ}$, where the large particle signal is minimized: $I_{\parallel}(\lambda, \theta < 180^{\circ}, \varphi = 45^{\circ})$. Given that the large particle distribution is extracted using any of the three enhancement methods described above, the large particle signal in backscattering can be subtracted to get the pure small particle signal.

Several light scattering instruments were built during the progress of this work. The first generation system is very similar to the original system built for polarization-gating experiments detecting a few degrees away from backscattering [3] and is used in rat tissue experiments. The latest version of the experimental system combines forward and backscattering geometries, controlled incident beam diameter/divergence, measures wavelength range of 430-710 nm, angular range of 0° - 10° in forward and 170° - 180° degrees in backscattering, and the system is adjustable to measure any azimuthal angle φ . The acquisition time has dropped from 5-10 minutes to 30-45 seconds for backscattering, while for forward scattering, measurement is on the order of 5 ms-200 ms.

System instrument response in wavelength is calibrated with atomic line sources, such as argon and mercury (20 nm, latest experimental system). Systems are calibrated using 5 μm , 10 μm and 50 nm polystyrene microsphere suspensions in water (for all methods) and index-matched oil (for forward scattering). The bead data are matched and show good agreement in shape for multiple angles/wavelengths with Mie theory using manual and

automated fitting, as well as a lookup table approach. From known bead suspension concentrations, the conversion factors are established between Mie theory (μm^2) and system normalization units of 1/R99 reflectance standard ($4 \cdot 10^{-6}$ for parallel/perpendicular and $4 \cdot 10^{-7}$). The angular range of the experimental systems is determined (0° - 10° , 170° - 180°) from bead measurements and the angular response is defined from measurement of unscattered beam on a detector (depending on the system 0.2° - 0.56°).

Enhancement methods were successfully tested in mixtures of large and small beads. System sensitivity is established through measuring variation in background measurements and small particle residual signal in enhancement techniques (0.5 - $2 \cdot 10^{-5}$ 1/R99 units for parallel and 1 - $1.5 \cdot 10^{-6}$ for perpendicular, see sections 7.1.6, 7.2.1).

Several experimental effects are taken into account in the latest system's design. Non-linear change in angular range depending on the refractive index of the media is taken into account using Snell's law and careful consideration of the experimental geometry. Forward scattering contribution to detected backscattering signal of the sample holder surface is dealt with by tilting the incident beam to a 45° incident angle to the sample surface. The mixing of two polarizations, while accessing various azimuthal angles φ by rotating two polarizers, is replaced with the rotation of a coherent imaging fiber bundle of an already analyzed image. Finally, the polarization response of the diffuse reflectance standard, which is actually found to be non-uniform in scattering angle θ , is taken into account by experimentally measuring the ratio between parallel and perpendicular polarizations.

9.1.2 Single cell results

Single cell experiments are described in Chapter 6. Single cell experiments are based on the measurement of 3D-index distributions of individual cells [4]. Tomogram modification allows for a selective enhancement of signals of nuclei, cell-border or other cellular components. The index-distribution can be transformed into scattering by virtue of Born, Rytov or Projection approximation. The cell border and nucleus contributions are compared for the HT29 cell. Born approximation enhances oscillatory component of the angular/wavelength spectrum, which, in the angles near exact forward scattering ($\theta < 10^\circ$), can be fit with Mie theory. The Mie theory fit is using the average refractive index of the cell/nucleus, which gives refractive index contrast of $m_{\text{cell}}=1.021$ and $m_{\text{nucleus}}=1.004$, and the cell dimension along the measurement axis. The applicability of Mie has been tested for non-spherical objects on ellipsoids, where each individual axis of the ellipsoid could be analyzed

using a Mie sphere of the diameter corresponding to the ellipsoidal projection onto the detection axis.

The nuclear scattering is about 1% of whole cell forward scattering and about 10% when the scattering of the cell border is index-matched with average cell index. Also, nuclear scattering is more sensitive to contributions from other sub-cellular (sub-nuclear) structures. These results are also obtained with Rytov approximation, which best reproduces the original scattering data, used to generate the tomogram. The current drawback of the single cell study is that index information is acquired only using $-60^\circ < \theta < 60^\circ$ forward scattering, and therefore backscattering information is not extracted.

9.1.3 Cell monolayer and cell suspension results

Cell monolayer and cell suspension results are presented in Chapter 7. Single cell results are bridged with multi-cellular results through experiments with cell suspensions. The major difference between cell suspension and single cell is in the distribution of cell diameters. Even for non-spherical cells, the distribution of cell diameters on a detection axis is Gaussian (see section 6.5). Therefore a single Gaussian Mie will correctly reproduce distribution of cell diameters. The width of the cell distribution within 15%-25% of the mean cell diameter leads to the loss of all oscillatory structure in the forward direction except for a single feature near 2° forward scattering.

Forward scattering of suspensions of HT29 and HeLa cells is measured in an intensity-based light scattering instrument. Data are collected for wavelength ranges of 430-700 nm and angular ranges of 0° - 10° . Only HeLa cell suspension measurements are analyzed, since HT29 cells show a significant degree of clumping even at smaller concentrations and cannot be analyzed with an isolated scatterer model. Mie fitting analysis of forward scattering is focused on simultaneous fitting of wavelength and angular spectra around the single oscillatory feature at 2° . Fits produce a diameter distribution of $d=16 \pm 1.6 \mu\text{m}$ and an index contrast value $m=1.027$.

In order to further confirm that the cell border is a major source of the signal, the medium index is raised by introducing protein solution to reduce index-contrast between the medium and the cell border to $m=1.005$. Mie predicted change in forward scattering signal agrees very well with the change in experimental signal, mainly in the disappearance of the oscillatory feature and the proportional increase in scattering near exact forward direction.

The same HeLa suspension samples with and without index-matching are measured in backscattering $\varphi=45^\circ$ geometry. If scattering signal is due to large particles, the expected drop of the signal intensity in two polarizations should be a factor of 30 for parallel and a factor of 3000 for perpendicular. The observed signal change is only a factor of 1.5 in parallel and 1.2 in perpendicular. The contribution of the cell border to backscattering can be calculated using results of forward scattering experiment. In parallel, Mie theory predicts a cell border scattering signal with the largest DC component near exact backscattering of $3-4 \times 10^{-5}$ and amplitude variations (2×10^{-6}). These variations are small compared to background variations of $0.5-2 \times 10^{-5}$, and the DC component is small compared to overall cell scattering of the order of 4×10^{-4} . In perpendicular, the largest signal observed at $\theta=178.8^\circ$ is of an amplitude of 4×10^{-6} , dropping below the system sensitivity level of 10^{-6} below 600 nm. Also, the background scattering signal on the order of 11×10^{-5} can be suppressed significantly by θ -differential technique to about 2×10^{-5} , which is still larger than the cell border signal. In conclusion, in backscattering, the cell border contribution to scattering signal is not observed above system sensitivity level, even in the most optimized geometry. Moreover, if the refractive index is reduced to the nuclear index contrast ($m=1.021$ to $m=1.004$), that will drop the amount of scattering signal (given the same number of nuclei as cells, and at any rate no more than twice the number) by at least an order of magnitude in parallel and three orders of magnitude in perpendicular. Also, smaller nuclear size compared to cell size will add to the decrease of the cross-section. Therefore, in order to see cell nuclei even in an index-matched experiment, the system sensitivity has to be increased by several orders of magnitude.

In experiments with HeLa, HT29 and T84 cell monolayers, the θ -differential technique at $\varphi=45^\circ$ is used to measure maximum possible amplitude of the large particle signal. Given that nuclear distribution is measured under a microscope, the maximum value of the refractive index contrast is calculated using Mie theory (see Table 9.1). Also, the system sensitivity is not established in that specific set of experiments.

Cell type	ΔI	Nuclear size, μm	Max(m)
T84	$<3 \times 10^{-6}$	14.6 ± 2.65	1.025
HT29	10^{-5}	12.8 ± 2.19	1.034
HeLa	$<2 \times 10^{-5}$	10.3 ± 1.45	1.033

Table 9.1 Summary of cell monolayer residual data with residual signal amplitude, nuclear size distribution and maximum refractive index

The φ -differential method is applied to scattering from HT29 cell monolayers. Residual signal is on the level of 6×10^{-5} . Using background measurement instead of a sample and 50 nm bead measurement, system sensitivity limits are established at the level of 4×10^{-5} . Therefore, most of the residual signal amplitude and all of the residual signal variations are below system sensitivity limits.

The rest of the work is focused on analysis of power laws in backscattering parallel geometry from cell monolayers $I(\lambda) \sim \lambda^{-\gamma}$. In two sets of experiments at different angles $\varphi = 45^\circ$ and $\varphi = 0^\circ, 90^\circ$ and different system alignments, backscattering power laws are measured in three types of cell monolayers: HT29, HeLa, and T84. The absolute values of the power law exponents have a shift between two measurements, but vary consistently between sample types: 1.21 ± 0.08 (HT29), 1.27 ± 0.13 (HeLa), 1.54 ± 0.1 (T84) and 1.47 ± 0.11 (HT29), 1.47 ± 0.2 (HeLa), 1.92 ± 0.19 (T84). The variation is due to potential presence of a DC component in original $\varphi = 45^\circ$ measurements, causing a shift in the absolute value of power law exponent.

The origin of the power law exponents is first analyzed using monodisperse and polydisperse Mie spheres. Monodisperse distribution can only reproduce exponents between 3 and 4. Polydisperse power law distribution of spherical sizes $N(d) \sim d^{-\beta}$ can reproduce the power law in scattering with exponent values equal to the ones observed in cells. Moreover, exponent values from size distribution and spectrum are related through $\beta = \gamma + 3$. In the limits of the Born approximation, this relation can be obtained analytically [5, 6]. Using results of work by Foster [7], the majority of cell backscattering is related to spheres between 10 nm and 500 nm in diameter, peaking between 100 and 200 nm. In another approach using Born approximation, scattering wavelengths can be directly related to spatial features detected in the object through scattering momentum [5]. The range of spatial features detected in intensity-based experiments is between 160 nm and 260 nm, similar to extracted dominant scatterers in discrete experiments. The continuous model has an advantage of not having any assumptions except for validity of the Born approximation. Finally, if the von-Karman model is assumed to be valid along with Born approximation [8], fractal dimension can be extracted for cell monolayers using $D = 4 - (4 - \gamma)/2$: 2.735 ± 0.055 (HT29), 2.735 ± 0.1 (HeLa), 2.96 ± 0.095 (T84).

9.1.4 Rat tissue experiments in backscattering

Rat tissue sample preparation and grading is discussed in Chapter 3, while all of the experimental results are in Chapter 8. Exact backscattering spectra are measured in normal, dysplastic rat tissue and extracted rat epithelium. Polarization-gating technique is applied to reduce diffuse scattering contribution. Correction factor for is used for perpendicular component to minimize the hemoglobin contribution. The correction factor is independent of the tissue type and equals 0.857 on average. Extracted power law spectra are fit for power law exponents with average values of: $\gamma_{\text{normal}}=1.25\pm0.2$, $\gamma_{\text{curcumin_normal}}=1.17\pm0.22$, $\gamma_{\text{dysplastic}}=0.72\pm0.22$, $\gamma_{\text{curcumin_dysplastic}}=0.91\pm0.14$. The difference between normal and dysplastic is statistically significant, as well as difference between dysplastic exponents with and without chemopreventive with p-values well below 0.05. Amplitudes of the residual signal at 475 nm both give a statistically significant difference between normal and dysplastic samples measurements, but are not separating dysplastic with and without chemopreventive.

Residual data from rat epithelia also follow power law behavior. Absolute values for epithelium exponents are higher than corresponding tissue exponents:
 $\gamma_{\text{normal+curcumin}}=1.98\pm0.19$, $\gamma_{\text{NMBA_dysplastic}}=1.36\pm0.16$ and $\gamma_{\text{NMBA_curcumin_dysplastic}}=1.49\pm0.19$. Means of normal and dysplastic samples are well separated, but dysplastic samples with and without chemopreventive are not separated anymore.

Correlation between tissue exponents and epithelium thickness change has been established. Tissue exponents seem to increase with the decrease of tissue thickness. Note that normal epithelium (exact thickness not measured) is the thinnest sample and has the highest exponent. Although exponents for epithelium are on a higher end of exponent values for cell monolayer, dysplastic tissue is below the lowest values of cell exponents. Therefore, at some limit, there is an interplay between microscopic parameters characterizing scattering from cells and macroscopic parameters characterizing scattering of the whole tissue. Much larger and consistent data sets are needed to study the functional dependence of this transition.

Contrary to expectation from previous polarization gating experiments [1], the residual signal amplitude changes significantly (25-40%) when comparing isolated epithelium vs. whole tissue. At the same time, the optical density of epithelium is above one, and epithelium has a strong perpendicular component. The degree of saturation is checked

with 10 and 3 μm microsphere suspensions, in which optical density is varied by changing density of the particles. Polarization-gated signal has 60% and 80% of saturation value for 10 μm at optical densities 1 and 2, compared to previously reported 85% and 95%. Polarization gated signal for 3 μm does not really saturate at optical density of 18, and has only 38% and 57% of that signal at optical densities 1 and 2. Therefore, polarization gating is really a function of the structure of the sample and not as universal, as was believed originally.

Finally, Born-von Karman model applicability to the analysis of tissue data is discussed. In the Born-von Karman model, fractal behavior is associated with the power law in the scattering spectrum and is described by a fractal exponent related to the spectral exponent through $(4-\gamma)/2=\alpha$. Deviation from fractal behavior into limiting Rayleigh behavior is controlled by outer scale of fractal behavior L . In order to truly determine von Karman behavior, a broad range of wavelength (i.e., spatial frequencies) should be studied, while the experimental range is $1/0.16 - 1/0.26 \mu\text{m}$. It was previously thought that dysplastic spectra exhibit deviations from power law behavior, thus showing an important piece of information, mainly the outer scale of fractal behavior [8]. Upon closer examination, normal tissue samples have this deviation, while a lot of dysplastic samples demonstrate excellent power law fits. Also, deviation has features of a larger of hemoglobin peaks, and can therefore be a data correction issue.

Therefore, von Karman model applicability for rat data interpretation cannot be established experimentally. And, if applied, all the data have to be assumed in a fractal regime with a large undetermined outer scale. Then fractal dimension of the sample can be calculated from the spectral exponent and assuming a certain dimensionality of scatterers:

$$D_{\text{dysplastic}}=2.36\pm 0.11, D_{\text{curcumin_dysplastic}}=2.45\pm 0.07, D_{\text{normal}}=2.625\pm 0.1 \text{ and} \\ D_{\text{curcumin_normal}}=2.585\pm 0.11.$$

9.2 Modeling scattering from cells. Comparison with previously published works

9.2.1 Unified model of scattering based on single cell and cell monolayer studies

An advantage of the presented work over all of the previous studies is in the true measurement of refractive index in single cells. Based on the above measurements, the

following view on scattering is applicable to HeLa, HT29 and T84 cell monolayer types, rat esophagus tissue, and possibly to other cell monolayer and tissue types.

Overall conclusions:

Forward scattering from cell suspensions in scattering angle of 0° - 10° is dominated by the cell-media interface and can be analyzed with single-distribution Mie and average index values. Forward scattering from cell monolayers in this angular range is also dominated by the cell-media interface, but could not be analyzed using Mie due to the featurelessness of the signal, coming from combined effect of the cell-media interface and sub-cellular structures. Backscattering of cell suspensions, cell monolayers and studied rat tissues at angles 170° - 180° and in visible range of wavelengths is dominated by power law scattering described by either a discrete distribution of small particles or a continuous distribution of small spatial features. The nucleus and the whole cell do not have a significant contribution to backscattering in all of the studies.

Detailed forward scattering conclusions:

1. Single cell forward scattering in the angles below 10° is dominated by the cell-media interface. Scattering can be modeled with Mie theory using average cell refractive index and cell size along the measurement axis even for non-spherical cells.
2. The nuclear signal is only 1% of forward scattering of a single cell due to very low nuclear index contrast.
3. If the cell border is matched, then the nucleus is about 10% of cell border signal, and it is buried in the combination of cell border and other sub-cellular components in a single cell.
4. Size distribution degrades oscillatory components in light scattering signals, which is relevant to any multi-cellular object.
5. Cell suspensions in forward scattering have at most one oscillatory feature around 2 - 3° forward scattering. This feature can be fit with an average index of cell and cell diameter distribution. The origin of the signal can be confirmed with index-matching experiments for cell-media interface.

Detailed backscattering conclusions:

1. The parallel component is at least 10 times larger than the perpendicular component in backscattering.

2. In angles 170-180 degrees, backscattering is dominated by the small particle signal in parallel and the no-cell border/no-nuclei signal is detected in parallel or perpendicular above the system sensitivity level.

2. The cell border signal (from cell suspension experiments in backscattering) is only a few percent of the total signal detected and below or near system sensitivity level, even when the θ -differential method is applied. For nuclei, given smaller size and refractive index contrast, system sensitivity has to be improved by a few orders of magnitude, and still it may be hard to extract on a background of all other signals.

3. The Φ -differential technique does not show any large particle contribution to the cell monolayer signal above system sensitivity.

4. θ -differential backscattering measurements can be used to set limits on the maximum refractive index contrast of the nuclei, if nuclei are considered the dominant scatterers.

5. Cell monolayer backscattering can be well fit by a power law in wavelength.

6. Extracted power law exponents range between 0.9 and 2, and are sensitive to DC off-sets in the data .

7. The true morphological structure responsible for power law behavior has not been found, and therefore differences in power laws between cell types could not be explained.

8. Given 7, discrete and continuous models are suggested explaining origins of power law behavior $I(\lambda) \sim \lambda^{-\gamma}$:

a. Power law size distribution of Mie spheres $N(d) \sim d^{-\beta}$. In the limits of Born [1] approximation, can be shown analytically, that $\beta = \gamma + 3$ Power law size distribution times backscattering cross-section gives dominant scatterer between 100 and 200 nm.

b. In the limits of Born approximation, the wavelength of scattering spectra can be converted to detected spatial frequencies of the object. 430-710 nm correspond to the spatial frequency range of $1/0.16 - 1/0.26 \mu\text{m}^{-1}$ or structural features between 160 and 260 nm.

c. Assuming fractal behavior, without enough spatial frequency range to prove it experimentally, fractal dimension can be extracted from exponents power laws $D = 4 - (4 - \gamma)/2$.

Detailed tissue backscattering conclusions:

1. Power laws are detected in polarized cell residual signals after removal of diffuse scattering and absorption.

2. Power law exponents range between 0.4 for dysplastic tissue and 2.3 for normal epithelium without the stroma.

3. Power law exponents of tissue differentiate between normal and dysplastic tissue, and power laws exponents of epithelium differentiate between normal and dysplastic epithelial samples.

4. The same analysis can be applied as for power laws in cell monolayers. Also, tissue has much more complicated structure: for example, power law exponents correlate with thickness of the sample, with the highest exponents for the thinnest sample of normal epithelium.

9.2.2 Other works with HT29, HeLa and T84 cell monolayers

There are only five studies of light scattering from HT29, T84 and HeLa cell monolayers focused on studying cellular morphology [1, 3, 9-11]. Light scattering from HeLa cell suspension is measured for scattering angles between 2.5° and 25° at wavelength 632 nm [11]. Authors report a smooth featureless decay of scattering signal over three orders of magnitude and failed to analyze the data due to lack of structure. According to our data in HeLa cell suspension, the oscillatory feature is most pronounced at 2° at 633 nm, followed by smooth decay up to 10° , which agrees quite nicely with the study above.

Backscattering of HT29 cell monolayer has been measured using an interferometry-based light scattering system with a coherence length of $14.3 \mu\text{m}$, collected angular range of 180° - 162.5° , 0.45 mm beam diameter (at least a few hundred cells are detected) and wavelength of 845 nm [9]. After removal of slowly varying polynomial component, the rest of the signal (about 25-40% of total signal) has a clear oscillatory pattern. This oscillatory pattern is fit with Mie theory and the best fit parameters are $m=1.066$ ($n_{\text{nuclei}}=1.046$, $n_{\text{cytoplasm}}=1.37$) and Gaussian size distribution for diameters of $d=9.9 \pm 0.6 \mu\text{m}$ (standard deviation of $0.69 \mu\text{m}$). The distribution agrees quite well with the microscopy measurement of $d=10.6 \pm 0.4 \mu\text{m}$ (standard deviation of $0.6 \mu\text{m}$).

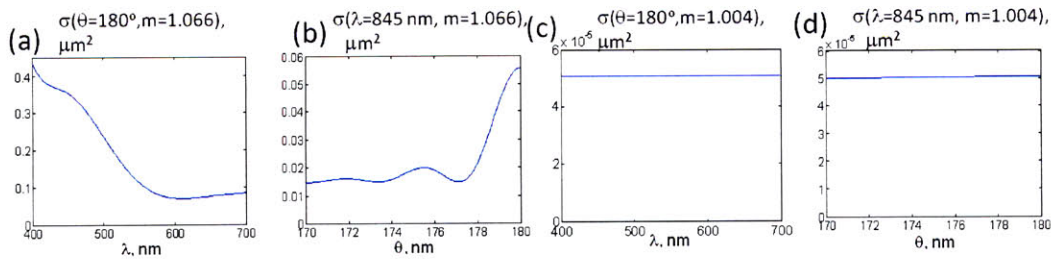


Figure 9.1 Mie predictions for backscattering of HT29 cells **a)** Wavelength prediction, from interferometry reference [9] using size distribution and refractive index contrast from the reference **b)** Angular spectra with same set of parameters **c)** Wavelength prediction based on reference size distribution and single cell measured refractive index contrast **d)** Angular spectra with same set of parameters

The refractive index is one of the fit parameters, and the reported nuclear index of 1.46 is extremely high compared to the values measured in single cell studies of 1.3744. At the same time, the cytoplasmic index is lower than in single cell studies: 1.37 vs. 1.38. Wavelength and angular spectra for reported nuclear size distribution are generated using the fitted refractive index vs. the refractive index from single cell data (Figure 9.1.a-b vs. c-d). The ranges relevant for intensity-based measurements are considered. Cross-sections drop by approximately 3 orders of magnitude and lower index contrast spectra have little to no AC component of spectral variations. Note that from intensity-based HT29 cell monolayer measurements, no large particle component is detected above system sensitivity level (compared to 25%-40% of only AC component), and a limit on the possible value of HT29 nuclei index contrast is imposed at $m < 1.034$. Therefore, knowledge of the correct refractive index distribution can make the difference between correct and incorrect interpretation of the data. From our predictions, the nuclear signal in backscattering should not be observed.

In another polarization gating experiment, a T84 cell monolayer is placed on top of a diffusive substrate [1]. Polarized residual signal is measured at the level of 0.04-0.06 of 1/R99 units and is quoted at 1-10% of total scattering signal. The polarized signal is fit to the nuclear size distribution of $d=9.8 \mu\text{m}$, $\Delta d=1.5 \mu\text{m}$ and $m=1.04$. Numbers are claimed to have good agreement with morphometry. Authors do not provide measurements for cell monolayers alone, which will be the logical step before measuring cell monolayer on top of a highly scattering standard. For comparison with presented work, an assumption is made that the signal for polarized residual is similar to measuring the cell monolayer by itself. The absolute signal value of the above residual signal is about an order of magnitude higher than observed in the cell monolayer work described in Chapter 7. Moreover, in cell monolayer data, no large particle signal is observed at the signal levels below 10^{-4} in 1/R99 units, which is below 5% of total single scattering component. Finally, the refractive index contrast limit

for nuclei is set below $m < 1.025$ by intensity-based measurements, and given HT29 index measurements in single cell and cell suspensions, may be much lower than that. One possible explanation could be that somehow additional scattering is present due to substrate reflectance. For example, forward scattering is detected along with backscattering as described in work by Drezek *et al.* [12]. Although, even in the case of forward scattering, according to single cell studies, a larger part of the signal is expected from the cell border and other sub-cellular components, and only about 10% from the nuclei.

The same results for nuclei detection of T84 cell scattering at exact backscattering are effectively repeated in another paper [3]. Also, the author of the thesis was amongst the paper authors, and some of the concepts behind conclusions were not clearly realized by him. This specific study makes an attempt on reporting small particle enhancement over large particles

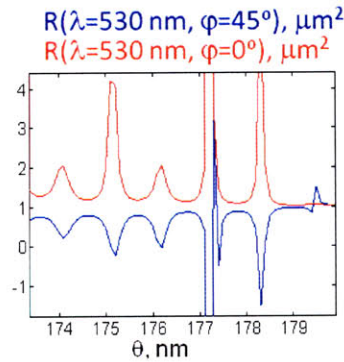


Figure 9.2 Enhancement ratio for ΔI of 22 and 0.4 μm for two values of azimuthal angle $\varphi=0^\circ, 45^\circ$

for a residual signal at $\varphi=45^\circ$. The claim is that polarization-gated signal for large particles, $\Delta I(22 \mu\text{m})$ is minimized at this azimuthal angle compared to $\Delta I(0.4 \mu\text{m})$. However, the actual ratio of reported Mie calculations is for parallel, and not for polarization-gated signal. If the polarization-gated signals are actually compared, there is no difference between the ratio at $\varphi=45$ and $\varphi=0$, for example, due to presence of a large perpendicular component of 22 μm beads (Figure 9.2).

The actual number of large particles is not known, but small and large polystyrene microspheres are assumed to have same optical density. Therefore, the actual ratio between signals has the following form:

$$R = \left\{ \frac{\Delta\sigma(22 \mu\text{m}) \cdot \sigma_{\text{total}}(0.4 \mu\text{m}) / \sigma_{\text{total}}(22 \mu\text{m}) + \Delta\sigma(0.4 \mu\text{m})}{\Delta\sigma(22 \mu\text{m}) \cdot \sigma_{\text{total}}(0.4 \mu\text{m}) / \sigma_{\text{total}}(22 \mu\text{m})} \right\} \quad (9.1)$$

The absolute value of the ratio does not have much meaning, since the relative number of particles is not known. Instead, ratios for the two azimuthal angles should be compared. The negative values of the ratio are due to perpendicular signal being larger than the parallel for 22 μm data, which only happens at $\varphi=45$. Overall, the ratio at $\varphi=0$ is even higher than the ratio at $\varphi=45^\circ$. Therefore, the claim about specific enhancement of small scatterers in T84 cell monolayer in polarization-gated signal at $\varphi=45^\circ$ is not correct.

The last study on T84 cell backscattering is conducted using Fourier-domain low-coherence interferometry [10]. Authors assume that the scattered field from the front of the nuclei will interfere either constructively or destructively with that from the rear of the nuclei, given an additional signal on top reference signal. It is not clear why at this point, the authors neglect the contribution of the cell-media interface, which will have larger effect than the nuclei. Similar to the projection approximation in single cell studies, the total phase delayed through the sample is considered equal to $2*n*d$. The authors convert a peak of the correlation function at a round trip path of 19.15 μm into nuclear longitudinal diameter of 6.86 μm using the refractive index of the nuclei $n=1.395$. Note that knowledge of the refractive index is the key piece of information allowing for a specific size assignment, but the refractive index is not measured. Therefore, the assignment of a scattering signal to nuclei seems to be rather arbitrary despite a good agreement between morphometry and nuclear diameter measurements.

As an intermediate conclusion, the knowledge of refractive index distribution is the key to making realistic predictions of absolute and relative amplitude contributions of whole cells, nuclei and sub-cellular components. Comparing current knowledge of the refractive index values and results of the experiments presented in this thesis, along with the way published results are obtained, claims of observing nuclear contributions in backscattering signals seem to be doubtful.

9.2.3 Other cell monolayer/suspension scattering studies

In a few other studies, nuclear scattering signals are reported from direct measurements of isolated cell monolayers and cell suspensions. All these works are based on the assumption about refractive index values in cells, specifically, a large refractive index contrast of nuclei is assumed and that the index of nuclei is larger than that of the cytoplasm. In one of the early scattering papers [11], the forward scattering of CHO (Chinese hamster ovary) cell suspensions is analyzed, assuming a refractive index of nuclei of 1.39 and

cytoplasm of 1.372. The authors conclude, that scattering between 2.5° and 12.5° can be well fit with a homogeneous sphere model (also the nuclear size is used, not cells). Authors of Fourier interferometric light scattering measurements conduct scattering measurements of nuclei in a MCF7 breast cell line and detect a distribution of nuclei dominating the whole scattering signal with refractive index of 1.42 over media index of 1.34, and extracted size distribution of $d=9.51 \mu\text{m}$, $\Delta d=0.34 \mu\text{m}$, that well reproduces measured nuclear distribution of 70 cells [13].

Several studies report either the combination of nuclear/whole cell and small particle signals or just small particle signal from cell monolayers/suspensions. In the extensive study of SiHa cell suspensions [14, 15], the forward-to-side-to-backscattering ($1.1^\circ < \theta < 165^\circ$, $400 \text{ nm} < \lambda < 700 \text{ nm}$) is measured. An interesting experimental system is developed in a previous publication, where goniometry-based fiber-detection light scattering instrument has delivery and collection submerged into the cell media [16]. Scattering data are analyzed using a combined Mie model of large particles (whole cells and nuclei) and small particles, described by a fractal distribution of Mie spheres [14, 15, 17]. Authors detect scattering over a very large dynamic range by changing integration time from 10 ms to 30s. Oscillatory structure is reported for data below 10° from exact forward direction in wavelength. Angular spectrum plotted on a log scale does not show any oscillatory structure, which is possibly due to the very large range of angles. The structure below 10° is analyzed with a Mie theory model for large scatterers, where scattering comes from the nucleus and the whole cell. Size distribution of the nucleus and cells are measured independently, and therefore the fitting parameters are indexes of the nucleus and cell. The authors find that the nuclei have an index of ~ 1.39 , while the cell has an index of 1.367. Consequently, authors find that about 50% of the scattering is due to cell nuclei in the range of 1° - 10° . This is in disagreement with the single cell study, which determines a nuclear scattering contribution of $\sim 1\%$ in case of cell suspensions due to low nuclear index contrast. The authors attribute scattering from angles above 20° to a fractal model of refractive index fluctuations, which effectively explains the smooth behavior of scattering index in this range, and complements the behavior near exact backscattering observed in the cell monolayer experiments of this thesis work. The discrepancy in the spectral interpretation of the nuclear/cellular contribution can now be directly resolved by measuring the refractive index distribution in SiHa cells (not a part of this thesis work), similar to study of HT29 single cell scattering [18, 19]. Also, tangential evidence that the refractive index of nuclei is not determined correctly, is in the

phase contrast of SiHa cells presented in ref. [12], which shows a lighter nucleus compared to the cytoplasm intensity of phase contrast variations. The second question is about the validity of the fractal model, which is not proven by an independent measurement, but rather a theoretical abstract describing an experimental curve.

Backscattering ($\theta \sim 170\text{-}180^\circ$, λ - 450–700 nm) is measured from a settled suspension of about 2×10^5 cells of primary human foreskin keratinocytes (HFK) and an HPV-infected human keratinocyte cell line [20]. When polarized-gating is applied, the residual signal follows power law behavior in wavelength. The amplitude of the power law is on the order of 10^{-2} of $1/R99$ units. The residuals in wavelength are fit to power law with exponents of 1.62 for HFK and 1.28 HPV-infected HFK. The exponents are within or near the range of cell monolayer exponents observed in the intensity-based measurements (see Chapter 7.2.2). Given that HFK and HPV-infected HK are coming from two different sources, it is not clear how the change in power law exponent is different from, for example, a similar in magnitude change in exponents between HeLa and T84 cell monolayers (1.5 and 1.9). The authors go further with the analysis by looking at the difference between the polarized-gating residual and the power law fit. The resultant signal is fit to Mie theory, reporting a single Gaussian size distribution $d_{\text{HFK}} = 7.25 \pm 0.275 \mu\text{m}$, $m = 1.05$ and $d_{\text{HPV-HK}} = 4.38 \pm 0.437 \mu\text{m}$, $m = 1.055$. Both distributions are well correlated with the longitudinal dimension distribution of fluorescence stained nuclei. There are three general problems with the authors' conclusions. First, the nuclear index contrast is very high compared to our work from either single cell or cell monolayer measurements, and it is not allowed to go below $m = 1.04$ in the fitting routine. Second, the cell-border contribution is completely neglected. Third, the system sensitivity limits are not stated, while the fits have fine oscillatory structure at the level of 10^{-4} of $1/R99$ units.

An angular scattering study of EMT6 mouse mammary cell suspension is discussed in section 7.2.3 [7]. Forward scattering ($5^\circ < \theta < 90^\circ$, $\lambda = 633 \text{ nm}$) data have a smooth decay. The authors fit the decay with three types of small particle distributions (2 log-normal, 2-gaussian, 2-exponential) and conclude that the product of the distribution and the total scattering cross-section behave similarly for all three fitted results. The product has two peaks with the largest one around $2 \mu\text{m}$ and the smaller one near 100 nm . When same distributions are used in backscattering, the power law behavior observed in the cell monolayer studies is not reproduced: rather, the wavelength spectra are flat. Also, the maximum value of the product of these distributions times the backscattering cross-section is shifted towards the larger

value, compared to the value of the same product for power law size distribution reproducing the data (180 nm vs. 140 nm). There are two explanations for the difference in spectral behavior. Either EMT6 has different backscattering from HeLa, HT29, T84 and HFK cell suspensions/monolayers, or, in a more likely scenario, different particle distributions are responsible for scattering at different angles. If Born approximation is used, and angles are converted into spatial features (See section 7.2.3), the detected spatial features vary between 10 μm and 0.55 μm , which is quite different from a discrete sphere outcome of 2 μm . The lack of additional data does not allow for determination of which interpretation would be the correct one. The authors also analyze data from another paper [21], where a 2-log-normal distribution is generated from forward-side scattering data ($6^\circ < \theta < 170^\circ$, $\lambda = 633 \text{ nm}$) of AT3.1 and AT6.1 rat prostate cell lines. The result of the product of extracted distribution and total cross-section similarly peaks around 2 μm . In the following studies, the authors use their interpretation to describe scattering changes in mitochondria and lysosomes [22-24].

In another study of human retina cell monolayers (RPE), a power law in wavelength is measured in backscattering [25]. The curious part is that the extracted size distribution is not a power law, but rather a two peak distribution, which authors relate to the distribution of mitochondria measured with electron microscopy, similar to their original study in organelle fractions [26].

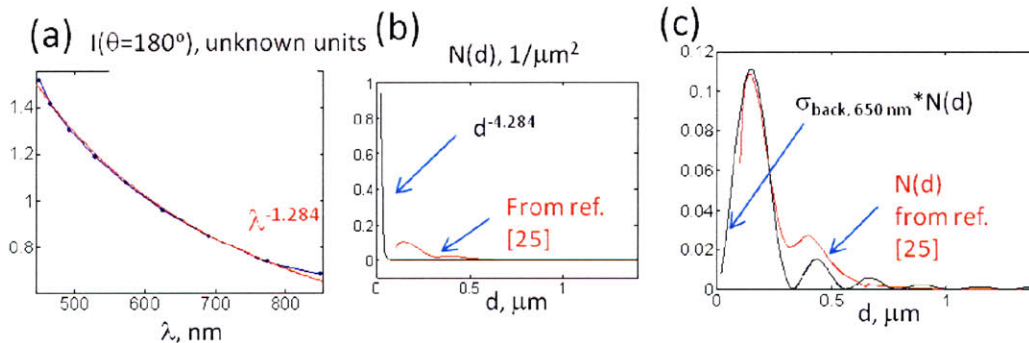


Figure 9.3 Analyses of backscattering power law in wavelength in ref. [25] a) Fit of the ref. data to power law in wavelength b) Comparison of the extracted power law size distribution to reported size distribution c) Product of the power law size distribution and backscattering cross-section at 650 nm, compared with reported size distribution

At the same time, this scattering spectrum can be fit well with a power law size distribution (Figure 9.3.a). When comparing, one can notice that two distributions are quite different (Figure 9.3.b). If the distribution from the paper is used, the power law in backscattering is not reproduced, which is quite a perplexing result. In light of the paper by Foster *et al.*, [7], and section 7.2.3, the product of the extracted power distribution and

backscattering cross-section at 650 nm is taken and agrees pretty well with the distribution from the paper (Figure 9.3.c). Therefore, most likely, the authors mistakenly report a product of size distribution and backscattering cross-section as a pure size distribution. But the takeaway message is that again a power law distribution with exponent of 1.284 is observed in backscattering of a cell monolayer and dominant scatterers are between 100 and 200 nm very similar to results of section 7.2.3.

Several studies are conducted with cells placed on top of highly scattering sample to model tissue scattering. These studies use polarization-gating to suppress the diffusely scattering signal [1, 3, 12, 27], which is discussed in detail in Chapter 8. All of these studies lack an important step of comparing cell signals with and without a highly scattering background.

In backscattering experiments with SiHa cells [12], the high relative nuclear index is reported to be 1.43-1.45 (with the cytoplasm at 1.39) and the signal is largely due to nuclear scattering. An interesting attempt is made by the authors of the study to interpret polarization-gated backscattering signal as a combination of backscattering and forward scattering of the light reflected back from interface of the underlying high reflectance standard. Therefore, backscattering is modeled as a linear combination of nuclear and cytoplasmic backscattering and forward scattering. The smoothness of the scattering spectra, and a number of model parameters makes the potential results of the fitting ambiguous.

In side scattering ($29^\circ < \theta < 48^\circ$) experiments of MCF7 and SiHa cells [28], high concentration (3×10^6) cell suspension scatterings are measured on top of a high-scattering reflector. The authors use polarization-gating and fit 11 residual wavelength spectra with a single Gaussian distribution. Given sensitivity of the Mie fits to the initial condition (see section 5.2.4), the authors vary the starting point of the fit. The lowest error and best fit is found for particle sizes of 2-3 μm . For SiHa cell, it provides an alternative interpretation of results to the fractal distribution treatment [14].

Some studies use theoretical approximations to understand aspects of cellular scattering. Their main weakness is the lack of knowledge about the refractive index contrast. For example, in a theoretical study of nuclear scattering modeling, an FDTD method is used to solve Maxwell's equations directly for the cervical cell nuclei [29]. The input of the FDTD simulation is a 3D-refractive index grid, which is determined from intensity of nucleus histopathological staining and assumed indexes of 1.39 for normal and 1.42 for dysplastic nucleus, while the cytoplasm is fixed at 1.36. In another study, the authors study the effect of

an inhomogeneous index distribution inside the sphere, using FDTD simulations [30]. Similarly to the results of single cell modeling in forward scattering (section 6.3.3), the authors conclude that particle-media interface dominates the total scattering cross-section, even with a fairly large index variation of inhomogeneities.

Two different groups address the effect of non-spherical shape of the scatterer (meaning nucleus) on using Mie theory or its approximations. In one case [31-33], the authors find that an approximate formula for total scattering cross-section of a sphere under certain conditions can be applied to describe the total scattering cross-sections of ellipsoids and higher order non-spherical objects. A different group of researchers theoretically studies angular backscattering from spheroids using the T-matrix formalism [34, 35]. In the study, one of the spheroidal dimensions can be fit to Mie theory, depending on the proper selection of the polarization axis. Also, the authors find a good fit to Mie theory for randomly oriented spheroids in the backscattering. The last paper's conclusions overlap quite nicely with the results from the single cell study in section 6.2.4, which state that forward scattering of a projection of an ellipsoid on a detection axis corresponds to scattering of a Mie sphere with a projection dimension.

9.2.4 Relevance of other tissue studies

Given the amount of variance in scattering modeling and interpretations for a relatively simple sample of cell monolayers or cell suspensions, it is very hard to compare data across tissue studies. The question of observing or not observing nuclear signatures in tissues, given the single cell, cell monolayer and cell suspension results, described in this thesis work, is supposed to be answered negatively (see Appendix for more). Until distribution of the refractive index is measured for a specific sample, the validity of the nuclear model of scattering cannot be readily established. For example, it is the case for rat esophagus tissue study, described below.

The same rat esophagus tissue has been studied using a low coherence Interferometry technique [36]. The coherence-gated signal allows focusing down on scattering from a specific optical depth in the tissue. The authors measure scattering between 180° and 155° at 845 nm. The authors claim that by focusing on or near the basal cell layer, they can extract a scattering signal, which has a smooth fractal component and a nuclear component with a size distribution in excellent agreement with histopathology, and a nuclear index contrast of ~ 1.045 - 1.06 . In a subsequent study with the same rat esophagus tissue [37], the authors

demonstrate the processing of the spectra in details. The raw spectrum is Fourier-filtered to exclude spatial frequencies above $10.4 \mu\text{m}$ (Figure 9.4.a), followed by a polynomial is fit to the data (Figure 9.4.b), and finally the difference between the smoothed data and polynomial fit is fit with Mie theory (Figure 9.4.c).

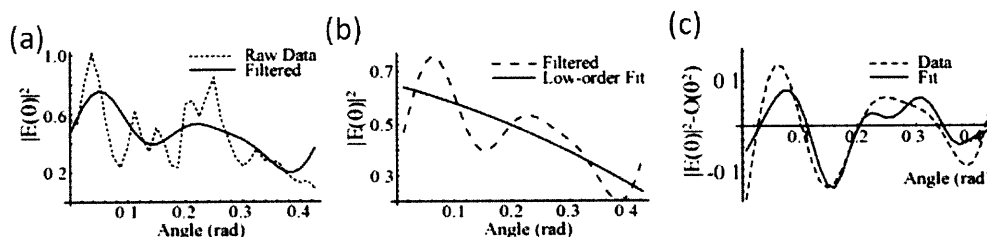


Figure 9.4 Figures are taken from reference [37, Figures 5-7], ©OSA reproduced with permission. Analysis of low-coherence interferometry measurements a) Raw experimental results and Fourier-filtered data b) Fourier-filtered data and low-order polynomial fit c) Data vs. Mie fit, low order polynomial is subtracted from both

First of all, authors leave out fractal interpretation, although the data is quite similar to the previous study. Second, from the measurements, the oscillatory part of the nuclear angular spectrum is at least 25% of the total signal and would have an even greater contribution, if the DC component of nuclear signal were taken into account. This high contribution of nuclei to scattering would be in agreement with a very high relative refractive index contrast of nuclei 1.058. Third, Fourier filtering of the signal effectively reduces the frequency of the observed scattering oscillations, cutting off particles above $10.4 \mu\text{m}$. It is possible that the scattering signal can be as well explained by a much larger particle size, for example, corresponding to the cell size.

9.3 Conclusion and future studies design

9.3.1 Conclusion and summary of this thesis and published works

Two types of scattering behavior are reported for a visible range of wavelengths and angular range of forward-to-backscattering in this thesis work: oscillatory behavior near exact forward and exact backscattering, as well as smooth power-like behavior in wavelength for all scattering angles except near forward scattering. Two key questions are addressed for diagnostic value of light scattering: detection of nuclear scattering signature, which can be directly related to cancer diagnostics, and parameter(s) characterizing smooth power law decay, which have to be shown to be diagnostically relevant. The 3D distribution of the refractive index contrast of intact cells was not measured previously, until my colleague Dr. Wonshik Choi developed a method for refractive index measurements in live cells [4]. The

value of the refractive index affects amplitude and shape of scattering contributions of various sub-cellular components. The index distribution within a cell will affect the feasibility of Mie analysis. Therefore, it is crucial for finding correct or, at least, discarding incorrect interpretations of scattering signals.

A lot of freedom has been taken with assigning a very large index contrast to the nuclei, making nuclei a major contributor to cell backscattering, as well as a significant contributor to cell forward scattering. As the author of this thesis is showing, even intensity-based measurements with index-matching and large particle signal enhancement methods can be used to test the presence of the large particle signatures (cell border and nucleus) in backscattering or forward scattering from cell monolayer or cell suspensions. These experiments show that the nuclear or cell border signal is not present in backscattering in detectable amounts, while forward scattering of cell suspensions is dominated by the cell border signal. The maximum **possible** average refractive index-value can be imposed on the nucleus, given a pre-measured size distribution using morphometry. These values are significantly lower than some of the previously reported numbers for the **same** cell types. Finally, the knowledge of the refractive index distribution allows to predict expected scattering signatures exactly; for example, the average index contrast of the nucleus compared to cytoplasm is much lower than previously predicted or observed. Therefore, the author of this thesis thinks, that the presence of nuclear signatures in scattering is unlikely or, at the very least, far from proven.

Smooth power law-like signals in wavelength are observed for most of the scattering angle range in cell suspension/monolayers and even tissue studies. Again, the power law is analyzed with discrete and continuous models, all of which work under certain assumptions. Under Born approximation, the wavelength spectrum can be converted into a relative contribution of spatial features, given the continuous distribution of the refractive index. This seems to be the least restrictive of all approaches. If one represents cell scattering by a discrete sphere distribution, then the power law of sphere distribution models backscattering, as well as some other distributions modeling side scattering. If one assumes a fractal distribution of refractive index in tissue and the Born approximation, then a couple of different interpretations are possible to model the scattering spectrum. The definite parameters are extracted from the measurements themselves, such as amplitude and the power law exponent of scattering spectrum. These parameters themselves show some diagnostic ability within a single sample, but their dynamic range is not large enough to make

these conclusions unique for any given sample. The extracted model parameters are sensitive to the fitting and do not really provide significantly more diagnostic information than purely experimental values, unless an independent conclusion about sub-cellular structure organization can be made. For example, in the 3D-refractive index measurements, no clear structure borders (which can cause scattering) are measured besides the cell border, nucleus and nucleoli, so the spherical model may be the most questionable one.

9.3.2 Future designs of light scattering studies

With the development of the refractive index measurement technique in intact cells, the intensity-based light scattering experiments should follow refractive index measurements. Scattering changes are directly related to changes in the refractive index in the sample, which in turn are directly related to changes in sub-cellular structure. Therefore, monitoring refractive index changes allows more direct access to sub-cellular structure changes, which has been shown in acetic acid application studies [18]. Currently, refractive index measurements can only be done at a single cell level, but a lot of diagnostically relevant applications are at the multi-cellular level. Therefore, establishing a connection between single-cell refractive index studies and multi-cellular light scattering studies is important in developing diagnostically relevant applications. The current thesis works is an example of such a connection being established.

References

- [1] Backman V, Gurjar R, Badizadegan K, Itzkan L, Dasari RR, Perelman LT, Feld MS. Polarized light scattering spectroscopy for quantitative measurement of epithelial cellular structures in situ. *Ieee Journal of Selected Topics in Quantum Electronics* 1999;5:1019.
- [2] Yu CC, Lau C, Tunnell JW, Hunter M, Kalashnikov M, Fang-Yen C. Assessing epithelial cell nuclear morphology by using azimuthal light scattering spectroscopy. *Optics Letters* 2006;31:3119.
- [3] Backman V, Gopal V, Kalashnikov M, Badizadegan K, Gurjar R, Wax A, Georgakoudi I, Mueller M, Boone CW, Dasari RR, Feld MS. Measuring cellular structure at submicrometer scale with light scattering spectroscopy. *Ieee Journal of Selected Topics in Quantum Electronics* 2001;7:PII S1077.
- [4] Choi W, Fang-Yen C, Badizadegan K, Oh S, Lue N, Dasari RR, Feld MS. Tomographic phase microscopy. *Nature Methods* 2007;4:717.
- [5] Born M, Wolf E. *Principles of Optics*. Cambridge: Cambridge University Press, 2005.
- [6] Lembke U, Hoell A, Kranold R, Muller R, Schuppel W, Goerigk G, Gilles R, Wiedenmann A. Formation of magnetic nanocrystals in a glass ceramic studied by small-angle scattering. *Journal of Applied Physics* 1999;85:2279.
- [7] Wilson JD, Foster TH. Mie theory interpretations of light scattering from intact cells. *Optics Letters* 2005;30:2442.

- [8] Hunter M, Backman V, Popescu G, Kalashnikov M, Boone CW, Wax A, Gopal V, Badizadegan K, Stoner GD, Feld MS. Tissue Self-Affinity and Polarized Light Scattering in the Born Approximation: A New Model for Precancer Detection. *Physical Review Letters* 2006;97:138102.
- [9] Wax A, Yang C, Backman V, Badizadegan K, Boone CW, Dasari RR, Feld MS. Cellular Organization and Substructure Measured Using Angle-Resolved Low-Coherence Interferometry. *Biophysical Journal* 2002;82:2256.
- [10] Graf R, Wax A. Nuclear morphology measurements using Fourier domain low coherence interferometry. *Opt. Express* 2005;13:4693.
- [11] Brunsting A, Mullaney PF. Differential Light Scattering from Spherical Mammalian Cells. *Biophysical Journal* 1974;14:439.
- [12] Sokolov K, Drezek R, Gossage K, Richards-Kortum R. Reflectance spectroscopy with polarized light: is it sensitive to cellular and nuclear morphology. *Opt. Express* 1999;5:302.
- [13] Giacomelli MG, Chalut KJ, Ostrander JH, Wax A. Application of the T-matrix method to determine the structure of spheroidal cell nuclei with angle-resolved light scattering. *Opt. Lett.* 2008;33:2452.
- [14] Wu TT, Qu JY, Xu M. Unified Mie and fractal scattering by biological cells and subcellular structures. *Optics Letters* 2007;32:2324.
- [15] Xu M, Wu TT, Qu JAY. Unified Mie and fractal scattering by cells and experimental study on application in optical characterization of cellular and subcellular structures. *Journal of Biomedical Optics* 2008;13.
- [16] Wu TT, Qu JY. Assessment of the relative contribution of cellular components to the acetowhitening effect in cell cultures and suspensions using elastic light-scattering spectroscopy. *Applied Optics* 2007;46:4834.
- [17] Xu M, Alfano RR. Fractal mechanisms of light scattering in biological tissue and cells. *Optics Letters* 2005;30:3051.
- [18] Choi W, Yu C-C, Fang-Yen C, Badizadegan K, Dasari RR, Feld MS. Field-based angle-resolved light-scattering study of single live cells. *Opt. Lett.* 2008;33:1596.
- [19] Choi W, Yu CC, Fang-Yen C, Badizadegan K, Dasari RR, Feld MS. Field-based angle-resolved light-scattering study of single live cells. *Optics Letters* 2008;33:1596.
- [20] Claudia Mujat CG, Amy Baldwin, Jonathan M. Levitt, Fenghua Tian, Lee A. Stucenski, Martin Hunter, Young L. Kim, Vadim Backman, Michael Feld, Karl Menger, Irene Georgakoudi. Endogenous optical biomarkers of normal and human papillomavirus immortalized epithelial cells. *International Journal of Cancer* 2008;122:363.
- [21] Mourant JR, Johnson TM, Carpenter S, Guerra A, Aida T, Freyer JP. Polarized angular dependent spectroscopy of epithelial cells and epithelial cell nuclei to determine the size scale of scattering structures. *Journal of Biomedical Optics* 2002;7:378.
- [22] Wilson JD, Bigelow CE, Calkins DJ, Foster TH. Light scattering from intact cells reports oxidative-stress-induced mitochondrial swelling. *Biophysical Journal* 2005;88:2929.
- [23] Wilson JD, Cottrell WJ, Foster TH. Index-of-refraction-dependent subcellular light scattering observed with organelle-specific dyes. *Journal of Biomedical Optics* 2007;12.
- [24] Wilson JD, Foster TH. Characterization of lysosomal contribution to whole-cell light scattering by organelle ablation. *Journal of Biomedical Optics* 2007;12.
- [25] Georg S, Edward V, Philip H, Caitlin OC-R, Daniel P, Lev TP. Optical spectroscopy noninvasively monitors response of organelles to cellular stress. *Journal of Biomedical Optics* 2005;10:051404.
- [26] Fang H, Ollero M, Vitkin E, Kimerer LM, Cipolloni PB, Zaman MM, Freedman SD, Bigio IJ, Itzkan I, Hanlon EB, Perelman LT. Noninvasive sizing of subcellular organelles with light scattering spectroscopy. *Ieee Journal of Selected Topics in Quantum Electronics* 2003;9:267.

- [27] Bartlett M, Huang G, Larcom L, Jiang HB. Measurement of particle size distribution in mammalian cells in vitro by use of polarized light spectroscopy. *Applied Optics* 2004;43:1296.
- [28] Bartlett M, Huang G, Larcom L, Jiang HB. Measurement of particle size distribution in mammalian cells in vitro by use of polarized light spectroscopy. *Applied Optics* 2004;43:1296.
- [29] Drezek R, Guillaud M, Collier T, Boiko I, Malpica A, Macaulay C, Follen M, Richards-Kortum R. Light scattering from cervical cells throughout neoplastic progression: influence of nuclear morphology, DNA content, and chromatin texture. *Journal of Biomedical Optics* 2003;8:7.
- [30] Chen ZG, Taflove A, Backman V. Equivalent volume-averaged light scattering behavior of randomly inhomogeneous dielectric spheres in the resonant range. *Optics Letters* 2003;28:765.
- [31] Li X, Chen ZG, Gong JM, Taflove A, Backman V. Analytical techniques for addressing forward and inverse problems of light scattering by irregularly shaped particles. *Optics Letters* 2004;29:1239.
- [32] Chen ZG, Taflove A, Backman V. Concept of the equiphase sphere for light scattering by nonspherical dielectric particles. *Journal of the Optical Society of America a-Optics Image Science and Vision* 2004;21:88.
- [33] Li X, Chen ZG, Taflove A, Backman V. Equiphase-sphere approximation for analysis of light scattering by arbitrarily shaped nonspherical particles. *Applied Optics* 2004;43:4497.
- [34] Keener JD, Chalut KJ, Pyhtila JW, Wax A. Application of Mie theory to determine the structure of spheroidal scatterers in biological materials. *Opt. Lett.* 2007;32:1326.
- [35] Chalut KJ, Giacomelli MG, Wax A. Application of Mie theory to assess structure of spheroidal scattering in backscattering geometries. *J. Opt. Soc. Am. A* 2008;25:1866.
- [36] Wax A, Yang C, Muller MG, Nines R, Boone CW, Steele VE, Stoner GD, Dasari RR, Feld MS. In Situ Detection of Neoplastic Transformation and Chemopreventive Effects in Rat Esophagus Epithelium Using Angle-resolved Low-coherence Interferometry. *Cancer Res* 2003;63:3556.
- [37] Pyhtila J, Graf R, Wax A. Determining nuclear morphology using an improved angle-resolved low coherence interferometry system. *Opt. Express* 2003;11:3473.

Appendix

Feasibility of extracting nuclear morphology from tissue backscattering

Polarization-gating method, described in detail in sections 8.1.1 and 8.2.5 of the thesis, was originally designed to discriminate singly scattering components associated with cell nuclei in the top layer of the biological tissue from the diffuse scattering and absorption originated from a layer beneath the epithelial layer [1]. The so-called residual signal, the difference of angular scattering spectra acquired when polarizer and analyzer are in parallel and in perpendicular, was claimed to have scatterings only from the top layer of epithelial cells. The authors modeled the residual signal with Mie theory, extracted spherical size distribution for fixed index contrast and associated extracted size distribution with distribution of nuclear sizes. They validate this approach by measuring scattering from the phantom which consists of polystyrene beads immersed in either water or glycerol on top of highly scattering substrate. More realistic phantom was also tested in which a layer of epithelial cells, T84 cells, are prepared on top of the same substrate. Authors then proceeded with human tissue experiments and attributed residual backscattered signals to backscattering from cell nuclei.

It seems to be feasible to extract the size of polystyrene beads from the diffuse background due to high index contrast of beads to medium. But when it comes to the T84 cells, the residual signal is one or two orders of magnitude smaller than the original scattering spectra. Thus the subtraction operation can be highly subject to inaccuracy. Indeed, the residual signal of normal intestine cells and T84 cells are highly noisy and the accuracy of fitting the data with Mie theory is questionable.

In this thesis, the highly scattering substrate is replaced by a transparent coverglass in order to study backscattering purely originated from the top epithelial cell layer. This eliminates imperfectness of polarization gating method in rejecting the diffuse background. With this careful approach, it is shown that backscattering from a top layer by itself is dominated by smaller structures. Nuclear scattering is only about 0.1 % of the total scattering signal and was not detectable in three different types of cell monolayers, including the T84 type described in the original paper. With the aid of refractive index tomograms, it can be established that the relative contrast of the T84 cell nucleus to that of the cytoplasm is much smaller than was previously assumed. Repeating analysis of HT29 single cell tomogram from

section 6.3, the relative refractive index contrast of T84 cell nuclei is $m_{\text{tomogram}}=1.003$, which differs significantly from the previously reported value of $m_{\text{reported}}=1.04$. For the size distribution presented in the original paper $d=9.8\pm 1.5 \mu\text{m}$ [1], this difference in contrast can reduce the nuclear contribution to the single backscattering signal by more than 2 orders of magnitude. The value of the drop is estimated using Mie theory. This conclusion agrees with a lack of nuclear signal in intensity-based cell monolayer experiments described in section 7.2 of this thesis work. Therefore, backscattering in validation experiment for polarization-gating may not be interpreted correctly. Given these findings, further expansion of this analysis to interpretation of tissue backscattering seems highly unjustified.

The development of polarization-gating method is preceded by a model-based approach in analyzing backscattering from tissue [2]. Similar to polarization-gating, the tissue is assumed to be a two-layer structure: a top layer consisting of nuclei on top of the highly scattering and absorptive diffuse background. Nuclei are again assumed to be the only scatterers in the top layer. Unlike polarization-gating experiment, the underlying diffuse background contribution is removed through modeling, not by the experiment.

According to the model, tissue backscattering has three components: backscattering from nuclei, backscattering from the diffuse scattering layer, and forward scattering of diffuse light by the nuclei. In the case of T84 cell phantom (see first paragraph), the contribution of the bottom layer to backscattering can be directly measured without the top layer and was removed from the total backscattering signal. In the case of tissue, the scattering of the bottom layer is deduced using the model for diffuse scattering and absorption described by Zonios *et. al.* [3]. In the diffuse model, scattering is described as a function of scattering and absorption coefficients. The parameters of the model are varied until the best fit is determined. The difference between original scattering data and the diffuse model fit is taken. The residual signal is analyzed with the nuclear model, described below.

The key approximations in the nuclear model of Perelman *et. al.* is that backscattering and forward scattering contributions to the total backscattering signal have an oscillatory component related to nuclear scattering and can be expressed through an analytical formula based on the total scattering cross-section [4]. Forward scattering and backscattering from nuclei have the same oscillatory frequency in wavelength, but backscattering is out-of-phase with forward scattering. The authors conclude that Fourier transforming the oscillatory part of the signal will reveal the distribution of nuclear sizes, while the amplitude of the Fourier component is related to nuclear density. The model is applied to analyze the T84 cell

phantom described in the polarization-gating study and normal colon cells. Size distribution of nuclei is reported. The authors also measure nuclear size distribution in Barrett's esophagus tissue ex-vivo. In subsequent studies, this analysis is combined with fluorescence analysis in tri-modal spectroscopy and applied to cancer diagnoses in various tissues. The nuclear size distribution is an important diagnostic measurement in these studies [5-8].

In the paper by Lau *et. al.* [9], a critical analysis of the model-based approach to extract backscattering is conducted. The authors re-analyzed the same tissue data as presented in the tri-modal spectroscopy tissue paper [6] including numerical simulations and polystyrene microsphere phantom experiments. First, the authors create a model of scattering by a two layer tissue phantom. For the bottom layer, the same model as in the original paper [2] is used to describe diffuse scattering using realistic optical properties. For the top layer, distributions of Mie spheres are used with various relative refractive index contrast values. After the diffuse scattering contribution is removed, the residual signal does not exhibit the same oscillatory component as the total or forward scattering component generated from the sphere distribution, contrary to the prediction by *Perelman et al.* Moreover, the residual signal is quite similar for different size distributions in the top layer. Therefore, scatterers in the top layer have little effect on the residual signal. The latter conclusion is confirmed with phantom studies of polystyrene microspheres solution in refractive-index matched oil on top of intralipid. In these experiments, backscattering spectra do not change for large differences in particle size and refractive index contrasts of the top layer scatterers.

Second, the authors modify the model of the bottom layer reflectance to include a heterogeneous distribution of hemoglobin. Hemoglobin is confined to blood vessels, and its density throughout the tissue varies greatly. Then authors re-analyze the original data from *Georgakoudi et. al.* and compare residual spectra obtained with and without the use of hemoglobin correction. The fits to the reflectance spectra are improved with the correction, and the residual signal previously attributed to the scattering from epithelial layer is simply due to heterogeneity of the blood distribution. Finally, the numerical simulation of the diffuse reflectance data is performed. Scattering data for the bottom layer are generated for a range of feasible parameters with the hemoglobin correction factor included. The data are processed with the model of *Zonios et. al.* without hemoglobin correction. Fourier-transform analysis is performed on the residual spectra. The extracted size distributions are very sensitive to the exact wavelength range used. Changes in wavelength range by 40 nm (350-700 nm vs. 390-700 nm) cause a 40% change in extracted nuclear diameter.

According to the single cell and cell suspension/monolayer studies presented in this thesis, nuclear scattering is at most 0.1% of the backscattering signal and 10% of the forward scattering from the single cell layer (see sections 7.1, 7.2.1 and 6.3). Therefore the original two-layer model assumption by Perelman *et. al.* [2], that reflectance spectrum of the top layer is dominated by nuclear scattering, is incorrect due to the relatively small contribution of the nuclear scattering to the total scattering of the top layer. This is supported by the recent work of Lau *et. al* [9] in which they proved that the previously extracted nuclear signal [2] is not from nuclei but from improper subtraction of diffuse background, and the residual interpretation with nuclear model is very sensitive to noise level. This is mainly due to the weak contribution of nuclei to the scattering. In fact, the addition of diffuse background further increases an uncertainty in determining origins of the scattering signal, and decreases the relative contribution of the scattering by nuclei by another order or two orders of magnitude to about 0.001% of total scattering signal. Therefore, even slight errors in modeling of diffuse scattering will affect greatly the outcome of top layer scattering interpretation. The conclusions derived from this thesis work reinforce the negative outcome of the study of Lau *et. al* [9] on application of nuclear model of scattering to tissue.

References:

- [1] Backman V, Gurjar R, Badizadegan K, Itzkan L, Dasari RR, Perelman LT, Feld MS. Polarized light scattering spectroscopy for quantitative measurement of epithelial cellular structures in situ. *IEEE Journal of Selected Topics in Quantum Electronics* 1999;5:1019.
- [2] Perelman LT, Backman V, Wallace M, Zonios G, Manoharan R, Nusrat A, Shields S, Seiler M, Lima C, Hamano T, Itzkan I, Van Dam J, Crawford JM, Feld MS. Observation of periodic fine structure in reflectance from biological tissue: A new technique for measuring nuclear size distribution. *Physical Review Letters* 1998;80:627.
- [3] Zonios G, Perelman LT, Backman VM, Manoharan R, Fitzmaurice M, Van Dam J, Feld MS. Diffuse reflectance spectroscopy of human adenomatous colon polyps in vivo. *Applied Optics* 1999;38:6628.
- [4] Hulst H. *Light scattering by small particles*. New York: Dover Publications, 1981.
- [5] Backman V, Wallace MB, Perelman LT, Arendt JT, Gurjar R, Muller MG, Zhang Q, Zonios G, Kline E, McGillican T, Shapshay S, Valdez T, Badizadegan K, Crawford JM, Fitzmaurice M, Kabani S, Levin HS, Seiler M, Dasari RR, Itzkan I, Van Dam J, Feld MS. Detection of preinvasive cancer cells. *Nature* 2000;406:35.
- [6] Georgakoudi I, Jacobson BC, Van Dam J, Backman V, Wallace MB, Muller MG, Zhang Q, Badizadegan K, Sun D, Thomas GA, Perelman LT, Feld MS. Fluorescence, reflectance, and light-scattering spectroscopy for evaluating dysplasia in patients with Barrett's esophagus. *Gastroenterology* 2001;120:1620.
- [7] Georgakoudi I, Sheets EE, Muller MG, Backman V, Crum CP, Badizadegan K, Dasari RR, Feld MS. Trimodal spectroscopy for the detection and characterization of cervical precancers in vivo. *American Journal of Obstetrics and Gynecology* 2002;186:374.

- [8] Muller MG, Valdez TA, Georgakoudi I, Backman V, Fuentes C, Kabani S, Laver N, Wang ZM, Boone CW, Dasari RR, Shapshay SM, Feld MS. Spectroscopic detection and evaluation of morphologic and biochemical changes in early human oral carcinoma. *Cancer* 2003;97:1681.
- [9] Lau C, Scepanovic O, Mirkovic J, McGee S, Yu CC, Fulghum S, Wallace M, Tunnell JW, Bechtel K, Feld M. Re-evaluation of model-based LSS for tissue spectroscopy. *Journal of Biomedical Optics* 2009;in press.

Curriculum Vitae

MAXIM KALASHNIKOV

EDUCATION

- Massachusetts Institute of Technology, Cambridge, MA*
Ph.D. in Physical Chemistry **2000-2009**
Dissertation: "Validation of angle-resolved polarized light scattering spectroscopy as a diagnostic tool for pre-cancer detection"
- Stanford University, Palo Alto, CA*
Graduate Student in Physical Chemistry **1999-2000**
- Moscow Institute of Physics and Technology, State University, Moscow, Russia*
B.S. in Mathematics and Physics **1995-1999**
Area of Concentration: Chemical physics

RESEARCH EXPERIENCE

- Massachusetts Institute of Technology, Cambridge, MA*
Research Assistant: **2000-2009**
Project: "Application of light scattering spectroscopy to study of sub-cellular structures"
Biological samples: Growth, maintenance, and characterization of cell cultures. Histopathological processing and analysis of tissue sections
Instrumentation: Design, construction and calibration of angle and wavelength-resolved light scattering instruments
Theoretical modeling: Interpretation of scattering data from cells and tissues using numerical and analytical models of scattering
- Stanford University, Palo Alto, CA*
Research Assistant **1999 – 2000**
Project: "Photo-induced electron transfer in complex liquids"
Sample preparation and measurement of life-times of electron transfer in complex liquids
- Semenov Institute of Chemical Physics, Moscow, Russia*
Undergraduate Research Project **1998-1999**
Project: "Study of nuclear vibrational dynamics using ultrafast laser spectroscopy"

TEACHING EXPERIENCE

- Massachusetts Institute of Technology, Cambridge, MA*
Teaching assistant **2000**
Course: "Experimental methods in physical chemistry"
- Stanford University, , Palo Alto, CA*
Teaching assistant **1999 – 2000**
Courses: "Physical chemistry laboratories" and "Organic chemistry laboratories"

PUBLICATIONS AND PAPERS

- Hunter M, Backman V, Popescu G, **Kalashnikov M**, Boone CW, Wax A, Gopal V, Badizadegan K, Stoner GD, Feld MS. Tissue Self-Affinity and Polarized Light Scattering in the Born Approximation: A New Model for Precancer Detection. *Physical Review Letters* 2006;97:138102.
- Yu CC, Lau C, Tunnell JW, Hunter M, **Kalashnikov M**, Fang-Yen C. Assessing epithelial cell nuclear morphology by using azimuthal light scattering spectroscopy. *Optics Letters* 2006;31:3119.
- Seeing Small Biological Structures with Light, Popescu G, Fang-Ye C, Deflores L, Chu M, Hunter M, **Kalashnikov M**, Badizadegan K, Boone C, Dasari RR and Feld MS, in *Laser Spectroscopy XVI*, Hannaford P, Sidorov A, Bachor H and Baldwin, K, editors. (World Scientific, Singapore, 2003); 375-382.
- Wax A, Yang CH, Backman V, **Kalashnikov M**, Dasari RR, Feld MS. Determination of particle size by using the angular distribution of backscattered light as measured with low-coherence interferometry. *Journal of the Optical Society of America a-Optics Image Science and Vision* 2002;19:737.
- Backman V, Gopal V, **Kalashnikov M**, Badizadegan K, Gurjar R, Wax A, Georgakoudi I, Mueller M, Boone CW, Dasari RR, Feld MS. Measuring cellular structure at submicrometer scale with light scattering spectroscopy. *Ieee Journal of Selected Topics in Quantum Electronics* 2001;7:PII S1077.
- "Photoinduced Intermolecular Electron Transfer in Complex Liquids: Experiment and Theory," H. L. Tavernier, **M. M. Kalashnikov**, and M. D. Fayer. *J. Chem. Phys.* **113**, 10191-10201 (2000).

CONFERENCE PRESENTATIONS

- Hunter M, **Kalashnikov M**, Backman V., Popescu G., Badizadegan K, Stoner GD, Feld MS. , Light scattering spectroscopy for measurement of sub-cellular structure, Poster session, Gordon Research Conference, 2006
- **Kalashnikov M**, Hunter M., Backman V., Popescu G., Boone C., Badizadegan K., Nines R., Stoner G., Feld M, Pushing the limits of particle sizing using polarized light scattering spectroscopy, Poster session, Gordon Research Conference, 2004
- "Diffuse Reflectance Spectroscopy as an *In Vivo* Tool for Characterizing Changes in Tissue Organization during Neoplastic Development" Georgakoudi I, Backman V, Müller M, Wallace M, Jacobson B, Badizadegan K, Wax A, **Kalashnikov M**, Hunter M, Dasari RR, Van Dam J, and Feld MS. Biomedical Topical Meeting of the Optical Society of America, Miami Beach, Florida, April 7-10, 2002.
- Imaging and Measurement of Cell Structure and Organization with Submicron Accuracy Using Light Scattering Spectroscopy, Backman V, Gurjar R, Perelman L, Gopal V, **Kalashnikov M**, Badizadegan K, Wax A, Georgakoudi I, Müller MG, Boone CW, Itzkan I, Dasari RR and Feld MS. *Proceedings of the SPIE* **4613**: 101-110 (2002).